# EFFECTS OF PHYSICAL PROPERTIES AND RHEOLOGICAL

# CHARACTERISTICS ON CRITICAL SHEAR STRESS

# OF FINE SEDIMENTS

A Dissertation
Presented to
The Academic Faculty

By

Yung-Chieh (Becky) Wang

In Partial Fulfillment
Of the Requirements for the Degree
Doctor of Philosophy in Civil Engineering

Georgia Institute of Technology

May 2013

# EFFECTS OF PHYSICAL PROPERTIES AND RHEOLOGICAL

# CHARACTERISTICS ON CRITICAL SHEAR STRESS

# OF FINE SEDIMENTS

Approved by:

Dr. Terry W. Sturm, Advisor
School of Civil and Environmental
Engineering
*Georgia Institute of Technology*

Dr. Philip J. Roberts
School of Civil and Environmental
Engineering
*Georgia Institute of Technology*

Dr. Donald R. Webster
School of Civil and Environmental
Engineering
*Georgia Institute of Technology*

Dr. Susan E. Burns
School of Civil and Environmental
Engineering
*Georgia Institute of Technology*

Dr. Karl I. Jacob
School of Materials Science and
Engineering
*Georgia Institute of Technology*

Date Approved: March 25, 2013

# ACKNOWLEDGEMENTS

# TABLE OF CONTENTS

# LIST OF TABLES

# LIST OF FIGURES

# LIST OF SYMBOLS

| | |
|---|---|
| $A_f$ | Frontal area of a particle |
| $A_h$ | Hamaker constant |
| $A_{MB}$ | Area covered by one MB molecule |
| $AIC_p$ | Akaike's information criterion for model selection |
| $b$ | Width of the flume |
| $C_D$ | Drag coefficient |
| $Clay$ | Clay content (particle smaller than 2 µm) by mass; decimal fraction |
| $C_v$ | Volumetric concentration of solids |
| $C_p$ | Mallows' $C_p$ criterion for regression model selection |
| $CV$ | Coefficient of variation |
| $c_0$ | Ionic concentration of pore fluid |
| $D$ | Hydrodynamic drag force |
| $d$ | Spherical particle diameter; sediment grain size |
| $d_{50}$ | Median particle size |
| $E$ | Erosion rate of sediments |
| $E_y$ | Young's modulus |
| $e$ | Volumetric erosion rate of sediments |
| $e_i$ | Residuals of the $i$th data point of a response variable |

| | |
|---|---|
| $e_0$ | Electron charge $= 1.602 \times 10^{-19} C$ |
| $F$ | Faraday's constant $= 9.6485 \times 10^4 \, C/mol$ |
| $F_A$ | Interparticle adhesion or cohesion force |
| $F_i$ | Attracting forces between two particles; $i = c, pp, ss, sp$ |
| $Fines$ | Fine content; decimal fraction of particles smaller than 62 µm by mass |
| $Fr$ | Froude number |
| $f$ | Friction factor |
| $f_b$ | Wall friction factor |
| $f_w$ | Bed friction factor |
| $G_s$ | Specific gravity |
| $I_p$ | Plasticity index |
| $IS$ | Ionic strength |
| $k$ | Boltzmann's constant $= 1.38 \times 10^{-23} \, J/K$ |
| $k_s$ | Equivalent sand grain roughness height |
| $\kappa_s$ | Specific conductivity |
| $Kaolin$ | Kaolin content by dry weight; decimal fraction |
| $MW$ | Molecular weight of MB |
| $M_s$ | Mass of soil solids in suspension |
| $m_{wet}$ | Mass of the wet sediment |
| $m_s$ | Mass of solid (dry sediment) |
| $m_w$ | Mass of pore water |

| | |
|---|---|
| $m_{pw}$ | Mass of pycnometer and water |
| $m_{pws}$ | Mass of pycnometer, water, and soli solids |
| $N_{av}$ | Avogadro's number $= 6.022 \times 10^{23} \ 1/mol$ |
| $N_{drop}$ | Number of drops of MB solution added |
| $n$ | Total number of the observations (data points) |
| $n_b$ | Manning's roughness coefficient |
| $Q, Q_0$ | Flow rate, measured flow rate |
| $p$ | Number of the parameters in an multiple regression model |
| $q_i$ | Charge of a particle; $i = 1, 2, ...$ |
| Re | Reynolds number |
| $R$ | Hydraulic radius |
| $R_b$ | Bed hydraulic radius |
| $R_i$ | Radius of a spherical particle; $i = 1, 2, ...$ |
| $R_{DL}$ | Double layer repulsion force per unit area |
| $R^2$ | Coefficient of multiple determination |
| $R_a^2$ | Adjusted coefficient of multiple determination |
| $r$ | Distance between two particles |
| $S_0$ | Channel bed slope |
| St. dev. | Standard deviation |
| $SE$ | Standard error |

| | |
|---|---|
| $SSA$ | Specific surface |
| $SS_E$ | The unexplained variance (random variance) of the response variable |
| $SS_R$ | The explained variance of the response variable by a regression model |
| $SS_T$ | The total variance of the response variable |
| $T$ | Temperature |
| $t$ | Time |
| $U$ | Buoyancy acts on a soil particle |
| $u_*$ | Shear velocity |
| $V$ | Approach flow velocity; mean flow velocity in open channel flow |
| $V_t$ | Total volume of the sediment matrix |
| $V_w$ | Volume of pore water |
| $V_s$ | Volume of solids (dry sediments) |
| $V_{sol}$ | Volume of MB solution |
| $(VIF)_k$ | Variance inflation factor of a predicting variable $x_k$ |
| $W$ | Weight of a soil particle |
| $W_s$ | Submerged weight of a soil particle in water |
| $w$ | Water (moisture) content |
| $w_{LL}$ | Liquid limit |
| $w_{PL}$ | Plastic limit |
| $x_{k,i}$ | The $i^{\text{th}}$ data point of the predicting variable $x_k$ |
| $y$ | Flow depth at the centerline of the channel |

| | |
|---|---|
| $y_i$ | The $i^{th}$ data point of the response variable |
| $z_i$ | Ionic valence of a particle; $i = 1,2,...$ |
| $\varepsilon_f$ | Flow erosion rate at $\tau = \tau_c$ |
| $\varepsilon_0$ | Permittivity of vacuum $= 8.85 \times 10^{12} \, F/m$ |
| $\rho_w$ | Density of water |
| $\rho_b$ | Bulk density of sediments |
| $\rho_s$ | Density of solids |
| $\rho_d$ | Dry density of sediments |
| $\rho_{silt}$ | Dry density of silt |
| $\rho_{kaolin}$ | Dry density of Georgia kaolin |
| $\nu$ | Kinetic viscosity of water |
| $\mu$ | Dynamic viscosity of fluid |
| $\mu_1, \mu_2, G_1, G_2$ | Material constants in viscoplastic constitutive equations |
| $\mu_0, \mu_\infty$ | Asymptotic dynamic viscosities at zero and infinite strain rates |
| $\eta_0, \eta_{pl}$ | Zero-shear-rate viscosity, plastic viscosity |
| $\tau$ | Applied or bed shear stress |
| $\tau_c$ | Critical shear stress |
| $\tau_{c,z}$ | Critical shear stress of sediment layer at depth $z$; at the surface: $z = 0$ |
| $\tau_c^*$ | Shields parameter |

| | |
|---|---|
| $\tau_L$ | Upper limit of shear stress under which fine sediments show the linear viscoelastic behavior |
| $\tau_{min}, \tau_{max}$ | Minimum and maximum applied shear stress during rheometer tests |
| $\tau_B, \tau_y, \tau_{y1}, \tau_{y2}$ | Bingham yield stress, yield stress; lower yield stress, upper yield stress |
| $\tau_y^*$ | Dimensionless yield stress |
| $\vartheta$ | Double layer thickness of a clay particle |
| $\gamma$ | Shear strain |
| $\dot{\gamma}$ | Strain rate |
| $\gamma_w$ | Specific weight of water |
| $\gamma_s$ | Specific weight of sediments |
| $\Delta$ | Strain rate increment per unit time |
| $\lambda_1, \lambda_2$ | Time constants: relaxation time, retardation rime |
| $M, n, \alpha, \beta, a_i, b_i$ | Constants relating to sediment erosion |
| $k, m, \lambda, \eta, \xi$ | Constants in constitutive equations |

# SUMMARY

Flow obstruction in a river such as that caused by a bridge pier or abutment causes perturbation of the river flow field which introduces a complex local flow condition. During high flow rates, the acceleration of flow and generation of turbulence around bridge foundations leads to scouring, defined as the removal of bed sediments. Due to the interparticle physico-chemical forces of clay particles, erodibility and transport mechanisms for fine sediments are different from those for coarse sediments. From the current research on sediment transport, the capability to predict erosion resistance of fine sediments is still in question. In this study, silt-clay soil mixtures with different kaolin contents, ranging from 10% to 100%, were prepared by mixing ground silica and Georgia kaolin with tap water for the purpose of measuring their erosion resistance and relating it to soil properties. Geotechnical tests were carried out to obtain the physical properties of the specimens including water content, bulk density, and grain size distribution. The temperature, pH value, and specific conductivity of the soil mixtures were measured by a portable pH/conductivity meter. The critical shear stress and yield stress of the soil mixtures were determined through hydraulic flume experiments and rheometer tests, respectively. Particle associations of the soil specimens were observed using the technique of scanning electron microscopy (SEM).

From the laboratory work and data analysis, relationships among the critical shear stress, yield stress, and the soil physical properties were developed from multiple regression analysis. Specifically, values of the critical shear stress and yield stress can be predicted by bulk density and clay content. In dimensionless form, a relationship for the Shields parameter and dimensionless yield stress as a function of water content and clay

content is proposed. Finally, a single relationship is obtained to predict the Shields parameter as a function of the corresponding dimensionless yield stress of the silt-clay mixtures in this study. The results from this research can be used to provide a methodology for engineering applications requiring the value of critical shear stress such as estimating fine sediment bed stability and assessing the erosion risk of river beds in proximity to bridge foundations and other flow obstructions.

# CHAPTER I

# INTRODUCTION

## 1.1 Background

Degradation, aggradation, and transport of sediments are recognized as important factors in river morphology and evolution. For very long time scales, undisturbed river systems develop a dynamic equilibrium between the erosion and deposition of alluvial sediments caused by the hydrodynamic forces of the flow; such rivers are called "graded streams" (Mackin, 1948). When a river is disturbed from its natural evolution by a flow obstruction such as a bridge pier and abutment on a much shorter engineering time scale, perturbation of the flow field introduces a complex local flow condition, including horseshoe vortices, surface rollers, and wake vortices (Ettema et al., 2006). During high flow rates, acceleration of flow through the contracted section caused by bridge abutments, as well as high bed shear stresses and turbulence around bridge foundations lead to removal of bed sediments, which is known as scour. The contraction and local scour result in undermining of bridge foundations and are found to be the main causes of hydraulic construction failure historically (Debnath and Chaudhuri, 2010b).

Stability of the river bed depends on the balance between hydrodynamic forces and the resistive forces within bed sediments due to gravity and interparticle interactions. While the submerged weight of particles is the dominant resistive force for coarse particles (gravel and sand), it is the interparticle electrochemical forces of fine-grained sediments which are responsible for the resistance to erosion. Erodibility is a measure of

sediment resistance to erosion and is often expressed as erosion threshold or erosion rate (Sanford, 2008). Critical shear stress ($\tau_c$) is defined as the erosion threshold of the minimum bed shear stress developed by the flow for soil erosion to be initiated. Erosion that occurs for bed shear stresses smaller than the critical shear stress is assumed negligible (Osman and Throne, 1988; Hanson, 1990; Karmaker and Dutta, 2011).

Fined-grained (cohesive) sediments, which are usually formed from weathering, transport and biological processes, are mixtures of inorganic minerals and organic material. Generally referred to as "mud" in estuaries (hydraulic engineers use the term "cohesive sediment" while geotechnical engineers prefer "fine-grained sediment"), they play a significant role in the health of aquatic ecosystems, water quality, and riverbed stability. Ecologically, fine-grained sediments are habitats for benthic organisms, stores for organic carbon and sites of biological cycling (Grabowski et al., 2011). Pollutants including heavy metals and anthropogenic bacteria can bind to these small, electrochemically active particles and accumulate in them (Ravisangar et al., 2005; Grabowski et al., 2010). During flood events or hydraulic structure construction, resuspension of fine sediments becomes a significant source of contaminants affecting water quality and aquatic life (Ravisangar et al., 2005). Therefore, understanding of erosion and transport mechanisms involving fine-grained sediments is required when dealing with engineering problems such as mitigation of sediment loss from catchments, stream bed/bank erosion, bridge foundation stability, water quality, and stream ecosystem balance.

In the past few decades, erosion and transport properties of coarse sediments and scouring around cylinders in non-cohesive sediment beds have been studied extensively

(e.g. Raudkivi and Ettema, 1983; Melville, 1997; Ettema et al., 1998; Ting et al., 2001; Sheppard et al., 2004). However, the erodibility and transport mechanisms of fine-grained sediments are different from those of coarse sediments (Debnath and Chaudhuri, 2010a). While the interparticle forces in coarse sediments depend on gravity alone, clay sediments consist of a plate-like crystalline structure held together in different configurations by physico-chemical forces. The extrapolation of erosional and local scouring characteristics from coarse sediment beds to fine sediments is therefore not appropriate. While hydrodynamics and erosion/transport mechanisms of granular sediments are well understood, erosional properties of fine sediments have proved more difficult to describe and quantify.

Although progress has been made to show the various sediment properties affecting erosion of fine sediments in recent years, the capability to predict the erodibility of cohesive or fine sediments is still in question (Grabowski et al., 2011). Fine sediments are composed of particles smaller than 62 μm in diameter, and can be classified as silt and clay, in general. Clay-size particles, mostly platy-shaped, provide the cohesive nature of river beds, and the cohesiveness is highly dependent on the soil structure. Recent research has focused on the erodibility of sand-mud (silt and clay) mixtures collected from the field or made by artificial mixing in the laboratory (e.g. Mitchener and Torfs, 1996; Reddi and Bonala, 1997; Reddi et al., 2000; van Ledden et al., 2004; Debnath et al., 2007; Ternat et al., 2008). Most of the studies have lumped silt and clay together as "mud" (or fines) in the soil mixture, and a few studies have worked on characterizing the erosional characteristics and affecting factors of clay-sized sediments (e.g. Ravisangar et al., 2001, 2005). While it is important to note that it is actually the clay particles within

3

the fine sediment fraction which provide cohesive properties (van Ledden et al., 2004), there has been little effort to study cohesive effects of clays as distinguished from silts on sediment erosion. In addition, the nature of clay and silt is different in mineralogy, water confinement capability, and electrochemistry at the particle surface due to their differences in particle size (Santamarina et al., 2001). Clay content should be distinguished from silt in fine sediments and considered as one of the key factors influencing fine sediment erodibility.

In addition to the hydrodynamic condition of flow, erosion depends on the propensity of sediments to be eroded. For fine sediments, erodibility is governed by many factors including physical properties of the sediments, electrochemical reactions, consolidation, and biostabilization (Stone et al., 2011). Among these factors, physical properties such as mean or median particle size, clay content, bulk density or water content, as well as pore water chemistry and clay mineralogy, have been recognized as important causative agents affecting the erodibility of fine sediments (Ravisangar et al., 2005; Karmaker and Dutta, 2011; Grabowski et al., 2011). Various laboratory approaches and in situ apparatuses have been developed to determine the erodibility of sediments such as laboratory flumes, circulating and straight in situ flumes, annular flumes and submerged jets (Debnath et al., 2007; Karmaker and Dutta, 2011). Measurements from these devices are analyzed to estimate the erosion rate and critical shear stress ($\tau_c$); that is, the shear stress at which erosion begins. Despite the many devices available for measuring soil erodibility, they are all time consuming and expensive, and the values obtained from different approaches are not unified due to the difficulty of determining initiation of erosion, which is often based on operator judgment (Black and Paterson,

1997; Tolhurst et al., 2000). Moreover, estimation of critical shear stress from the available literature on in-situ sediments is usually site specific and thus is limiting in application.

Rheology is a science describing the behavior of a material subjected to applied stresses which provides an approach to quantifying the flow resistance of fine sediments. For hyperconcentrations such as fluid muds, rheological properties indicate how the sediment matrix responds under a hydrodynamic shear stress induced by the flow. One of the rheological characteristics of sediments is the yield stress ($\tau_y$), defined as the limiting value of shear stress required for the sediment to begin to flow (Nguyen and Boger, 1992). In other words, when the applied shear stress is smaller than the yield stress, there is no real macroscopic flow and the deformation of mud is considered reversible and elastic. In contrast, when the applied shear stress exceeds the yield stress, the deformation is irreversible and the mud starts to flow (van Kessel, 1998). Thus, yield stress can be considered as an indication of critical shear stress needed to initiate the sediment erosion. Otsubo and Muraoka (1988) and Ravisangar et al. (2001) studied the rheological and erosion behavior of natural muds and pure kaolinite, respectively, and both studies found positive correlations between the rheological properties and erosion threshold for fine sediments. Yield stress can be measured using a rheometer, which is recognized as a more robust method to determine a sediment property compared to flume experiments for measuring soil erodibility (Hoepner, 2001; Hobson, 2008). In this study, efforts are made to investigate the relationship between the yield stress and critical shear stress, obtained from rheometer tests and flume experiments, respectively, as well as the effects of physical properties on the two threshold stresses for movement of fine sediments.

## 1.2 Research Objectives and Approach

This study aims to (1) determine the critical shear stress of fine sediments with different physical properties; (2) investigate how the physical properties of fine sediments affect the value of critical shear stress; (3) measure the rheological characteristics (mainly $\tau_y$) and relate the yield stress to critical shear stress for fine sediments with different physical properties; (4) identify and quantify the relationships among critical shear stress, yield stress, and the physical properties of fine sediments for engineering problems such as channel design, sediment erosion control, and bridge foundation stability analysis. Specifically, the research objectives were pursued through completion of the following tasks, which are also outlined in Figure 1.1, the research plan flow chart.

First, samples of fine sediment mixtures were prepared by mixing industrial ground silica (SIL-COSIL 106, US Silica) and Georgia kaolin (Hydrite Flat D, Dry Branch Kaolin Company, Dry Branch, Georgia), representing silt- and clay-size particles respectively, with tap water. By varying the dry weight ratio between ground silica and Georgia kaolin, soil mixture specimens containing different kaolin contents were prepared. Second, conventional geotechnical tests were carried out for each type of specimen to obtain its physical properties including Atterberg limits, grain size distribution, median particle size, and specific gravity. Water content was determined by measuring the wet weight and oven-dried weight of the sediments for each specimen, and thus the bulk and dry densities were also obtained. In addition, temperature, pH value, and conductivity of tap water and the soil mixture slurries were measured using a waterproof electronic meter.

After the specimens were prepared and their properties were recorded, the critical shear stress was estimated from the flume experiments by measuring erosion rates of the specimens under different applied bed shear stresses with at least three replicates for each condition. On the other hand, the yield stress was estimated from the stress-strain rate relationship obtained from a stress-controlled rheometer test for soil specimens that were prepared identically to those used in the flume experiments. The technique of scanning electron microscopy (SEM) was then applied to examine the interparticle arrangements of the silt-clay soil mixtures. From the SEM images, the appearance of the soil specimens was described and used to discriminate among the soil mixtures containing different kaolin contents.

Results from the different experiments (geotechnical tests, hydraulic flume test, rheometer test, and SEM) were first analyzed individually and then compared with one another. For instance, the critical shear stress and yield stress were plotted individually against bulk density with clay content as a parameter to show influences of sediment physical properties on the erosion threshold and rheological characteristics, respectively. Meanwhile, dimensionless forms of those two stresses were developed and multiple regression analysis was applied to seek their relationships with soil properties such as water and clay contents. Then the correlation between the critical shear stress and yield stress of fine-grained sediments was obtained through regression analysis as well.

In the discussion of the experimental results and analyses, experimental data and results from previous studies such as Navarro (2004), Ravisangar et al (2005), and Hobson (2008) were included to compare with the findings from this research. Through comprehensive analyses and discussion, the correlation between critical shear stress and

yield stress, as well as the effects of soil physical properties on both stresses were illustrated, and the erosional and rheological behavior of fine-grained soils was interpreted from the structure of the sediment network and particle associations.

## Literature Review

1. Fine grain sediment characteristics
2. Mechanism, properties, and measurements of soil erosion
3. Rheology principles and studies of soil matrix

## Specimen Preparation

1. Silt-clay mixtures (silica flour + Georgia kaolin)
2. Soil property investigation: Geotechnical tests
   (*e.g.* Atterberg limits, Bulk Density, Grain size distribution)

## Experiments

| Hydraulic flume test: Sediment erosion rate | Mechanical rheology test: Stress-strain rate relation | Scanning Electron Microscopy: Particle structural association |

| Data analysis: Predicting critical shear stress ($\tau_c$) | Data analysis: Predicting yield stress ($\tau_y$) | SEM image description: E-E, E-F, F-F particle association |

## Comprehensive Analysis and Discussion

1. Effects of soil physical properties (clay content, water content, bulk density)
   to erosion and rheological characteristics of fine sediments
2. Correlation between critical shear stress and yield stress
3. Mechanics of erosion resistance of fine-grained sediments in terms particle
   association and soil fabric

## Final Comment and Recommendations

1. Conclusion, contribution, and implication of the study
2. Possible modifications and recommendations of future study

Figure 1.1 Flow chart of the research plan

## 1.3 Potential Implications and Contributions

At present, erosional properties such as critical shear stress of fine-grained sediments cannot be predicted and must be measured through in situ devices or laboratory experiments for the sediment of interest (Grabowski et al., 2011). Although models and empirical relationships have been carried out for estimating the erodibility, and the causative factors have been discussed for many field-collected fine sediment samples in recent years, the results are usually case-dependent and the applicability is thus limited. Furthermore, a very limited number of studies which discuss and quantify the influences of physical properties on the erosion threshold (critical shear stress) and rheological characteristic (e.g. yield stress) for fine sediments have been carried out previously. Therefore, the outcomes of this study are intended to contribute to the fundamental understanding of erosion threshold and the influences of physical properties of fine-grained sediments in flowing aquatic systems. Specifically, the relationship between critical shear stress and yield stress, and the influences of physical properties on the erosion and rheological characteristics of fine-grained sediments were developed through laboratory experiments and data analysis. By quantifying these relationships and effects of physical properties (e.g. mean particle size, clay content, water content, and bulk density) on the critical shear stress and yield stress of fine-grained sediments, this research has the goal of providing a methodology for engineering applications requiring the value of critical shear stress such as estimating fine sediment bed stability and assessing the erosion risk of river beds in proximity to bridge foundations and other flow obstructions.

## 1.4 Outline of the Thesis

Following the introduction stated in this chapter, Chapter II introduces the literature review of recent publications on sediment characteristics, the mechanism, properties, and measuring methodology of soil erosion, as well as the principles, measurements, mathematical models, and studies of rheology regarding fine sediments; Chapter III details the research approach and experimental procedures of soil mixture specimen preparation, soil geotechnical tests, hydraulic flume experiments, rheometer tests, and scanning electron microscopy (SEM). Chapter IV focuses on the results from the laboratory work, including the geotechnical tests, flume experiments, rheometer tests, and SME images. Chapter V includes the analyses of the experimental data, comparison with some previous studies, and discussion of the analyzed results relating to the erosion resistance of fine-grained sediments. Chapter VI finalizes the conclusions, contributions and implications of this study, and makes recommendations for future research.

# CHAPER II

# LTERATURE REVIEW

This chapter provides some detailed information on fine-grained sediments and their erosion characteristics based on a review of studies completed during the past few decades. The first section gives an overview of the properties of fine-grained sediments and focuses on the interparticle forces and soil structure. In the following sections, modes of erosion, along with methods and apparatuses for erosion measurements are presented, followed by a discussion of some physical properties of fine sediments affecting the erosion behavior. Then mathematical models of sediment erosion developed by previous researchers are described. The last four sections cover the principles, measuring methods, mathematical models, and some rheological studies relating to fine-grained sediments.

## 2.1 Fine-Grained Sediment Characteristics

Cohesive bed sediment in rivers, harbors, and estuaries is a heterogeneous, particulate and porous material which consists of inorganic particles, organic material, pore liquid (predominantly water), and sometimes gases (such as air and methane). Fine-grained sediment is primarily composed of soil particles smaller than 62 μm in diameter (by American Geophysical Union, AGU scale) and is further divided into the two categories, silt and clay. Silt-sized particles, ranging from 2 μm to 62 μm, are an intermediate size between sand and clay particles. Commonly generated by physical weathering of primary minerals, they are mostly composed of quartz but with feldspars or micas sometimes (Grabowski et al., 2011). Clay-sized particles are generally identified as

those smaller than 2μm. Predominantly platelike clay particles, generally referred to as "phyllosilicates", are formed by chemical weathering of primary minerals, and the building elements are tetrahedral sheets of silicon-oxygen and octahedral sheets of aluminum- or magnesium-oxygen (Velde, 1995). The different configurations of superposition of these sheets result in different clay minerals; they are classified as two-layer type, three-layer type, regular mixed-layer type, and chain-structure type crystalline structures in general (Murray, 2007). Some minerals of major importance in sediments include kaolinites, montmorillonites, vermiculites, and illites (Ravisangar et al., 2001). Kaolinites belong to the two-layer type crystals, which have sheet structures composed of units of one layer of silica tetrahedrons and one layer of alumina octahedrons; montmorillonites, vermiculites, and illites are examples of the three-layer type crystals with sheet structures of two layers of silica tetrahedrons and one central dioctahedral or trioctehedral layer (Velde, 1995; Murray, 2007).

Since soils are particulate materials, their behavior is determined by the forces that particles experience (such as gravitational, hydrodynamic, and interparticle electrical forces), and the relative importance of these forces varies with the particle size. Therefore, the size of particles being eroded is one of the principal factors that determines the dominant force which resists erosion. As the particle gets smaller, the surface area per unit mass (i.e. specific surface, $SSA$) increases, which leads to the increasing effect of interparticle electrical forces in fine sediments. For fine-grained materials, the gravitational forces (such as submerged weight of particle) no longer provide the most significant resistance to erosion, and the electro-chemical forces including Coulombian attraction, van der Waals attraction, and double layer repulsion start to act. Reviews of

the forces experienced by fine sediments in flowing water are presented following Santamarina (2001) and Santamarina et al., (2001).

Gravitational forces acting on a soil particle submerged in water include the weight ($W$) of soil grain and the buoyancy ($U$) which is the surface integral of the fluid pressure acting on the particle. For a spherical particle with diameter $d$, these two components are given by:

$$W = \frac{1}{6}\pi G_s \gamma_w d^3 \tag{2.1}$$

$$U = \frac{1}{6}\pi \gamma_w d^3 \tag{2.2}$$

where $G_s$ = specific gravity of the mineral that forms the particle; and $\gamma_w$ = specific weight of water. The submerged weight ($W_s$) of a particle in water is defined as:

$$W_s = W - U \tag{2.3}$$

In a viscous moving fluid, the hydrodynamic drag force ($D$) acting on a soil particle is related to the flow velocity and the frontal area projected onto a plane perpendicular to the resultant flow velocity:

$$D = C_D \rho_w A_f \frac{V^2}{2} \tag{2.4}$$

where $C_D$ = drag coefficient; $\rho_w$ = density of water; $V$ = approach flow velocity; and $A_f$ = frontal area of the particle. In sediment transport research, the hydrodynamic force is usually presented as the applied or bed shear stress ($\tau$), which is the drag force per unit area. The bed shear stress for steady uniform flow in an open channel is given by (Sturm, 2001):

$$\tau = \gamma_w R S_0 \tag{2.5}$$

14

where $R=$ hydraulic radius; and $S_0=$ bed slope. The movement of particles is initiated when the hydrodynamic force of the flow overcomes the resisting forces of sediments, e.g. submerged weight and interparticle cohesion (discussed in the following). For a given type of sediment, the threshold of particle movement is defined as the critical shear stress ($\tau_c$). In other words, $\tau_c$ is the minimum applied shear stress required to initiate the movement of given sediments. Critical shear stress is affected by several factors including properties of the fluid and the sediment itself, which will be discussed in detail in section 2.4.

From the perspective of soil and sediment erosion, cohesion is used to describe attraction between chemically similar particles (Jumars and Nowell, 1984), which refers to the electro-chemical forces such as Coulombian and van der Waals attraction. While quartz particles (e.g. silts) carry weak electro-chemical charges on their surfaces, the cohesion of fine sediments is primarily attributed to the interparticle attractions between clay particles. Coulombian attraction exists when there are counter charges interacting. Between clay particles, attraction develops between the positively charged edges and negatively charged faces. The magnitude of the attracting force ($F_c$) is expressed by Coulomb's law, which states that $F_c$ between the two charges $q_1$ and $q_2$ is inversely related to the square of the distance $r$ between them:

$$F_c = \frac{1}{4\pi\varepsilon_0\kappa'}\frac{q_1 q_2}{r^2} = \frac{e_0^2}{4\pi\varepsilon_0\kappa'}\frac{z_1 z_2}{r^2} \tag{2.6}$$

where $\varepsilon_0 = 8.85\times10^{-12}\ F/m$ is the permittivity of vacuum; $\kappa'=$ real relative permittivity of the medium; $e_0 = 1.602\times10^{-19}\ C$ is the electron charge; $z=$ ionic valence; and $r=$ distance between edge and face of clay particles.

Van der Waals attraction between two particles suspended in a medium is a function of the Hamaker constant ($A_h$), which is a measure of the permittivity of the medium between particles and can be evaluated from Lifshitz's theory (Israelachivili, 1992). The attraction is dependent on the shape of particles and can be expressed as:

$$F_{pp} = -\frac{A_h}{6\pi r^3} \qquad \left(N/m^2\right) \qquad \text{two parallel platy particles} \qquad (2.7)$$

$$F_{ss} = -\frac{A_h}{6\pi r^2}\frac{R_1 R_2}{\left(R_1 + R_2\right)} \qquad (N) \qquad \text{two spheres} \qquad (2.8)$$

$$F_{sp} = -\frac{A_h}{6\pi r^2} R \qquad (N) \qquad \text{sphere and platy particle} \qquad (2.9)$$

where $A_h = 0.64 \times 10^{-20} J$ for silica-water-silica and $10 \times 10^{-20} J$ for kaolinite-water-kaolinite (Santamarina, 2001); $r =$ distance between edges or faces; $R_1 =$ radius of sphere one for the two-spheres case; $R_2 =$ radius of sphere two for the two-spheres case; and $R =$ radius of sphere for the sphere and platy-particle case. When the separation is smaller than 15 nm, $A_h$ does not vary; however, it decreases for larger separations (Lyklema, 1991).

On the other hand, repulsion occurs when two clay particles with their associated double layers approach each other, and the water molecules and hydrated ions between the plates are displaced. The double layer repulsion force per unit area ($R_{DL}$) is a function of both interparticle distance ($r$) and double layer thickness ($\vartheta$) and is estimated by Israelachili (1992) as:

$$R_{DL} = 64\left(RTc_0\right)d^{-\gamma/\vartheta} \qquad (2.10)$$

where $R = 8.314 \, J/(K \cdot mol)$ is the gas constant; $T =$ temperature; and $c_0 =$ ionic

concentration of the pore fluid. The double layer thickness can be further estimated as:

$$\vartheta = \sqrt{\frac{\varepsilon_0 R}{2F^2} \frac{\kappa' T}{c_0 z^2}} = \sqrt{\frac{\varepsilon_0 k}{2e_0^2 N_{av}} \frac{\kappa' T}{c_0 z^2}} \tag{2.11}$$

where $F = 9.6485 \times 10^4 \, C/mol$ is Faraday's constant, $k = 1.38 \times 10^{-23} \, J/K$ is the

Boltzmann's constant; $N_{av} = 6.022 \times 10^{23} \, mol^{-1}$ is Avogadro's number and

$\mathrm{Re}_0^2 N_{av} = kF^2$. In short, the double layer thickness of a clay particle is proportional to

the square root of temperature and to the inverse of the square root of pore fluid ionic

concentration. Although there are other estimations of $R_{DL}$ based on different

assumptions, it is concluded by Santamarina et al. (2001) that "two particles move closer

to each other when ions are replaced with higher valence ions, when the ionic

concentration of the pore fluid increases, or when the temperature decreases."

The relative contributions to resistance of gravitational and interparticle forces

vary with the size and structure of sediments. For instance, Figure 2.1 shows the

estimations of the submerged weight and van der Waals attraction for different-sized

spherical particles by equations 2.3 and 2.8, respectively, with separation between

particles of 30 Å. The submerged weight of particle is overwhelmed by the van der Waals

attraction when the particle is smaller than 60 μm and 15 μm for kaolin and silica,

respectively, as shown in Figure 2.1; this illustrates the significance of interparticle forces

of fine sediments in resisting erosion.
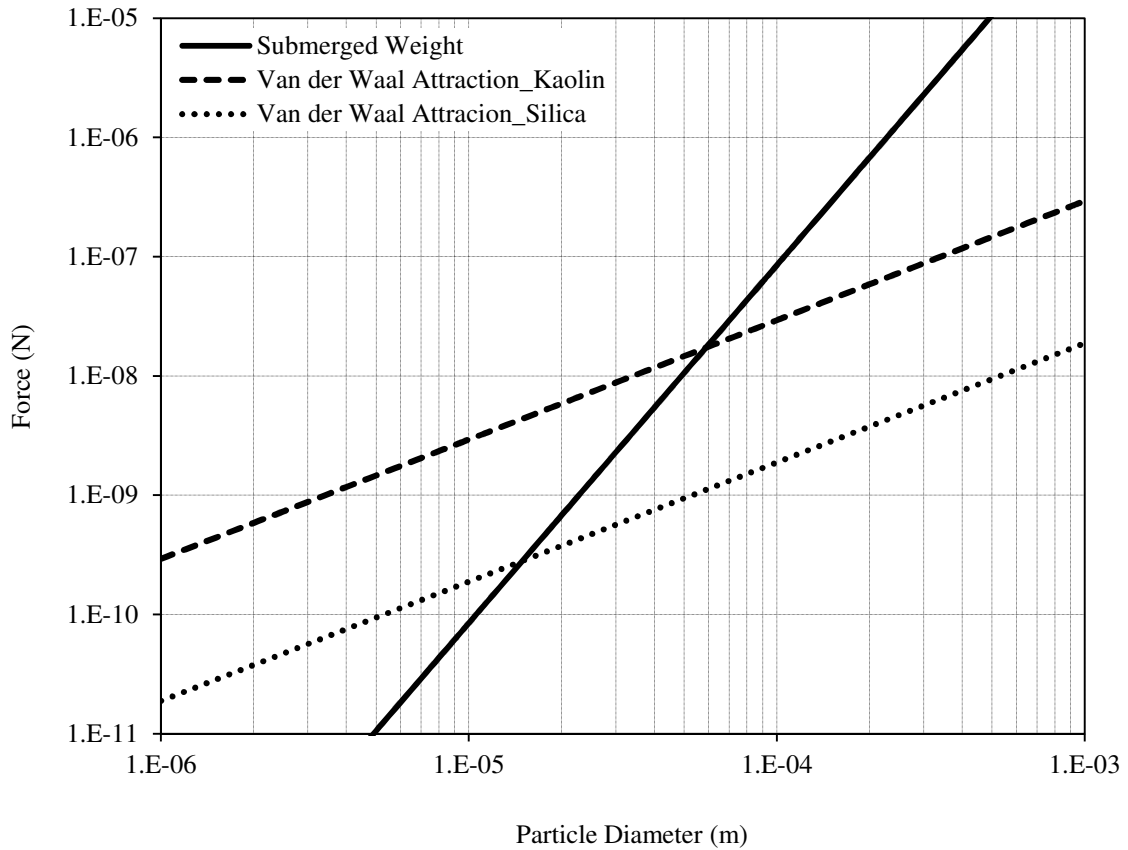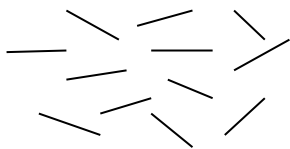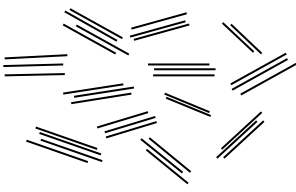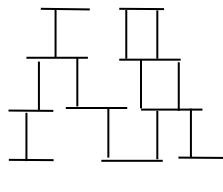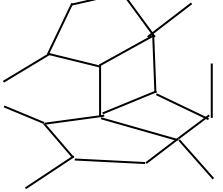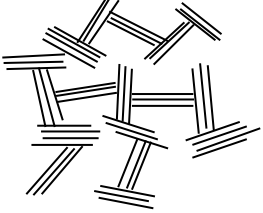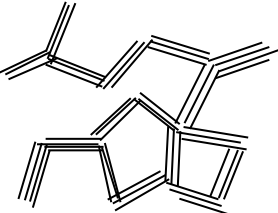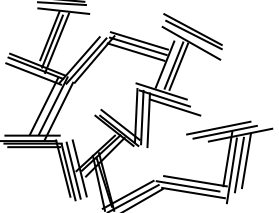
Figure 2.1 Relative contribution of submerged weight (in water) and van der Waals
attraction for different size of particles (after Santamarina, 2001)

Soil structure, i.e. the arrangement of soil particles, is an important factor that
determines the strength of erosion-resisting forces. Van Olphen (1977) studied the
arrangements of fine sediment deposits and proposed four main categories of structural
associations: Edge-to-Face, Edge-to-Edge, Face-to-Face and shifted Face-to-Face. Edge-
to-Face (E-F) arrangements are governed by Coulombian forces produced from the
counter charges existing at the faces and edges of particles. Face-to-Face (F-F)
arrangements occur in high ionic concentration fluids when van der Waals attraction
prevails over the double layer repulsion between particles. Edge-to-Edge (E-E)
arrangements are described as an arrangement in which there is not a dominant force that

governs the configuration. An illustration of fine sediment structural configurations is given in Table 2.1.

Table 2.1 Particle associations in fine-grained sediments (after van Olphen, 1977)

| Clay Particles | Dispersed, Deflocculated | | |
|---|---|---|---|
| |  | | |
| Simple Particle Associations | F-F Aggregated, but Deflocculated | E-F Flocculated, but Dispersed | E-E Flocculated, but Dispersed |
| |  |  |  |
| Complex Particle Associations | E-F Flocculated, F-F Aggregated | E-E Flocculated, F-F Aggregated | E-F, E-E Flocculated, F-F aggregated |
| |  |  |  |

The formation of these particle associations depends on the balance between electro-chemical interactions (Hillier, 1995); the importance of the short-range hydration and Born repulsion forces have also been demonstrated in determining the total interaction force between particles of different structural associations (Raveendran and Amirtharajah, 1995). Mahmood et al. (2001) analyzed the microscopic interactions

related to fine-sediment associations of kaolinite particles (E-E, E-F, and F-F arrangements) including van der Waals forces, electrical double layer forces, hydration forces, and Born repulsion. Their analysis showed that the total interactive force between two plate-like interacting particles varied with the particle geometric association. By analyzing the "total interactive force" (sum of the van der Waals forces, electrical double layer forces, hydration forces, and Born repulsion) between particles, the magnitude of cohesion between kaolinite platelets was reported to follow the sequence: F-F >> E-F > E-E arrangements under constant chemical conditions (same pH value of pore fluid). The adhesive forces of E-F arrangement were found stronger than those of the E-E arrangement by a factor of $\sqrt{2}$ (Mahmood et al., 2001). The F-F structures are typically formed from dispersed particles settling individually; thus, the deposits have higher bulk density (or lower water content) than E-F structures which are formed predominantly during settling of flocculated suspension (van Olphen, 1977; Ravisangar et al., 2005).

Due to the chemical structure of clay minerals, these phyllosilicates carry negative charges on the face surfaces whereas charges at edges are due to broken bonds and thus are highly pH dependent (Mahmood et al., 2001; Ravisangar et al., 2001). Edge charges of clay particles are predominantly positive at low pH condition and become more negative under increasing pH conditions because of the adsorption of different ions ($H^+$ in low pH and $OH^-$ in high pH). The E-F particle associations are more probable at low pH conditions (pH <5.5); the F-F associations are more common in high pH pore fluid (pH > 7.5); and the E-E associations exist at intermediate pH conditions, along with E-F and F-F associations (Hillier, 1995; Mahmood et al., 2001). Ravisangar et al. (2001) studied the erosion rates of kaolinite samples that had settled under different pH

conditions. It was found that the erosion rates of kaolinite increased as pH increased from 4 to 6. High erosion rates persisted for pH values from 5.5 to 7 due to the reorientation of particles from E-F to E-E associations. Then erosion rates decreased as pH continually increased to a value of about pH = 8 at which F-F associations were dominant.

Later studies on clay particle structures discussed the effects of ionic strength and organic matter in addition to the pH value of pore fluids. Ravisangar et al. (2005) estimated the erosional strength (critical shear stress, $\tau_c$) of kaolinite deposits under conditions of varying values of pH, ionic strength, and organic content (added natural organic matter, NOM) in flume experiments. From their results, it is suggested that the effect of pH depended on the ionic strength. At low ionic strength (0.004M), the kaolinite bed that was settled under low pH (<5.5) conditions had higher $\tau_c$ than the bed settled under high pH (>7) conditions. However, this effect was not obvious under high ionic strength conditions (0.1M) since the importance of high ion concentration on clay mineral coagulation outweighed the effect of pH (Grabowski et al, 2011). Ravisangar et al. (2005) also demonstrated the influence of organic matter at low ionic strength and low pH conditions. Under these conditions, the addition of high NOM (0.8mg C/g Kaolin) decreased $\tau_c$ but increased the bulk density. On the other hand, under high ionic strength conditions, the high ionic concentration appeared to neutralize the influence of NOM which occurred in the low ionic strength case. Lastly, it was found that $\tau_c$ is much more sensitive to variation in bulk density when E-F association predominates compared to the case of F-F association dominance.

Effects of adsorbed NOM on the erosion of kaolinite sediments were investigated specifically by Dennett et al. (1998). The erosion rates were lower for sediment samples

with the lowest and highest concentrations of NOM tested; slightly higher erosion rates were obtained for intermediate concentrations of NOM samples. The sediment water content decreased as increasing concentration of NOM was added to the sample. From the variations of erosion rates and sediment water contents, Dennett et al. (1998) suggested that the clay particles reoriented from a predominantly E-F association at low NOM concentrations to more F-F associations at higher NOM concentrations. The critical shear stress decreased as NOM concentration in samples increased, indicating that higher NOM concentration sediments, which may be more reactive with environmental contaminants, may be more susceptible to erosion (Dennett et al., 1998). Nevertheless, some field studies on riverine sediments (Aberle et al., 2004; Gerbersdorf et al., 2007), found positive correlations between organic matter and critical shear stress, suggesting a stabilizing role of organic content on cohesive sediment beds. Organic molecules, including polysaccharides, proteins, and colloids, can create a highly chemically active environment and are believed to enhance flocculation by adhering particles together (Winterwerp and van Kesteren, 2004; Grabowski et al, 2011). Aberle et al. (2004) suggested that layers of fibrous organic matter acted as a structural barrier to prevent erosion of sediment underneath. Generally, it is recognized that the median particle size, organic matter, carbon exchange capacity, extracellular polymeric substances (EPS), pore fluid pH and ionic strength are factors to determine the dominant particle structural arrangement which leads to differences in erosion resistance.

## 2.2 Modes of Erosion

Because it is dependent on the magnitude of bed shear stress and the nature of the sediment deposit, erosion may occur in different forms (Mehta et al., 1988). Modes of

erosion have been identified as three major forms including surface erosion, mass erosion and fluidization (Partheniades, 1965; Mehta, 1991). During the erosion process, these three modes are not exclusively independent and may co-exist in some proportion, yet one is typically predominant (Mehta, 1991).

Identification of surface and mass erosion was presented by Partheniades (1965). Surface erosion refers to the aggregate-by-aggregate erosion of a bed, which occurs when particles and small flocs are washed away due to the breakage of interparticle electrochemical bonds by hydrodynamic forces. This type of erosion is prevalent in estuaries subject to currents of low to moderate shear stress, and the rate of surface erosion increases with the excess shear stress ($\tau - \tau_c$) (Mehta et al., 1988). Under hydrodynamic conditions of large excess shear stress or rapidly accelerating flows, mass erosion takes place as the bed fails along an entire plane below the surface and clumps of sediment are eroded and transported. This point of failure was identified as the macroscopic shear strength of the bed by Partheniades (1965). Mass erosion usually predominates in areas of strong tidal currents and under storm events, and the erosion rates are much greater than those of surface erosion (Mehta et al., 1988). Mehta et al. (1988) firstly discussed the entrainment of stationary suspensions and then proposed the third mode of erosion as 'fluidization" (Mehta, 1991). Fluidization occurs when fluid waves invade the sediment structure and relieve the load of skeleton forces on the particles. The flow-induced destabilization causes interfacial entrainment and mixing of the fluid mud-water interface as downstream sediment transport occurs.

Based on the time-dependency of erosion rate, Mehta and Partheniades (1982) indentified two main types of erosion from laboratory studies, referred to as Type I and

Type II erosion. Type I erosion is characterized by an asymptotically decreasing erosion rate with time under a constant bed shear stress condition. At a constant flow, Type I erosion decays exponentially with time and ceases when the critical shear stress of the exposed layer equals the applied bed shear stress. In other words, this behavior can be explained by the stratification of the bed in which $\tau_c$ increases with depth. Type I erosion is therefore called depth-limited or supply-limited erosion as well (Van Prooijen and Winterwerp, 2010). Amos et al. (1992a) reported a further distinction between Type Ia and Type Ib erosion. Type Ia erosion is a surface phenomenon that occurs in low-forcing and high benthic activity regions, and it is associated with the erosion of 1 mm organic pellets formed by an amphipod; Type Ib erosion occurs at relatively high forcing conditions with bed shear stress ranging from 1.0 ~ 4.4 Pa (Amos et al., 1992a).

In the case of a relatively homogeneous bed over depth, the erosion rate remains constant in time under a constant bed shear stress, which is referred to as Type II erosion (Mehta and Partheniades, 1982), or unlimited erosion (Van Prooijen and Winterwerp, 2010). Under the assumption that the critical shear stress is constant with depth and the erosion rate remains unchanged during the whole testing period under constant forcing, power (Owen, 1975; Sheng and Lick, 1979; Villaret and Paulic, 1986) or linear (Ariathurai and Krone, 1976; Ariathurai and Arulanandan, 1978) relationships have been developed to describe the dependence of erosion rate on applied shear stress. From Amos et al. (1992a)'s study, Type II erosion was found under applied bed shear stresses of 2 ~ 10 Pa. The distinction between Type I and II erosion has been found in both laboratory and field studies (Van Prooijen and Winterwerp, 2010).

## 2.3 Erosion Measurements

For engineering and research purposes, the needs for collecting and estimating soil and sediment erosion properties led to the development of various measuring methods and devices in both laboratory and field. Most of the devices can be classified as one of the three general categories: laboratory flumes, benthic in situ flumes and submerged jets. Classification and referenced literature of the erosion measuring instruments are summarized in Table 2.2.

Table 2.2 Summary of erosion measuring instruments

| Type | | | Sample source | Author(s) |
|---|---|---|---|---|
| Applied in | Flume shape | Device name | | |
| Laboratory | Straight, recirculating flume | -- | Kaolinite; river samples | Dennett (1995) |
| | | Sedflume | Undisturbed samples from riverbeds | McNeil et al. (1996) |
| | | | Reconstructed samples for riverbeds | Jepsen et al. (1997) |
| | | | Quartz particles | Roberts et al. (1998) |
| | | | Undisturbed and reconstructed samples from field; Pure clay (Kaolinite, Bentonite); Quartz particles | Lick and McNeil (2001) |
| | | ASSET | Quartz particles | Roberts et al. (2003) |
| | | -- | Georgia kaolinite | Ravisangar et al.(2001, 2005) |
| | | -- | Sand and clay mixture | Barry et al. (2006) |
| | | -- | Undisturbed samples from riverbed and coastal area | Ganaoui et al. (2007) |
| | | -- | Undisturbed samples from lakes | Rightti and Lucarelli (2007) |
| | | -- | Undisturbed samples from riverbeds | Ternat et al. (2008) |
| | Straight, recirculating duct | EFA | Silt and clay mixture; Kaolinite | Briaud et al. (1999, 2001, 2004) |
| | Rotating annular flume | -- | Boston Blue Clay | Zreik et al. (1998) |
| | | -- | Sand and clay mixture | Jiang et al. (2004) |
| Field | Submerged impinging jet | -- | Mixture of clay (40%), silt (53%), and fine sand (7%) | Mazurek et al. (2001) |
| | | -- | Sand and clay mixture | Ansari et al. (2003) |

*(Table 2.2 continued)*

| | | Sea Carousel | Bay of Fundy, Canada | Amos et al. (1992a, b) |
|---|---|---|---|---|
| | Benthic recirculating annular flume | VIMS Sea Carousel | Chesapeake Bay and Middle Atlantic Bight | Maa et al. (1993) |
| | | | Baltimore Harbor | Sanford and Maa (2001) |
| | | -- | Humber estuary, U.K. | Widdows et al. (1998) |
| | Benthic recirculating race-track shaped flume | MORF | South Wales, U.K. | Black and Cramp (1995) |
| | Benthic vertical recirculating flume | ISEF | Dutch Wadden Sea coast | Houwing and van Rijn (1998); Houwing (1999) |
| | Benthic flow-through flume | Seaflume | Buzzards Bay, Mass | Young (1977) |
| | | | Puget Sound Basin | Gust and Morris (1989) |
| | | -- | Boston harbor | Ravens and Gschwend (1999) |
| | | NIWA I, II | Several rivers, wetlands, and lakes | Aberle et al. (2003, 2004, 2006); Debnath et al. (2007) |
| | Submerged impinging jet | CSM | Severn estuary, U.K. | Paterson (1989) |
| | | modified CSM | Sylt mudflat, Germany | Tolhurst et al. (1999) |
| | | | Tollesbury, Essex, U.K. | Watts et al. (2003) |
| | | -- | Urbanizing basin near Toronto, Canada | Shugar et al. (2007) |
| | Circular inverted bell-shaped funnel | ISIS | Severn estuary, U.K. | Williamson and Ockenden (1996) |

### 2.3.1 Laboratory Flumes

Laboratory flumes have been commonly used to study the erosion characteristics of sediments (e.g. Dennett, 1995; McNeil et al., 1996; Jepsen et al., 1997; Roberts et al., 1998; Zreik et al., 1998; Briaud et al., 1999, 2001, 2004; Lick and McNeil, 2001; Ting et al., 2001; Roberts et al., 2003; Barry et al., 2006; El Ganaoui et al., 2007; Righetti and Lucarelli, 2007; Ternat et al., 2008).

Dennett (1995) studied the erosion characteristics of kaolinite clay and bottom sediment from the Calcasieu River in Louisiana using a rectangular-recirculating laboratory flume in the hydraulic lab of Georgia Tech. The flume was 0.38 m wide, 0.4 m deep, and 6.1 m long with a bed filled with gravel having a of $d_{50}$ of 3.5 mm. The experiments were performed under uniform flow conditions. Using the same apparatus, erosion tests on artificially-mixed or field samples have been conducted by Hoepner (2001), Ravisangar et al. (2001), Navarro (2004), and Hobson (2008). McNeil et al. (1996) developed a straight, recirculating laboratory flume called Sedflume, to erode rectangular sediment cores sampled from rivers in Michigan and Wisconsin, US. The sample cores, with cross sections 10 cm by 15 cm, were placed at the downstream end of the rectangular acrylic flume which was 10 cm in width, 120 cm in length, and 2 cm in depth. Under applied shear stresses ranging from 0.2 Pa to 10 Pa, the sediments in the core were continually extruded upwards by an operator to level the sediment-water interface with the bottom of the inlet section. The critical shear stress was defined as the applied shear stress at which the volumetric erosion rate was between $10^{-3}$ and $10^{-4}$ cm/s. The vertical erosion rate was found to vary with sampling sites, depth, and as a function of the applied shear stress. Using the same device, Jepsen et al. (1997), Roberts et al.

(1998), and Lick and McNeil (2001) did further studies to investigate the effects of sediment bulk properties on the volumetric erosion rate. Jepsen et al. (1997) correlated bulk density, which was mainly a function of water content, with the volumetric erosion rate of field samples. The volumetric erosion rate decreased as bulk density increased, and the volumetric erosion rate could be expressed as a product of powers of the applied shear stress and bulk density. Roberts et al. (1998) completed further studies on the erosion of quartz particles as influenced by the particle size and bulk density. Power relationships for volumetric erosion rate as a function of bulk density were proposed for different sizes of particles. In addition, equations were proposed by Roberts et al. (1998) to estimate the critical shear stress by the mean particle size. Besides particle size and bulk density, effects of organic content, presence of gas, salinity, sediment mineralogy, and particle size distribution (fine sediment content) on the volumetric erosion rate of river sediments were studied by Lick and McNeil (2001) using Sedflume and they obtained similar results.

Based on the erosion testing device of Sedflume, Roberts et al. (2003) proposed the Adjustable Shear Stress Erosion and Transport (ASSET) Flume that directly measured both erosion rate and sediment transport modes as a function of applied shear stress and depth of the eroded sediment layer. The ASSET Flume, a rectangular (5 cm tall, 10.5 cm wide, 180 cm long), enclosed flume was designed to measure the erosion rate, suspended and bedload transport, and total eroded mass of quartz particles and fine-grained field sediments. The erosion test followed the same procedure as described for Sedflume previously, and the total mass eroded was measured by collecting and drying the sediment particles which remained in sediment traps after the experiments. More

29

effort was focused on analyzing and distinguishing between suspended and bedload transport in this study. It was concluded by Roberts et al. (2003) that the aggregated bedload transport was a function of sediment bulk properties including bulk density, particle size, and mineralogy.

The rotating annular flume was originally developed in the mid-1960s by Partheniades et al. (1966) and has been adopted in several studies on various muds (e.g. Partheniades et al., 1968; Parchure and Mehta, 1985; Kuijper et al., 1989; Sheng and Villaret, 1989). Zreik et al. (1998) ran laboratory erosion tests on Boston Blue Clay using a large rotating annular flume that was 5 m in diameter with rectangular cross sectional dimensions of 30 cm by 30 cm. The clay slurry was prepared and poured into the flume for the suspensions to settle, consolidate, and age before starting the erosion tests. In all cases of the applied shear stress ranging from 0.1 Pa to 1.0 Pa, surface erosion was observed. From their results, they concluded that the resistance to erosion at a given depth and for a given bed structure increased as bed age increased, which was attributed to thixotropic hardening. While age and structure were found to affect the bed erosion resistance over the full depth, the temperature effect predominated at the surface (only about 0.5 mm). Although mechanical strength tests on Boston Blue Clay using the Automated Fall Cone Device indicated that the mechanical strength was also influenced by the bed age, structure, and temperature, Zreik et al. (1998) concluded that bulk measures of shear strength were not useful in characterizing erosion strength.

A laboratory device known as Scour Rate in Cohesive Soils-Erosion Function Apparatus (SPRICOS-EFA) was developed by Briaud et al. (1999) and then applied in some following studies (e.g. Briaud et al., 2001, 2004; Ting et al., 2001). The SCRICOS

procedure involves a method to predict the time-dependent scour depth curve around a cylindrical bridge pier in a uniform cohesive sediment bed with constant velocity flow. As part of the procedure, EFA tests on soil samples were performed to obtain the relationship between vertical erosion rate ($\dot{z}$) and applied shear stress. The EFA consists of a straight rectangular acrylic pipe with a bottom port connecting to a standard Shelby tube (76.2 mm outside diameter) containing the sample to be tested. Pressure flow was obtained by pumping through the pipe, and the applied shear stress was measured indirectly by the head loss between two pressure ports immediately upstream and downstream of the sample. During the test, the sample was extruded continuously to maintain a steady height of 1 mm above the pipe bottom by a piston attached at the sample bottom. The vertical erosion rate was defined as the extruding height per unit of time during the test. A series of tests with applied shear stress ranging from 0.1 Pa to 100 Pa was performed on fine-grained sediments in Briaud et al. (1999). In later studies, the SPRICOS-EFA was further applied in erosion tests for both fine and coarse sediment beds (Briaud et al., 2001) and the scouring characteristics for complex pier geometry in fine-grained soils (Briaud et al., 2004). Ting et al. (2001) adapted the SPRICOS procedure (but did not use the EFA to obtain the relation between $\dot{z}$ and $\tau$) to measure the depth and shape of scour hole around cylindrical piers with different diameters (25, 75, 150, 210 mm) in a variable-slope flume and an in-floor concrete flume. They found that the extrapolated equilibrium scour depth correlated well with the pier Reynolds number but not the Froude number for these experimental cases.

To study the lubrication effect of clay particles on sand grain erosion, Barry et al. (2006) carried out erosion experiments in a 4.3 m long, 15 cm wide, and 19 cm deep

flow-recirculating rectangular flume. Samples were prepared with sand particles of median particle size ranging from 0.41 mm to 1.20 mm mixed with 0% to 15% of clay and placed at the last 0.6 m of the flume. Besides the rectangular flume, another set of erosion tests was conducted in a rotating cylinder apparatus (7.6 cm tall and 9.6 cm in diameter) (Jiang et al., 2004). Acceptable agreement was found between the erosion rates obtained from the two apparatuses, which indicated the flume experiment measurements were reasonably accurate (Barry et al., 2006). The resulting values of critical shear stress decreased to a minimum value with the addition of 3% to 6% clay particles to the sand bed, demonstrating the lubrication influence of the fines. As the clay fraction increased to around 5% to 13%, the critical shear stress increased back to the value of pure sand; this range of clay fraction was identified as the pore space-filling clay volume fraction beyond which the sand erosion was significantly influenced by clay.

El Ganaoui et al. (2007) tested samples from two surface river bed sites and one coastal site (160 m deep) using a 3.6 long PVC recirculating flume with 40 cm by 40 cm cross-section in the main channel. Eight sediment cores were sampled from each of the three sites for resuspension tests in the flume and sediment property analysis (e.g. water content and grain size distribution). The resuspension of sediments was monitored through turbidity, which was related to the suspended load measured by filtering the water samples collected every 3 minutes. The surface layer, representative of recent deposits of suspended particles, was identified to have much smaller critical shear stress then the other layers in both freshwater and marine sediments. Referred to as the "fluff layer", the surface layer was shown to consist of fine and unconsolidated sediments that

behaved like non-cohesive sediments while the second layer and those below were characterized as being cohesive.

Righetti and Lucarelli (2007) analyzed benthic sediment samples from seven lakes in Italy to discuss the applicability of Shields theory to cohesive benthic sediments. The critical shear stress of sediments was evaluated using a 6 m long, recirculating sedflume. This straight plexiglass flume was 30 cm wide and 4 cm high and had a test section with an open bottom through which a circular coring tube with filled sediment could be inserted. During the test, the particle-floc erosion process was monitored by a progressive scan DV Camera mounted at one side of the experimental device to record the material dislodged from the core by the flow through a defined control volume. Then the critical stage of sediment erosion was digitally quantified by automatic image processing. The rational analysis and parameterization of the incipient motion for cohesive sediments performed in the study led to a modified critical Shields parameter. The modification explained the experimental evidence that (1) the critical conditions for cohesive sediments were reached for values of the critical Shields parameter higher than those obtained for non-cohesive sediments; (2) critical conditions depended on the bulk density of cohesive sediments.

In the study of erosion threshold for saturated natural cohesive sediments by Ternat et al. (2008), field sample cores collected from two river beds were tested to deduce the erosion threshold parameters from erosion flux measurements. The erosion tests were carried out in a straight recirculating flume, which was 13.5 m long overall with an 8 m long test section. The cross section of the rectangular channel was 0.6 m in width, and the flume was horizontal with no storage tank in order to enhance sediment

33

circulation. At 5.5 m from the testing zone entrance, 8 sediment cores, each of them being cylindrical and 15 cm in diameter, were anchored at the channel bed under flowing water during the test. Turbidity measurements performed with two optical backscatter sensors were recorded during the erosion test and then related to suspended sediment concentration from which the erosion flux was deduced. An erosion model developed in this study based on the cohesion and coordination number of particles, i.e. the total number of neighbors touching to a central particle, confirmed that the cohesion force becomes efficient for clay-sized particles. From the experiment results, the erosion threshold of the natural sand-clay mixture bed sediments increased when porosity decreased and when the clay content increased at least up to 20%.

### 2.3.2 Benthic In Situ Flumes

Due to the abundance and complexity of sediment properties in the field, the need for collecting field data has led to the development of in situ flumes and devices. Generally, most of the existing in situ erosion instruments may be classified as benthic flumes or miscellaneous devices (e.g. submerged jets) (Aberle et al., 2003). Benthic in situ flumes can be further divided into (1) recirculating flumes (Amos et al., 1992b; Maa et al., 1993; Black and Cramp, 1995; Houwing and van Rijn, 1998; Widdows et al., 1998) and (2) straight flow-through flumes (Young, 1977; Gust and Morris 1989; Ravens and Gschwend, 1999; Aberle et al., 2003; Debnath et al., 2007). The common concept applied by most benthic flumes is relating the turbidity of water to the amount of sediment eroded to obtain the rate of erosion. Benthic flumes are placed on the bed of a body of water such as a lake, river, or harbor where the sediment erosion is of concern. As water is pumped through or into the flume, the erosion and sediment transport rate can be

estimated by measuring the suspended sediment concentration (SSC) in the flow under different hydrodynamic conditions.

A benthic annular flume developed by Amos et al. (1992b), Sea Carousel, was developed to measure in situ erodibility of fine-grained sediments in intertidal and subtidal environments. The carousel was 1 m in radius with an annulus of 0.15 m wide and 0.3 m high, and equipped with three optical backscatter sensors, a lid rotation switch and an electromagnetic current meter. The flow was induced by lid rotation and detected by the electromagnetic current meter. During the test period, erodibility of sediments was inferred from the rate of change in SSC detected in the annulus. The field study on fine-grained sediment erosion from the Bay of Fundy in Canada by Amos et al. (1992a) using Sea Carousel detected three patterns of erosion (i.e. Type Ia, Ib, II) in the studied area. A similar device was proposed by Maa et al. (1993), VIMS Sea Carousel, to determine the threshold of shear stress necessary for sediment entrainment in situ. This annular flume was composed of two cylinders which were 0.2 m high with diameters of 2.0 m and 2.3 m from the inner and outer walls of the flume. Field application of the flume on the inner shelf of the Middle Atlantic Bight showed that the sandy inner shelf sediment had a higher critical bed shear stress (0.22 Pa) for resuspension than that for silty sediments (0.1~0.19 Pa) generally. Data from partially cohesive sediments in the lower Chesapeake Bay indicated seasonal variations in the critical shear stress, which was attributed to bioturbation or microflora living on the bed (Maa et al., 1993). Furthermore, in situ erosion rate measured in Baltimore Harbor, MD by VIMS Sea Carousel (Maa et al., 1993) was applied by Sanford and Maa (2001) to develop a general algorithm for fine sediments to describe both Type I (depth-limited) and Type II (unlimited) erosion.

Black and Cramp (1995) developed a small size, field-portable recirculating flume to examine the erodibility of estuarine muds. Rather than an annular configuration, the flume was designed as a race-track shaped circulating system where water was continuously recirculated by a rotating paddle wheel. The flume was 1.2 m in length and 0.5 m in width, with a rectangular hole (0.08 m by 0.25 m) in the floor for bed sediment erosion testing. During the test, changes of SSC were recorded by optical backscatter probe and the collected data were related to erosion behavior of sediments. Another portable in situ benthic flume for intertidal cohesive sediments was proposed by Widdows et al. (1998). The annular flume, constructed of acrylic material with a 0.64 m (outer) and 0.44 m (inner) diameter, represented a smaller modified version of Sea Carousel (Amos et al., 1992b; Maa et al., 1993). Applications of the portable annular flume in both field and laboratory experiments confirmed the importance of maintaining both the physical and biological structure of cohesive sediments when measuring erodibility (Widdows et al., 1998). Instead of the horizontal flow circulating system (e.g. Amos et al., 1992b; Maa et al., 1993; Black and Cramp, 1995; Widdows et al., 1998), the In Situ Erosion Flume (ISEF) designed by Houwing and van Rijn (1998) circulated the flow in the vertical plane which reduced the dimension of the instrument. Consisting of a lower horizontal test section, two bent sections and an upper flow propelling section, ISEF was 1.8 m long (containing the 0.9 m long horizontal test section) and 0.7 m high. Calibration and validation of ISEF were carried out by the measurement of erosion of a kaolinite sediment bed under laboratory conditions. Field application of ISEF was conducted to determine the critical erosion threshold of cohesive sediments on intertidal mudflats along the Dutch Wadden Sea Coast (Houwing, 1999).

Young (1977) proposed a flow-through flume (Seaflume) deployed at sea to study erosion of undisturbed muddy sediments under controlled flow conditions. The Seaflume was designed as an open-bottomed rectangular duct with a sloping, open mounted entrance section, and a straight observation section. The channel for the flow-through section was 4 m long with a 0.15 m by 0.61 m cross-section. As the flow was pumped through the channel under control of a panel valve, a deep-sea camera provided close-up photography for observing the erosional behavior of sediments. A modified version of Seaflume was presented and tested in the field by Gust and Morris (1989). In the modified Seaflume, instantaneous SSC was calculated from the signal differences obtained by the optical attenuation meters positioned at the inlet and outlet of the duct. Ravens and Gschwend (1999) used an acrylic plastic in situ flume to observe the sediment erodibility in Boston harbor. Measuring 2.4 m long, 0.12 m wide and 0.06 m high, the flume had a grill over the flow entrance to keep large objects out. During the test, flow velocity and turbidity were measured by a nonintrusive laser Doppler anemometer and a turbidimeter, respectively. The resulting erodibility under the absence of algal mats agreed with other in situ studies of high salinity, silty sediments. The values of critical shear stress and erosion constant were found to be depth sensitive.

Applications of the National Institute of Water and Atmosphere Research in situ flume (NIWA I) to measure the erosion characteristics of natural cohesive sediment beds have been reported by Aberle et al. (2003, 2004, 2006). The basic structure of NIWA I was composed of a flume canal and a propulsion unit which sucked the water through the flume canal. Consisting of a contracting, open-mounted entrance section, a straight erosion section, and a straight fixed-bed section, the flume canal was basically a 1.2 m

long rectangular conduit. In the erosion section, the flume cross section decreased gradually from 0.15 m by 0.30 m to 0.10 m by 0.20 m within 0.3 m. To estimate the erosion rate of sediment beds of interest, the SSC in the flume was monitored with optical backscatter sensors, diode, and photodetectors. Calibration of the device indicated that the photodetectors displayed a linear relationship with SSC for low turbidity, while the relationship became nonlinear beyond a threshold. Therefore, at high turbidity only the SSC data obtained from optical backscatter sensors were used. In addition to NIWA I, Debnath et al. (2007) applied a modified in situ flume developed by NIWA (NIWA II) (presented in Debnath et al., 2004) to examine the resuspension, bed load, and erosion patterns in the field. Field measurements by NIWA I and II in several freshwater and saltwater environments were compiled and analyzed. The data indicated that the assumption that erosion rate is equal to the resuspension rate is not always valid because of the significance of bed load in cohesive sediment erosion. In addition, the role of clay content and other sediment physical properties in cohesive sediment erosion research was highlighted.

### 2.3.3 Submerged Impinging Jets

Besides benthic flumes, another type of portable erosion testing device designed for use in the fields, cohesive strength meter (CSM), was first introduced by Dunn (1959) and applied by Paterson (1989) to intertidal areas which were inhabited by diatoms. The CSM employed the eroding stress of a perpendicular jet of pressurized water directed at the sediment surface in short pulses and examined the light transmission of the water body across the test chamber. By examining the decrease and recovery of light transmission percentage progressing with time, the erosion and resettling of sediments

can be determined, respectively. Later, a modified, automated and calibrated version of the CSM was presented and applied in situ on mudflat sediments in Sylt, Germany by Tolhurst et al. (1999). Calibration and field application of the modified CSM showed that the critical shear stress can be determined by the measurements for particles with median grain size from 2 μm to 1500 μm. However, for particles smaller than 2 μm, the critical shear stress for sediment suspension could not be detected by the device. Watts et al. (2003) conducted in situ measurements of intertidal sediments using the modified CSM and the fall-cone method to determine the critical shear stress and undrained surface shear strength, respectively. The undrained sediment shear strength obtained with the fall-cone apparatus was proved to provide a useful indication of the critical shear stress. Using a similar device, an in situ jet-testing method developed by Hanson (1991) was applied to determine the critical shear stress and erodibility of river beds in an urbanizing basin by Shugar et al. (2007). In their study, high risk areas of very erodible to moderately resistant were identified due to the relatively low critical shear stress and high erodibility coefficient. The jet-testing routine was recognized by the American Society for Testing and Materials (ASTM) to provide a relatively inexpensive assessment of streambed response to extreme flows.

Submerged vertical impinging jets have also been used in laboratory experiments to study the scour of cohesive soil. Mazurek et al. (2001) studied the erosion pattern and scour hole development by a circular impinging jet on a cohesive sediment bed, consisting of 40% clay, 53% silt, and 7 % fine sand. The jet was created by pumping tap water though an 83 cm long, 12 cm diameter circular pipe with a nozzle to impinge perpendicularly to the sediment surface. From the results, the observed predominant type

of erosion caused by the jet was mass erosion which required a much higher bed shear stress to initiate than that of surface erosion. Analysis based on impinging jet mechanics showed that the equilibrium scour hole dimensions were a function of the jet momentum flux, impinging height of the jet, and properties of eroding fluid and eroded sediment bed. Another study on scour holes formed by submerged circular vertical jets impinging on sediment beds composed of varying percentages of clay was carried out by Ansari et al. (2003). Cohesive sediment mixtures were prepared with clay percentage by dry weight from 10% to 60% with 10% increment in between. Dimensions of the scour hole generated by the impinging jet on the cohesive sediment bed were plotted and compared with data in sand (non-cohesive) bed from the literature. The scour occurring while the jet was running was termed as dynamic scour, and the scour depth remaining after the jet flow stopped was referred to as static scour depth. It was found that the difference between dynamic and static scour was much smaller in a cohesive sediment bed compared to that in a non-cohesive sediment bed under the same jet flow conditions (Ansari et al. 2003).

Instead of directing a fluid jet towards the sediment surface, Williamson and Ockenden (1996) developed an instrument to measure erosion shear stress in situ (ISIS) by sucking water into a bell-head PVC duct positioned just above the sediment bed. By drawing water radially across the bed into the bell-head center, a shear stress was generated on the sediment bed. Then the turbidity of the extracted water was measured using a nephelometer before being recirculated back to the water body. During the test, the incoming flow rate was gradually increased in user-defined steps and time intervals until a jump in turbidity was observed. Then the applied shear stress at the turbidity jump

was determined as the critical shear stress required to initiate erosion. Application of different in situ devices including the ISIS, sea carousel, and CSM to estuary areas has shown that the varying trends (but not values) of the surface critical shear stress from the three devices were comparable. A number of reviews or comparative studies of field erosion devices have been reported including Black and Paterson (1997), Cornelisse et al. (1997), and Tolhurst et al. (2000). Although following similar trends, the comparative studies showed that results from different devices cannot be directly compared due to fundamental differences such as flow condition, shear stress calibration, and operating time duration (Black and Paterson, 1997; Tolhurst et al., 2000). Therefore, it is important to compare hydrodynamic parameters in erosion areas rather than trying to establish comparable erosion parameters among different devices (Debnath et al., 2007).

## 2.4 Physical Properties Affecting Erodibility

The physical properties of fine sediments have been studied and discussed to apply as indicators of sediment resistance to erosion (Grabowski et al., 2011; Stone et al., 2011). The properties affect the erodibility of fine sediments through changes in size or material of sediment constituents which influence the particle structural associations (i.e. E-E, E-F, F-F associations). Mean particle or aggregate size, grain size distribution (i.e. contents of clay, silt, and sand), and bulk density or water content are some of the widely discussed physical properties which have been recognized to influence fine sediment erodibility.

### 2.4.1 Mean Particle Size

Mean (or median) particle size of sediments is one of the physical properties that has been studied to correlate with sediment erodibility. Early work on correlations

between particle size and the minimum flow velocity required to initiate sediment transportation, such as Hjulström (1939) and Postma (1967) plots, have become reference tools for hydraulic engineers. Laboratory flume tests by Smerdon and Beasley (1961) established the empirical relationships between erosion thresholds and soil properties including median particle size ($d_{50}$), plasticity index, and clay percentage by weight. Laboratory studies have demonstrated positive correlations between particle size and erosion threshold for non-cohesive, coarse sediments (sands and gravels) (Dade et al., 1992; Tolhurst et al., 1999). Nevertheless, more recent studies about the effects of particle size on soil erodibility suggest a negative correlation between particle (or aggregate) size and critical shear stress for clay- and silt-sized sediments (e.g. Roberts et al., 1998; Thomsen and Gust, 2000; Briaud et al., 2001; Lick et al., 2004; Kothyari and Jain, 2008).

Roberts et al. (1998) did a series of laboratory flume experiments to investigate the effects of particle size and bulk density on the erosion of quartz particles with mean size ranging from 5 μm to 1350 μm. Under applied shear stresses from 0.2 Pa to 6.4 Pa, the critical shear stresses were determined as a function of particle size with bulk density as a parameter. At a given constant bulk density, the volumetric erosion rate (in cm/s) increased with mean particle size and reached a maximum value at a particle size around 100μm then decreased as particle size became larger. The critical shear stress, defined as the applied bed shear stress at which the volumetric erosion rate was $10^{-4}$ cm/s by the authors, decreased as the particle size decreased from a maximum value of 1350 μm and reached a minimum for particles around 100μm in diameter before increasing again for smaller particles (Figure 2.2). The negative correlation between particle size and critical

shear stress of small (<120μm) quartz particles was concluded to be a behavior of

cohesive sediments by the authors; however, later studies argued that the inter-particle

attraction would have been partially caused by organic material rather than the cohesion

between quartz sediments due to the long consolidation time (Lick et al., 2004;

Grabowski et al., 2011).
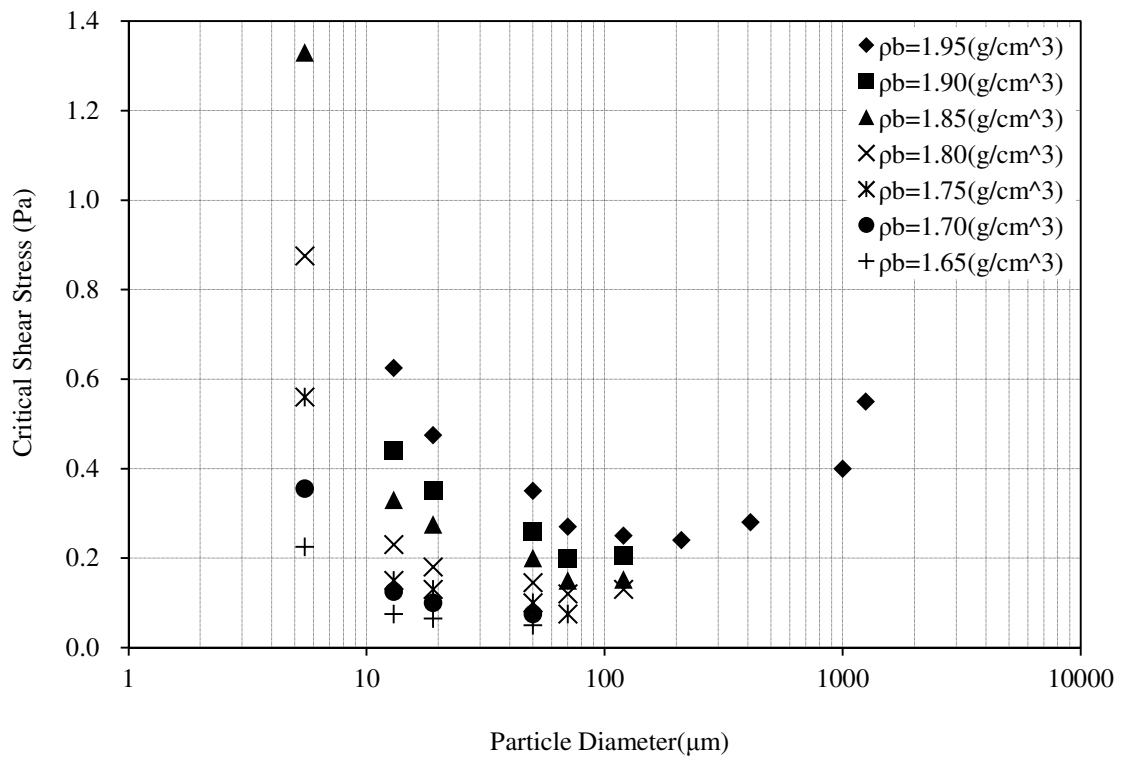


Figure 2.2 Critical shear stress as a function of particle size and bulk density
for quartz sediments (after Roberts et al., 1998)

From a field survey, Thomsen and Gust (2000) found a negative correlation

between critical shear stress and median particle size ($d_{50}$) for natural marine mud. From

the study, a two-layer concept of the surface and underlying aggregates was suggested

based on the characteristics of the critical shear stress measurements. The surface and underlying layers can be referred to as unconsolidated and consolidated sediment, respectively. In addition, the silty sediments with $d_{50} < 30$ μm behaved in a manner similar to clay particles, resulting in higher erosion thresholds than those reported from the literature (Miller et al., 1977) which was attributed to biological stabilization by the authors. Using a different measuring device (EFA), Briaud et al. (2001) reported a negative correlation with critical shear stress for consolidated fine-grained sediment beds sampled from the field. Kothyari and Jain (2008) studied the influence of cohesion on the initiation of sediment erosion by flume experiments using mixtures of clay in proportions varying from 10% to 50% with fine gravel or with fine gravel and fine sand in equal proportion. Data of critical shear stress versus mean particle size from Kothyari and Jain (2008) and from the literature were plotted and compared with Shield's function for non-cohesive sediment. A negative correlation between erosion threshold and particle size was also suggested for clay and fine silt in their study. The critical shear stress values and their variation with $d_{50}$ as obtained from the literature review are plotted in Figure 2.3.
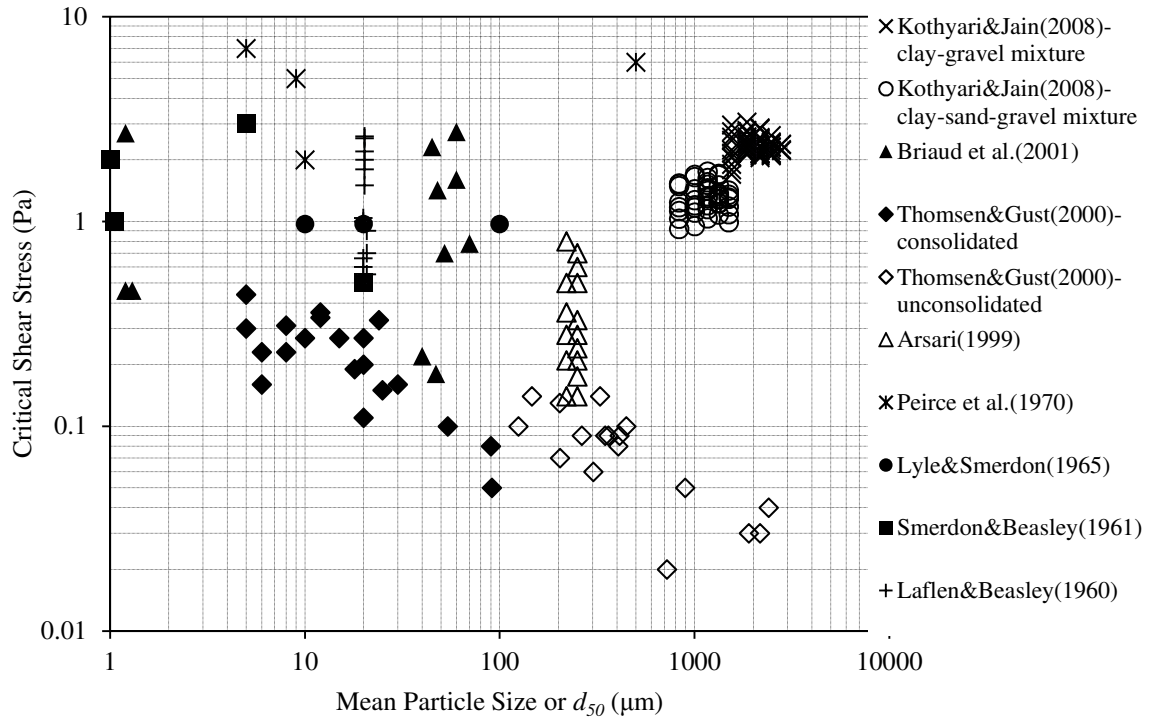
Figure 2.3 Critical shear stress varying with mean or median particle size

It is shown in Figure 2.3 that for sediments (or aggregates) with mean or median particle size smaller than about 100 μm, negative correlations between critical shear stress and particle size have been reported by several researchers. Nevertheless, critical shear stress has been reported to correlate either positively or negatively with particle size for larger sediments and aggregates (>100 μm). This contradiction may be explained by the different conditions under which the aggregates or sediment beds formed (Grabowski et al., 2011). For example, the continual reduction in critical shear stress with particle size for unconsolidated sediment in the data of Thomsen and Gust (2000) might be caused by the increased porosity and organic content of increasing aggregate size which leads to decreasing density (Droppo et al., 2007). In contrast, in cases where soil density increases with particle size (e.g. Kothyari and Jain, 2008), remarkable increases in sediment

erosion stability (resistance) with particle size are also observed. Despite the convenience, mean or median particle size alone does not seem to be enough to determine erosion threshold, especially for natural sediments formed with various constituents and under different deposition conditions.

## 2.4.2 Grain Size Distribution

Properties of sediments with the same mean particle size may deviate distinctively due to varying relative proportions of different sized particles, i.e. different grain size distributions. For natural sediments, the difference in grain size distribution is usually substantial enough to affect sediment erodibility. The amount of fines in the sediment is a prime factor that has been examined in studies using laboratory mixtures (e.g. Mitchener and Torfs, 1996; Panagiotopoulos et al., 1997; Reddi and Bonala, 1997; Lick et al., 2004; van Ledden et al., 2004; Barry et al., 2006; Kothyari and Jain, 2008; Debnath and Chaudhuri, 2010a, b; Grabowski et al., 2010; Geremew and Yanful, 2011) or field soil samples (e.g. Mitchener and Torfs, 1996; Houwing, 1999; Aberle et al., 2004; Dickhudt et al., 2011). In these studies, some investigators lumped proportions of silt and clay as "mud content" while some focused on the clay content only because it is the clay content within mud that provides interparticle cohesion (van Ledden et al., 2004). A few field studies reported changes in erosion behavior of sediments depending on the sand fraction in addition to mud or clay content (Mitchener and Torfs, 1996; Aberle et al., 2004; Dickhudt et al., 2011).

Based on data obtained from both laboratory and field experiments, Mitchener and Torfs (1996) examined the variation in erosion resistance when adding sand to mud or vice versa. By reviewing erosion resistance of artificial mixed or field sampled

sediments measured with different laboratory or in situ devices, including straight uni-directional current flumes, flow-through and recirculating benthic flumes, and ISIS, a few observations on the erosion behavior of mud-sand mixtures were obtained. The critical shear stress increased in both cases when mud was added to sand and vice versa; however, the addition of mud to a sand bed increased the critical shear stress more significantly (up to a factor of 10 by 30% mud addition) than in the case of sand being added to a mud bed ($\tau_c$ increased by a factor of 2 with 50% sand addition). The erosion threshold reached as high as maximum values of homogeneous beds when the addition of mud varied from 30% to 50% (Mitchener and Torfs, 1996). Similar findings were also reported by Panagiotopoulos et al. (1997); that is, the rate of increase in erosion thresholds became larger as more than 30% of mud content was added to sandy deposits. For small amounts of mud addition (3% to 15%) to sand, the mode of erosion changed from non-cohesive to cohesive behavior, which illustrated the substantial effect on erosion resistance exerted by fine cohesive particles (Alvarez-Hernandez, 1990; Dade and Nowell, 1991; Mitchener and Torfs, 1996). In the case of layered mixed beds, i.e. mud and sand segregated under deposition into discrete layers, it was suggested that the erosion of the layers could be treated as a series of muddy and sandy layer events owing to the difference in erosion processes (Mitchener and Torfs, 1996).

Later laboratory studies of mud- or clay-mixtures demonstrated that the clay content should be a more generic indicator than mud content for the transition between non-cohesive and cohesive erosion behavior (Panagiotopoulos et al., 1997; van Ledden et al., 2004). The difference in clay mineralogy also plays a key role in the increasing magnitude of erosion resistance with proportion of clay content. While many of the

studies used kaolinite as the predominant clay to mix with sand, Mitchener and Torfs (1996) showed deviations in the slopes of increasing critical shear stress with fine sediment content consisting of different minerals. Lick et al. (2004) also showed that the addition of 2% bentonite to quartz particles ranging from 100 μm to 400 μm in size significantly increased the critical shear stress of the mixture. Laboratory measurements of erosion resistance for a clay-sand mixture, as plotted in Figure 2.4, generally showed increasing trends of the critical shear stress with the increase of clay content from 5% by weight up to a maximum around a clay content of 30% to 50% by weight (Panagiotopoulos et al., 1997; Reddi and Bonala, 1997; Barry et al., 2006; Kothyari and Jain, 2008; Debnath and Chaudhuri, 2010a, b; Grabowski et al., 2010; Geremew and Yanful, 2011).

Critical Shear Stress (Pa)

10

1

0.1

0.01

1%    10%    100%

Clay or Mud Content (%)

◇ Geremew&Yanful(2011)

□ Grabowski et al.(2010)-
sand/kaolin mixture

△ Kothyari&Jain(2008)-clay-gravel
mixture

○ Kothyari&Jain(2008)-clay-sand-
gravel mixture

■ Barry et al.(2006)-clay mixture1

▲ Barry et al.(2006)-clay mixture2

◆ Barry et al.(2006)-
kaolinite(saline)

● Barry et al.(2006)-
kaolinite(fresh)

✖ Panagiotopouslos et al.(1997)-
Sand(152.2μm)

✕ Panagiotopouslos et al.(1997)-
Sand(215μm)

■ Mitchener&Torfs(1996)-kaolinite

▲ Mitchener&Torfs(1996)-
montmorillonite

● Mitchener&Torfs(1996)-scheldt
mud

Figure 2.4 Critical shear stress of soil mixtures with different clay content by weight
(Note: mud content was only used in Panagiotopoulos et al., 1997)

Field studies on sediment erodibility have focused on the effects of clay/mud or
sand content as well. One of the examples is from Houwing (1999), who reported a
negative correlation between erosion rate and the mud content of sediments. Namely, the
erosion rates of intertidal sediment decreased by 2 orders in magnitude as the mud
content increased from 4% to 35%. Some other field studies in riverine environments
found negative relationships between sand content and erosion threshold (Gerbersdorf et
al., 2005; 2007), and between mud content and erosion coefficient (small erosion
coefficient represents low erosion rate) (Debnath et al., 2007). Nevertheless, Aberle et al.
(2004) reported a positive relationship between mud content and erosion coefficient,

which was attributed to the particle size of sand that might be large enough to take over the cohesion from fines and increase the erosion resistance by its weight (Roberts et al., 1998; Debnath et al., 2007).

Analysis of the critical shear stress of Georgia sediments from bridge foundations by Navarro (2004) and Hobson (2008) led to an improved model used to predict the Shields parameter of a sediment based on the fine content. Specifically, the critical value of the Shields parameter was expressed as a function of median particle size and the proportion of fines (silt and clay) by weight. Although the relationship is limited to the ranges of size and fine content for the sampled Georgia soils, it includes the viscous effects of the flow and the effects of interparticle strength using the fine contents in sediments (Hobson, 2008). Later studies suggested evaluation of the volumetric fraction of fines instead of percentage by weight. Dickhudt et al. (2011) reported that the eroded mass of estuarine sediments under 0.4 Pa applied shear stress decreased from more than 2 $kg/m^2$ to less than 0.3 $kg/m^2$ when the volumetric clay fraction increased from 30% to 70%. No matter whether the volumetric or gravimetric proportion of fines is used, it is importance to recognize the correlation between mud content and bulk density (or water content) due to the water containing capacity of mud (clay). Changes in mud content are usually accompanied by variations in bulk density, especially for natural cohesive sediments (e.g. Panagiotopoulos et al., 1997), and both properties should be considered corporately as the controlling factors of cohesive sediment erodibility.

### 2.4.3 Bulk Density and Water Content

Bulk density and water content are measurements of the relative solid and liquid phases in sediments, which have been demonstrated to play important roles in the erosion

behavior of fine sediments in both laboratory and field studies (e.g. Mitchener and Torfs, 1996; Williamson and Ockenden, 1996; Jepsen et al., 1997; Roberts et al., 1998; Houwing, 1999; Krone 1999; Avnimelech et al., 2001; Lick and McNeil., 2001; Aberle et al., 2004; Ravisangar et al., 2005; Gerbersdorf et al., 2007). While the two measurements are approximately inversely correlated, they both indicate the degree of packing or consolidation of sediments (Grabowski et al., 2011). Generally, bulk density increases (or water content decreases) with increasing depth of sediment layers in both natural and artificial-mixed soils because of the increases in deposit age and consolidation level of deeper sediment layers (e.g. McNeil et al., 1996; Lick and McNeil, 2001; Ravisangar et al., 2005). As the significance of bulk density to cohesive sediment erosion has been supported in the literature, some researchers argued that water content should be a more intuitive factor as it directly influences the mechanical properties of clay (Grabowski et al., 2011). In fact, the assumption of saturated soil, i.e. the pores are filled with water and the existence of gas/air is neglected, has been used for studies of benthic and estuarine sediments. Under this assumption, bulk density can be expressed as a function of water content and the two properties have been applied interchangeably (e.g. McNeil et al., 1996; Jepsen et al., 1997; Roberts et al., 1998).

Bulk density, also referred to as wet bulk density in contrast to the dry (bulk) density in some studies, represents the overall density of sediment which depends on the soil particle density, the amount and density of pore fluid, and the existence of gas/air (Grabowski et al., 2011). Specifically, bulk density is defined as the total mass (including solid, liquid, and gas phases) of sediments divided by the total volume, while dry density only takes the mass of solid as the numerator. The proportion of water in sediments is

51

usually defined in a gravimetric way. The ASTM definition of water (moisture) content in soil and rock by mass (ASTM D 2216-05) determines the water content ($w$) as the ratio of mass of pore water to the mass of solids:

$$w = \frac{m_{wet} - m_s}{m_s} = \frac{m_w}{m_s} \tag{2.12}$$

where $m_{wet}$ = mass of the wet sediment; $m_s$ = mass of solid (dry sediment); and $m_w$ = mass of the pore water. Some researchers (e.g. McNeil et al., 1996; Jepsen et al., 1997; Roberts et al., 1998) defined the water content in a slightly different way by replacing the mass of solids with the mass of wet sediment as denominator:

$$w = \frac{m_{wet} - m_s}{m_{wet}} = \frac{m_w}{m_{wet}} \tag{2.13}$$

Using equation 2.13, Jepsen et al. (1997) and Roberts et al. (1998, 2003) related the bulk density ($\rho_b$) to water content by:

$$\rho_b = \frac{\rho_s \rho_w}{\rho_w + (\rho_s - \rho_w)w} \tag{2.14}$$

where $\rho_s$ = density of solids.

From previous studies, bulk or dry density has been found to be negatively correlated with sediment erodibility. In other words, denser beds usually have lower erosion rates under a certain applied shear stress; thus, deeper layers of sediment are more resistant to erosion than those at the surface that may be freshly deposited. El Ganaoui et al. (2007) reported that the critical shear stress of surface-layer sediments in both freshwater and marine areas can be 10 times smaller than those of the deeper layers. Other studies, including Jepsen et al. (1997), Lick and McNeil (2001), and Bale et al. (2006, 2007), also reported that dense sediment beds have much lower erosion rates(up to

100 times lower) and 5 to 8 times higher erosion thresholds than the less dense beds. Empirical expressions between sediment bulk density and critical shear stress have also been developed for artificially mixed (Mitchener and Torfs, 1996) and natural estuarine muds (Amos et al., 2004):

$$\tau_c = 0.015(\rho_b - 1000)^{0.73} \qquad \text{for artificial mixture} \qquad (2.15)$$

$$\tau_c = 5.44 \times 10^{-4} \rho_b - 0.28 \qquad \text{for natural estuarine muds} \qquad (2.16)$$

where $\rho_b$ = bulk density of sediments in $(kg/m^3)$; and $\tau_c$ = critical shear stress in Pa.

Values of critical shear stress varying with bulk density reported from the literature are plotted in Figure 2.5. It is shown that there is a common agreement of the increase in critical shear stress as sediment bulk density increases, even though the data were obtained using different instruments and different sources of natural cohesive sediments. Houwing (1999) and Bale et al. (2006) also reported the water content of each testing sample and plotted the relationship of critical shear stress versus water content. As expected, a negative correlation was identified from their data in both of the studies. Amos et al. (2004) and Bale et al. (2006) investigated the effects of environmental variables, including water temperature and salinity, on the erosion thresholds of natural estuarine muds. In was concluded that no significant seasonal fluctuation in bed stability cased by water temperature and salinity by Amos et al. (2004). At the whole-estuary scale, the erosion behavior of the sediments reflected an underlying physical control of sediment properties instead of the influences from biota which were affected by temperature and salinity (Bale et al., 2006).
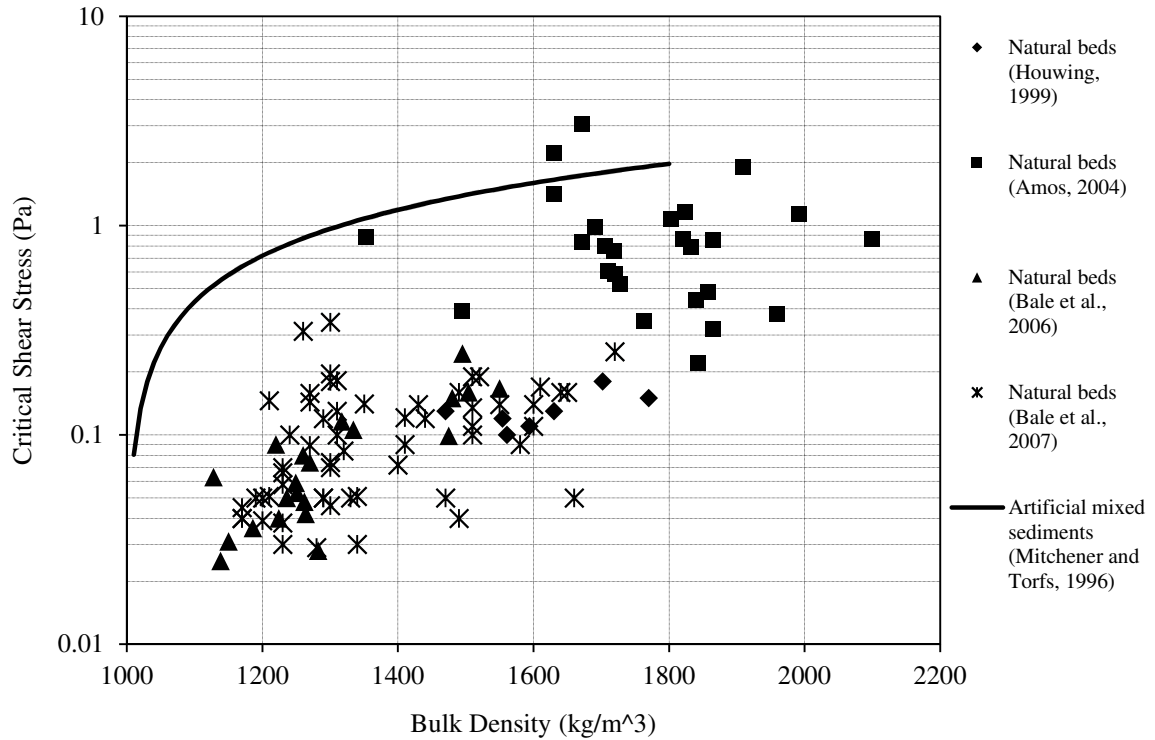
Figure 2.5 Critical shear stress of sediments with different bulk density

Changes in bulk density (or water content) also suggest variation in sediment structure. Krone (1999) found a critical value of bulk density for quartz particles by further analyzing the data from Roberts et al. (1998) and found the breakpoint of two different sediment structures. Specifically, the relationship of erosion rate versus bulk density was plotted for each of three different applied shear stresses. From each plot, two linear relationships with different slopes were indentified, representing the erosion rate-bulk density correlation for sediment with bulk density above and below 1770 kg/m$^3$, respectively. The two slopes reflected different structures of sediments. The steeper slope of sediment over the lower density range suggested a soil structure with large pores which easily collapsed from overburden and shearing while the flatter slope over a higher density range indicated a structure of a higher number of contacts per particle due to

denser packing and slower collapse (Krone, 1999). Ravisangar et al. (2005) investigated the influence of sediment structure on the critical shear stress of kaolinite sediment beds. Under settling conditions with different pore fluid properties (e.g. pH value, ionic strength, and addition of natural organic matter), correlations of critical shear stress (referred to as erosional strength in Ravisangar et al., 2005) versus sediment bulk density were reported and related to sediment structure (particle associations) over the range from about 1100 kg/m$^3$ to 1700 kg/m$^3$. From the study, the F-F association was reflected by small and gradually increasing critical shear stress from 0.5 Pa to 1.0 Pa for the whole bulk density range. In contrast, a significant increase of critical shear stress from 0.5 Pa to 3.0 Pa occurred as the bulk density increased from 1100 kg/m$^3$ to 1250 kg/m$^3$ representing the E-F association of clay particles.

## 2.5 Mathematical Models of Erosion

Erosion behaviors are generally recognized to be predominantly caused by bed shear stresses exerted under turbulence and influenced by sediment properties including particle size, fine content, bulk density and existence of organic matter. To describe the erosion resistance of sediments, mathematical formulations have been developed to determine the erosion rate of sediments. Notwithstanding the lack of agreement about the most appropriate mathematical expression, a few types of models have been applied in most studies (Sanford and Maa, 2001).

Power-law relationships between sediment erosion rate and the applied bed shear stress have been used by researchers who advocate that there is a critical value of bed shear stress below which there would be no erosion of sediment (or erosion rate is too small to be observed) (e.g. Lick, 1982; Gust and Morris, 1989; Amos et al., 1992a; Black

et al., 2002; Shugar et al., 2007; Ternat et al., 2008; Geremew and Yanful, 2011). The power law relationship can be expressed as:

$$E = M(\tau - \tau_c)^n \tag{2.17}$$

where $E =$ erosion rate $(Kg/m^2/s)$; $\tau =$ applied bed shear stress $(N/m^2)$; $\tau_c =$ critical shear stress, the value of $\tau$ at which $E \approx 0$ $(N/m^2)$; $M, n =$ experimental constants. In many studies, a simpler linear relation has been used by setting $n = 1$ in Equation 2.17 and the formulation is usually expressed with the applied bed shear stress non-dimensionalized by $\tau_c$ in the parentheses (e.g. Mehta et al., 1988; Hanson and Simon, 2001; Black et al., 2002):

$$E = M\left(\frac{\tau}{\tau_c} - 1\right) \tag{2.18}$$

which is referred to as the Ariathurai-Partheniades erosion formulation (Ariathurai, 1974). The linear formulation has been used most often to describe Type II erosion, which has a single, constant value of $\tau_c$ that does not change with depth of sediment layers (Sanford and Maa, 2001).

In some studies, an exponential form of erosion model has been suggested (e.g. Gularte et al., 1980; Parchure and Mehta, 1985; Houwing, 1999; Amos et al., 2004; 2010):

$$E = \varepsilon_f \exp\left[\alpha(\tau - \tau_c)^\beta\right] \tag{2.19}$$

where $\varepsilon_f =$ the flow erosion rate when $\tau - \tau_c = 0$; $\alpha, \beta =$ experimental constants; and $\beta = 0.5$ as reported by Parchure and Mehta (1985). The exponential expression is often used for Type I erosion, in which $\tau_c$ is a function of depth and generally increases for deeper sediment layers (Parchure and Mehta, 1985; Sanford and Maa, 2001). In Type I

erosion, resistance of sediment generally increases with depth and is usually proportional to sediment bulk density (Feagin et al., 2009). Mehta and Lee (1994) defined the rate of change in critical shear stress with depth or effective stress by the friction angle:

$$\sigma = (\rho_s - \rho_w)gz + P \tag{2.20}$$

$$\tau_{c,z} = \tau_{c,0} + \sigma \tan(\phi) \tag{2.21}$$

where $\sigma$ = the effective stress; $z$ = depth of sediment layer; $P$ = the in-situ excess pore pressure; $\tau_{c,z}$ = the critical shear stress of sediment layer at depth $z$; $\tau_{c,0}$ = the critical shear stress at surface; and $\phi$ = friction angle.

Some others champion the concept that the critical value of bed shear stress at which erosion initiates does not exist in reality, especially for fine-grained sediments; in other words, the zero erosion rate may only exist when there is no applied shear stress to sediment beds. The mathematical expression relating volumetric erosion rate ($e$) in length per unit time (e.g. $cm/s$) and the product of bed shear stress and sediment bulk density is used by Roberts et al. (1998), Lick and McNeil (2001), and Lick et al. (2004):

$$e = A\tau^n \rho_b^m \tag{2.22}$$

where the critical value of bed shear stress is defined as the bed shear stress at which a reasonably small $e$ is observed:

$$\tau_c = \left(\frac{e}{A}\right)^{1/n} \rho_b^{-m/n} \text{ at } e = 10^{-4}(cm/s) \tag{2.23}$$

where $e$ and $\rho_b$ are expressed in $(cm/s)$ and $(g/cm^3)$ respectively; and $A, n, m$ = experimental constants.

Later, Sanford and Maa (2001) developed a mathematical model for either Type I (depth-limited) or Type II (unlimited) erosion to resolve the discrepancy between formulations for the two types of erosion. In order to describe the transient behavior of erosion rate ($E$), they differentiated Equation 2.17 with respect to time, then solved the differential equation for step-wise increasing bed shear stress. Based on the assumptions of locally constant vertical gradient of critical shear stress and a direct proportionality between $M$ in Equation 2.17 and sediment concentration at the water-sediment interface defined by $M = \rho_d \beta$, the formulation is expressed as (Sanford and Maa, 2001; Aberle et al., 2004; Debnath et al., 2007):

$$E = \rho_b \beta (\tau - \tau_{c0}) \exp\left[-\gamma \beta (t - t_0)\right] \tag{2.24}$$

where $\beta$ = local constant; $\gamma = \dfrac{d\tau_c}{dt}$ is the vertical gradient of $\tau_c$; $t_0$ = time at which a new stress level is applied; and $\tau_{c0}$ = the value of $\tau_c$ evaluated at $t = t_0$.

From the probability point of view, Van Prooijen and Winterwerp (2010) presented a stochastic formulation for cohesive sediment erosion by analyzing the process of incipient motion and time dependency using stochastic forcing (applied shear stress) and critical bed shear stress (see Van Prooijen and Winterwerp, 2010 for detailed description). The formulation was then applied to previous flume data sets from Amos et al. (1992a) and Jacobs (2009) to demonstrate the applicability of the formulation using probability concepts. The mathematical relationships developed by previous investigators in the literature are summarized in Table 2.3.

Table 2.3 Mathematical expressions of erosion rate for cohesive sediment beds

| Investigator(s) | Expression | Note |
|---|---|---|
| Ariathurai (1974) | $E = M(\tau - \tau_c)$ | $E$ : erosion rate $(kg/m^2/s)$ <br> $\tau$ : bed shear stress $(N/m^2)$ <br> $\tau_c$ : critical shear stress, value of $\tau$ as <br> $E \approx 0\ (N/m^2)$ <br> $M, n$ : experimental constants |
| Lick (1982) and others | $E = M(\tau - \tau_c)^n$ | |
| Kandiah (1974) | $E = M\left(\dfrac{\tau}{\tau_c} - 1\right)$ | |
| Mehta (1991) | $E = M\left(\dfrac{\tau - \tau_c}{\tau_c}\right)$ | |
| Gularte et al. (1980) and others | $E = \varepsilon_f \exp\left[\alpha(\tau - \tau_c)^\beta\right]$ | $E$ : erosion rate $(kg/m^2/s)$ <br> $\tau$ : bed shear stress $(N/m^2)$ <br> $\tau_c$ : critical shear stress, value of $\tau$ as <br> $E \approx 0\ (N/m^2)$ <br> $\varepsilon_f$ : the flow erosion rate when <br> $\tau - \tau_c = 0$ , no mean flow velocity dependent surface erosion by definition; empirically determined. <br> $\alpha, \beta$ : experimental constants <br> $\beta = 0.5$ reported by Parchure and Mehta (1985) |
| Roberts et al. (1998) | $e = A\tau^n \rho_b{}^m$ <br> Define: <br> $\tau_c = \left(\dfrac{e}{A}\right)^{1/n} \rho_b{}^{-m/n} @\ e = 10^{-4}(cm/s)$ <br> $e = c\tau^n \exp(-k\rho_b)$ | $e$ : volumetric erosion rate $(cm/s)$ <br> $\tau$ : bed shear stress $(N/m^2)$ <br> $\rho_b$ : bulk density $(g/cm^3)$ <br> $A, n, m, c, k$ : experimental constants |
| Briaud et al. (1999) | $e = \left(\dfrac{5.54\tau - 2.77}{\tau + 0.875}\right) + 0.178\tau - 0.0809$ <br> $\tau_{max} = 0.094\rho_w V^2\left(\dfrac{1}{\log \mathrm{Re}} - \dfrac{1}{10}\right)$ <br> $e = e_i @\ \tau = \tau_{max}$ <br> $z_{max} = 0.18\ \mathrm{Re}^{0.635}$ <br> $z = \dfrac{t}{\dfrac{1}{e_i} + \dfrac{t}{z_{max}}}$ | $e$ : scour rate $(mm/hr)$ <br> $\tau$ : bed shear stress $(N/m^2)$ <br> $\rho_w$ : density of water $(kg/m^3)$ <br> $V$ : mean flow velocity <br> $\mathrm{Re} = \dfrac{VD}{\nu}$ ; $D$ : pier diameter, $\nu$ : kinematic viscosity of water <br> $e_i\ (mm/hr)$ : erosion rate at $\tau_{max}$ <br> $z$ : scour depth $(mm)$ after a period of scour developing time, $t\ (hr)$ |

*(Table 2.3 continued)*

| | | |
|---|---|---|
| Krone (1999) | $E = a_0 + a_1 \rho_b$ where $a_i = b_{2i}\tau^2$ <br> $\Rightarrow E = b_{20}\tau^2 + b_{21}\tau^2\rho_b$ | $E$ : mass erosion rate $(kg/m^2/s)$ or $(g/cm^2/s)$ <br> $\tau$ : bed shear stress $(N/m^2)$ or $(dynes/cm^2)$ <br> bulk density $(kg/m^3)$ or $(g/cm^3)$ <br> $b_{2i}$ : experimental constants |
| | $E = K_2(\rho_{max} - \rho_b)\tau^2$, <br> $\rho_b < \rho_{max}$ <br><br> Dimensional considerations: <br> $E = \dfrac{k}{\mu g}\dfrac{(\rho_{max} - \rho_b)}{(\rho_s - \rho_w)}\tau^2$ | $\rho_{max}$ : the maximum bulk density that can be reached before the sediment structure becomes denser; can be defined from the plot of $E$ vs. $\rho_b$ <br> $\rho_s$ : density of particle $(kg/m^3)$ or $(g/cm^3)$ <br> $\rho_w$ : density of water $(kg/m^3)$ or $(g/cm^3)$ <br> $\mu$ : viscosity of water $(N \cdot s/m^2)$ <br> $g$ : acceleration of gravity $(m/s^2)$ <br> $K_2$ : experimental constant <br> $k$ : dimensionless structure constant |
| Sanford and Maa (2001) | $E = \rho_b\beta(\tau - \tau_{c0})\exp[-\gamma\beta(t - t_0)]$ | $E$ : erosion rate $(kg/m^2/s)$ <br> $\rho_b$ : bulk density $(kg/m^3)$ <br> $\tau$ : bed shear stress $(N/m^2)$ <br> $\tau_c$ : critical shear stress $(N/m^2)$ <br> $\gamma = \dfrac{d\tau_c}{dt}$ <br> $t_0$ : time at which a new stress level is applied <br> $\tau_{c0}$ : the value of $\tau_c$ evaluated at $t = t_0$ <br> $\beta$ : local constant |

## 2.6 Rheology Principles

### 2.6.1 Fundamental Concepts

On the basis of classical mechanic principles like Newton's and Hooke's Laws, rheology studies describe the deformation or deformation rate of materials subject to an applied stress. To describe liquid-like behavior, the constitutive law for a Newtonian fluid states that the applied shear stress is proportional to the deformation rate of viscous flow with a constant coefficient, which is called *viscosity*. On the other hand, Hooke's Law of elasticity describes the solid-like behavior by relating the deformation to the applied stress with a proportionality coefficient called *Young's modulus*. In reality, the existence of elastic, plastic, and viscous properties of materials results in complex behavior that cannot be fully described as neither Newtonian nor Hookean behavior. The science of rheology describes "*any* relationship between force and deformation" of materials (Malkin, 1994). From this point of view, Newton's and Hooke's Laws present the behavior of ideal systems describing liquid and solid in rheology, respectively (Malkin, 1994; Czibulya et al., 2010).

Malkin and Isayev (2006) emphasized some special features of rheology to distinguish it from mechanics of a continuum:

- Rheology studies not only the behavior of deformation and flow but the properties of materials which determine this behavior.
- Rheology focuses on the materials for which deformations or rates of deformation are nonlinearly related to the applied forces or stresses.
- The deformation (rate) of such materials is usually caused by structure changes, and can be presented by the superposition of elastic, plastic, and viscous effects.

61

Therefore, the major goals of rheology are: first, to establish the relationship between an applied stress and the geometrical response of the material subject to the stress; and second, to establish the relationships between rheological characteristics and interparticle structure of a material (Malkin, 1994).

To describe the geometrical response of a material under an applied stress, some fundamental terminology is used in rheology studies when illustrating the material's deformation or deformation rate, which generally includes elastic, plastic, viscoelastic, viscoplastic, and viscous behavior. Elastic deformation refers to a temporary change in shape which reverses on release of the applied stress; the mechanical energy used for deformation does not dissipate during loading and removing of the stress. Plastic deformation occurs when the applied stress is sufficient to cause unrecoverable deformation of a material which involves breaking of some molecular or atomic bonds. The stress and energy dissipation during the load application are independent of the deformation rate for an ideal plastic flow. Viscous behavior describes the flow-resisting tendency of fluids due to internal friction. In contrast to the ideal plastic flow, the stress and energy dissipation depend on the deformation rate during viscous flow. Viscoelastic is a time-dependent property of a material which produces both elastic and viscous behavior when subjected to stresses. Hackley and Ferraris (2001) stated that "A viscoelastic material will exhibit viscous flow under constant stress, but a portion of mechanical energy is conserved and recovered after stress is released" (p.2). Viscoplastic behavior, usually associated with concentrated suspensions, describes a material that exhibits plastic deformation under low stress, and acts as viscous flow when the stress

exceeds a critical value, generally referred to as the yield stress (Keedwell, 1984; Hackley and Ferraris, 2001).

The subject of yield stress, regarding its existence and definition, has been studied, discussed, and debated in rheological literature since the last century. Among the various definitions of *yield stress* or *yield point* provided in dictionaries and literature, Barens (1999) stated a general definition of yield stress as "a point of stress at which a "solid" starts to deform continually when the applied stress increases; or a point of stress at which a "liquid" stops continual deformation when the applied stress decreases". In reality, liquids that are considered to have a yield stress are numerous. Many of the examples, including toothpaste, paint, drilling mud, and clay, were proposed by Bingham (1922) as early as the 1920s. Nevertheless, it has been shown that yield stress does not exist as a critical point of stress "below which no flow takes place" from the physical point of view (Barnes, 1999); "everything flows" given the observation time scale is sufficiently long, even to the geological scale (Reiner, 1949; Barnes, 1999). A more appropriate statement describing the concept of yield stress is the point of stress below which no observation of flow under the length and time scales of the experiment (Blair, 1949; Barnes and Walters, 1984). Harnett and Hu (1989) considered yield stress as an "engineering reality" for the sake of application. In other words, with a proper definition of the yield stress under reasonable scales of time and length, this concept has been approved to be correct and useful for applications (Barnes, 1999).

Based on the concept that the mechanical properties of materials change dramatically as the applied stress is below and above the value of yield stress, Bingham (1922) proposed the enduring Bingham plastic model to describe the behavior of non-

Newtonian fluids with a constant *plastic viscosity* under a shear stress exceeding the *Bingham yield stress*. After that, two yield stresses have been identified corresponding to transitions of different geometrical responses by Houwink (1958): the lower yield stress ($\tau_{y1}$) defines the transition from elastic behavior to plastic deformation, and the upper yield stress ($\tau_{y2}$) corresponds to the transition between plastic deformation and viscous flows.

### 2.6.2 Classification of Flow Curves

The behavior of fluids responding to an applied shear stress is described by the science of rheology, and it can be analyzed from the angular deformation rate, referred to as the *strain rate* of fluids under the prescribed shear stress. The graphical expression, illustrating the relationship between applied shear stresses and the responding strain rates of a fluid, is generally designated as the *flow curve*. Several types of the flow curve have been classified based on their characteristic shapes. The main classifications of the flow types are Newtonian, Bingham plastic, shear-thinning (pseudoplastic) without or with yield stress, and shear-thickening (dilatant) without or with yield stress behavior (Figure 2.6). The fluids that deform under an infinitesimal shear stress, and for which the strain rate increases linearly with the increase of applied stress are referred to as Newtonian fluids. In other words, a Newtonian fluid can be characterized by having a linear stress vs. strain rate relationship with an intercept at the origin, and the fluid viscosity is represented as the slope of this straight line (O'Brien and Julien, 1988).
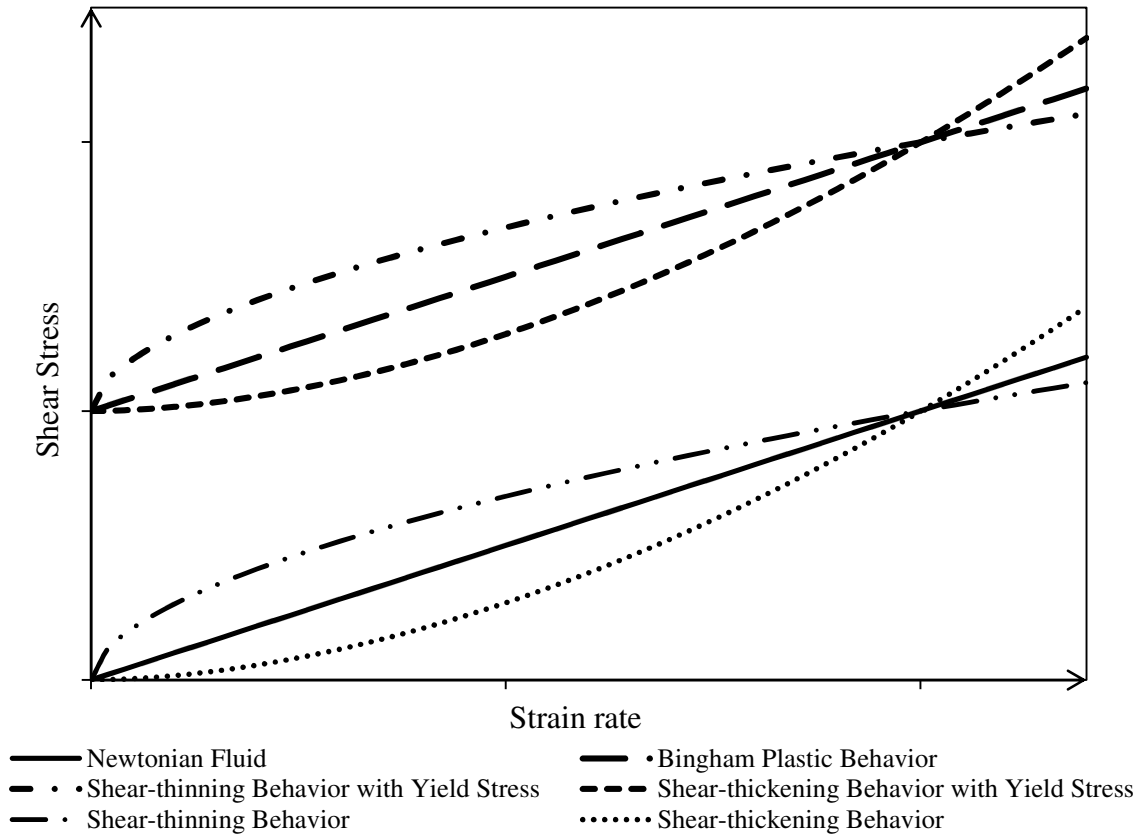
Figure 2.6 Flow curves of Newtonian and non-Newtonian fluids
(adapted from Nguyen and Boger, 1992)

For non-Newtonian fluids, the Bingham plastic equation is one of the classical

models describing fluids that do not flow until a threshold of shear stress is reached. In

other words, the fluids with Bingham plastic behavior can resist shear stress without

macroscopic motion (flowing) until a critical value of shear stress, the yield stress, is

applied. When the applied shear stress is less than the yield stress, such fluids deform

plastically with definite strain recovery upon the removal of the stress instead of flowing.

Once the yield stress is exceeded, the fluids start to flow as viscous materials with finite

viscosity (Nguyen and Boger, 1992). The viscosity of non-Newtonian fluids may remain

constant or vary with the strain rate. Shear-thinning (pseudoplastic) behavior indicates the

fluid viscosity decreases with the increase of strain rate. In contrast, shear-thickening (dilatant) behavior is exhibited in yield dilatant fluids whose viscosity increases with the stain rate (Hackley and Ferraris, 2001; Hobson, 2008).

## 2.7 Mathematical Models of Rheology

In order to describe and characterize the behavior of materials subject to shear stress mathematically, many phenomenological and empirical models (equations) have been proposed in the literature to present particular principal types of the material behavior, such as those mentioned in section 2.6.2. These models describe the behavior of materials by relating the applied stress to the rate of deformation; this relationship is known as the *constitutive equation*. Among the various models reported in the literature, only those associated with gels, pastes, and particle suspensions are introduced in the following sections.

### 2.7.1 Newtonian Model

Under a steady, simple shear, the Newtonian model relates the strain rate of a fluid to the shear stress with a constant proportionality and a zero intercept. The constitutive equation is given as:

$$\tau = \mu \dot{\gamma} \tag{2.25}$$

where $\tau =$ the applied shear stress; $\mu =$ the viscosity of the fluid; and $\dot{\gamma} = \dfrac{du}{dy} =$ the strain rate.

### 2.7.2 Viscoelastic Models

Linear viscoelastic models apply Hooke's Law of elasticity and Newton's Law of viscous flow, and can be represented by combinations of linear springs and linear viscous dashpots. Hooke's Law is expressed as a linear spring element which shows the relationship between shear stress and shear strain:

$$\tau = E_y \gamma \tag{2.26}$$

where $E_y$ = Young's modulus, and $\gamma$ = the shear strain.

On the other hand, Newton's Law is expressed as a linear viscous dashpot which shows the relationship between shear stress and strain rate as in equation 2.25.

Maxwell model is a two-element model which consists of linear spring and viscous dashpot elements connected in series (Figure 2.7a). The constitutive equation of the stress-strain rate relationship of the model is (Maxwell, 1867):

$$\tau + \frac{\mu}{G}\frac{\partial \tau}{\partial t} = \mu \dot{\gamma} \tag{2.27}$$

Equation 2.27 simplifies to a Newtonian fluid under steady state conditions; it results in a Hookean solid for a case of rapidly changing stresses when integrating the dominant time-derivative term of stress. If $\mu$ and $\frac{\mu}{G}$ are replaced by $\eta_0$ and $\lambda_1$, respectively, the Maxwell model can be expressed as (Bird et al., 1987):

$$\tau + \lambda_1 \frac{\partial \tau}{\partial t} = \eta_0 \dot{\gamma} \tag{2.28}$$

where $\eta_0$ = zero-shear-rate viscosity; and $\lambda_1$ = a time constant called relaxation time, which characterizes the responsive time of a viscoelastic material under an instant constant strain application (Hackley and Ferraris, 2001).

If a linear spring and a linear viscous dashpot element are connected in parallel, the Kelvin-Voigt model is presented as in Figure 2.7$b$; the constitutive equation is (Thomson, 1965):

$$\tau = \mu\dot{\gamma} + G\gamma \tag{2.29}$$

To describe the rheological properties of non-Newtonian fluids, more complicated networks consisting of spring and dashpot elements have been proposed. For instance, Jeffreys model is a three-element system that connects another dashpot to the Kelvin-Voigt system in series (Figure 2.7$c$). The constitutive equation of the model contains two time constants (Jeffreys, 1929; Bird et al., 1987):

$$\tau + \lambda_1 \frac{\partial \tau}{\partial t} = \eta_0 \left( \dot{\gamma} + \lambda_2 \frac{\partial \dot{\gamma}}{\partial t} \right) \tag{2.30}$$

where $\lambda_2 = $ a time constant called retardation time, which characterizes the responsive time of a viscoelastic material under an instant constant stress application (Hackley and Ferraris, 2001).

If a Maxwell and a Kelvin-Voigt model are connected in series, it results in the Burgers Model, as shown in Figure 2.7$d$, and the constitutive equation is given as (Burgers, 1935; Picornell and Nazarian, 1992):

$$\tau + \left( \frac{\mu_1}{G_1} + \frac{\mu_1}{G_2} + \frac{\mu_2}{G_2} \right) \frac{\partial \tau}{\partial t} + \frac{\mu_1\mu_2}{G_1 G_2} \frac{\partial^2 \tau}{\partial t^2} = \mu_1\dot{\gamma} + \frac{\mu_1\mu_2}{G_2} \frac{\partial \dot{\gamma}}{\partial t} \tag{2.31}$$

where $\mu_1$, $\mu_2$, $G_1$, and $G_2$ are material constants.
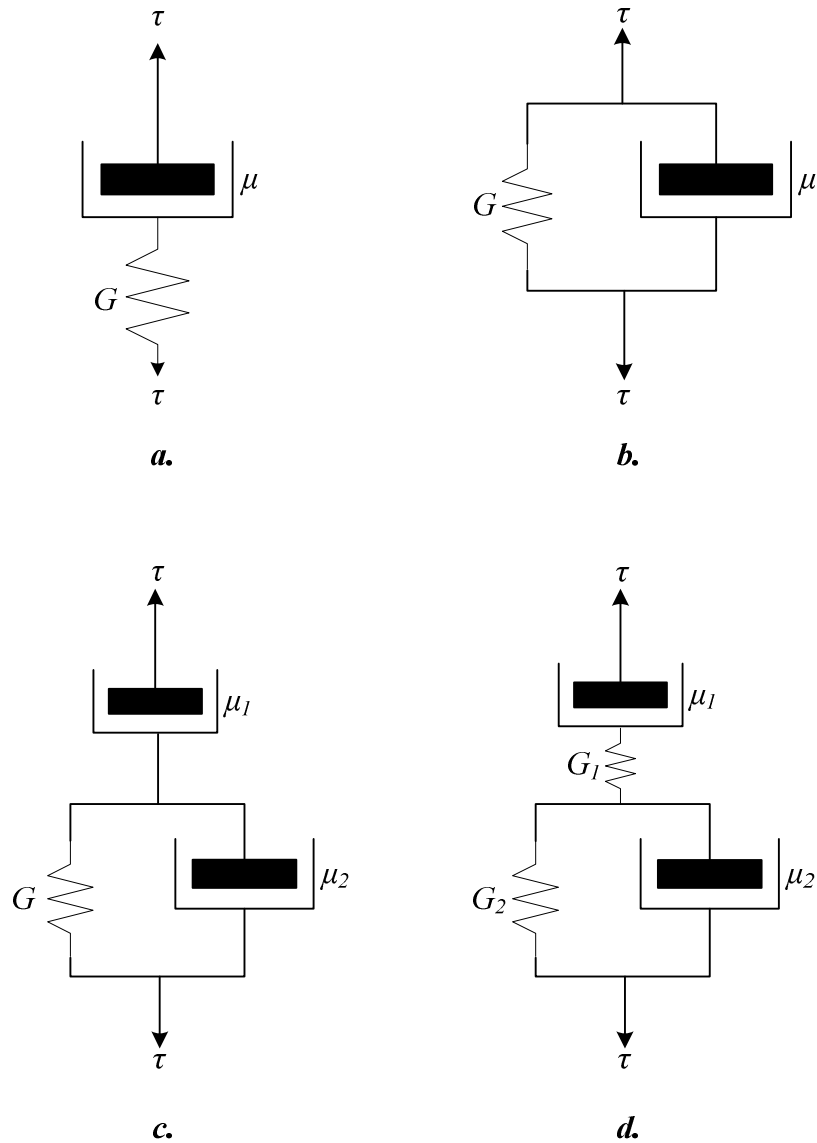
Figure 2.7 Mechanical analogs of simple linear viscoelastic models: (*a*) Maxwell model, (*b*) Kelvin-Voigt model, (*c*) Jeffreys model, and (*d*) Burgers model (adapted from Jain and Mehta, 2009)

### 2.7.3 Generalized Newtonian Models

Generalized Newtonian models result from the modification of the Newtonian constitutive equation given in equation 2.25. The concept of strain-rate-dependency of fluid viscosity is incorporated in the generalized Newtonian constitutive equations to

describe the characteristic of non-Newtonian fluid viscosity depending on the strain rate. However, the generalized Newtonian models do not describe the time-dependent elastic effects as those incorporated in the viscoelastic models (Bird et al., 1987). Two classifications of the frequently stated generalized Newtonian models in the rheology literature —Pseudoplastic and Viscoplastic Models—are reported in the following sections.

**Pseudoplastic Models**

Pseudoplastic models describe the shear-thinning behavior of viscosity, and the viscosity is shown as a function of strain rate. In many cases, limiting values of viscosity corresponding to the upper and lower Newtonian plateaus are included, and with an arbitrary function describing the intermediate zone, such as Cross model, Carreau-Yasuda model, and Meter model. The Cross model was proposed by Cross (1965):

$$\frac{\mu - \mu_\infty}{\mu_0 - \mu_\infty} = \frac{1}{1 + (k\dot{\gamma})^m} \tag{2.32}$$

where $\mu_0, \mu_\infty =$ the asymptotic viscosities at zero and infinite strain rates, respectively; $k =$ a constant with units of time; and $m =$ a dimensionless constant.

With a similar form, the Carreau-Yasuda model differs from the Cross model in the viscosity curve curvature and the power law region (Carreau, 1968; Yasuda, 1979):

$$\frac{\mu - \mu_\infty}{\mu_0 - \mu_\infty} = \left[1 + (k\dot{\gamma})^a\right]^{(n-1)/a} \tag{2.33}$$

where $(n-1) =$ the power law slope; and $a =$ a constant represents the width of the transition region between $\mu_0$ and the power law region. If $a = 2$, the model is known as the Bird-Carreau model (Hammarström, 2004).

70

The shear-thinning behavior of viscosity is expressed in terms of shear stress in the Meter model (Meter, 1964):

$$\frac{\mu - \mu_\infty}{\mu_0 - \mu_\infty} = \frac{1}{1 + (\tau/\tau_m)^{\alpha-1}} \tag{2.34}$$

where $\tau_m$ = the shear stress at which the value of viscosity assumes to $(\mu_0 + \mu_\infty)/2$; and $\alpha$ = a constant which describes the transition from $\mu_0$ to $\mu_\infty$. For fluids with $\mu_\infty \ll \mu_0$, $\tau_m$ can be assumes to $\tau_{1/2}$, i.e. the shear stress at which viscosity equals to $\mu_0/2$. Then the simplified Meter model is equivalent to the Ellis model (Gee and Lyon, 1957):

$$\frac{\mu}{\mu_0} = \frac{1}{1 + (\tau/\tau_{1/2})^{\alpha-1}} \tag{2.35}$$

The Sisko model describes a fluid possesses significant viscosity at a very large shear rate (Sisko, 1958):

$$\mu = k\dot{\gamma}^{n-1} + \mu_\infty \tag{2.36}$$

where $k$ = a consistency coefficient; and $n$ = the flow behavior index determining the power region slope.

In most industrial and engineering applications, the intermediate shear rate region is of most interest, and it is generally described by a two-parameter Power-law (Ostwald-de Waele) model (W. Ostwald, 1923):

$$\mu = \lambda\dot{\gamma}^{n-1} \tag{2.37}$$

where $\lambda$ = a consistency coefficient; and $n$ = the slope of the shear stress versus strain rate relationship on a log-log plot. The Power-law model describes the shear-thinning behavior when $n < 1$, and the shear-thickening behavior when $n > 1$.

**Viscoplastic Models**

Mechanical behavior of fluids that contain suspended particles or consist of more than one phases are usually described by the constitutive equations with a threshold, such as the viscoplastic models. Under the application of an infinitesimal shear stress, Newtonian and pseudoplastic (with no yield stress) fluids deform immediately. However, viscoplastic fluids will not flow or deform until the applied stress exceeds the value of yield stress. The Bingham plastic model describes the behavior of fluids with constant viscosity under a shear stress exceeding the yield stress (Bingham, 1922):

$$\dot{\gamma} = 0 \qquad\qquad , \tau < \tau_y$$
$$\tau = \tau_y + \eta_{pl}\dot{\gamma} \qquad , \tau \geq \tau_y$$
(2.38)

where $\eta_{pl}$ = the plastic viscosity; and $\tau_y$ = the yield stress, usually called the Bingham yield stress, $\tau_B$, in the literature (Barnes, 1999). The ideal Bingham materials behave as elastic solids at low shear stresses, and as Newtonian fluids under shear stresses larger than $\tau_B$ (Hackley and Ferraris, 2006).

Using the same form of Bingham model, the Casson model relates the square roots of shear stress and strain rate proportionally, with a non-zero intercept (Casson, 1959):

$$\dot{\gamma} = 0 \qquad\qquad\qquad , \tau < \tau_y$$
$$\sqrt{\tau} = \sqrt{\tau_y} + \sqrt{\eta_{pl}\dot{\gamma}} \qquad , \tau \geq \tau_y$$
(2.39)

where $\eta_{pl}$ = the plastic viscosity, sometimes called the Casson plastic viscosity in the literature to distinguish it from the Bingham model.

While the Bingham plastic model represents the ideal case of plastic flow in which the particle structure breaks down completely right after the applied shear stress

exceeds the threshold, many of the non-Newtonian fluids in practice do not have a linear stress-strain rate relationship as shown in the Bingham plastic model (Nguyen and Boger, 1992). Therefore, the Herschel-Bulkley model describes this nonlinear stress-strain relationship (Herschel and Bulkley, 1926; Nguyen and Boger, 1992):

$$\begin{aligned}\dot{\gamma} &= 0 & ,\tau < \tau_y \\ \tau &= \tau_y + k(\dot{\gamma})^m & ,\tau \geq \tau_y\end{aligned}$$ (2.40)

where $k$ and $m$ are constants used to approximate the behavior of viscous fluids. The stress-stain rate relation of a fluid approximated by Equation 2.40 is yield pseudoplastic (shear-thinning) if $m < 1$, and is yield dilatant (shear-thickening) if $m > 1$. The Herschel-Bulkley model reverts to the Bingham plastic equation when $m = 1$.

## 2.8 Rheology Measurements

Experimental methods that measure rheological properties of materials are generally referred to *rheometry*. A refined term, *viscometry*, is used for the measurements of viscosity particularly. Therefore, rheological instruments can be classified into two general categories: rheometers and viscometers. While a viscometer is used to measure viscosity principally, a rheometer is used to measure rheological properties under various conditions and settings provided in the device (Hackley and Ferraris, 2001). Depending on the geometries and the applied principles of the devices, rheological instruments for fluids usually belong to either the capillary or rotational types. For the sake of completion, both capillary and rotational methods are reported in sections 2.8.1 and 2.8.2, respectively. However, section 2.8.2 is more extensive and detailed since the rotational methods are considered more appropriate and precise, especially on the measurements of yield stress, which is the major rheological property focused on this research.

**2.8.1 Capillary Methods**

Capillary viscometry is widely used in determining the viscosity of Newtonian and non-Newtonian fluids because of its simplicity of experimental design and procedure, and relative low cost. On the basis of Poiseuille's Law, the application of capillary viscometry is subject to the assumptions: (1) the flow through the system is laminar; (2) circular and radial fluxes in the system can be ignored; (3) the flow is isothermal through the system; and (4) the no-slip condition applies at the wall of the tube (Malkin and Isayev, 2006). The glass capillary viscometers are widely used to measure the viscosity of Newtonian fluids, such as dilute solutions or suspensions. During the experiment, the time taken for a fluid of given volume to flow through a defined length of a glass capillary is measured. Then the flow time of this fluid is related to the viscosity based on Poiseuille's Law. Once the viscometer is calibrated using a standard fluid with known viscosity at a series of temperatures, a temperature correction can be applied to the measured viscosity for the test fluid (Hackley and Ferraris, 2001).

For viscous fluids, including concentrated suspensions and cements, extrusion capillary viscometers are usually used for measuring the viscosity of these non-Newtonian fluids. Basic geometry of extrusion viscometers consists of a cylindrical piston connecting to a reservoir with a contracted capillary tube as the back part. During an experiment, a test fluid in the reservoir is forced through the capillary tube at a constant velocity by the extrusion of the piston. The pressure drops across capillary tubes with different lengths (same diameter) are recorded as a function of flow rate; then the viscosity of the test fluid may be determined as a function of strain rate by relating the flow rate through the capillary tube to the fluid viscosity, i.e. Poiseuille's Law (Collyer,

1993; Hackley and Ferraris, 2001). Due to the experimental design and assumptions, the capability of capillary viscometers is subject to some limitations, which include the transition from laminar to turbulent flow, instability of flow resulting from fluid elasticity, degradation of test fluid, and failure to remain in isothermal condition at high strain rates (Malkin and Isayev, 2006).

## 2.8.2 Rotational Methods

Rotational methods have the advantage of measuring various parameters to characterize different rheological properties, and the capability to incorporate tests of normal stress and oscillatory motion to characterize the viscoelastic properties of materials. In rotational methods, the test fluid is placed in between two surfaces, and sheared continuously when one or both of the surfaces are rotating (Hackley and Ferraris, 2001). Because of its geometry and experimental setting, rotational instruments are capable of creating a homogenous deformation regime under strictly controlled conditions, and of maintaining the assigned flow regime for unlimited time period (Malkin and Isayev, 2006). Most rotational rheometers contain one of the geometries of cone and plate, parallel plate, and concentric cylinder, as shown in Figure 2.8.
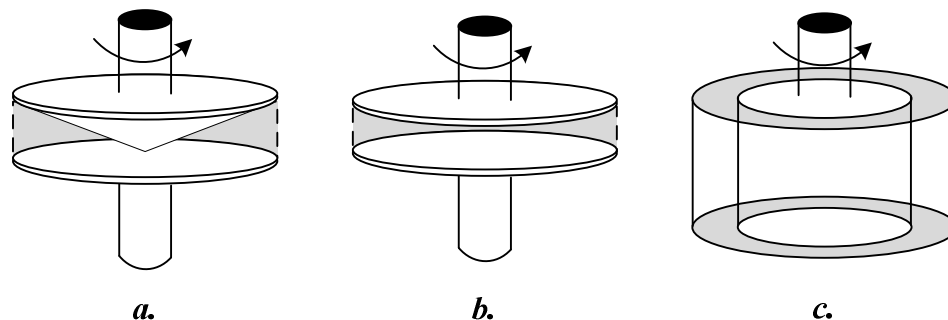


Figure 2.8 General geometries of rotational rheometers: (*a*) cone and plate, (*b*) parallel plate, (*c*) concentric cylinder

The cone and plate rheometer, consisting of an inverted cone with a designed angle smaller than 4° and a lower plate, is usually applied to measure the first normal stress difference and shear viscosity. In a parallel plate rheometer, the specimen is filled between two coaxial, parallel discs separated by a specific distance; during the test, the torque on the upper plate and the total normal force are measured to be related to the normal stress functions and the shear viscosity (Collyer and Clegg, 1988). Cone and plate, and parallel plate geometries are usually chosen in cases of measuring materials that are highly viscous and with high yield stress values (Schramm, 1994). The geometry of the concentric cylinder is also called Couette or coaxial geometry, in which the test specimen is contained in the annulus between two cylinder surfaces. To reduce the end effects, mainly the effects of shear stresses from the specimen on the bottom of the inner cylinder, alternative cylindrical rotor geometries like a hollow cavity or cone bottom, and a double gap concentric cylinder (Figure 2.9*a* to *c*), are used in most commercial instruments (Collyer and Clegg, 1988). For concentrated suspensions with yield values, wall effects which result in an apparent reduction in viscosity are usually significant (Nguyen and Boger, 1992). Modifications of rotor geometries, such as rough wall rotors and the vane geometry (Figure 2.9*d*), have been applied and validated to be useful for wall effect reduction (Liddell and Boger, 1996; Barnes, and Nguyen, 2001).
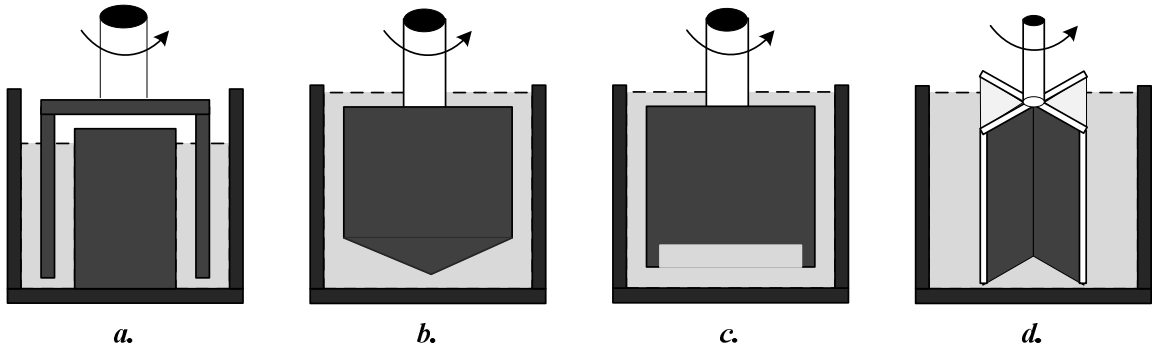
Figure 2.9 Alternative cylindrical rotor geometries for concentric cylinder rheometers:
(*a*) hollow cavity bottom, (*b*) cone bottom, (*c*) double gap concentric cylinder,
(*d*) vane geometry

Rotational rheometers are typically used for flow curve measurements and they are programmed as either strain- or stress- controlled when carrying out the experiments. The required shear stress is measured at each time step for reaching a prescribed specimen strain rate by a strain-controlled rheometer; in contrast, a stress-controlled rheometer applies a controlled magnitude of shear stress at each time step and measures the strain rate of the specimen. With geometries that reduce end and wall effects, such as the concentric cylinder with cone, hollow, and vane configurations, stress-controlled rheometers are particularly suitable to apply in yield stress measurement (Collyer and Clegg, 1988; Nguyen and Boger, 1992; Liddell and Boger, 1996; Barnes, and Nguyen, 2001; Hackley and Ferraris, 2001). Measurements of yield stress are usually obtained from either the direct judgment of fluid yield point or extrapolation of indirect flow curves. The direct measurements of yield stress usually depends on independent assessment of the shear stress threshold at which the fluid starts to flow; the indirect methods usually extrapolate the flow curve to zero stain rate (Nguyen and Boger, 1992).

**2.9 Rheology Studies of Fine Sediments**

While water-sediment mixtures with low sediment concentrations behave like Newtonian fluids, hyperconcentrations of fluid mixtures can resist shear stress without macroscopic motion (flowing) until a yield stress is reached, and are considered to be non-Newtonian fluids. The critical volumetric concentration for a water-sediment mixture to turn from Newtonian fluid behavior to non-Newtonian fluid with viscoplastic behavior has been reported by Fei (1981) to be highly correlated with the proportion of fines. When a bed shear stress is exerted at the sediment surface, the response of sediment to the applied shearing can be indicated by the rheological properties of sediment. Before sediment erosion or entrainment occurs, the sediment deforms reversibly and elastically until its yield stress is exceeded by the applied shear stress and irreversible motion of flow begins, which is the result of the broken interparticle structural network. Therefore, rheological parameters, including the plastic viscosity and yield stress, provide another approach to quantify the interparticle forces and particle associations of fine sediment suspensions (van Olphen, 1977; Ravisangar et al., 2001).

Studies based on experiments using viscometers or rheometers to determine the rheological properties of natural or nearly natural materials have remained as one of the focuses in rheology since the 1980s. Some of these studies relating to debris or mud flows are tabulated in Table 2.4. Some other recent studies focus on investigating the factors that influence rheological properties of soft-soil (Hu, 2005ab; Hu and Zhou, 2011), and developing physical or numerical rheological models of natural or artificial mud for the application of debris flow wave propagation (Major and Pierson, 1992; Jain and

Mehta, 2009; Oveisy et al., 2009; Czibulya et al., 2010; De Blasio et al., 2011; Soltanpour and Samsami, 2011).

Table 2.4 Experimental studies on rheological properties of debris or mud flow

| Author(s) | Materials | Experiments/Instruments |
|---|---|---|
| O'Brien and Julien (1988) | Natural mud flow deposits | Viscometric tests |
| Julien and Lan (1991) | | |
| Otsubo and Muraoka (1988) | Cohesive bed sediments | Rheometer tests |
| Major and Pierson (1992) | Fine-grained materials collected from debris flow deposits | Couette rheometer |
| Coussot and Piau (1995) | Natural coarse suspensions | Couette rheometer |
| Coussot et al. (1998) | Debris flow | Wide-gap Couette rheometer |
| van Kessel (1998) | China clay and Caland channel mud | Rheometers with Couette, double-gap concentric, and cone-plate geometries |
| Ravisangar (2001) | Commercial kaolin deposits | Controlled-stress Couette rheometer with a cone-bottom rotor |
| Bardou et al. (2003) | Debris flow | Couette rheometer and concrete-used rheometer |
| Coussot et al. (2003) | Mud suspensions | Combined MRI-Rheometry |
| Martino (2003) | Natural debris flow deposits | Couette rheometer |
| Schatzmann et al. (2003) | Natural samples (fine and coarse sediments) | Special BMS rheometer |
| Hobson (2008) | Reconstituted natural river bed sediments | Controlled-stress Couette rheometer with a cone-bottom rotor |
| Czibulya et al. (2010) | Reconstituted samples prepared from natural European soils collected in Hungary | Rotational rheometer with parallel plate and vane geometries |
| Soltanpour and Samsami (2011) | Commercial kaolin and natural coastal mud | Rheometer with rotational and oscillatory modes |

Studies by O'Brien and Julien (1988), and Julien and Lan (1991) analyzed the rheological properties of hyperconcentrations (or mud flow) by laboratory experiments. Van Kessel (1998) further compared the differences in these properties between artificial and natural mud. O'Brien and Julien (1988) measured the rheological properties of natural mudflow deposits in Colorado, and stressed the importance of carrying out rheological measurements at low strain rates which are usually the predominant conditions in the field. The resulting flow curves under low strain rates were fitted by the Bingham model, and both the viscosity and yield stress increased with the sediment concentration. The addition of sand to the fluid matrix did not have significant influences on the rheological properties until 20% volumetric concentration of sands was reached. A physically-based quadratic rheological model for hyperconcentrations was proposed by O'Brien and Julien (1985); it was tested and validated by the experimental data in Julien and Lan (1991):

$$\tau = \tau_y + \mu \frac{du}{dy} + \xi \left( \frac{du}{dy} \right)^2 , \quad \tau \geq \tau_y \tag{2.41}$$

where $\xi$ = the turbulent-dispersive parameter and $\frac{du}{dy}$ = the velocity gradient.

By considering the cohesion between particles, viscous friction between fluid and sediments, and impact of particles and the turbulence, the dimensionless form of equation 2.41 was used to describe the rheological behavior of both Newtonian and non-Newtonian fluids (Julien and Lan, 1991). From laboratory work on several natural and artificial muds with stress-controlled and strain-controlled rheometers, van Kessel (1998) measured the flow curves of these muds and compared the differences. It was found that the flow curves of the concentrated cohesive sediments were strongly non-Newtonian and

80

time-dependent, and therefore significantly affected by the sediment stress history at low strain rate ($< 5^{-1} s$).

Otsubo and Muraoka (1988) conducted a series of experiments including hydraulic flume tests, flow curve measurement, and settling tests to determine the relationships between the sediment transport threshold and rheological properties of cohesive bottom sediments. Two thresholds for mud transport were defined in the study as $\tau_{c1}$ and $\tau_{c2}$, representing the critical shear stress value at which mud particles begin to be dislodged and the value at which bed destruction initiates, respectively. From their results, $\tau_{c2}$ was positively correlated with the viscosity; both $\tau_{c1}$ and $\tau_{c2}$ were found as a function of the lower yield stress with a convex power relationship for the natural mud that was studied.

Using a stress-controlled Couette rheometer (HAKKE RS75) with the cone-bottom rotor geometry, Ravisangar (2001) and Hobson (2008) conducted flow curve measurements and determined the yield stress of commercial kaolin and reconstituted river bed sediments, respectively. Ravisangar (2001) found a direct correlation between measured yield stresses and the water content (or bulk density) of artificially-mixed kaolinite sediment beds under different pH conditions; the effects of ionic strength, pore water pH values, and added organic matter on the critical shear stress and yield stress were also investigated in his research. Hobson (2008) related the dimensionless form of both lower and upper yield stresses with the dimensionless particle diameter and the fine sediment contents in the river bed sediments investigated in the study. Although a direct relationship between the critical shear stress and the yield stress was not formulated due to the limitations of particle size and water content for the rheometer test specimens, Hu

(2005a, b) suggested that the proportions of clay and water in the mixture matrix were the main factors affecting the rheological parameters of muddy soft soil; these factors also have been recognized as important factors determining the critical shear stress for sediment erosion as discussed in sections 2.4.2 and 2.4.3.

A series of laboratory tests using soil specimens with controlled water content (from 24% to 30%) and clay content (from 15% to 35% with 5% increment) have been conducted by Hu and Zhou (2011). The experimental results showed that the viscosity of specimens reached a minimum value when the clay content was 25% due to the grading of solid constituents, and the viscosity increased rapidly when the clay content increased from 30% to 35%. The rapid increase in viscosity with clay content was explained as the increasing interparticle reaction and friction which strengthened the sediment flocculation structure as the clay particles were getting closer.  On the other hand, the viscosity and initial shear stress decreased with the specimen water content when it increased from 24% to 30%. These diminishing values of viscosity and initial shear stress were attributed to the increase of interparticle distance which loosened particle structure as more water filled in between the particles (Hu and Zhou, 2011). It is worthy to note that the clay and water content influenced the rheological characteristics of the soil-water mixture similarly to the effects on the erosion threshold as discussed in the section on factors affecting sediment erodibility (section 2.4).

While many of the rheological studies on mud or soft soil applied the viscoplastic constitutive equations, such as Bingham and Herschel-Bulkley models, Huynh et al.'s (1990) study using an oscillatory motion experiment reported that the mud studied in their research exhibited viscoelastic behavior at low shear rate, and Bingham fluid

82

behavior at high shear rate. Shibayama et al. (1989) introduced a *visco-elastic-plastic* model, which combined the viscoelastic and viscoplastic models. The behavior of the test mud is viscoelastic when the applied shear stress is less than the yield stress; the behavior is viscoplastic once the shear stress exceeds the yield stress. In other words, the visco-elastic-plastic model may be seen as a viscoplastic model with a viscoelastic state replacing the original elastic part (Oveisy et al., 2009). Both experimental and numerical studies have suggested that the rheological behavior of artificial and natural mud can be better characterized by this visco-elastic-plastic model, especially for the simulation of wave propagation and attenuation, and mud mass transport (Jiang and Watanabe, 1995; Oveisy et al., 2009; Soltanpour and Samsami, 2011).

# CHAPTER III

# EXPERIMENTAL MATERIALS AND PROCEDURES

## 3.1 Specimen Preparation

In this study, Georgia kaolin and ground silica manufactured by industry were used as the sediment material of soil mixture specimens, representing clay- and silt-size particles, respectively. The Georgia kaolin, obtained from Dry Branch Kaolin Company, Dry Branch, Georgia, is graded as Hydrite Flat D in the industry, and the grain size distribution is controlled by a centrifugal fractionation technique. The industrial ground silica (SIL-COSIL 106) from Ottawa, Illinois, was purchased from US Silica Company. Typical physical properties of the sediments are illustrated in Table 3.1 and Table 3.2.

Table 3.1 Typical physical properties of Georgia kaolin

| Property | Value |
|---|---|
| Median particle size ($d_{50}$) from the hydrometer test | $2.6\,\mu m$  (by weight) |
| Median particle size ($d_{50}$) by a Brinkman particle size analyzer [a] | $0.95\,\mu m$  (by number count) |
| Mean particle size by a Brinkman particle size analyzer [a] | $1.5\,\mu m$  (by number count) |
| pH of 20% aqueous slurry | 4.2 ~ 5.2 |
| BET ($N_2$ adsorption) specific surface | $10.5 \sim 10.9\,m^2/g$ |
| Methylene blue adsorption [b] specific surface | $10.5 \sim 11.2\,m^2/g$ |
| Specific gravity | 2.58 |

[a] Value reported in Ravisangar et al. (2005)
[b] Conducted by following the procedure suggested in Santamarina et al. (2002)

Table 3.2 Typical physical properties of ground silica (SIL-COSIL 106)

| Property | Value |
|---|---|
| Median particle size ($d_{50}$) | $32\mu m$ (by weight) |
| Hardness (Mohs) | 7 |
| Mineral | Quartz |
| pH | 7 |
| Specific gravity | 2.65 |

In order to investigate the effects of clay particles on the erosion behavior and rheological characteristics of fine-grained sediments, soil mixtures were prepared from the mixed sediments consisting of different proportions of ground silica and Georgia kaolin by dry weight. Simple sedimentation tests of sediment suspensions (Figure 3.1) were conducted for the mixtures. In each settling test, mixtures consisting of different kaolin proportions were allowed to settle naturally. The initial sediment concentration, the settling period, and the increment of kaolin content percentage for the mixtures were measured. After several trials of mixing different amounts of tap water with the air-dry sediments, the ratio of 160 ml water to 100 g sediments was selected for the mixtures which resulted in an initial sediment concentration in the suspension of 625 g/L. The suspension was then poured into a sedimentation cylinder in order to settle naturally for slightly more than 48 hours.

During the settling period, two types of sedimentation behavior were observed and recorded. Sedimentation behavior of soil slurries can be described as dispersed or flocculated depending on the clarity of the interface between sediment and water during settling (Ravisangar et al., 2005; Hobson, 2008). As shown in Figure 3.1, the sediment-water interface was dispersed and muddy for the 0%-kaolin soil mixture (pure silt); the other slurries with additions of kaolin content, ranging from 10% to 60% by weight,

showed a flocculated and clear interface between water and sediment. The dispersed suspension in the pure silt mixture may have resulted from the fraction of silt particles smaller than 2 μm (Figure 4.2). On the other hand, the sedimentation in 10% to 60% kaolin mixtures could also be caused by a physical mechanism, such as settling of large kaolinite particles along with some small silt/kaolinite particles attached at the edge, rather than an electrical mechanism (flocculation) between silt and kaolinite particles.
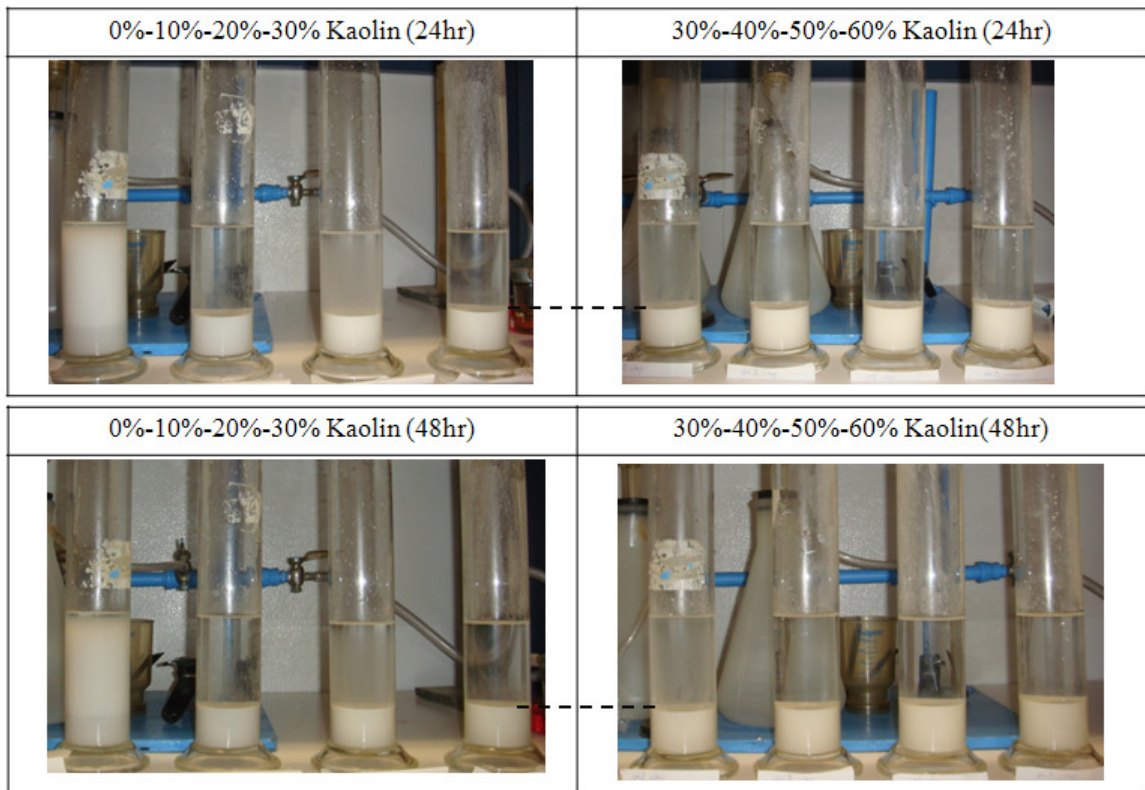


Figure 3.1 Sedimentation tests in glass cylindrical of soil mixture with different kaolin contents (after 24-hr and 48-hr sedimentation periods)

In addition, heights of each settled sediment specimen were measured and recorded. No difference was found between the sedimentation heights after a 24 hour-

and a 48 hour-settling period; therefore, a 24-hour settling period was determined to be adequate for specimen preparation. At the end of the sedimentation test, the excess water was poured out and water content of the surface layer was measured to estimate the maximum amount of water contained in the sediment matrix for each type of soil mixture (Figure 3.2).
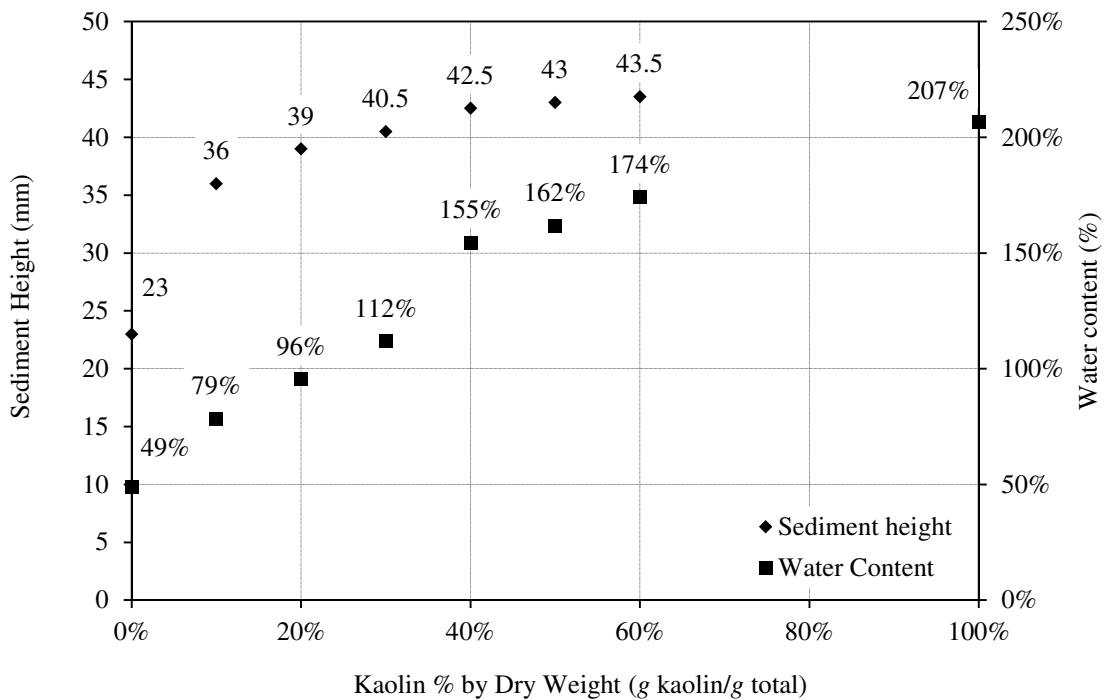


Figure 3.2 Sedimentation heights and surface layer water contents after 48-hr settling periods for soil mixtures consisting of different kaolin proportions

The increment of kaolin content percentage was determined from a few preliminary flume erosion tests. Because the erosion behavior of the specimens did not show significant variations between soil mixtures having 10% kaolin content difference when the kaolin content exceeded 20%, it was decided to use a 20% kaolin content

increment for successive specimens containing more than 20% kaolin (Table 3.3). After the water-soil ratio and the settling period had been determined, the soil mixture was prepared by mixing 450 g of air-dry sediments with 720 ml of tap water using an electronic blender for each specimen. The sediment suspension was then poured into the coring container, which is a cut-off section of a Shelby tube with a calibrated inner diameter of 72.50 mm and a height of 294 mm. The Shelby tube was inserted into the bottom of the flume so that the sediment sample could be extruded into the flume flow by an alloy piston which served as the bottom of the tube. The suspension was allowed to settle naturally for 24 hours. After that, the excess water for each specimen was suctioned out with as little disturbance as possible before running flume experiments or rheometer tests.

Table 3.3 Proportions of ground silica and Georgia kaolin of soil mixture specimens

| ID | Ground silica | | Georgia kaolin | | Total weight (g) |
|---|---|---|---|---|---|
| | Dry weight (g) | Proportion (%) | Dry weight (g) | Proportion (%) | |
| 10%K | 405 | 90 | 45 | 10 | 450 |
| 20%K | 360 | 80 | 90 | 20 | 450 |
| 40%K | 270 | 60 | 180 | 40 | 450 |
| 60%K | 180 | 40 | 270 | 60 | 450 |
| 100%K | 0 | 0 | 450 | 100 | 450 |

**3.2 Soil Characteristics Testing**

To characterize the typical physical properties of soil mixture specimens, conventional geotechnical tests including water (moisture) content, dry and bulk densities, Atterberg limits, grain size distribution, specific gravity, and specific surface area were

carried out for each type of soil mixture consisting of different kaolin proportions. In addition, temperature, pH value, and conductivity of tap water and soil slurry of each specimen were measured and recorded.

### 3.2.1 Water Content, Bulk and Dry Densities

The water content in each specimen was determined by following the procedure suggested in ASTM D 2216-05, which defines the water content as the ratio of pore water mass to the solid mass (equation 2.12). Specifically, weights of specimens before and after oven-drying were measured using an electronic balance and then substituted into equation 2.12 for calculating the water contents. The dry density and the bulk density are defined as the mass of dry or wet soil per unit total volume ($V_t$), respectively, as shown in equations 3.1 and 3.2:

$$\rho_d = \frac{m_s}{V_t} \tag{3.1}$$

$$\rho_b = \frac{m_{wet}}{V_t} \tag{3.2}$$

In this study, the dry and bulk densities were estimated from the measured water content ($w$ in equation 2.12) by assuming all the specimens were 100% saturated as discussed in section 2.4.3. In other words, the total volume was calculated as the summation of volumes of dry sediment and pore water only, which assumes that the pore spaces between particles were filled with water and negligible air. Derivations of dry and bulk densities as functions of measured water content are shown as follows:

$$V_t(w) = V_w + V_s = \frac{m_w}{\rho_w} + \frac{m_s}{\rho_s} = \frac{w \times m_s}{\rho_w} + \left[ \frac{m_s \times (1 - Kaolin)}{\rho_{silt}} + \frac{m_s \times Kaolin}{\rho_{kaolin}} \right] \tag{3.3}$$

$$\rho_d(w) = \frac{m_s}{V_t(w)} = \frac{m_s}{\dfrac{w \times m_s}{\rho_w} + \left[\dfrac{m_s \times (1-Kaolin)}{\rho_{silt}} + \dfrac{m_s \times Kaolin}{\rho_{kaolin}}\right]} \qquad (3.4)$$

$$\rho_b(w) = \frac{m_{wet}}{V_t(w)} = \frac{m_{wet}}{\dfrac{w \times m_s}{\rho_w} + \left[\dfrac{m_s \times (1-Kaolin)}{\rho_{silt}} + \dfrac{m_s \times Kaolin}{\rho_{kaolin}}\right]} \qquad (3.5)$$

where $V_w$ = volume of water; $V_s$ = volume of solids (dry sediments); $Kaolin$ = kaolin content by dry weight in decimal fraction; $\rho_{silt}$ = dry density of silt, taken as $2.65\, g/cm^3$ (Table 3.2); $\rho_{kaolin}$ = dry density of Georgia kaolin, taken as $2.58\, g/cm^3$ (Table 3.1).

## 3.2.2 Grain Size Distribution and Atterberg Limits

Grain size distributions of the ground silica, Georgia kaolin, and silt-clay mixtures were determined by sieve analysis and hydrometer tests. The tests were carried out in accordance with ASTM C136-01 and ASTM D1140-00 for dry and wet sieve analyses, respectively. Sieves with mesh openings of 53µm (No.270), 63µm (No.230), 75µm (No.200), 106µm (No.140), 150µm (No.100), and 212µm (No.70) were used in the sieve analysis (ASTM C136-01) of ground silica. On the other hand, wet-sieve analyses (ASTM D1140-00) were applied to the Georgia kaolin and the mixtures, using sieves No.200, 230, and 270. Guidelines detailed in ASTM D 422-63-02 were followed for hydrometer tests. In these tests, either hydrometer 151H or 152H was used. After the curve of grain size distribution was constructed though sieve and hydrometer analyses, the median particle size ($d_{50}$) was determined by estimating the value of diameter at which 50% of the particles by weight is smaller. For example, the grain size distributions of ground silica and Georgia kaolin used in specimen preparation are shown in Figure 3.3.
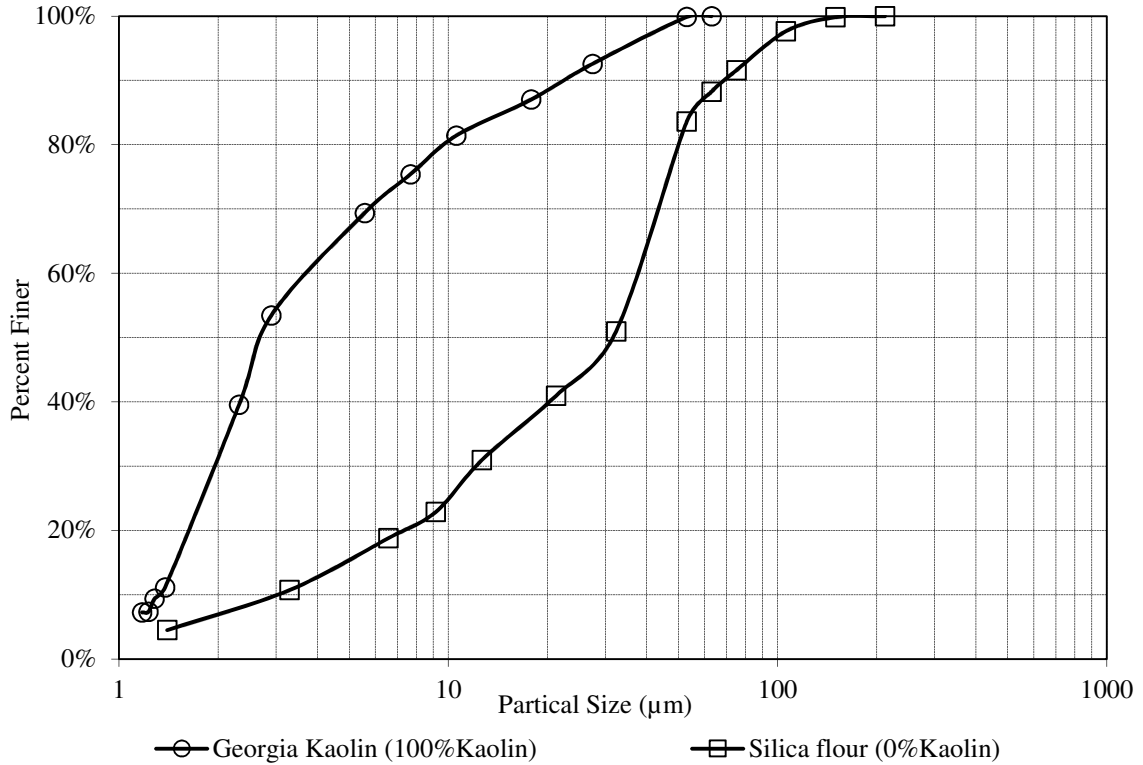
Figure 3.3 Grain size distributions of ground silica and Georgia kaolin

Atterberg limits identify four states of behavior associated with various levels of soil water content. The limits can be defined as liquid limit (lower limit of viscous flow), plastic limit (lower limit of the plastic state), and shrinkage limit (lower limit of volume change) (Holtz and Kovacs, 1981). Determination of the Atterberg limits is important in soil mechanics because it indicates the interaction between solid and liquid phases in soils, and provides the possibility to classify soils in groups with similar mechanical properties. Plasticity index ($I_p$) shows the range of water content over which a soil behaves plastically and is defined as (ASTM D4318-05):

$$I_p = w_{LL} - w_{PL} \tag{3.6}$$

91

where $w_{LL}$ = liquid limit (%); $w_{PL}$ = plastic limit (%). Soil classification related to plasticity index describes the soil as non-plastic for $I_p = 0$, low plastic for $I_p < 7$, medium plastic for $7 \le I_p \le 17$, and highly plastic for $I_p > 17$ (Ranjan and Rao, 2000). In this study, liquid limit and plastic limit of the soil mixtures with different clay contents were investigated and determined by following the experimental guidelines specified in ASTM D4318-05. Specifically, the liquid limit determined from the Casagrande cup test is defined as the water content (%) of soil at 25 blows of the cup from the best-fit line (Figure 3.4).
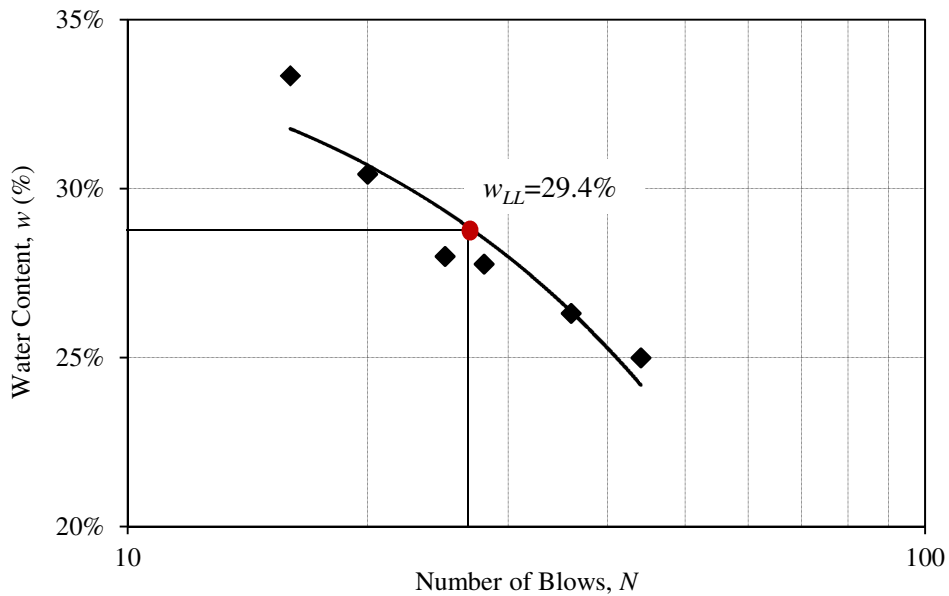


Figure 3.4 Liquid limit test data using Casagrande cup apparatus

### 3.2.3 Specific Gravity and Specific Surface

The specific gravity of ground silica and Georgia kaolin was determined using a water pycnometer with the experimental procedure specified in ASTM D854-06. Specifically, Method B—procedure for oven-dried specimens—was applied to perform

the test. The specific gravity is defined as the ratio between the densities of solids and

water, and can be calculated using:

$$G_s = \frac{\rho_s}{\rho_w} = \frac{m_s}{m_{pw} - (m_{pws} - m_s)} \qquad (3.7)$$

where $m_s$ = mass of the oven-dried solids; $m_{pw}$ = mass of the pycnometer and water; and

$m_{pws}$ = mass of the pycnometer, water, and soil solids.

The specific surface (SSA) of a particle is defined as the ratio between the surface

area and mass of a particle (Santamarina et al., 2002). The importance of interparticle

forces increases as SSA increases; thus, the amount of surface per unit soil mass

determines the balance between surface-related and gravimetric forces, and affects

interparticle structure, especially for fine-grained sediments such as clay particles

(Santamarina, 2001; Santamarina et al., 2002). The most common method of determining

the SSA of a given material involves determining how much of a chemical with a known

molecular cross section is required for completing monolayer coverage on the material's

surface (Avena et. al., 2001). The specific surface of Georgia kaolin used in this study

was determined using two different methods, which are the nitrogen gas ($N_2$) adsorption

using BET method (Brunauer et al., 1983) and the methylene blue (MB) adsorption

method. The BET method was carried out by the *Micromeritics ASAP 2020 Surface Area*

*and Porosity Analyzer* (Figure 3.5) located in the Geoenvironmental Engineering

Laboratory at Georgia Tech. The MB adsorption method was carried out in the same

laboratory following the experimental procedures outlined in Santamarina et al. (2002),

and the value of SSA was calculated using:

$$SSA = \frac{1}{MW} \frac{1}{V_{sol}} (0.5N_{drop}) A_{av} A_{MB} \frac{1}{M_s} \qquad (3.8)$$

where $MW = 373.87$ g/mol , molecular weight of MB ($C_{16}H_{18}ClN_3S\cdot3H_2O$); where

$V_{sol} = 200ml$ , volume of MB solution; $N_{drop}$ = number of 0.5$ml$ drops added;

$A_{av} = 6.022\times10^{23}$ particles/mol, Avogadro's number ; $A_{MB} = 1.30nm^2$ , area covered by

one MB molecule; $M_s$ = mass of soil in suspension in grams.
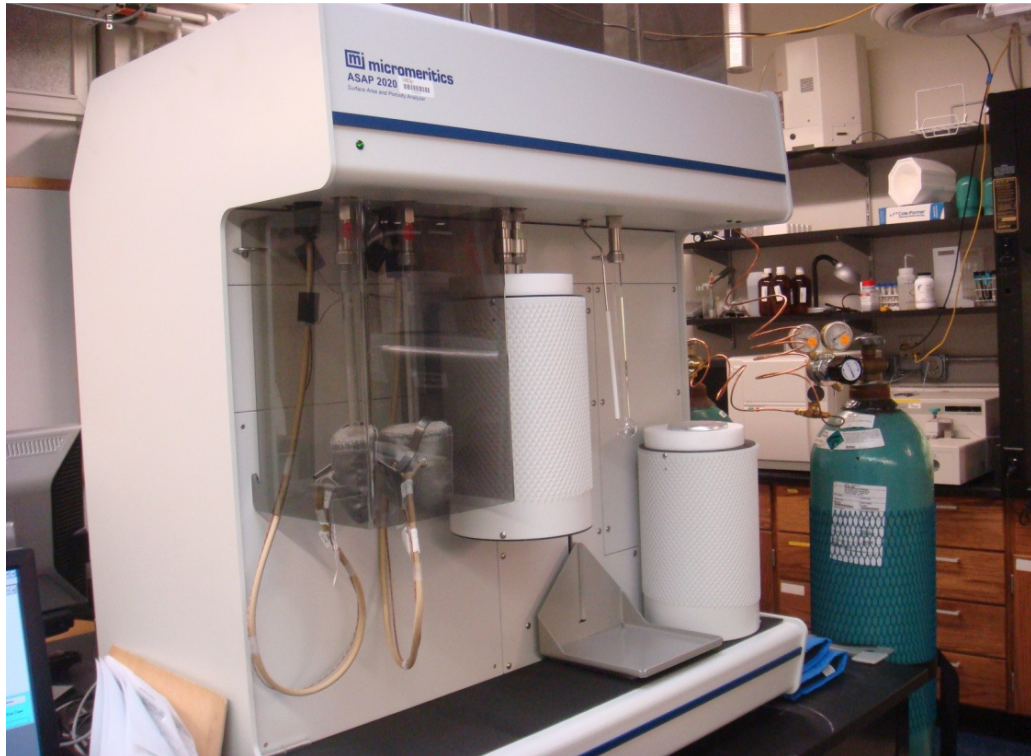


Figure 3.5 Micromeritics ASAP 2020 Surface Area and Porosity Analyzer

### 3.2.4 Temperature, pH value, and Conductivity

The temperature, pH value, and conductivity of the tap water and soil mixture specimens were measured by the *Oakton waterproof PC 300 hand-held Meter* (Figure 3.6), which compensates the temperature effects automatically when the conductivity

electrode with a built-in temperature sensor supplied with the meter is plugged in. While the temperature calibration had been done by the manufacturer, calibrations of pH and conductivity were performed using standard calibration buffers before taking measurements.



Figure 3.6 Oakton waterproof PC 300 hand-held pH/Conductivity/TDS/Temperature Meter

## 3.3 Hydraulic Flume Experiment

### 3.3.1 Experimental Setup

The flume experiments were conducted using a recirculating, rectangular, tilting flume located in the Hydraulics laboratory in the School of Civil and Environmental

Engineering at the Georgia Institute of Technology. The flume dimensions are 6.1 m in length, 0.38 m in width, and 0.38 m in depth. The fixed gravel bed of the flume with $d_{50} = 3.3mm$ ensures a fully-rough ($u_* k_s / v > 70$, $k_s \cong 5/3 d_{50}$) turbulent flow condition around the specimen during the flume erosion test (Hobson, 2008). At the bottom of the flume, a hole with the diameter of the Shelby tube was cut for inserting the soil specimen. The flow to the flume is provided from a 1.9 m$^3$ storage tank using a variable-speed slurry pump that can pass large solids. A comprehensive view of the system layout and a photo of the flume apparatus are shown in Figure 3.7.
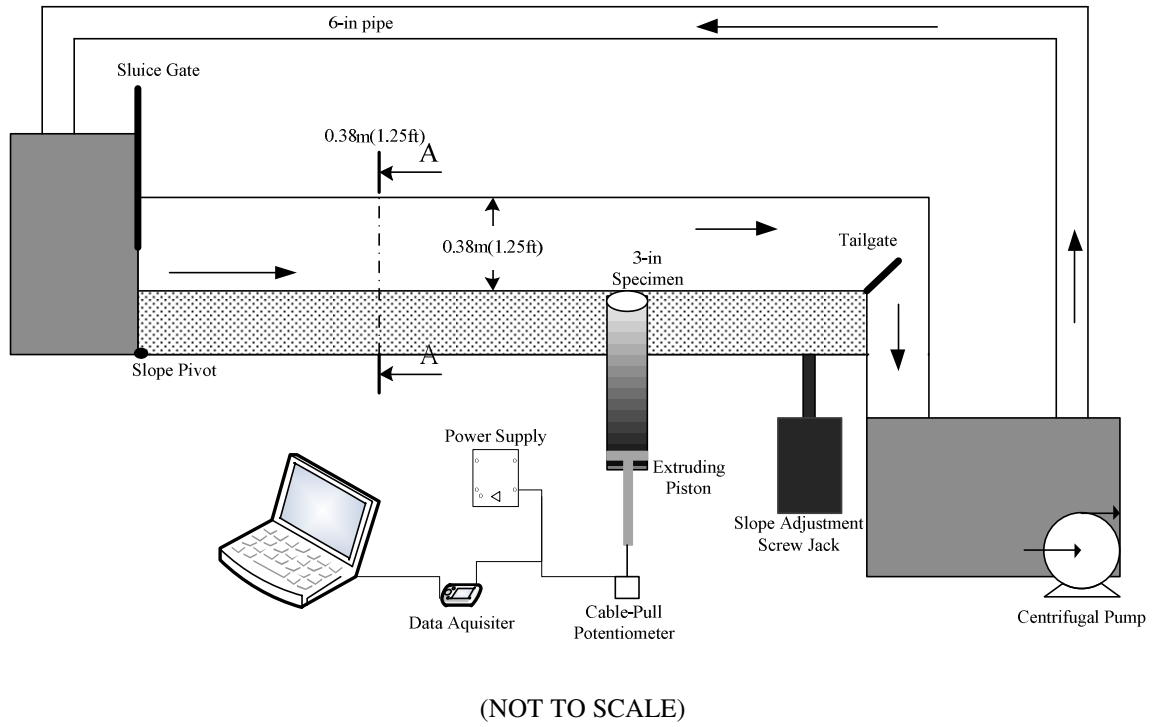
Figure 3.7 Flume apparatus for the erosion test: system layout (upper) and photo (lower)

A desired bed shear stress ($\tau$) for the flume erosion test is produced by operator-controlled flow rate, flow depth, and channel bed slope. To control the flow condition and the channel slope, an impeller pump along with a bend meter, and a slope counter were calibrated by previous researchers (Hoepner, 2001; Ravisangar et al., 2001). Calibration relationships of the flow rate versus the manometer deflection of the bend meter, and the slope counter versus the measured slope from Hoepner (2001) and Ravisangar et al. (2001)'s results are shown in Figure 3.8 and Figure 3.9, respectively.
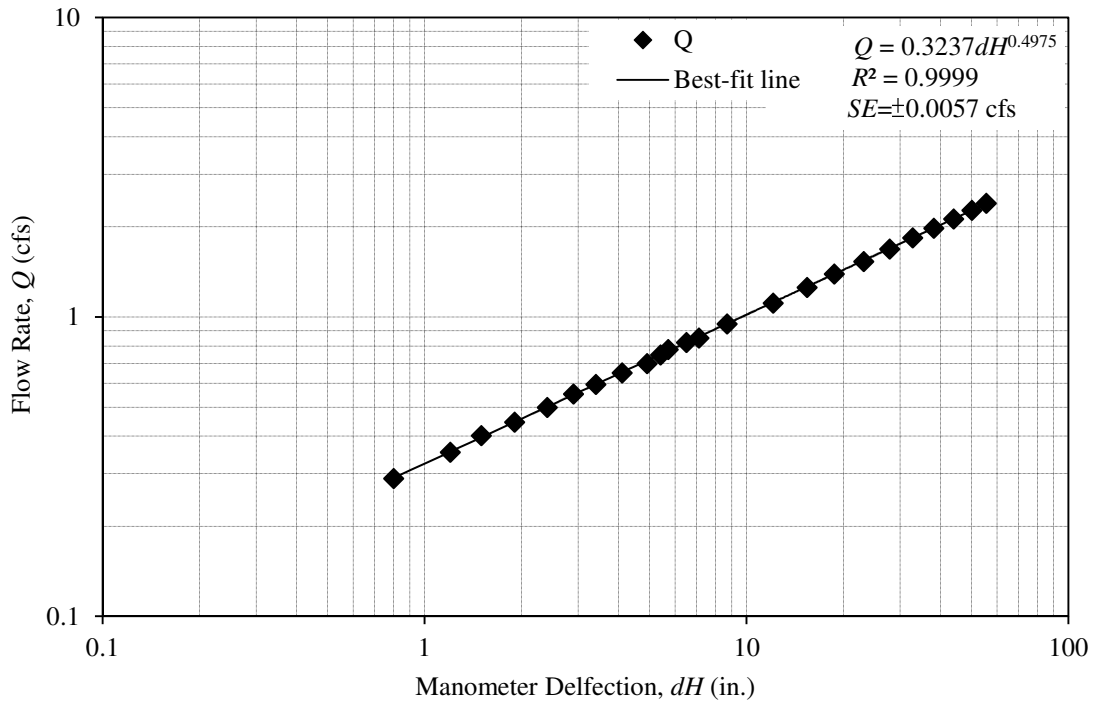


Figure 3.8 Pump and bend meter calibration
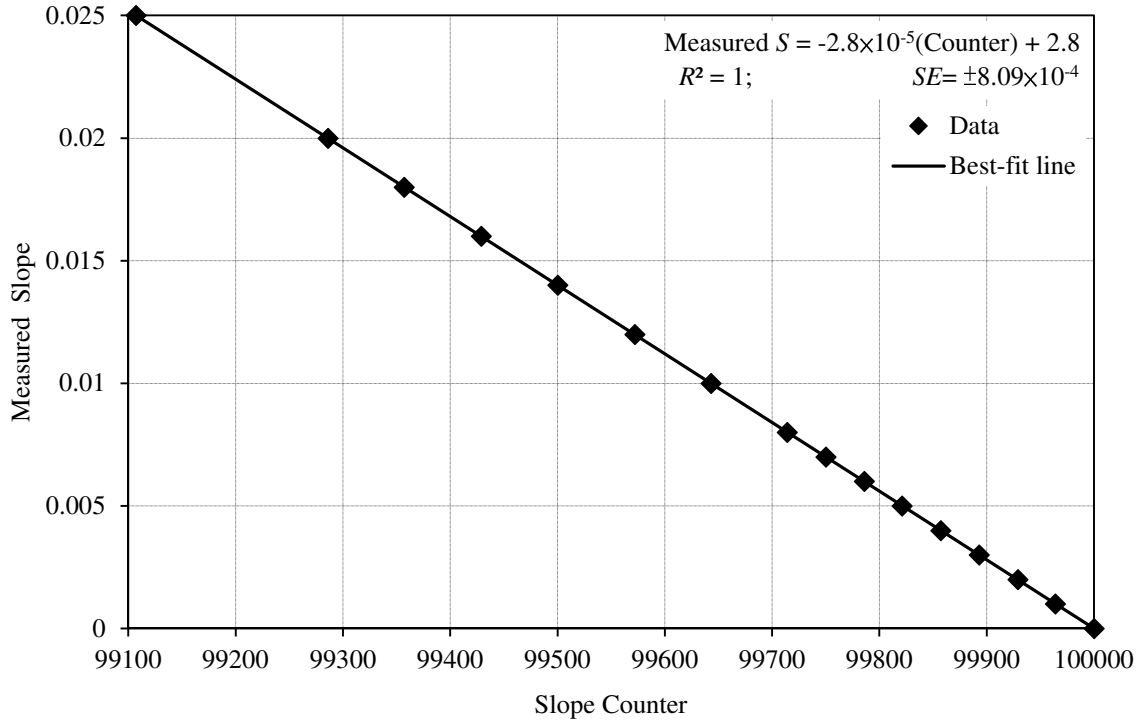
Figure 3.9 Flume slope counter calibration

The depth of flow is controlled by the tailgate at the outlet of the channel for subcritical flows which were used in this study. For each combination of flow rate and channel slope, the normal depth is determined from the asymptotic depth approached for measured M1 and M2 water surface profiles of gradually-varied flows (Sturm, 2001). The use of normal depth guarantees a uniform flow condition and allows the bed shear stress to be determined from the uniform flow equation in a wide open channel (Sturm, 2001):

$$\tau = \gamma_w y S_0 \tag{3.9}$$

where $y$ = flow depth; $S_0$ = bed slope of the channel. The confirmation of using Equation 3.9 for the applied flow conditions in this study was carried out by calculating the bed shear stress from the slope of the centerline velocity profiles, which were measured with

a laser Doppler velocitymeter (LDV), and fitted with a logarithmic distribution by Ravisangar et al. (2001).

To validate the usage of equation 3.9 for calculating the bed shear stress, the following steps were taken in some initial experiments by Ravisangar (2001) and Hobson (2008). First, the measured flow rate ($Q_0$) was obtained from the bend meter and validated by integrating the velocity profiles measured by a LDV over the depth and width at a uniform flow section, and the water depth ($y$) was obtained from the asymptotic normal depth, for a given bed slope ($S_0$). Second, the bed shear stress ($\tau$) was calculated by equation 3.9, and the mean flow velocity ($V$), hydraulic radius ($R$), Reynolds number ($\mathrm{Re}$), and friction factor ($f$) were calculated as follows:

$$V = \frac{Q_0}{by} \tag{3.10}$$

$$R = \frac{by}{b + 2y} \tag{3.11}$$

$$\mathrm{Re} = \frac{4RV}{\nu} \tag{3.12}$$

$$f = \frac{8gRS_0}{V^2} \tag{3.13}$$

where $\nu$=kinetic viscosity of water; $b =$ the width of the flume.

To account for the different roughness values of the smooth (acrylic) sidewalls and the rough (gravel) bed, a sidewall correction procedure prescribed by Julien (1995) was applied to determine the roughness factors corresponding to walls and the bed at different Reynolds numbers, including wall friction factor ($f_w$), bed friction factor ($f_b$),

bed hydraulic radius ($R_b$), and bed Manning's roughness coefficient ($n_b$). The wall and bed friction factors are calculated as:

$$f_w = 0.0015\left[\log\left(\frac{\mathrm{Re}}{f}\right)\right]^2 - 0.0428\log\left(\frac{\mathrm{Re}}{f}\right) + 0.1884 \tag{3.14}$$

$$f_b = f + \frac{2y}{b}(f - f_w) \tag{3.15}$$

Then the bed hydraulic radius is given as the hydraulic radius corrected with the bed friction factor from equation 3.16:

$$R_b = \frac{f_b}{f}R \tag{3.16}$$

After that, the Manning's roughness coefficient for the bed can be found by the relationship between Manning's $n$ and the friction factor ($f$):

$$n_b = \frac{K_n}{\sqrt{8g}}R_b^{1/6}f_b^{1/2} \tag{3.17}$$

where $K_n = 1.0$ for SI unit system and $K_n = 1.49$ for English unit system.

The equivalent sand grain roughness height ($k_s$) was adjusted by trial and error to select the value for obtaining the best-fit curve of Keulegan's equation:

$$\frac{n_b}{k_s^{1/6}} = \frac{\dfrac{K_n}{8g^{1/2}}\left(\dfrac{R_b}{k_s}\right)^{1/6}}{2.0\log\left(12.2\dfrac{R_b}{k_s}\right)} \tag{3.18}$$

The resulting value of $k_s$ is selected as $5.52mm \pm 0.025mm$, approximately $(5/3)d_{50}$ of the fixed-bed gravel, by Ravisangar (2001) to produce the best fit of Equation 3.18 (Figure 3.10).
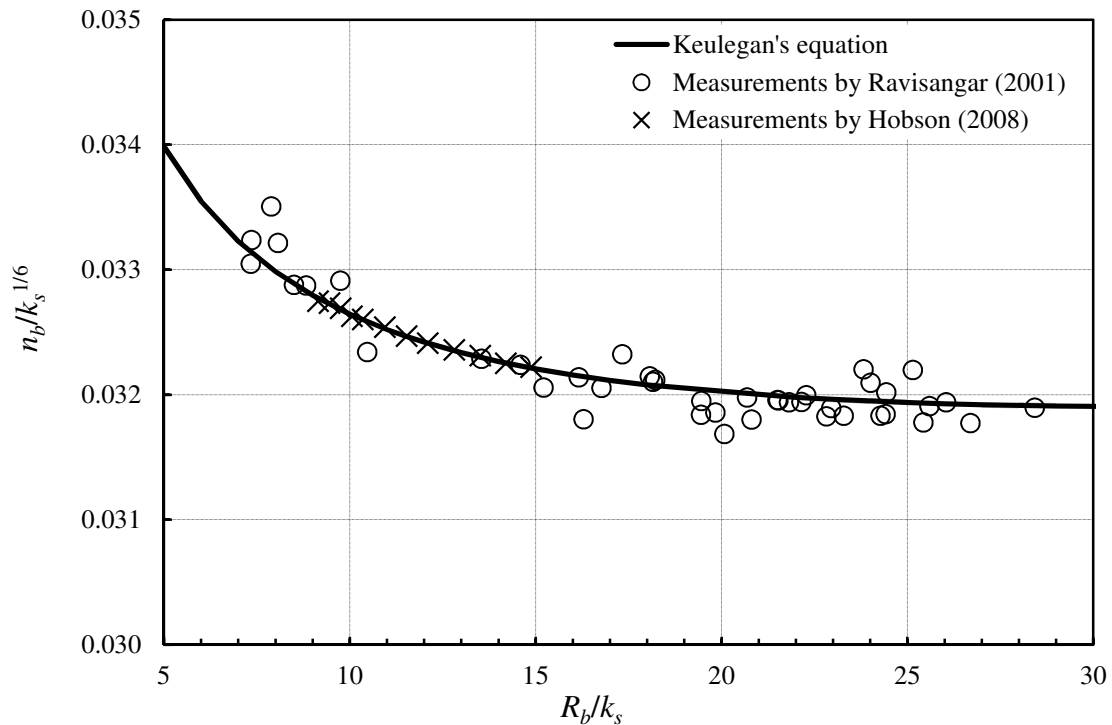
Figure 3.10 Measured (symbols) and calculated (solid curve) bed roughness at various shear stress conditions

Finally, the flow rate ($Q$) calculated from Manning's equation using $R_b$ and $n_b$ from Equations 3.16 and 3.17, respectively, was used in an iteration procedure to verify that it was equal to the measured $Q_0$. This iteration procedure was used to determine the normal depth at a given bed slope for a designated bed shear stress by assuming an initial value of flow rate $Q_0$. Then values of $R_b$ and $n_b$ can be obtained through Equations 3.10 to 3.17, which resulted in the calculated $Q$ from Manning's equation using $R_b$ and $n_b$. By iterating on $Q_0$ until $Q_0 = Q$, the normal depth at the designed bed shear stress can be obtained. Past flume experiments corroborated the normal depth predictions for the hydrodynamic conditions of bed shear stress up to 21 Pa (Ravisangar, 2001; Navarro,

2004; Hobson, 2008). The hydrodynamic conditions used in this study including flow rate, channel bed slope, flow depth, mean water velocity, bed shear stress, Froude number, and Reynolds number are shown in Table 3.4.

Table 3.4 Hydrodynamic conditions for the flume erosion tests in the study

| Flow rate (cms) | Slope ($\times 10^{-3}$) | Water depth, $y$ (cm) | Average velocity, $V$ (m/s) | Bed shear stress (Pa) | $Fr = \dfrac{V}{\sqrt{gy}}$ | $Re = \dfrac{4RV}{v}$ | $\dfrac{u_* k_s}{v}$ |
|---|---|---|---|---|---|---|---|
| 0.0227 | 1.99 | 10.95 | 0.543 | 2.15 | 0.523 | $3.51 \times 10^5$ | $2.55 \times 10^2$ |
| 0.0283 | 1.99 | 12.65 | 0.588 | 2.48 | 0.528 | $3.89 \times 10^5$ | $2.74 \times 10^2$ |
| 0.0227 | 3.00 | 9.60 | 0.619 | 2.83 | 0.638 | $3.93 \times 10^5$ | $2.93 \times 10^2$ |
| 0.0283 | 3.00 | 11.00 | 0.677 | 3.24 | 0.651 | $4.39 \times 10^5$ | $3.14 \times 10^2$ |
| 0.0283 | 4.00 | 10.05 | 0.741 | 3.94 | 0.746 | $4.73 \times 10^5$ | $3.47 \times 10^2$ |

To begin the flume erosion test of a specimen, the Shelby tube containing the settled soil mixture was inserted into the flume bottom, and the soil surface was leveled with the channel bed. Then the top of the specimen was covered by a metal cap as the flow conditions ($Q$, $S_0$, and $y$) were adjusted. Once the test began, the operator gradually extruded the specimen upward with a hydraulic jack to maintain the sediment surface level with its surrounding channel bed as the specimen was eroded. The height of extrusion progressing with time was measured with a cable-pull potentiometer attached to the hydraulic piston that extruded the specimen into the flume. Meanwhile, the voltage output from the potentiometer was read through a data acquisition system developed by National Instruments, which was connected to a recording program written in Matlab

interface. The calibrated relationship between the displacement and the output voltage of the potentiometer is shown in Figure 3.11.
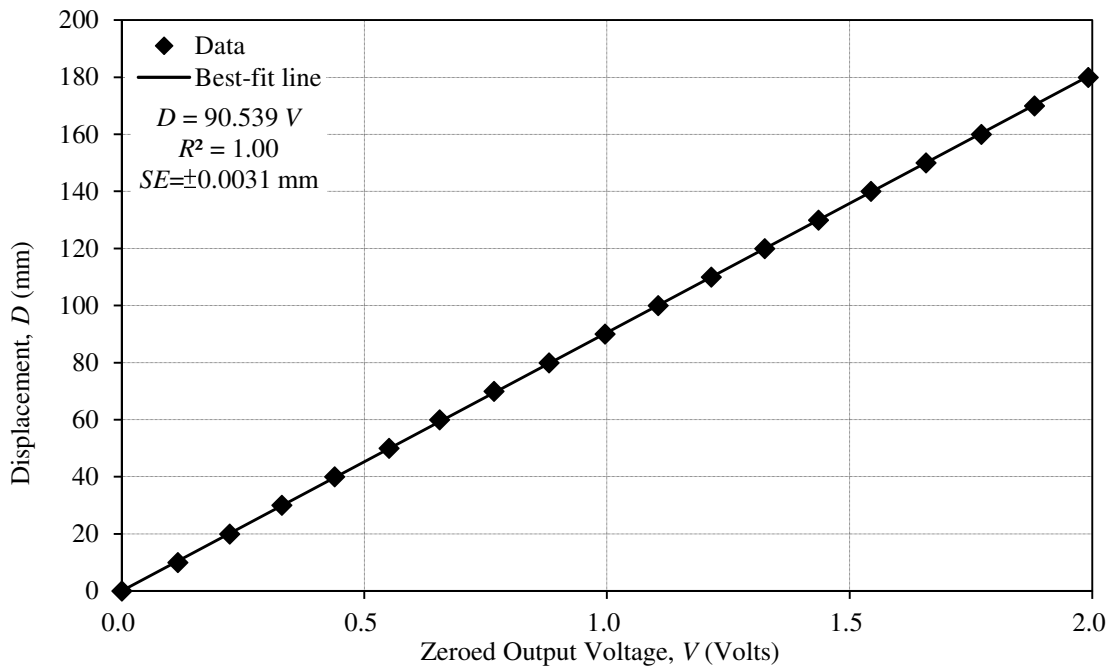


Figure 3.11 Potentiometer calibration for piston displacement determination

### 3.3.2 Measuring Erosion Rate

Since the entire flume experiment relies on visual observation of the sediment surface exposed to the flow, the end of one erosion testing trial was determined by the operator to occur when the eroded sediment in the flow impeded visual observation. Then the specimen surface was covered by the cap, and the flume was entirely shut down, drained, and refilled with fresh water for the next trail. The testing duration of each trial ranged from 30 sec to 10 min, depending on both the erosion resistance of the specimen and the applied bed shear stress. For each trial, the water content and depth of the

sediment layer in the specimen were measured, and the relationship between the piston

displacement and testing time was plotted to obtain the erosion rate ( $E$ ) in $kg/m^2/s$ by

calculating:

$$E = 0.001 \frac{\Delta D}{\Delta t} \rho_d \qquad (3.19)$$

where $\frac{\Delta D}{\Delta t} =$ the slope (in $mm/s$) of best-fit line of the piston displacement data as shown

in Figure 3.12 The relative standard error (*SE*) of $E$ (%) is estimated from the

propagation of error theorem as:

$$\frac{SE_E}{E} \times 100\% = \left( \sqrt{\left( \frac{SE_{\Delta D/\Delta t}}{\Delta D/\Delta t} \right)^2 + \left( \frac{SE_{\rho_d}}{\rho_d} \right)^2} \right) \times 100\% \qquad (3.20)$$

Three replicated runs were conducted for each combination of specimen type and bed

shear stress. The uncertainty between the three replicates was expressed by the relative

standard deviation:

$$\frac{SD_E}{\overline{E}} \times 100\% = \left( \sqrt{\frac{\sum_{i=1}^{n} \left( E_i - \overline{E} \right)^2}{n-1}} \bigg/ \overline{E} \right) \times 100\% \qquad (3.21)$$

where $\overline{E} =$ average erosion rates of the three replicates; $E_i =$ the erosion rate of one

replicate; $n =$ number of replicates, which is 3 in the study.

Take the example of the 100% kaolin specimen being eroded under a bed shear

stress of 2.48 Pa (Figure 3.12). In this case, the relative standard error of the erosion rate

( $\frac{SE_E}{E}$ ) for one realization is 2.5 % and the uncertainty of the erosion rate estimated from

105

the three replicated runs ($\frac{SD_E}{\overline{E}}$) is around 2.8%. For all the tests, values of $\frac{SE_E}{E}$ and

$\frac{SD_E}{\overline{E}}$ fall in the range of 2% to 8%, and 2% to 10%, respectively. In other words, the

estimated experimental errors in erosion rate were consistent with the observed errors.
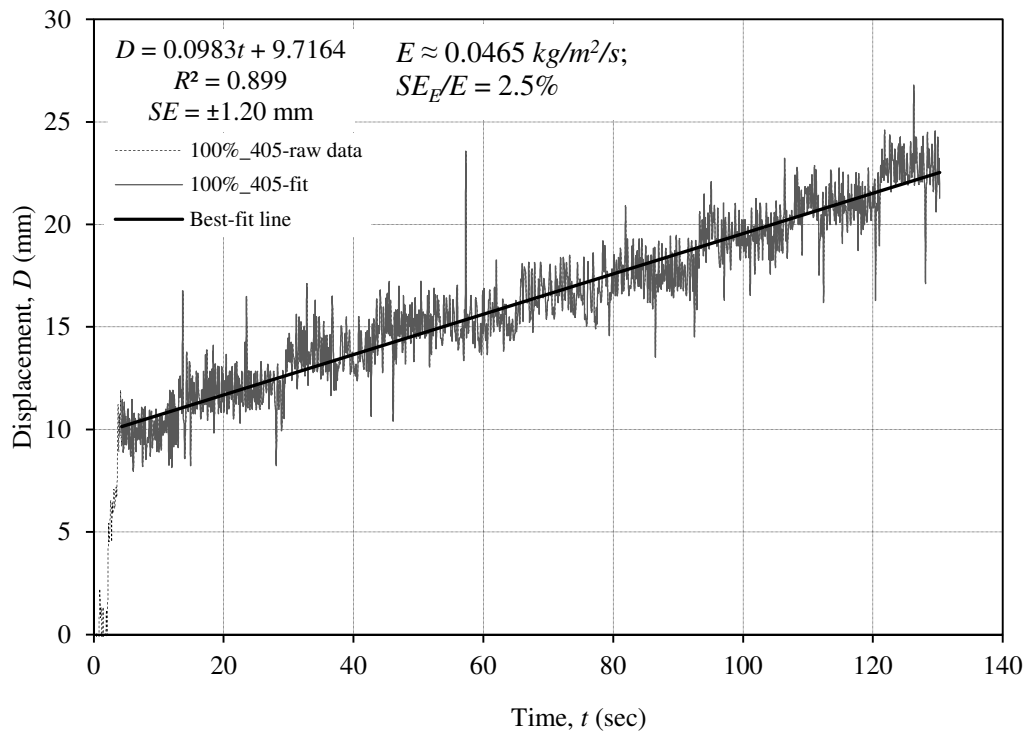


Figure 3.12 Example flume erosion measurement of 100% clay specimen with an applied bed shear stress of $\tau = 2.48$ Pa

### 3.3.3 Estimating Critical Shear Stress

After a series of erosion tests conducted under five different applied bed shear stresses, the calculated erosion rates were plotted versus the applied bed shear stresses. Then equation 2.17, $E = M(\tau - \tau_c)^n$, was used as the model to fit the plotted data points

using a nonlinear least-squares optimization technique, Gauss-Newton algorithm, developed in Matlab. In the Matlab program, values of erosion rate ( $E_i$ , $i = 1, 2,...,5$ ) and applied bed shear stress ( $\tau_i$ , $i = 1, 2,...,5$ ) were used as input data; and the parameters $M$, $n$, and $\tau_c$ were sought iteratively using the Gauss-Newton algorithm such that the model was in agreement with the input data. Iteration of parameters was set to terminate when

$$\frac{1}{3}\sqrt{\left(M_j - M_{j-1}\right)^2 + \left(n_j - n_{j-1}\right)^2 + \left(\left(\tau_c\right)_j - \left(\tau_c\right)_{j-1}\right)^2} < 10^{-5} \text{, where } j \text{ is the index of iteration,}$$

and $M_j$, $n_j$, and $\left(\tau_c\right)_j$ were obtained as the best-fit parameters.

To interpret those parameters, $M$ and $n$ are the empirical constants and $\tau_c$ is the critical shear stress, which was taken as the shear stress corresponding to zero erosion rate from the best-fit equation of erosion rate versus bed shear stress. Three replicated runs were carried out for each combination of applied bed shear stress and specimen-type because of uncertainties due to operator judgment and the instrumentation in the erosion test results. Previous studies using the same apparatus have also demonstrated the applicability and credibility of this flume erosion testing procedure (e.g. Ravisangar, 2001; Ravisangar et al., 2001, 2005, Navarro, 2004; Hobson, 2008). For example, Navarro (2004) and Hobson (2008) investigated the critical shear stress of river bed sediments sampled from different bridge sites in the state of Georgia using the flume erosion testing procedure as described in section 3.3. The values of critical shear stress resulting from the two studies fall in the same range (1 Pa to 20 Pa); and the measurements of the critical shear stress can be predicted by the same equation although they were carried out by different operators.

## 3.4 Yield Stress Analysis

The rheological characteristics of soil mixtures sought in this study are focused on yield stress analysis, which was performed with a Haake RheoStress RS75 stress-controlled rheometer since stress-controlled instruments perform well on yield stress measurements (van Kessel, 1998). A rotational rheometer basically consists of a cup and a concentric cylinder (rotor) which is submerged to rotate in the fluid. The rotor with the geometry of a cone bottom was chosen to reduce the end effects in this study. Under the stress-controlled mode, the rheometer measured the rheological characteristics, such as fluid viscosity as a function of the applied shear stress; the test can be used to estimate the strength of cohesive bonds in fine sediments. It has to be noted that only fine sediments can be used for the rheometer test in order to prevent significant damage to the cup and rotor of this device. The rheometer apparatus consists of a desktop installed with RheoStress monitoring software, the control unit, the rheometer installed with the cup and rotor sensor, the constant thermo controller filled with de-ionized water, and the compressed air providing a pressurized environment during the test. A systematic layout and a photo of the experimental setup are shown in Figure 3.13.

Compressed air, regulator, and filters

Rheometer and Sensor

Control Unit

Constant thermo controller
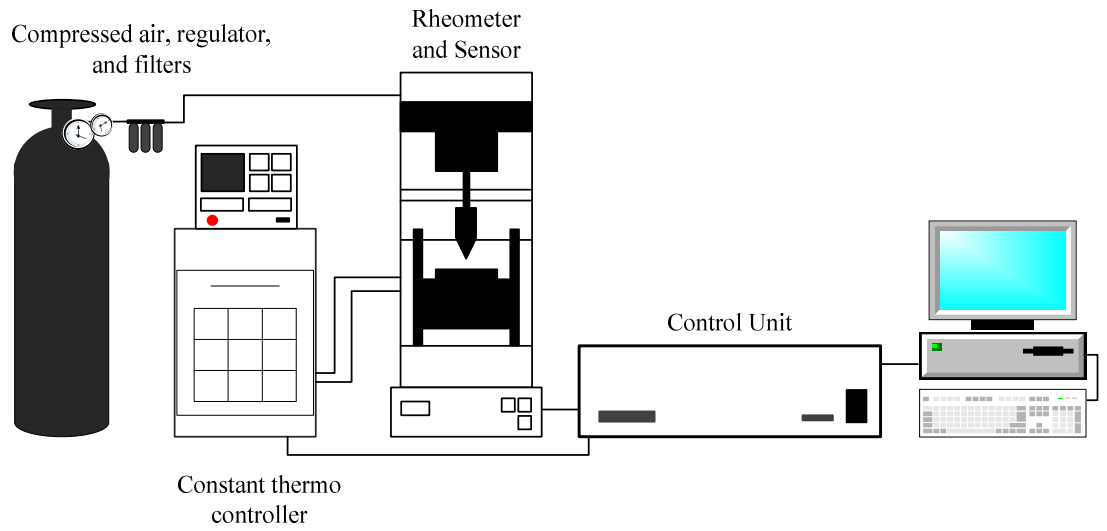
(NOT TO SCALE)
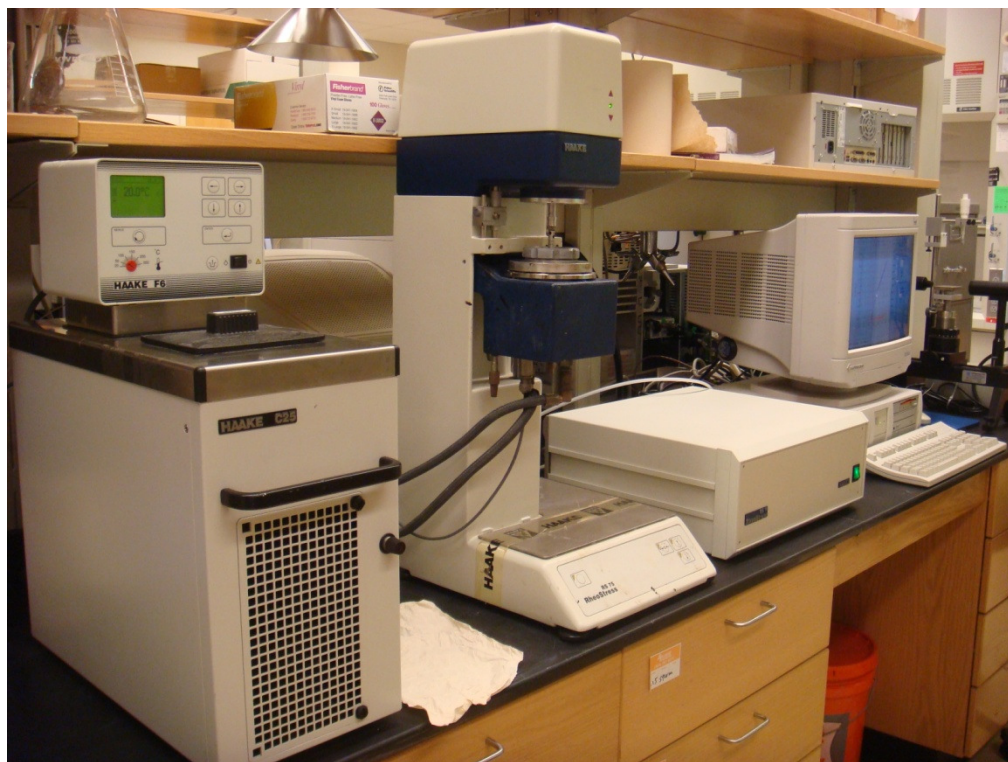
Figure 3.13 Stress-controlled rheometer apparatus: system layout (upper) and photo (lower)

Soil mixture specimens for the rheometer tests were prepared in the identical way as those for the flume erosion tests, except that the slurry was poured into the rheometer cup instead of the Shelby tube. After a 24-hour settling period, the excess water was suctioned out and the rheometer test began. Depending on the resistance of the specimen, the apparatus was programmed to logarithmically increase the shear stress from 0.04 Pa to a maximum stress of 12 Pa, 24 Pa, 48 Pa, 96 Pa, or 192 Pa over an assigned testing period. For different maximum stress cases, the testing period was determined in order to produce the same logarithmic rate factor ($\Delta$), which is defined as:

$$\Delta = \frac{\log\left(\tau_{max}/\tau_{min}\right)}{t} \qquad (3.22)$$

where $\tau_{max}$ = the maximum applied shear stress; $\tau_{min} = 0.04 Pa$ = the minimum applied shear stress; $t$ = the testing period. For instance, a 300-second testing period was selected for the case in which applied shear stress increased from 0.04 Pa to 12 Pa, resulting in $\Delta \cong 8.257 \times 10^{-3} \left(1/s\right)$ in accordance with the previous studies by Hoepner (2001) and Hobson (2008) who applied the same apparatus and methodology.

During the rheometer test, the applied shear stress, strain, strain rate, and viscosity were recorded by the rheometer. The determination of the lower and upper yield stresses using graphical methods suggested by the manufacturer (Schramm, 1994) are shown in Figure 3.14 and Figure 3.15, respectively. The lower yield stress ($\tau_{y1}$) was determined from the stress-strain relationship by the intersection of the two tangential fitting lines for low-strain and high-strain curves as illustrated in Figure 3.14. The upper yield stress ($\tau_{y2}$) is determined from a stress vs. strain rate relationship, usually called the flow curve, as shown in Figure 3.15.
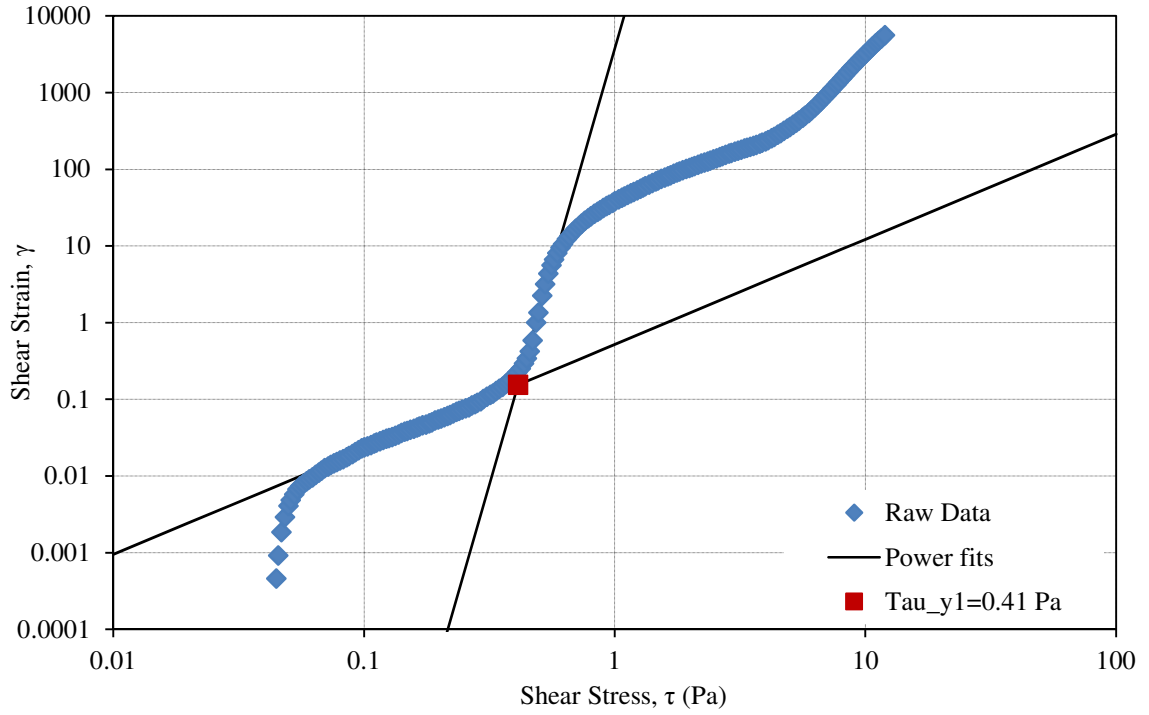
Figure 3.14 Determination of the lower yield stress
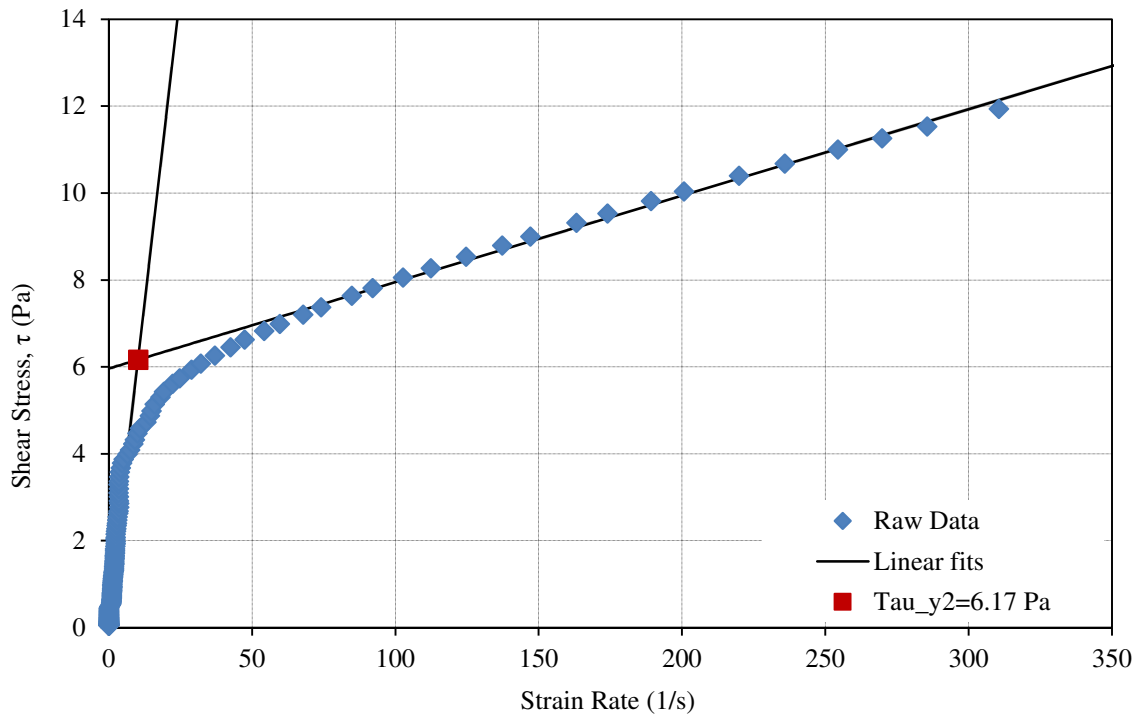


Figure 3.15 Determination of the upper yield stress

From a physical point of view, the utilization of viscoplastic mathematical models for particle suspensions, such as Bingham plastic, Casson, and Herschel-Bulkley models, have been reported in many rheology studies as discussed in sections 2.7 and 2.9. The yield stress can be estimated as the fitted stress value at the zero strain rate of a flow curve. In the study, the Herschel-Bulkley model $\tau = \tau_y + k(\dot{\gamma})^m$ (Herschel and Bulkley, 1926) was selected to estimate the yield stress of the soil specimens by fitting the flow curves from the rheometer tests using the Gauss-Newton algorithm, as shown in the example in Figure 3.16. The curve-fitting technique here applied the same procedure as that for estimating the critical shear stress. However, measurements of shear stress and strain rate from rheometer tests were the input data, and $k$, $m$, and $\tau_y$ were the parameters sought to obtain the best-fit model.
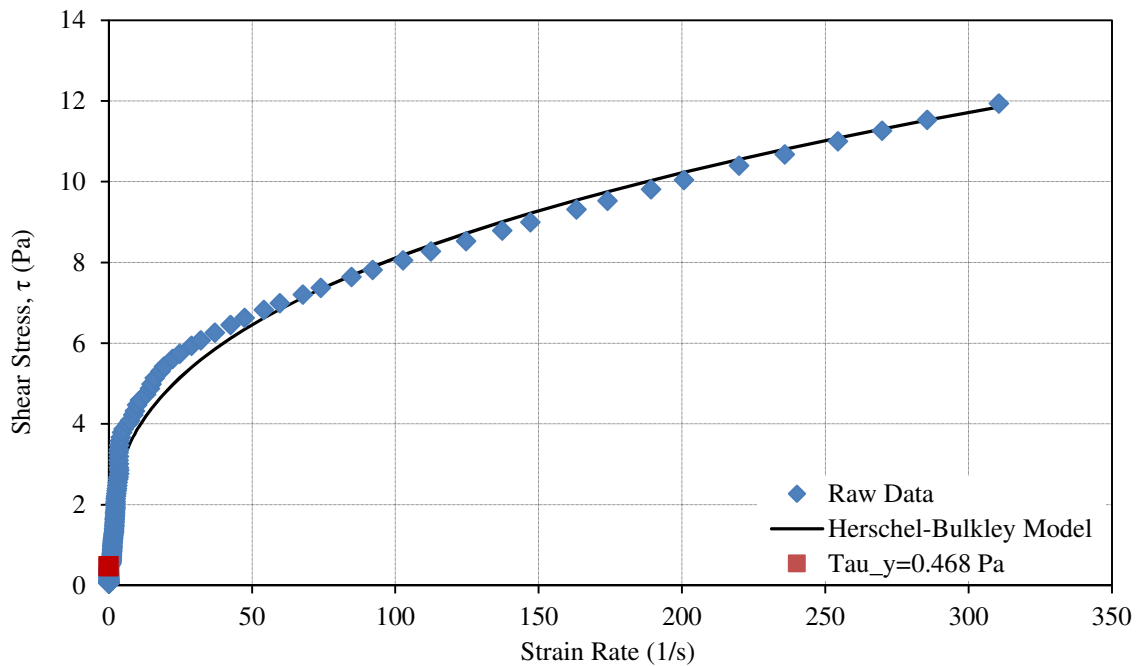


Figure 3.16 Determination of the yield stress using Herschel-Bulkley Model

### 3.5 Scanning Electron Microscopy

The technique of scanning electron microscopy (SEM) was applied to examine the interparticle arrangements of the soil mixtures containing different proportions of silt- and clay-size particles. The SEM images were obtained from the *Hitachi S-3700 Variable Pressure SEM*, which is located in the Marcus Organic Cleanroom of Institute for Electronics and Nanotechnology at Georgia Tech. Due to the low vacuum observation feature of the Variable Pressure SEM, this machine enables imaging of non-conductive samples without traditional sample preparation like gold coating. Therefore, this feature dramatically simplified the sample preparation process of the SEM samples. After the soil mixtures were prepared in accordance with the specimen preparation guidelines in section 3.1, a small chunk of the mixtures was taken to be oven dried before placing onto the SEM sample stage, which has a copper tape adhered to the surface. To distinguish the appearance of the ground silica and Georgia kaolin, SEM images were taken for each material separately; then the images of soil mixtures were taken under different amplifying magnitudes. For each type of the mixture, the specimen was sectioned into at least 3 layers, and sediments were sampled from each layer to apply the SEM technique.

# CHAPTER IV

# RESULTS

This chapter covers the experimental results from the geotechnical tests, flume experiments, rheometer tests, and SEM method as described in Chapter III. In section 4.1, the geotechnical properties of the soil specimens, including water content, bulk density, grain size distribution, and Atterberg limits are presented first; then follow the temperature, pH value, and conductivity of the soil mixtures. After that, sediment erosion and rheological characteristics are given in sections 4.2, and 4.3, respectively. Lastly, SEM images of soil specimens containing different kaolin proportions are illustrated in section 4.4.

## 4.1 Sediment Properties

### 4.1.1 Water Content and Bulk Density

For each run of the flume experiments, water content of sediments was measured and converted to sediment bulk density using equations 3.2 to 3.5. As described in the procedure for flume erosion experiments (section 3.3), five bed shear stress values in uniform flow were applied to measure the corresponding erosion rates of each soil-mixture specimen, and at least three replicates were conducted for each bed shear stress and each specimen having different clay percentages. Therefore, for each soil mixture containing a specific kaolin proportion, 15 specimens were prepared identically in the flume experiments. During each experiment on a particular specimen, it was sectioned into three to four layers; with the same applied shear stress, the resulting erosion rate for

each layer was different due to the variation in the bulk density. At the end of each run, some portion of the sediment was taken from each layer for water content measurement. Layers of sediments sectioned from one specimen were labeled as top, middle(1), middle(2), and bottom, indicating the locations of sediment layers in the whole specimen. Measurements of water content of the same sediment layer among different specimens with the same kaolin content were compared, and the maximum, minimum, mean, and standard deviation of water content measurements are shown in Table 4.1.

As shown in Table 4.1, the maximum, minimum, and average water contents decrease from the top to bottom layers for all mixtures of specimens. Comparison between different mixtures of specimens shows that measurements of sediment water content increase with the increase of kaolin content, except for the 10% kaolin specimens. This trend of increasing water content with kaolin content in specimens is due to the property of clayey, plastic soils that water is more likely to be held between particles if the soils contain a higher proportion of clay particles. Although specimens with the same kaolin content were prepared follow the identical procedure, uncertainties in flow conditions and operation led to some scatter in the water content measurements, which are estimated by the standard deviations (st. dev.). The relative standard deviations are around ±5% in comparison to the average water contents for most sediment layers.

Table 4.1 Statistics of water content measurements of the soil mixture specimens

| Specimen type | Sediment layer | Max. water content (% water) | Min. water content (% water) | Avg. water content (% water) | St. dev. of water content (% water) | Relative st. dev. |
|---|---|---|---|---|---|---|
| 10% kaolin | Top | 84.6 | 62.5 | 77.0 | ± 7.0 | ± 9% |
| | Middle | 51.9 | 40.9 | 46.1 | ± 3.9 | ± 8% |
| | Bottom | 38.7 | 34.1 | 36.7 | ± 1.6 | ± 4% |
| 20% kaolin | Top | 73.0 | 61.7 | 66.2 | ± 2.9 | ± 4% |
| | Middle | 64.2 | 55.6 | 60.3 | ± 2.7 | ± 4% |
| | Bottom | 57.9 | 50.0 | 54.2 | ± 2.3 | ± 4% |
| 40% kaolin | Top | 109.6 | 100.0 | 103.8 | ± 3.2 | ± 3% |
| | Middle(1) | 101.8 | 87.4 | 93.6 | ± 4.2 | ± 4% |
| | Middle(2) | 89.9 | 74.5 | 83.2 | ± 4.0 | ± 5% |
| | Bottom | 83.0 | 70.4 | 77.0 | ± 4.0 | ± 5% |
| 60% kaolin | Top | 175.0 | 150.0 | 163.7 | ± 8.7 | ± 5% |
| | Middle(1) | 154.2 | 127.5 | 142.1 | ± 10.8 | ± 8% |
| | Middle(2) | 145.7 | 116.1 | 127.7 | ± 8.7 | ± 7% |
| | Bottom | 108.3 | 85.6 | 96.2 | ± 6.1 | ± 6% |
| 100% kaolin_(1) | Top | 190.2 | 175.9 | 182.8 | ± 5.6 | ± 3% |
| | Middle(1) | 189.4 | 170.8 | 182.2 | ± 7.3 | ± 4% |
| | Middle(2) | 176.8 | 154.0 | 166.7 | ± 8.5 | ± 5% |
| | Bottom | 161.9 | 151.5 | 156.3 | ± 4.3 | ± 3% |
| 100% kaolin_(2)[a] | Top | 121.7 | 116.9 | 119.1 | ± 2.4 | ± 2% |
| | Middle(1) | 115.1 | 111.8 | 113.3 | ± 1.3 | ± 1% |
| | Middle(2) | 116.8 | 107.1 | 112.1 | ± 4.4 | ± 4% |
| | Bottom | 112.8 | 105.4 | 109.5 | ± 2.8 | ± 3% |

[a] made with less tap water added initially compared to all the other types of soil mixtures

Figure 4.1(*a*) to (*f*) shows the bulk densities of the sediment layers located at different depths from the surface of soil specimens containing 10%, 20%, 40%, 60%, and 100% kaolin contents, respectively. Among those, Figure 4.1(*e*) and (*f*) show the bulk density data of 100% kaolin specimens prepared with two different initial water contents of 160% and 100%, respectively. The first pure clay specimen, designated as 100%Kaolin(1), was prepared with the ratio of 160 g of water to 100 g of solids, which is the same as the other specimens with 10% to 60% kaolin contents. The second pure clay specimen, 100%Kaolin(2), was prepared with less water (100 g) added to the equivalent amount of solids to produce higher bulk densities.

From Figure 4.1, an increasing trend of sediment bulk density with depth of the sediment layer from the surface is observed in all soil mixtures. However, scattering of the data points as well as the varying range of bulk density values decreases as the specimen kaolin content increases. In other words, the increase of kaolin proportion in the soil mixture leads to a more homogeneous soil mixture in terms of bulk density variation with respect to depth. In particular, soil specimens made with 100% Georgia kaolin (Figure 4.1(*e*) (*f*)) can be considered as essentially homogenous with respect to bulk density throughout the depth of the sediment layers. The standard error of estimate and the slope of the best-fit equations for bulk density as a function of depth are given in Table 4.2 along with the range of bulk density for each of the soil mixtures.
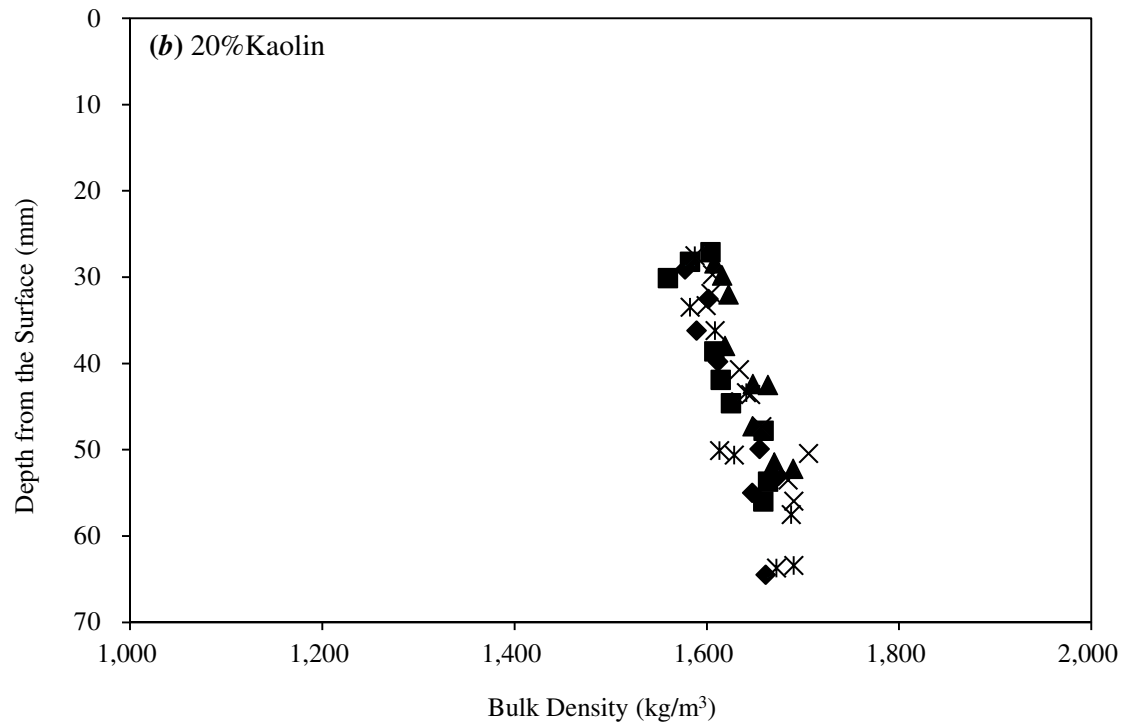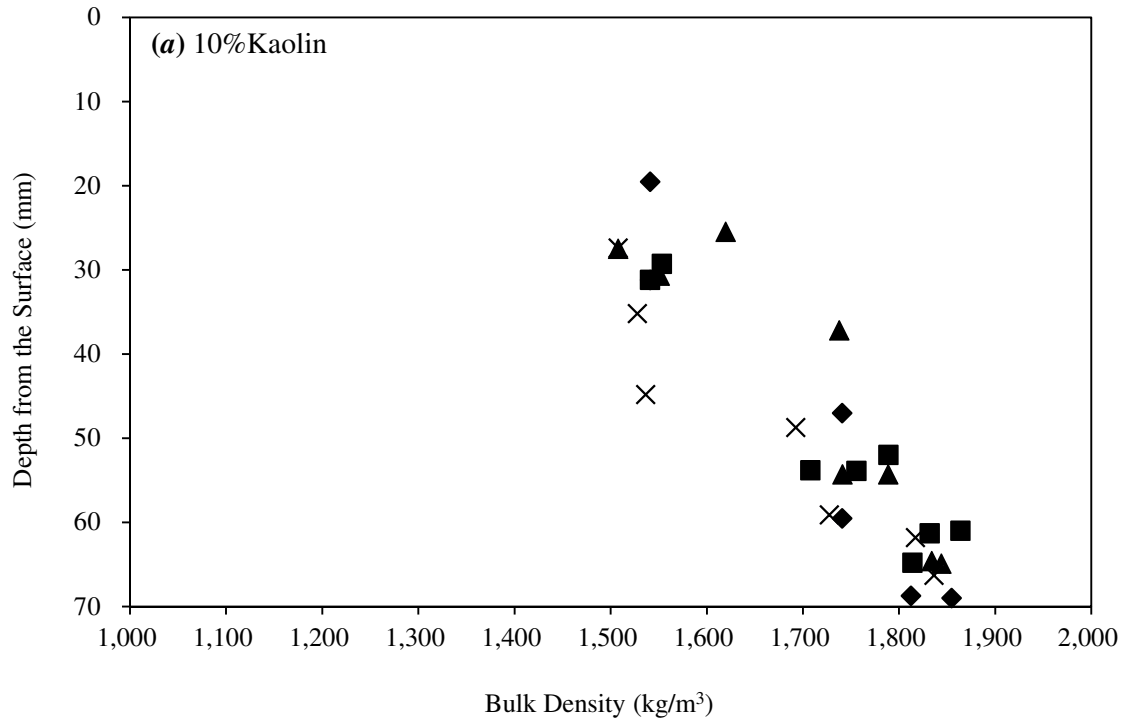
Figure 4.1 Bulk densities of the sediment layers located at different depths from the surface of specimens with (*a*) 10% kaolin content, (*b*) 20% kaolin content, (*c*) 40% kaolin content, (*d*) 60% kaolin content, and (*e*) and (*f*) 100% kaolin content

(Figure 4.1 Continued)

119

(*e*) 100%Kaolin(1)

Depth from the Surface (mm)

Bulk Density (kg/m³)



(*f*) 100%Kaolin(2)

Depth from the Surface (mm)

Bulk Density (kg/m³)

◆ Tau=2.15 Pa     ■ Tau=2.48 Pa     ▲ Tau=2.83 Pa     ✕ Tau=3.24 Pa     ✳ Tau=3.94 Pa
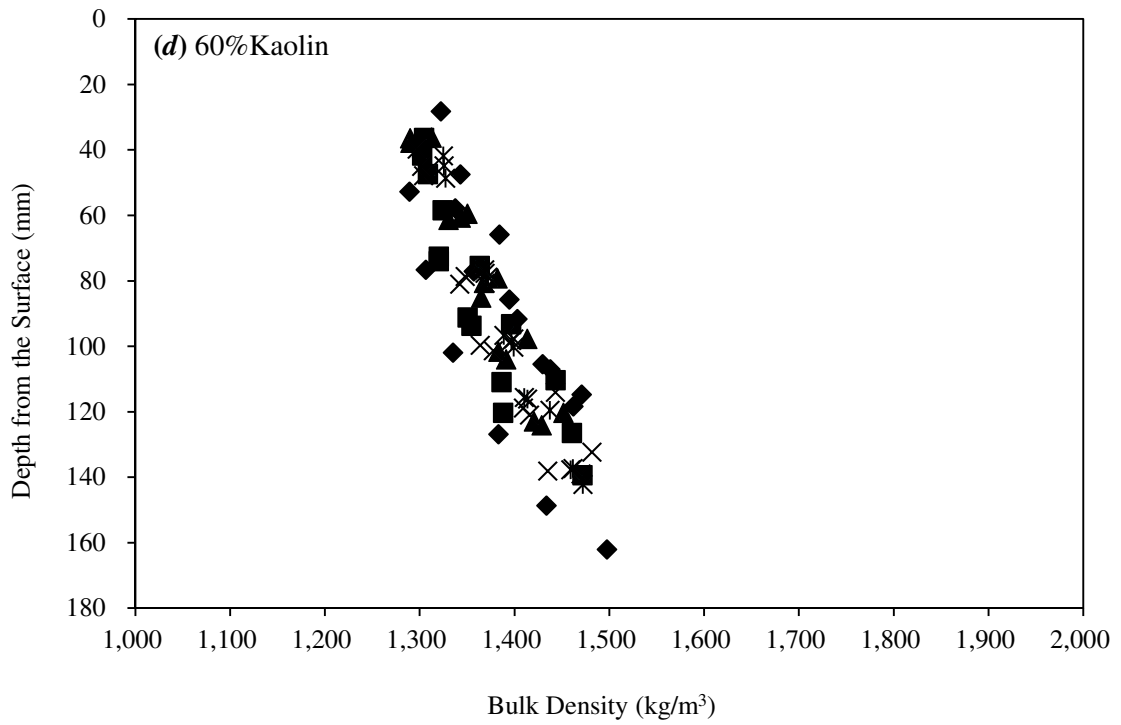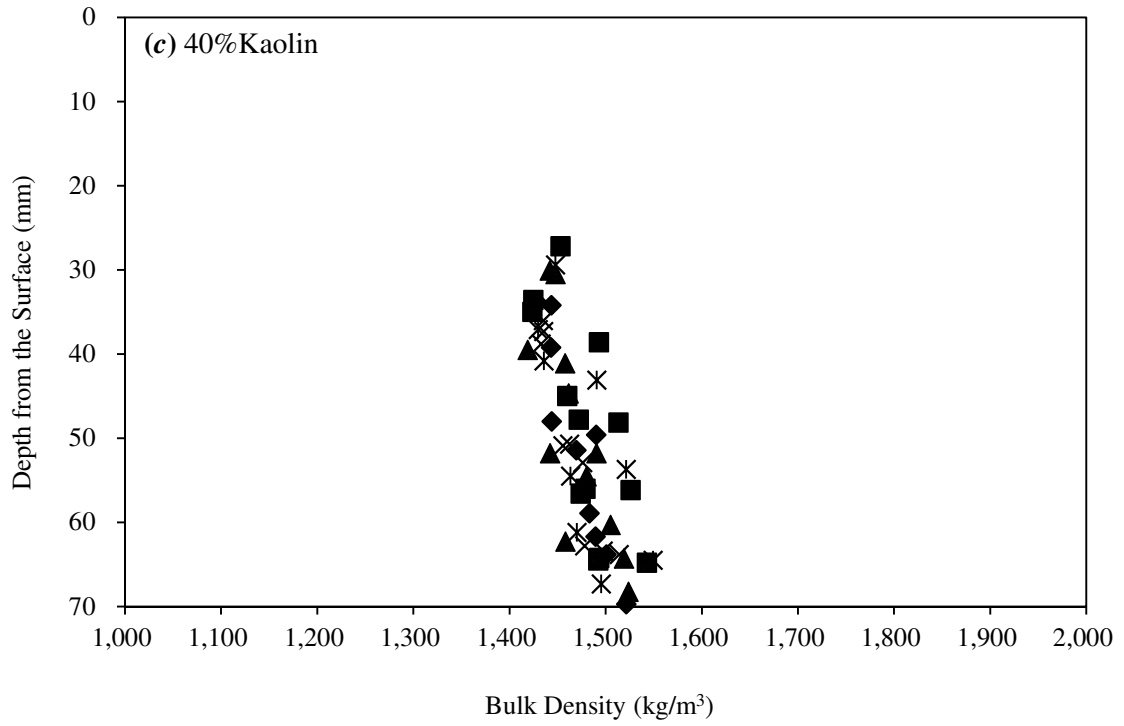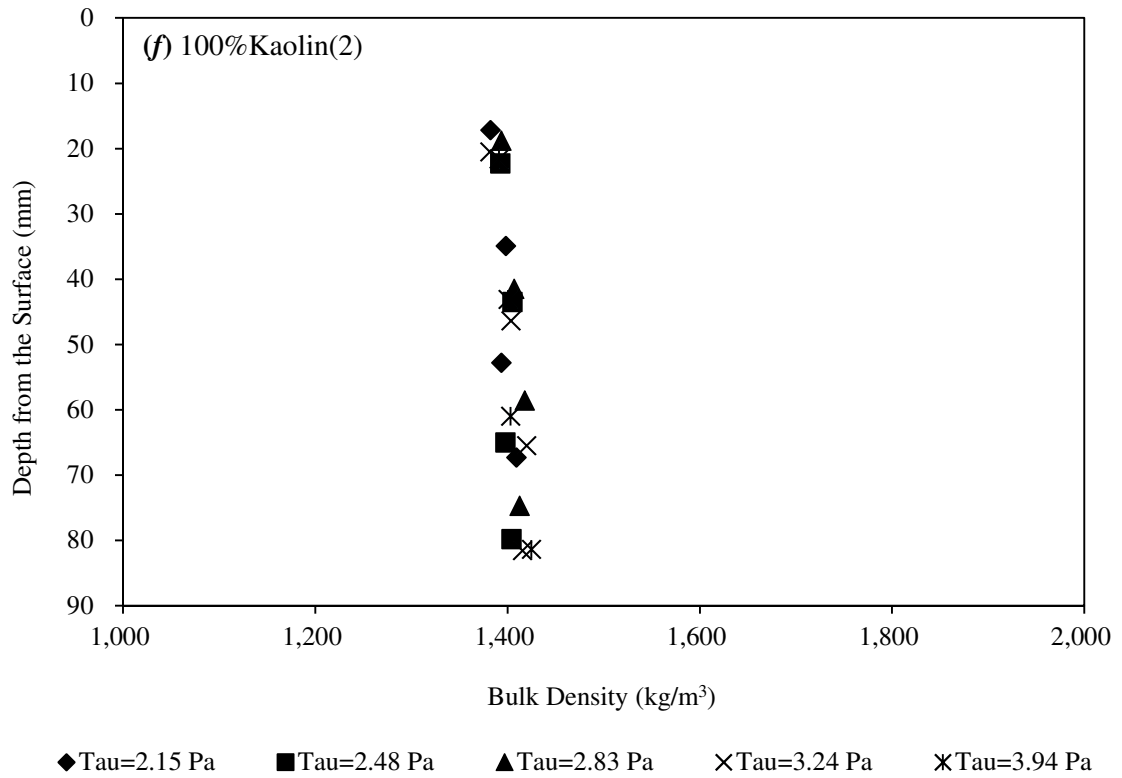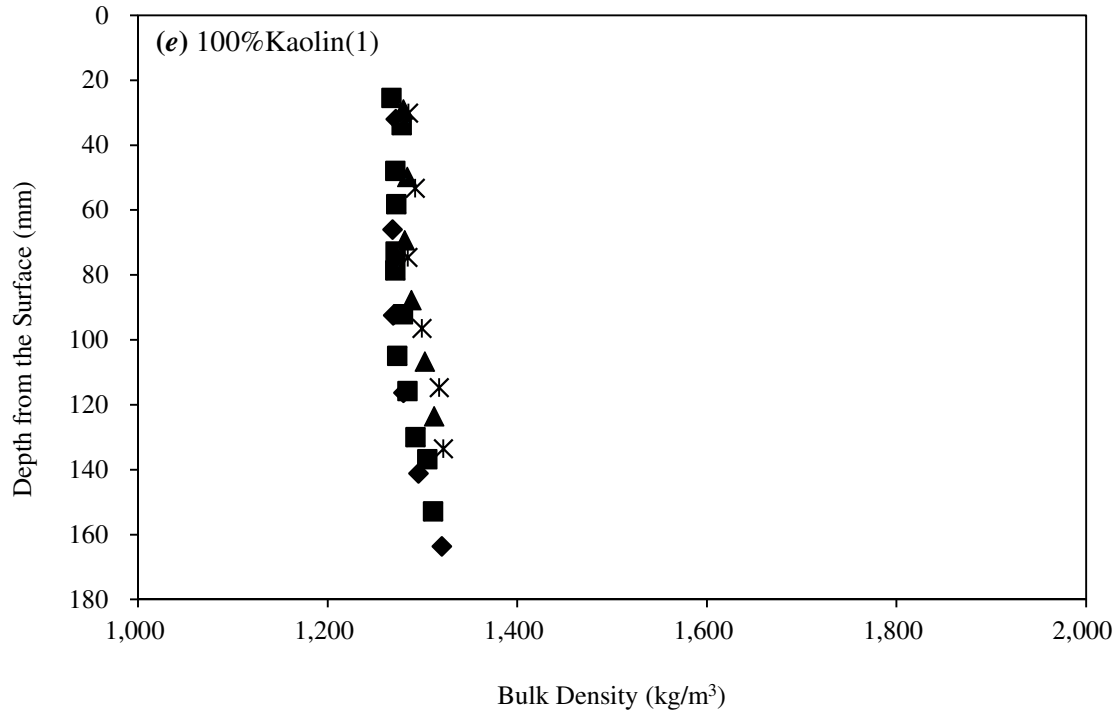
(Figure 4.1 Continued)

From Table 4.2, sediment bulk density of the soil mixture specimens used in this study covers the range from 1285 kg/m$^3$ to 1825 kg/m$^3$. The standard error of estimate (s.e.e) in sediment bulk density indicates the scattering of the data for each best-fit relationship of bulk density as a function of depth for specimens prepared for different shear stresses. The s.e.e. is approximately 50 kg/m$^3$ for 10% kaolin specimens and decreases to less than 10 kg/m$^3$ for 100% kaolin specimens. This indicates that the bulk density measurements of specimens with different kaolin content were affected by the sediment depth and applied shear stress; however, these effects decrease when the specimen kaolin content increases. The slope of the best-fit equation of bulk density versus sediment depth measures the degree of stratification of bulk density relative to depth. For 10% kaolin specimens, the stratification is 7.44 ± 0.66 kg/m$^3$/mm decreasing to 0.30 ± 0.06 kg/m$^3$/mm for the 100% kaolin specimens. The latter value indicates that pure kaolin specimens were essentially unstratified relative to bulk density.

Table 4.2 Statistics of sediment bulk density variation with depth of sediment layer

| Kaolin content (%) | Standard error of estimate (kg/m$^3$) | Slope of the best-fit equation (kg/m$^3$/mm) | Varying range of bulk density (kg/m$^3$) |
|---|---|---|---|
| 10 | ± 53.73 | 7.44 ± 0.66 | 1505~1865 |
| 20 | ± 19.46 | 2.84 ± 0.27 | 1555~1710 |
| 40 | ± 21.29 | 1.91 ± 0.14 | 1415~1570 |
| 60 | ± 23.26 | 1.52 ± 0.08 | 1285~1500 |
| 100(1) | ± 11.89 | 0.03 ± 0.06 | 1265~1325 |
| 100(2) | ± 7.22 | 0.43 ± 0.07 | 1380~1425 |

Variation in sediment bulk density with respect to depth is usually caused by sediment segregation or self-weight consolidation of sediment particles (McNeil, 1996; Lick and McNeil, 2001; Ravisangar et al., 2005; Gerbersdorf et al., 2007). Sediment segregation is usually found in well-graded or gap-graded soils which have a wide range of particle sizes compared to uniformly-graded soils. On the other hand, stratification relative to bulk density in uniformly-graded soils is usually caused by self-weight consolidation of sediments (Zreik et al., 1998), in which sediment particles are squeezed together and less voids are left in between particles due to the heavier loading on deeper sediment layers. The variation in sediment bulk density of the silt-clay soil mixtures in this study may be attributed to one or both of the reasons mentioned; however, the significant bulk density variation with respect to sediment depth found in 10% kaolin specimens may be caused by sediment segregation, which is discussed based on the analysis of grain size distribution in the next section.

### 4.1.2 Grain Size Distribution and Atterberg Limits

Figure 4.2 shows the grain size distributions of the soil mixture specimens with different kaolin contents, as well as the distributions of pure Georgia kaolin and pure silica flour. The sediments used in this study cover the size range from around 1 μm to more than 200μm, which coincides with the range from fine clay (1 to 5 μm) to fine (125 to 250 μm) sand according to the American Geophysical Union (AGU) scale. However, most of the particles are located in the size range of fine clay to very fine sand. The grain size distributions of pure kaolin (100% kaolin) and silica flour (0% kaolin) bracket most of the grain size distribution curves except for the bottom layer of the 10% kaolin specimen, *i.e.* 10%Kaolin(3) (5.5~7cm). From Figure 4.2, curves of grain size

distribution of different sediment layers in the same type of soil mixture generally show a similar shape and tend to collapse together, except for those of the 10% kaolin specimen. This division in the grain size distribution curves indicates that a significant segregation between sediment layers is observed only in the 10% kaolin specimens. Therefore, each layer of the specimens with different kaolin contents can be treated as a true size mixture rather than a segregated layer except for those of the 10% kaolin specimens. In the following chapter, experimental results and properties of the same sediment layer for each mixture with different kaolin contents are analyzed and discussed.
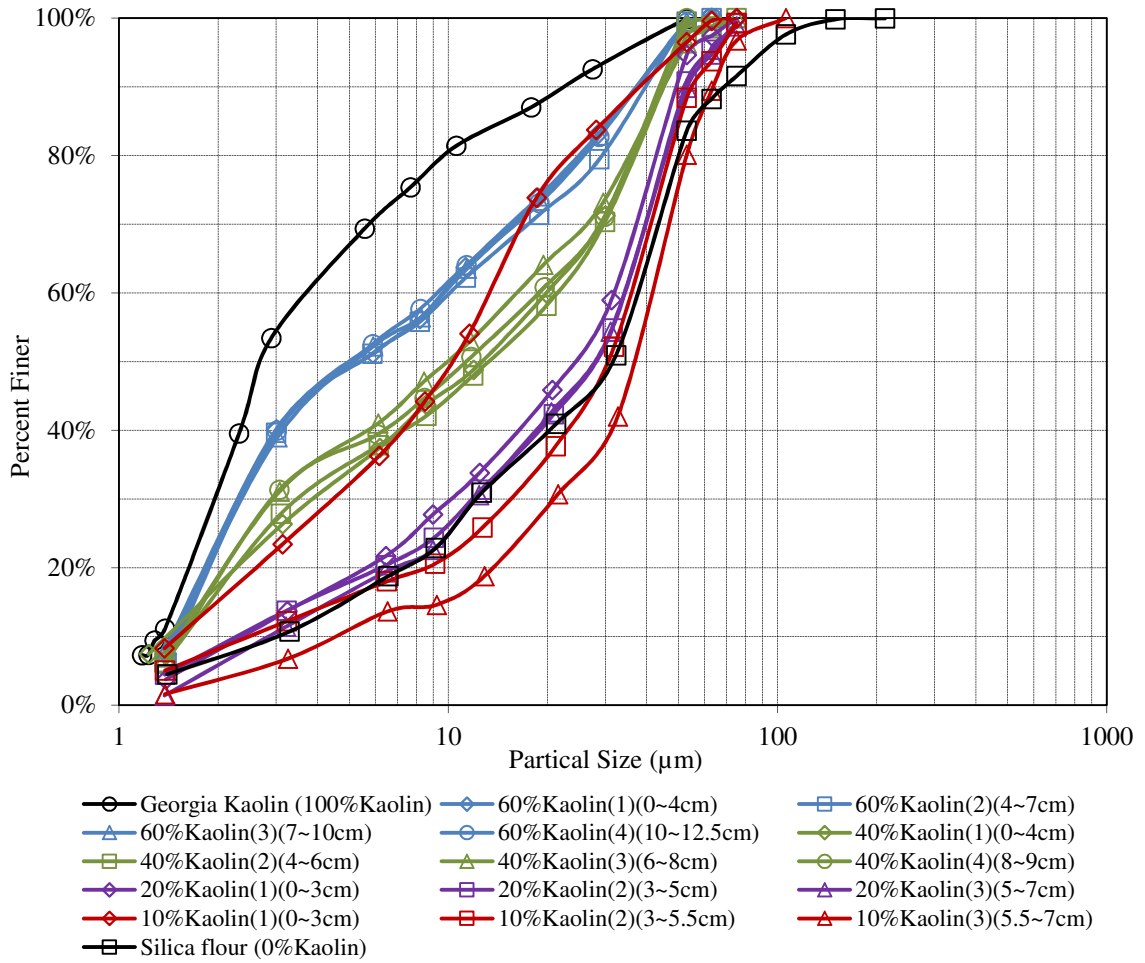
Figure 4.2 Grain size distributions of the silt-clay soil mixture specimens with different kaolin contents

From the grain size distributions, some useful geotechnical quantities regarding sediment particle size are obtained through interpolation and/or calculation, and they are shown in Table 4.3. These quantities include some specific values of particle size (diameter) at which a specific percentage of total particles by weight are smaller than those sizes. For example, each of $d_{60}$, $d_{50}$, $d_{30}$, and $d_{10}$ represents the particle size that 60%, 50%, 30%, and 10% of total particles by weight is smaller than that size, respectively. Except for the cases of 10% kaolin specimens, values of $d_{60}$, $d_{50}$, $d_{30}$, and $d_{10}$ decrease as the kaolin contents in soil mixtures increase. In addition, for each particle with a specific passing percentage, i.e. $d_{60}$, $d_{50}$, $d_{30}$, or $d_{10}$, values among different layers of sediments with the same kaolin content are similar.

Coefficients of uniformity ($C_u$) and curvature ($C_c$) are two important parameters for grading a soil, which are defined as:

$$C_u = \frac{d_{60}}{d_{10}} \tag{4.1}$$

$$C_c = \frac{d_{30}^2}{d_{10} \cdot d_{60}} \tag{4.2}$$

While the grading criteria are generally applied to coarse sediments, which are retained on the No. 200 sieve (with 75 μm mesh openings), these criteria may still be applicable to the silica flour and the bottom layer of 10% kaolin specimens used in this study since those sediments fall within the range of sizes from coarse silt to fine sand. Based on the grading criteria for sand, both sediments are classified as well graded since their $C_u$ values are larger than 4 and $C_c$ values are between 1 and 3 (Santamarina et al., 2001).

For the purpose of data analysis, the percentage of clay content was estimated from the interpolation of the grain size distribution for each sediment layer. Specifically,

the clay content is defined as the proportion of particles with diameter smaller than 2 $\mu$m by weight, which is shown in Table 4.3 as well. Therefore, the clay content increases as the kaolin content of the soil mixtures increases. Specifically, the clay content increases from slightly more than 3% to 30% as the kaolin content in the soil mixtures increases from 0% to 100%.

Table 4.3 Geotechnical quantities regarding particle size of the soil mixtures with different kaolin contents

| Sample kaolin content | $d_{60}$ (µm) | $d_{50}$ (µm) | $d_{30}$ (µm) | $d_{10}$ (µm) | $C_u$ | $C_c$ | Percent of Clay (%)[a] |
|---|---|---|---|---|---|---|---|
| 0% (Silica flour) | 38 | 32 | 12.5 | 3 | 12.7 | 1.37 | 6.5 |
| 10% (1) (top) | 11.7 | 10 | 4.5 | 1.5 | 7.8 | 1.15 | 13.7 |
| 10% (2) (middle) | 36 | 30 | 16 | 2.5 | 14.4 | 2.84 | 7.4 |
| 10% (3) (bottom) | 55 | 40 | 21.5 | 4.5 | 12.2 | 1.87 | 3.3 |
| 20% (1) (top) | 31.5 | 23 | 10 | 2.3 | 13.7 | 1.38 | 7.0 |
| 20% (2) (middle) | 35 | 26 | 12 | 2.3 | 15.2 | 1.79 | 7.6 |
| 20% (3) (bottom) | 35 | 26 | 12.2 | 3 | 11.7 | 1.42 | 4.8 |
| 40% (1) (top) | 19.8 | 12.2 | 4 | 1.4 | 14.1 | 0.58 | 15.1 |
| 40% (2) (middle_1) | 21 | 13 | 3.5 | 1.55 | 13.6 | 0.38 | 14.1 |
| 40% (3) (middle_2) | 16.5 | 10 | 3 | 1.55 | 10.7 | 0.35 | 15.8 |
| 40% (4) (bottom) | 19.5 | 11.6 | 3 | 1.55 | 12.6 | 0.30 | 15.3 |
| 60% (1) (top) | 9.5 | 5.6 | 2.2 | 1.5 | 6.3 | 0.34 | 19.8 |
| 60% (2) (middle_1) | 10 | 5.6 | 2.25 | 1.5 | 6.7 | 0.34 | 18.8 |
| 60% (3) (middle_2) | 9.5 | 5.5 | 2.25 | 1.5 | 6.7 | 0.36 | 19.6 |
| 60% (4) (bottom) | 9.4 | 5.6 | 2.25 | 1.5 | 6.3 | 0.36 | 20.3 |
| 100% (Georgia kaolin) | 3.5 | 2.6 | 2 | 1.5 | 2.3 | 0.76 | 30.0 |

[a] Refers to the fraction of particles smaller than 2 µm by mass

The liquid limits ($w_{LL}$), plastic limits ($w_{PL}$), and plasticity indices ($I_p$) of soil mixtures consisting of different kaolin contents by dry weight are tabulated in Table 4.4. In addition, soil classifications according to Ranjan and Rao (2000) and the ASTM standard 2487-06 are also listed in the same table (Table 4.4). The values of $w_{LL}$, $w_{PL}$, and $I_p$ range from 18% to 49%, 11% to 23%, and 6% to 26%, respectively. For the Georgia kaolin (100% kaolin content specimen) used in this study, the values of $w_{LL}$ (49%), $w_{PL}$ (23%), and $I_p$ (26%) are found to be comparable with the typical values of kaolinite reported in the literature (Seed et al., 1964). Generally, the values of liquid limit, plastic limit, and plasticity index increase with the increasing kaolin contents in the soil mixtures, which transformed the mixtures from low plastic to medium and high-plastic soils according to the classification reported in Ranjan and Rao (2000).

Table 4.4 Atterberg limits of soil mixtures with different kaolin contents (by dry weight)

| Kaolin content (%) | $w_{LL}\,(\%)$ | $w_{PL}\,(\%)$ | $I_p\,(\%)$ | Classification in Ranjan & Rao (2000) | Classification in ASTM 2487-06 |
|---|---|---|---|---|---|
| 10 | 18.2 | 11.8 | 6.5 | Low plastic | CL-ML |
| 20 | 18.4 | 12.5 | 5.9 | | |
| 30 | 22.9 | 13.3 | 9.6 | Medium plastic | CL |
| 40 | 30.1 | 15.3 | 14.9 | | |
| 50 | 31.9 | 15.4 | 16.5 | | |
| 60 | 33.1 | 15.5 | 17.6 | High plastic | |
| 100 | 48.7 | 22.8 | 25.9 | | |
| kaolinite[a] | 42-58 | 19-32 | 21-26 | High plastic | CL |

[a] Range of typical values reported in Seed et al. (1964)

128

Figure 4.3 shows the plot of $w_{LL}$, $w_{PL}$, $I_p$, and versus kaolin content ($Kaolin$) in the soil mixtures, respectively, along with the best-fit relationships. The best-fit linear equations found between the values of $w_{LL}$, $w_{PL}$, or $I_p$ and $Kaolin$ are as follows:

$$w_{LL} = 0.351 Kaolin + 0.135 \qquad R^2 = 0.98; \ SE = \pm 1.83 w_{LL} \qquad (4.3)$$

$$w_{PL} = 0.119 Kaolin + 0.100 \qquad R^2 = 0.94; \ SE = \pm 0.95 w_{PL} \qquad (4.4)$$

$$I_P = 0.232 Kaolin + 0.035 \qquad R^2 = 0.96; \ SE = \pm 1.6 I_P \qquad (4.5)$$

where $Kaolin$ is the kaolin content in decimal fraction; $w_{LL}$, $w_{PL}$, and $I_p$ are water contents in decimal fractions. Comparing equations 4.3 and 4.4, the slope in the $w_{LL}$-$Kaolin$ linear equation is more than three times slope in the $w_{PL}$-$Kaolin$ relationship, which indicates that the liquid limit of the soil mixtures is more sensitive to the kaolin content in the mixtures. Similarly, the slope in the $I_p$-$Kaolin$ linear equation indicates that the sensitivity of kaolin content to the plasticity index is between those of liquid and plastic limits.

If the explanatory variable, kaolin content, is replaced by the clay content in decimal fraction ($Clay$) in the soil mixtures in equations 4.4 to 4.6, and the data of 20%, 40%, 60%, and 100% kaolin specimens are used for regression analysis, the least-squares linear relationships become:

$$w_{LL} = 0.656 Clay + 0.145 \qquad R^2 = 0.92; \ SE = \pm 2.34 w_{LL} \qquad (4.6)$$

$$w_{PL} = 0.136 Clay + 0.117 \qquad R^2 = 0.83; \ SE = \pm 0.73 w_{PL} \qquad (4.7)$$

$$I_P = 0.520 Clay + 0.027 \qquad R^2 = 0.94; \ SE = \pm 1.6 I_P \qquad (4.8)$$

Therefore, similar conclusions can be drawn regarding changes in soil plasticity with changes in the proportion of kaolin or clay in the soil mixtures.
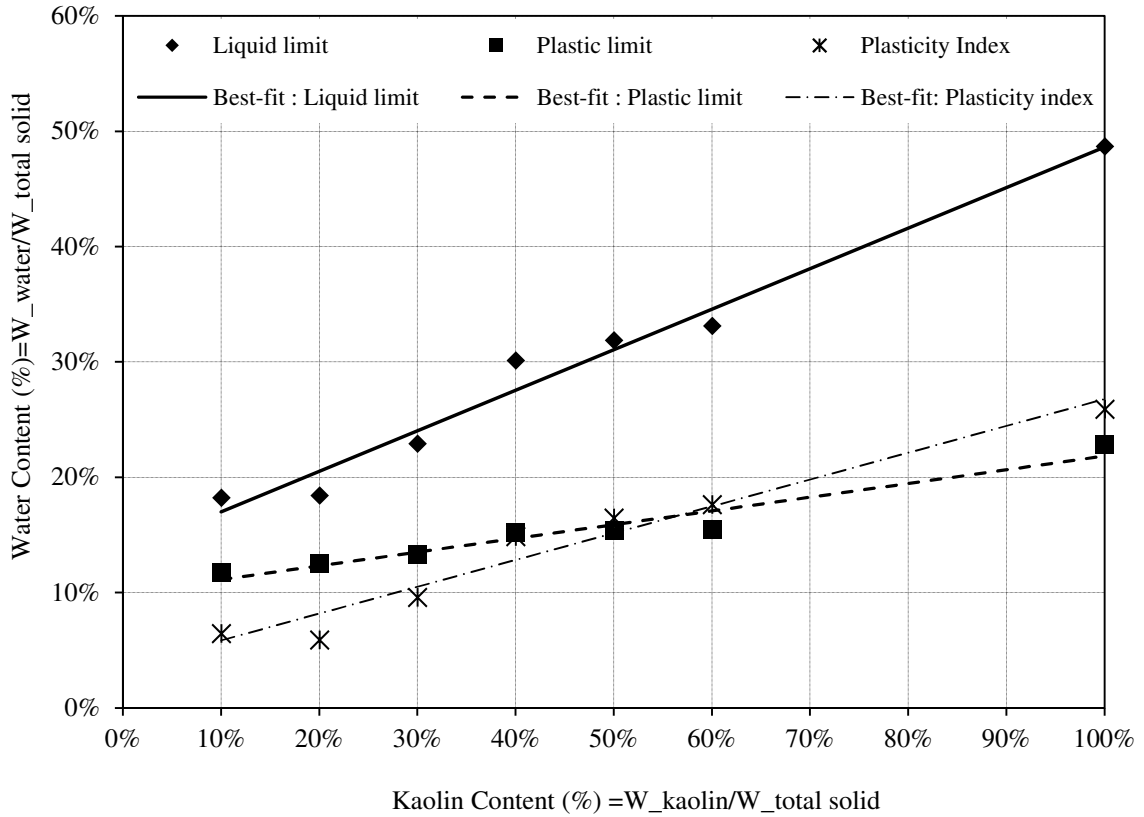


Figure 4.3 Relationships of liquid limits-, plastic limits-, and plasticity index- versus kaolin contents in the soil mixtures

If values of liquid limit and plasticity index are plotted on the Plasticity Chart suggested in ASTM D2487-06, it is shown in Figure 4.4 that all the data points of the soil mixtures used in this study fall in the regions defined by the "A" line and "U" line on the Plasticity Chart. Specifically, the 10% and 20% kaolin content mixtures are classified as silty clay (CL-ML) and all the others belong to lean clay (CL) since there is no organic content in the soil mixtures of this study.
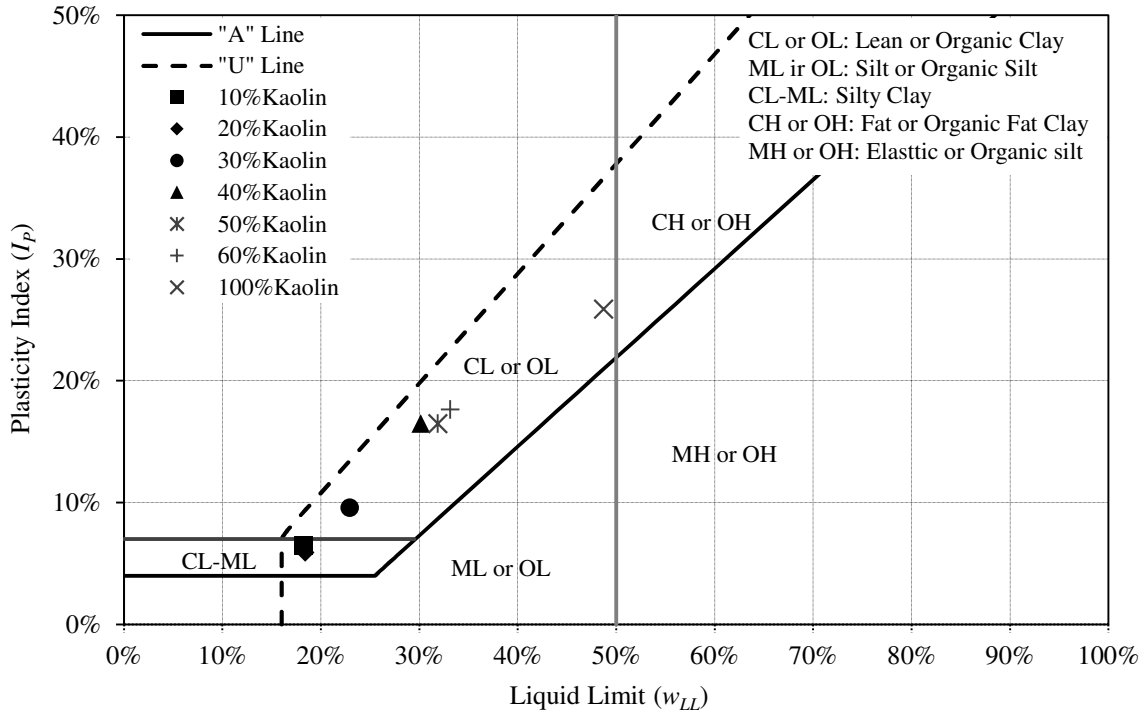
Figure 4.4 Liquid limit and plasticity index data of the soil mixtures in this study plotted on the Plasticity Chart suggested in ASTM D2487-06

### 4.1.3 Temperature, pH value, and Conductivity

After the soil mixture specimens were prepared, temperature, pH value, and conductivity of each sediment layer were measured using the Oakton waterproof PC 300 hand-held meter by dipping the probes of pH and conductivity electrodes into the soil slurry. For comparison, measurements of temperature, pH value, and conductivity of the tap water used in specimen preparation were also recorded before preparing the soil mixture each time. The average values (Avg.) and standard deviations (St. dev.) of temperature, pH value, and conductivity measurements of the tap water and soil mixtures are shown in Table 4.5.

Table 4.5 Temperature, pH value and conductivity of tap water and soil mixtures

| Slurry type | Temperature (°C) | | pH value | | Conductivity (µS/cm) | |
|---|---|---|---|---|---|---|
| | Avg. ±St. dev. | Relative St. dev. | Avg. ±St. dev. | Relative St. dev. | Avg. ±St. dev. | Relative St. dev. |
| Tap water | 21.2±0.3 | 1.6% | 6.97±0.07 | 1.1% | 239±12 | 5.2% |
| 10%Kaolin | 21.6±0.3 | 1.3% | 5.90±0.11 | 1.8% | 188±29 | 15.8% |
| 20%Kaolin | 21.2±0.3 | 1.4% | 5.08±0.03 | 0.6% | 150±18 | 12.1% |
| 40%Kaolin | 21.3±0.4 | 1.7% | 4.82±0.03 | 0.7% | 172±21 | 12.5% |
| 60%Kaolin | 21.2±0.2 | 1.0% | 4.74±0.03 | 0.7% | 173±12 | 7.2% |
| 100%Kaolin | 21.2±0.1 | 0.5% | 4.55±0.02 | 0.5% | 129±9 | 6.7% |

From Table 4.5, temperature measurements of the tap water and soil mixtures are mostly between 21 °C to 22 °C, and the relative standard deviations are less than 2%. The proportion of kaolin in the soil mixture affects the pH and conductivity values. The tap water used in specimen preparation was neutral (pH value around 7) and with conductivity measurements around 240 µS/cm. However, pH values decrease from around 6 to 4.5 as the kaolin content increases from 10% to 100% by weight. Although lower conductivities were measured in soil mixtures than in tap water, the trend of average conductivity measurements with increasing kaolin content is not as clear as the trend of pH values. One of the reasons is the larger uncertainty in conductivity measurements. While the relative standard deviations of pH values are smaller than 2%, the maximum relative standard deviation of conductivity measurements is close to 16%. Although the higher values of conductivity standard deviation are attributed to the fluctuating nature of conductivity measurements, they also indicate that the ionic strength has high spatial variation and the probe location in a specimen is important.

Due to the instrument uncertainty and spatial variation of conductivity and/or pH values, both the average values and standard deviations need to be considered when comparing different soil mixtures. Figure 4.5 shows the average measured pH and conductivity values, as well as the envelope curves of the average values plus/minus one standard deviation for the tap water and soil mixtures. From the figure, a general decreasing trend can be found in both pH values and conductivity with increasing kaolin content.
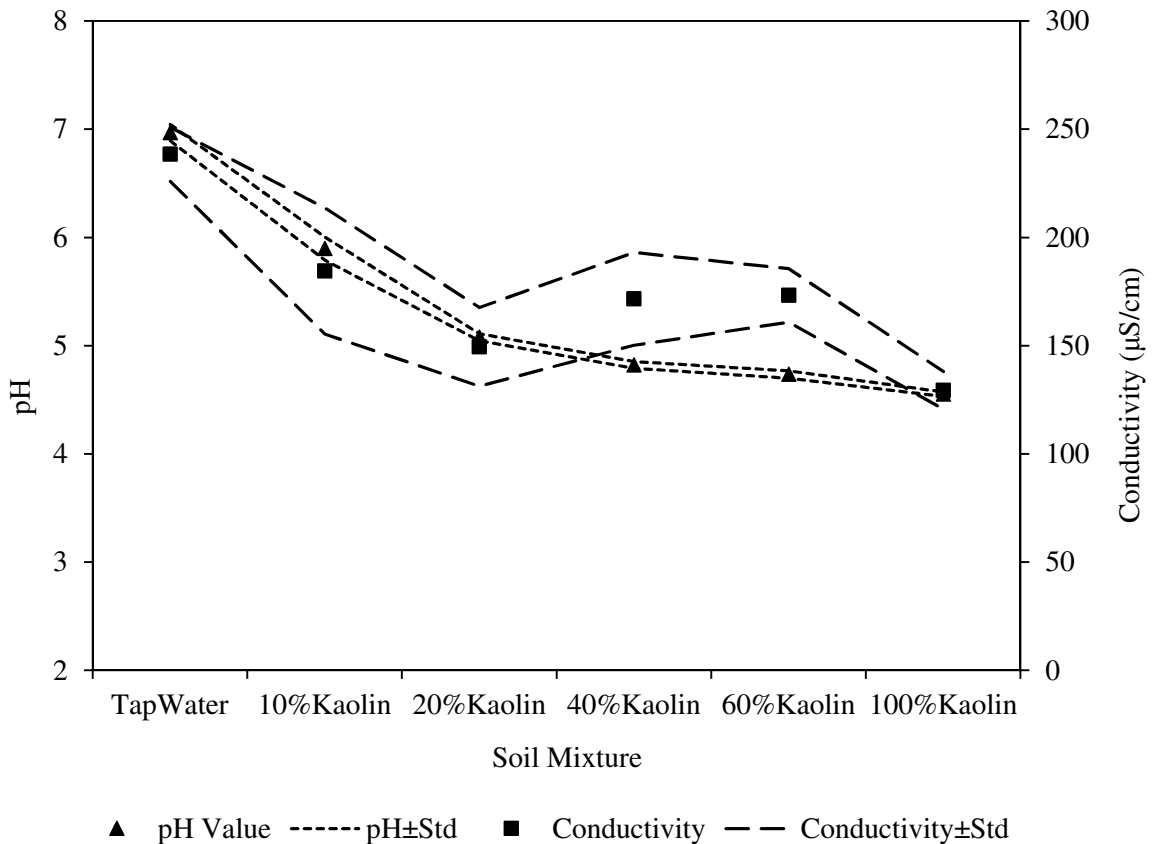


Figure 4.5 Variations of average pH and conductivity measurements (plotted with envelopes of standard deviations) with kaolin content in soil mixtures

## 4.2 Sediment Erosion Characteristics

### 4.2.1 Erosion Rates

Using equation 3.19, the erosion rate of a sediment layer was obtained by the product of sediment dry density and the thickness of eroded sediment layer per unit time ($\frac{\Delta D}{\Delta t}$) during each run of the flume experiments. Because erosion rate was found to depend on bulk density which varied with the depth of sediment layers, different erosion rates were obtained for sediments located at different depths from the surface for the same shear stress and kaolin content. Figure 4.6 illustrates the variations of erosion rate with the depth of sediments and under different bed shear stress conditions for each type of soil mixture containing 10%, 20%, 40%, 60%, and 100% kaolin proportions. As discussed previously, Figure 4.6(*e*) and 4.6(*f*) show the measured erosion rates for 100% kaolin specimens prepared with 160% and 100% initial water contents, respectively.
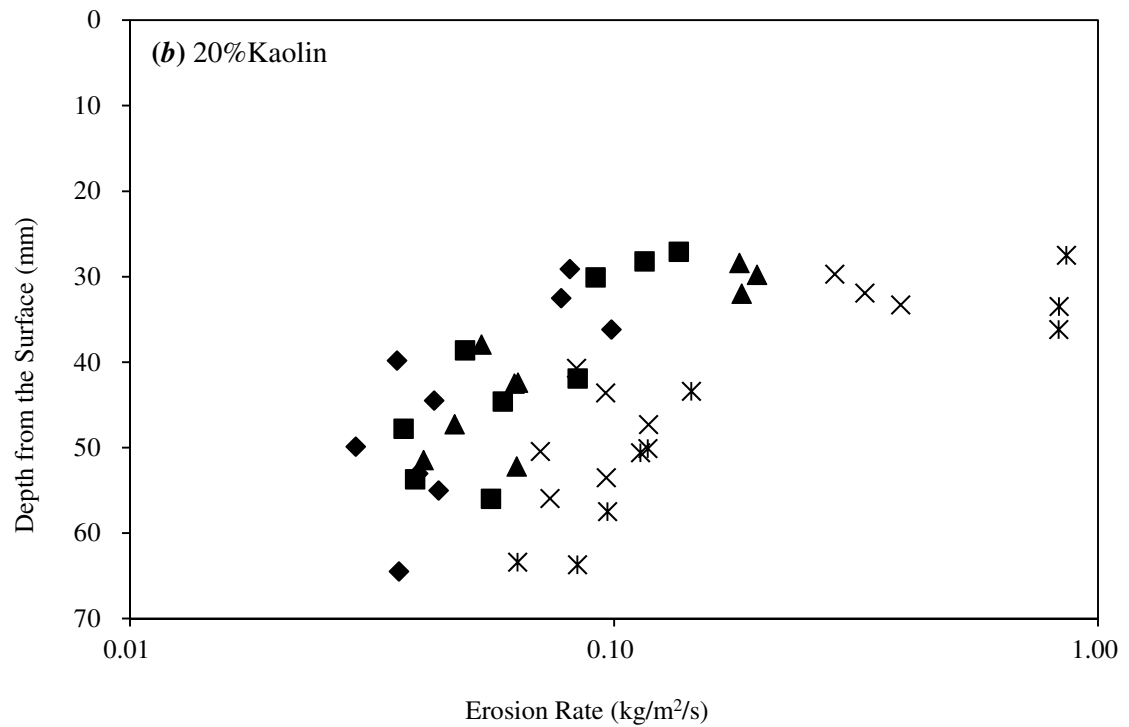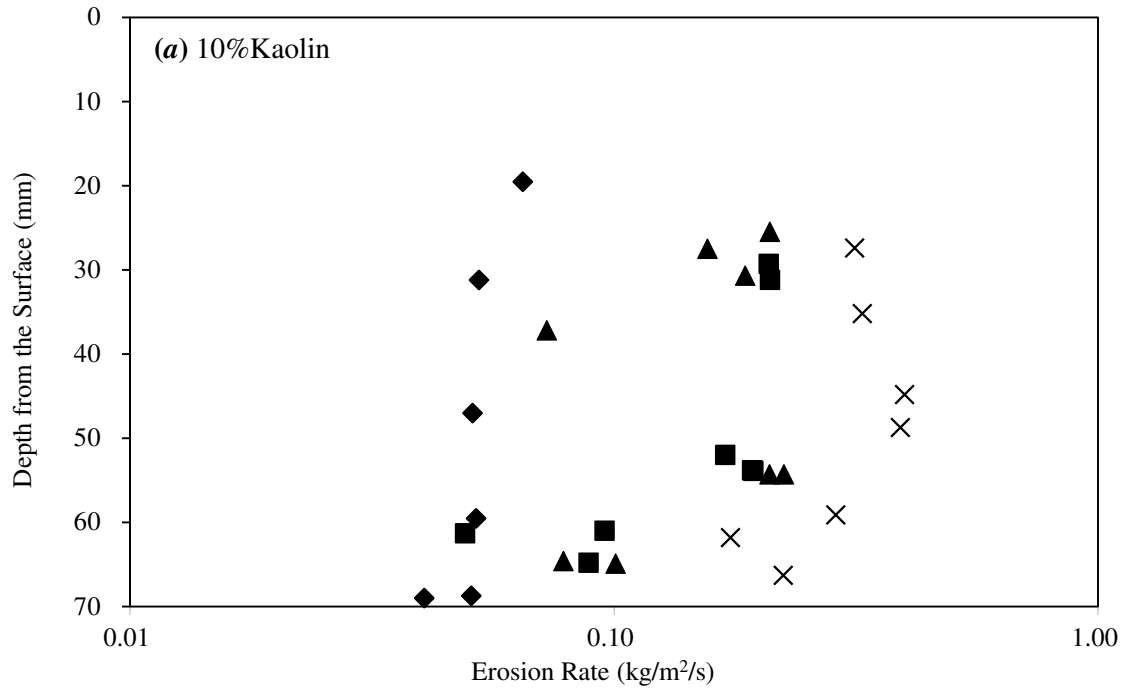
Figure 4.6 Measured erosion rates of the sediment layers locate at different depths from the surface of specimens with (*a*) 10% kaolin content, (*b*) 20% kaolin content, (*c*) 40% kaolin content, (*d*) 60% kaolin content, and (*e*) and (*f*) 100% kaolin content

135

(Figure 4.6 Continued)

136

(Figure 4.6 Continued)

137
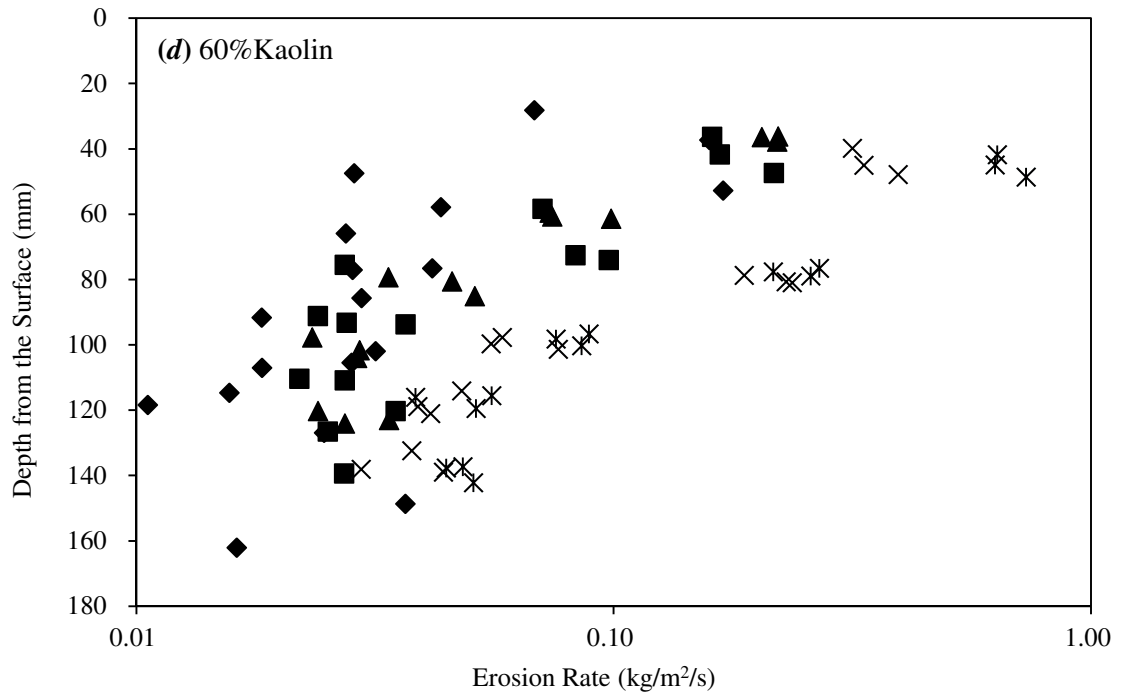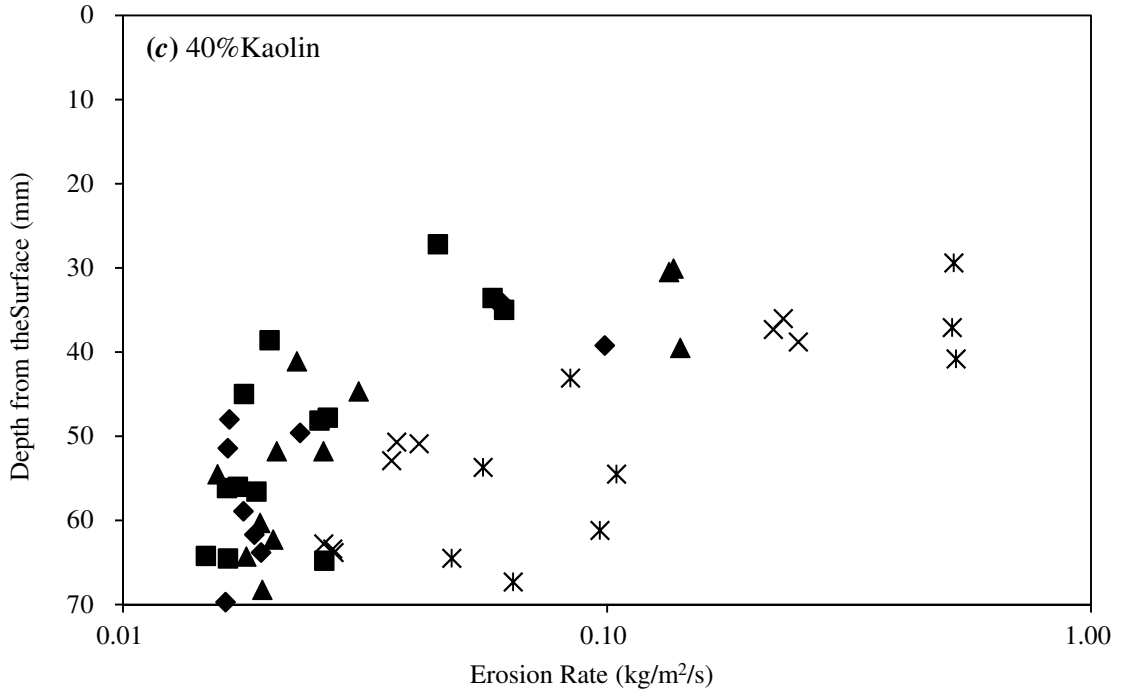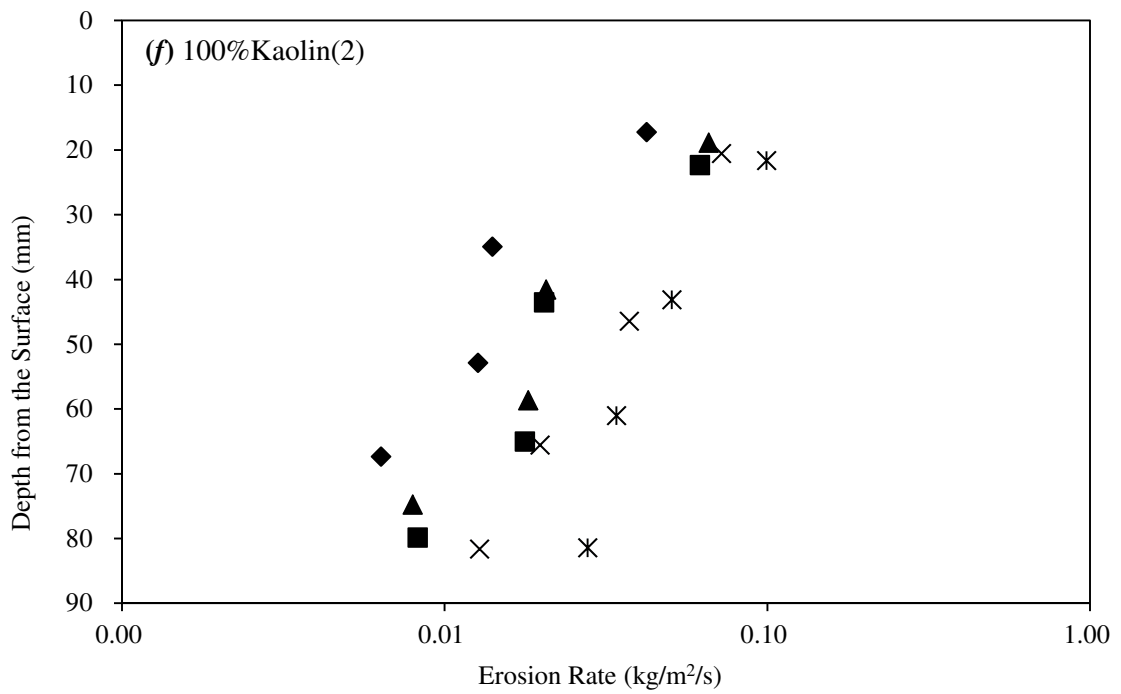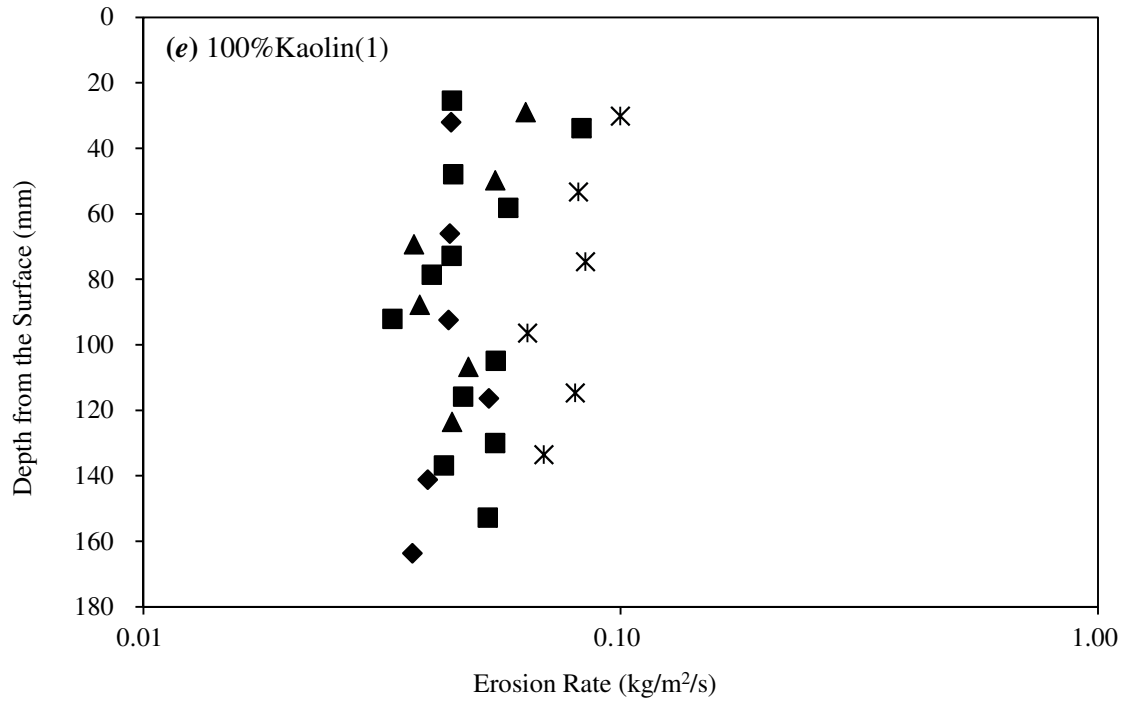
Generally, for all types of soil mixtures, erosion rate decreases as the depth of sediment layer increases since deeper sediment layers have higher bulk densities (Figure 4.1). Under a higher bed shear stress condition, higher erosion rates were observed for sediments located at similar depths (Figure 4.6). Magnitudes of the erosion rates range from 0.01 to 1.0 $kg/m^2/s$ for sediments containing 10% to 60% kaolin proportions. For sediments of 100% kaolin content, the measured erosion rates are generally smaller; they range from less than 0.01 $kg/m^2/s$ to 0.1 $kg/m^2/s$. For sediments containing 20%, 40%, and 60% kaolin proportions (Figure 4.6($b$) to ($d$)), the increase in erosion rates under conditions of increasing bed shear stress is greater for shallow sediment layers, especially the top layers of sediments; the erosion rates tend to collapse to the same order of magnitude as deeper sediments are eroded. This convergence of the data points suggests that the critical shear stress of the bottom layer sediments of 20% to 60% kaolin content specimens may have similar values which are smaller than but close to 2 Pa.

The measured erosion rate was plotted versus the applied bed shear stress for each sediment layer of different types of soil mixtures. Although three replicated flume experiment runs were conducted for each specimen, results from only one of the replicates for each combination are illustrated in Figure 4.7 as examples. The Gauss-Newton algorithm was applied to obtain the best-fit parameters of equation 2.17, i.e. $E = M(\tau - \tau_c)^n$ for each series of data associated with different values of shear stress applied to each layer of the specimen. The best-fit nonlinear curves are shown in Figure 4.7 as well.
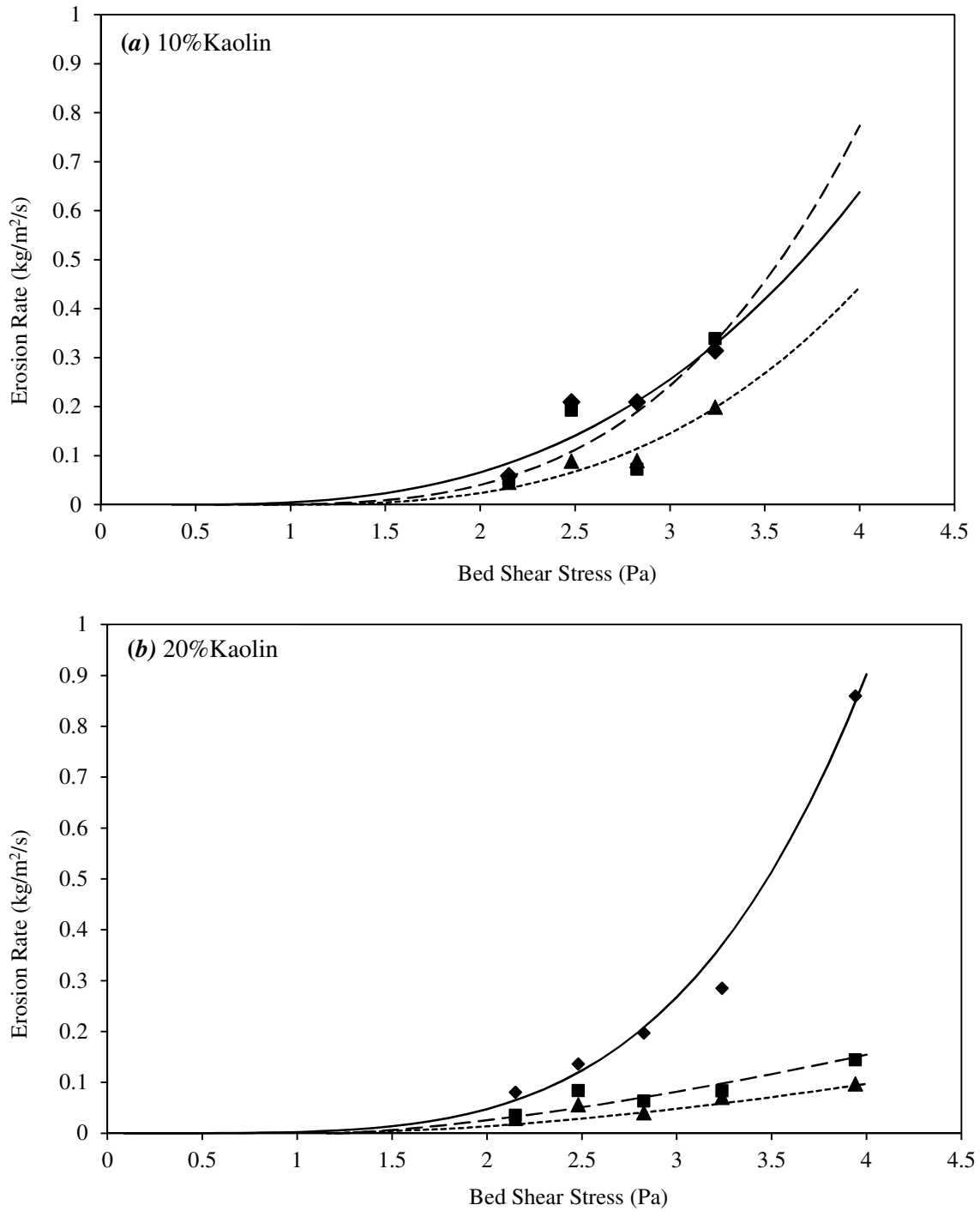
Figure 4.7 Measured erosion rates of sediment layers of soil mixtures with (*a*) 10% kaolin content, (*b*) 20% kaolin content, (*c*) 40% kaolin content, (*d*) 60% kaolin content, and (*e*) and (*f*) 100% kaolin content; under different bed shear stress conditions

(Figure 4.7 Continued)

140

(*e*) 100%Kaolin(1)

(*f*) 100%Kaolin(2)

◆  Top layer ——— Top layer-fit ■ Middle1 layer — — — Middle1 layer-fit

●  Middle2 layer — · — · Middle2 layer-fit ▲ Bottom layer ------- Bottom layer-fit
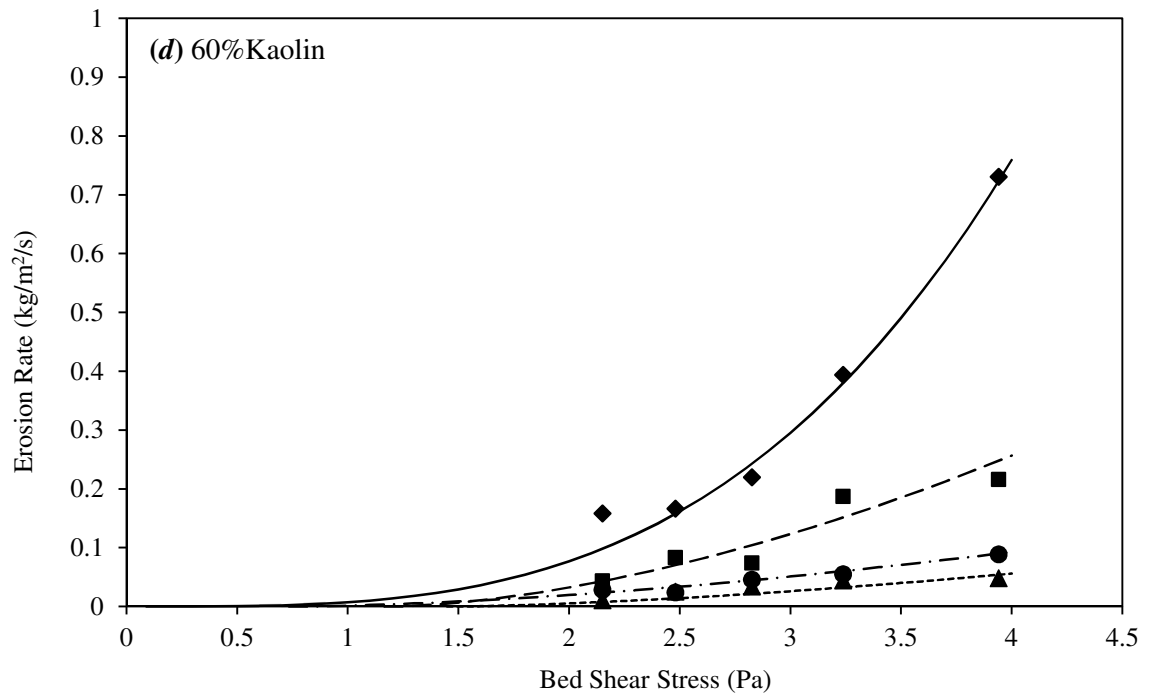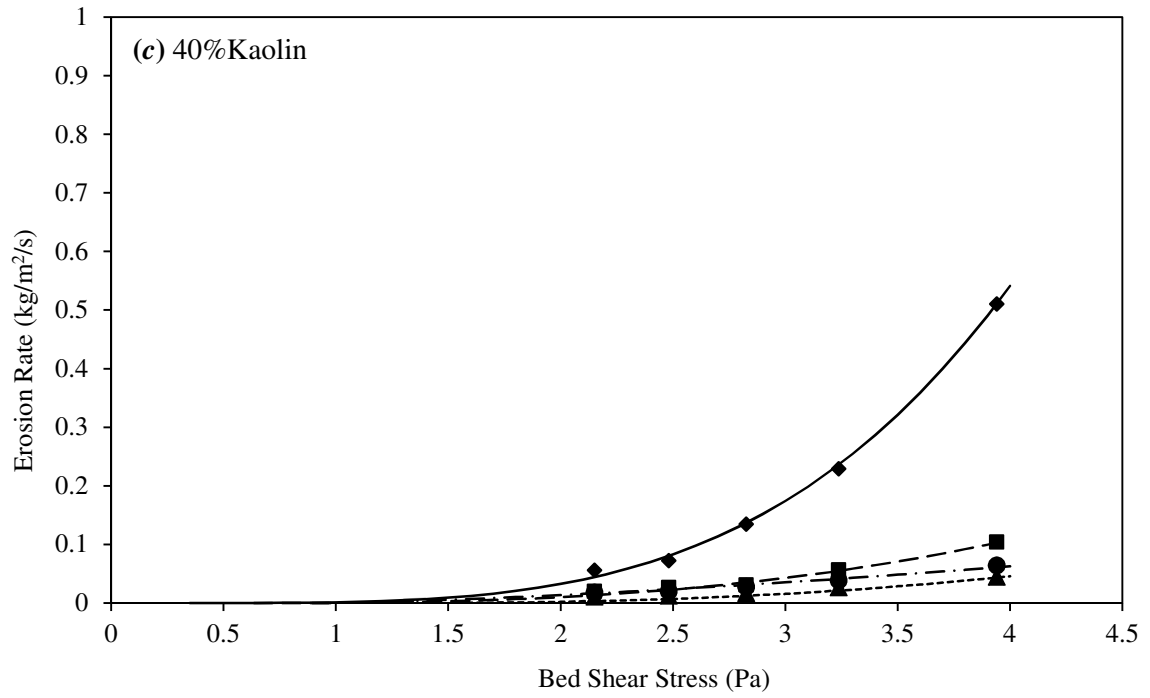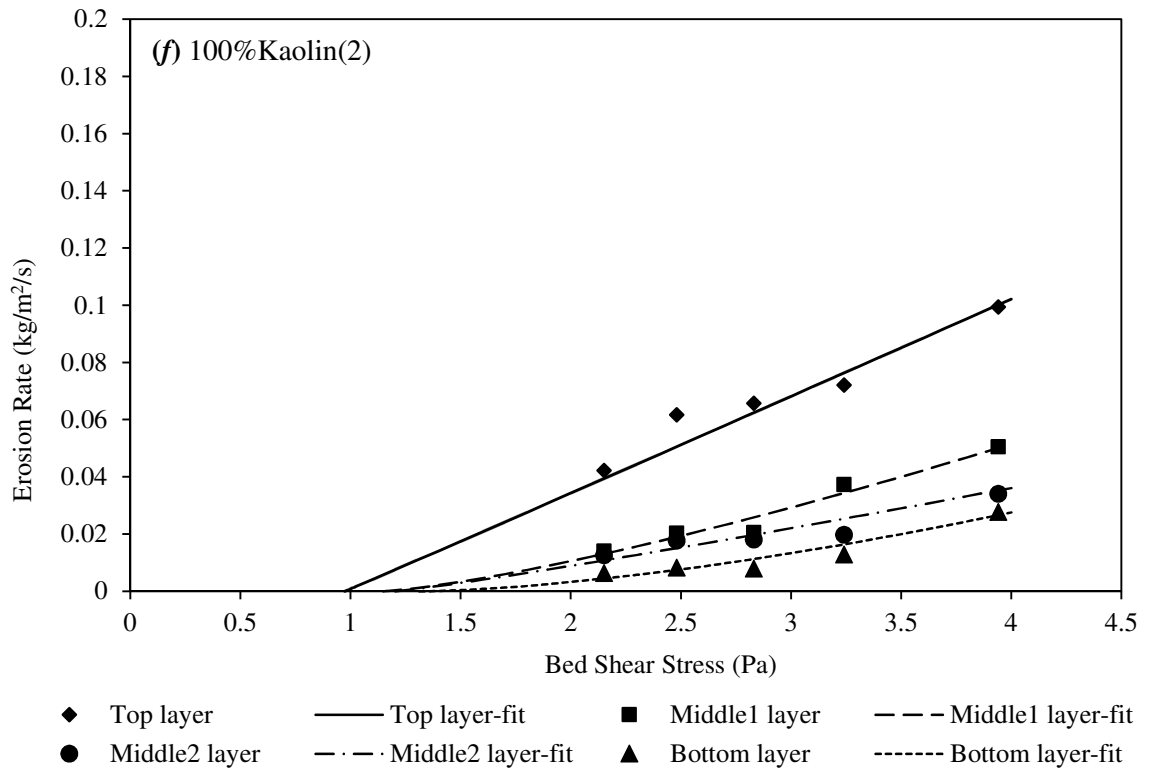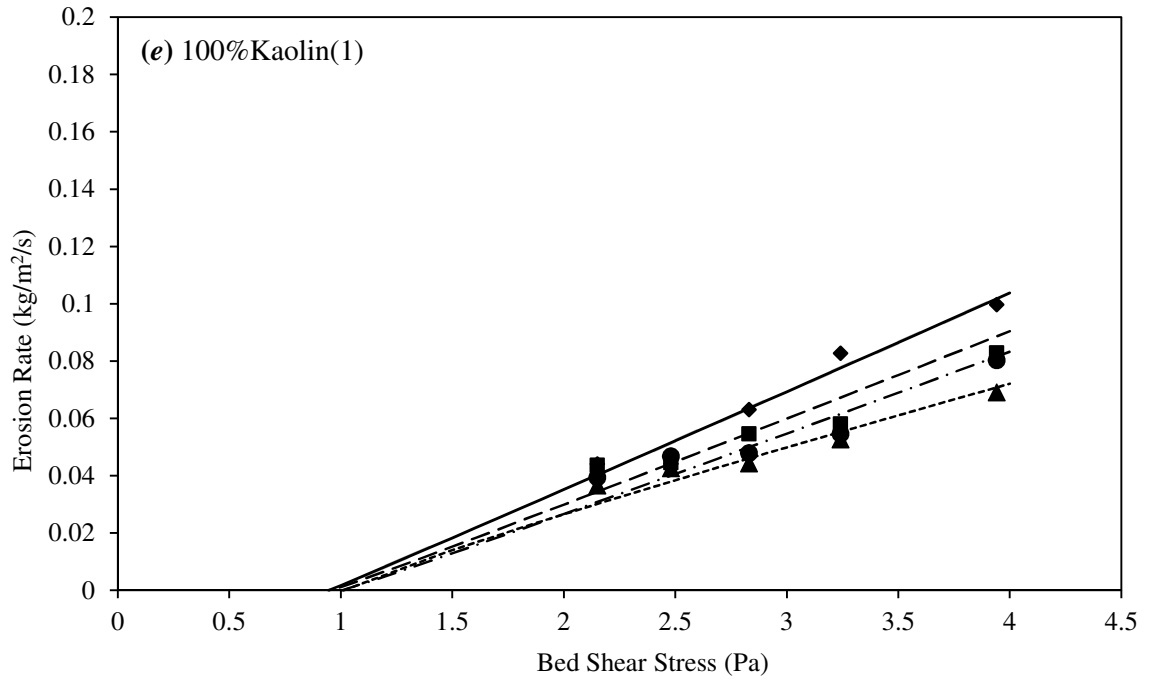
(Figure 4.7 Continued)

From Figure 4.7(*a*) to (*d*), a concave curve is observed in each series of data of sediments with 10% to 60% kaolin contents, and this nonlinear relationship indicates that the sediments were eroded more rapidly when subjected to a larger bed shear stress. Among the curves, data series of the top layers of 20%, 40%, and 60% kaolin content sediments show a significant deviation from the curves of the other layers in the same specimen; that is, a trend of concave up occurs when the bed shear stress exceeds 2.5 Pa. Data series of 100% kaolin specimens generally exhibit erosion rates that are almost one order of magnitude smaller than those of the other types of specimens. In addition, instead of a concave-up curve, a linear relationship between the erosion rate and bed shear stress, which ranges from 2 to 4 Pa, is mostly found in the sediments of 100% kaolin content (Figure 4.7(*e*) and (*f*)).

To validate the precision of the Gauss-Newton algorithm for parameter optimization of nonlinear relationships, the fitted erosion rates were calculated by substituting different values of bed shear stress into equation 2.17 with values of $M$, $n$, and $\tau_c$ obtained from the Gauss-Newton algorithm. Figure 4.8 shows the fitted erosion rates ( $E_{fit}$ ) plotted against measured erosion rates ( $E_{measure}$ ) of the soil mixture specimens with different kaolin contents used in this study. Using the least-squares regression, the linear relationship between $E_{fit}$ and $E_{measure}$ was found to be:

$$E_{fit} = 0.984 E_{measure} \tag{4.9}$$

The coefficient of determination $R^2 = 0.98$ and the standard error $SE = \pm 0.025 \, \text{kg/m}^2/\text{s}$, both of which indicate the high precision of the Gauss-Newton algorithm used for nonlinear fitting of equation 2.17.
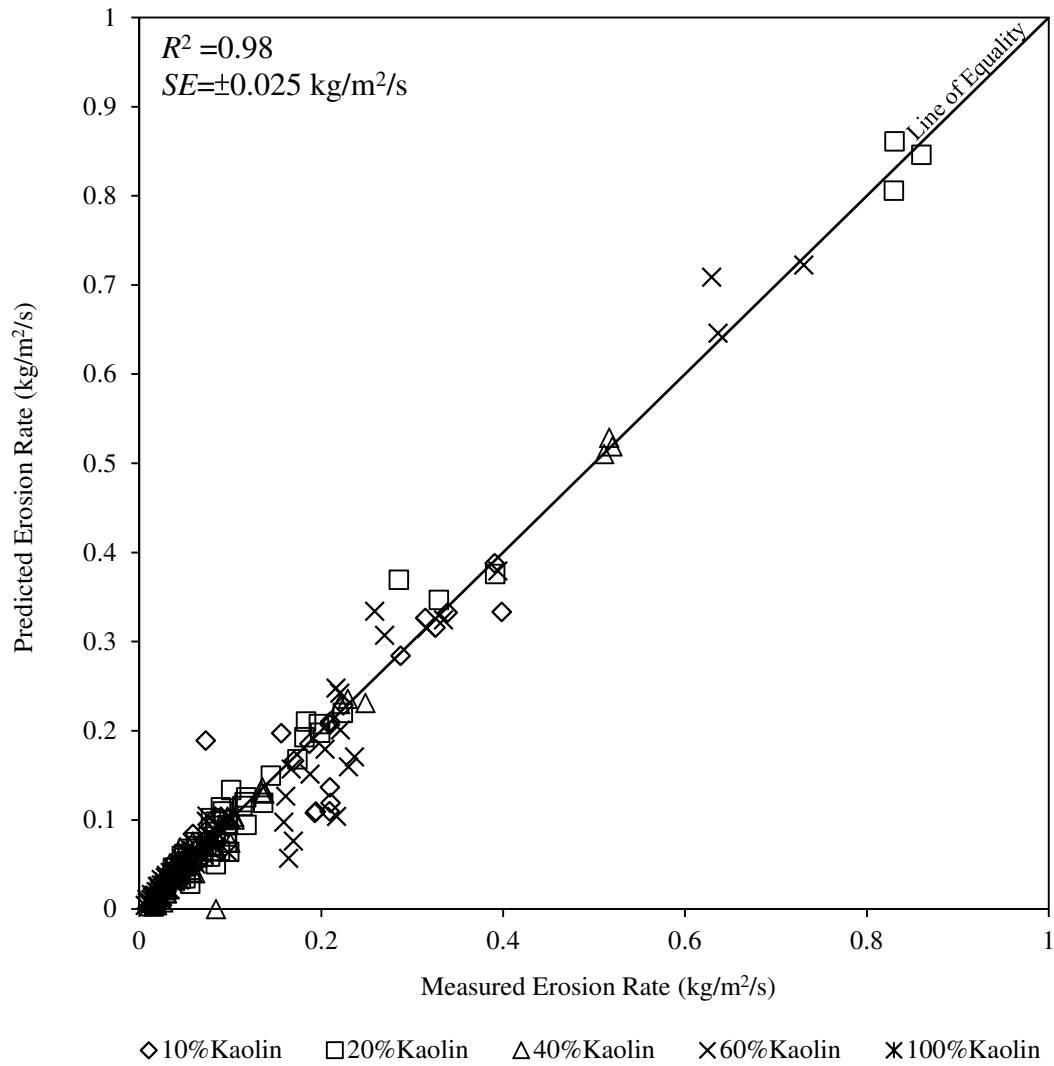
Figure 4.8 Predicted erosion rates versus measured erosion rates of soil mixtures containing different kaolin proportions.

## 4.2.2 Erosion Constants and Critical Shear Stress

Using the Gauss-Newton algorithm, erosion constants ($M$ and $n$) and the critical shear stress ($\tau_c$) of the best-fit nonlinear relationship (equation 2.17) of measured erosion rates for each layer of a soil specimen under different bed shear stress conditions were obtained. For soil specimens with 10%, 20%, 40%, and 60% kaolin contents, three

replicated runs of flume experiments were conducted for each layer of the specimens, which resulted in three sets of erosion constants and critical shear stresses for each of top, middle1, middle2, and bottom layers of soil specimens with the same kaolin content. For each of the three sets of erosion constants, the mean and standard deviation (St. dev.) were calculated and are shown in Table 4.6. Only one run was made for each of the 100% kaolin specimens as shown in Table 4.6.

For all the soil specimens used in the flume experiments, values of $M$ fall in the range between $5\times10^{-3}$ and $5\times10^{-2}$; the standard deviations are an order of magnitude smaller than the mean values of $M$. The values of $n$, which indicates the power on the difference between the applied bed shear stress and the critical shear stress, are either greater than or close to unity. From Table 4.6, the values of $n$ suggest that an obvious nonlinear relationship (concave-up) between erosion rate and bed shear stress is generally found in soil specimens containing 10% to 40% kaolin contents. On the other hand, the relationship between erosion rate and bed shear stress tends to be linear within the range of bed shear stress from 2 Pa to 4 Pa, as the kaolin content in soil specimens increases to 60% and then to 100% by weight. Although the best-fit equation of the bottom layer of 100%Kaolin(1) specimen shows a slightly convex curve with its $n$ value of 0.9, a linear relationship between erosion rate and bed shear stress may still be considered to be suitable for this layer within the expected experimental uncertainty.

Table 4.6 Statistics of erosion constants of soil specimens with different kaolin contents

| Specimen type | Layer | $M$ value | | $n$ value | |
|---|---|---|---|---|---|
| | | Mean | St. dev. | Mean | St. dev. |
| 10% Kaolin | Top | $1.08 \times 10^{-2}$ | $\pm 6.28 \times 10^{-3}$ | 2.89 | $\pm 0.07$ |
| | Middle | $1.80 \times 10^{-2}$ | $\pm 6.65 \times 10^{-3}$ | 4.09 | $\pm 0.11$ |
| | Bottom | $1.36 \times 10^{-2}$ | $\pm 1.19 \times 10^{-3}$ | 1.17 | $\pm 0.37$ |
| 20% Kaolin | Top | $3.63 \times 10^{-3}$ | $\pm 9.45 \times 10^{-4}$ | 1.01 | $\pm 0.54$ |
| | Middle | $4.24 \times 10^{-2}$ | $\pm 2.35 \times 10^{-2}$ | 3.98 | $\pm 0.33$ |
| | Bottom | $3.99 \times 10^{-2}$ | $\pm 1.95 \times 10^{-2}$ | 2.89 | $\pm 0.26$ |
| 40% Kaolin | Top | $3.88 \times 10^{-3}$ | $\pm 1.77 \times 10^{-3}$ | 2.21 | $\pm 0.80$ |
| | Middle1 | $3.23 \times 10^{-3}$ | $\pm 9.84 \times 10^{-4}$ | 2.21 | $\pm 0.83$ |
| | Middle2 | $6.65 \times 10^{-3}$ | $\pm 5.50 \times 10^{-3}$ | 3.54 | $\pm 0.41$ |
| | Bottom | $7.65 \times 10^{-3}$ | $\pm 8.26 \times 10^{-3}$ | 2.28 | $\pm 0.52$ |
| 60% Kaolin | Top | $6.43 \times 10^{-3}$ | $\pm 3.20 \times 10^{-3}$ | 1.40 | $\pm 0.30$ |
| | Middle1 | $2.63 \times 10^{-2}$ | $\pm 1.57 \times 10^{-2}$ | 1.14 | $\pm 0.34$ |
| | Middle2 | $2.11 \times 10^{-2}$ | $\pm 1.16 \times 10^{-2}$ | 1.01 | $\pm 0.01$ |
| | Bottom | $1.87 \times 10^{-2}$ | $\pm 5.02 \times 10^{-3}$ | 1.17 | $\pm 0.19$ |
| 100% Kaolin(1) [a] | Top | $3.33 \times 10^{-2}$ | -- | 1.02 | -- |
| | Middle1 | $2.87 \times 10^{-2}$ | -- | 1.03 | -- |
| | Middle2 | $2.68 \times 10^{-2}$ | -- | 1.03 | -- |
| | Bottom | $2.69 \times 10^{-2}$ | -- | 0.90 | -- |
| 100% Kaolin(2) [a] | Top | $3.34 \times 10^{-2}$ | -- | 1.01 | -- |
| | Middle1 | $1.31 \times 10^{-2}$ | -- | 1.31 | -- |
| | Middle2 | $1.15 \times 10^{-2}$ | -- | 1.11 | -- |
| | Bottom | $5.90 \times 10^{-3}$ | -- | 1.56 | -- |

[a] Two different initial water contents were used to prepare 100% kaolin specimens, 160%$w$ for 100%Kaolin(1) and 100%$w$ for 100%Kaolin(2). There is no standard deviation of $M$ or $n$ value of 100% kaolin specimens since only one run of flume experiment was conducted for each layer of 100% Kaolin(1)or (2) under one bed shear stress condition.

Figure 4.9 shows the bar charts of mean values of $M$ and $n$ describing the erosion equations of soil specimens with 10% to 100% kaolin contents. From the upper bar chart in Figure 4.9($a$), the variations of $M$ values between layers do not show a specific trend except for the $M$ values of 100% kaolin specimens. In both types of the 100% kaolin specimens, the $M$ value of the top layer is the highest compared to the other layers in the same specimen, and then the $M$ value decreases for deeper sediment layers, i.e. the middle1, middle2, and bottom layers. The lower bar chart in Figure 4.9($b$) shows a decreasing trend of $n$ value from top to bottom layers in most of the soil specimens in general. All of the top layers of 10% to 60% kaolin specimens have a value of $n$ larger than 3, which are illustrated in the concave curves in Figure 4.7(a) to ($d$). The variations of $n$ values among different layers of 100% kaolin specimens do not show a significant trend but are considered as fluctuations around unity caused by experiment uncertainties.
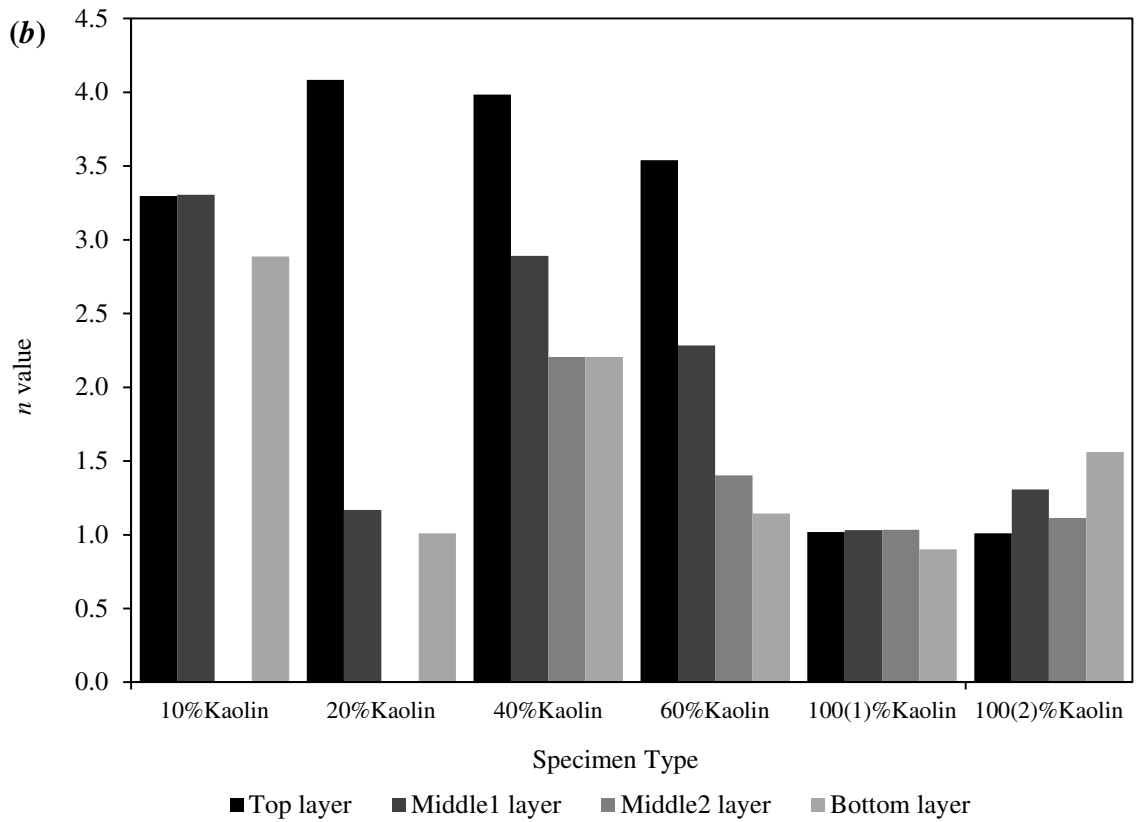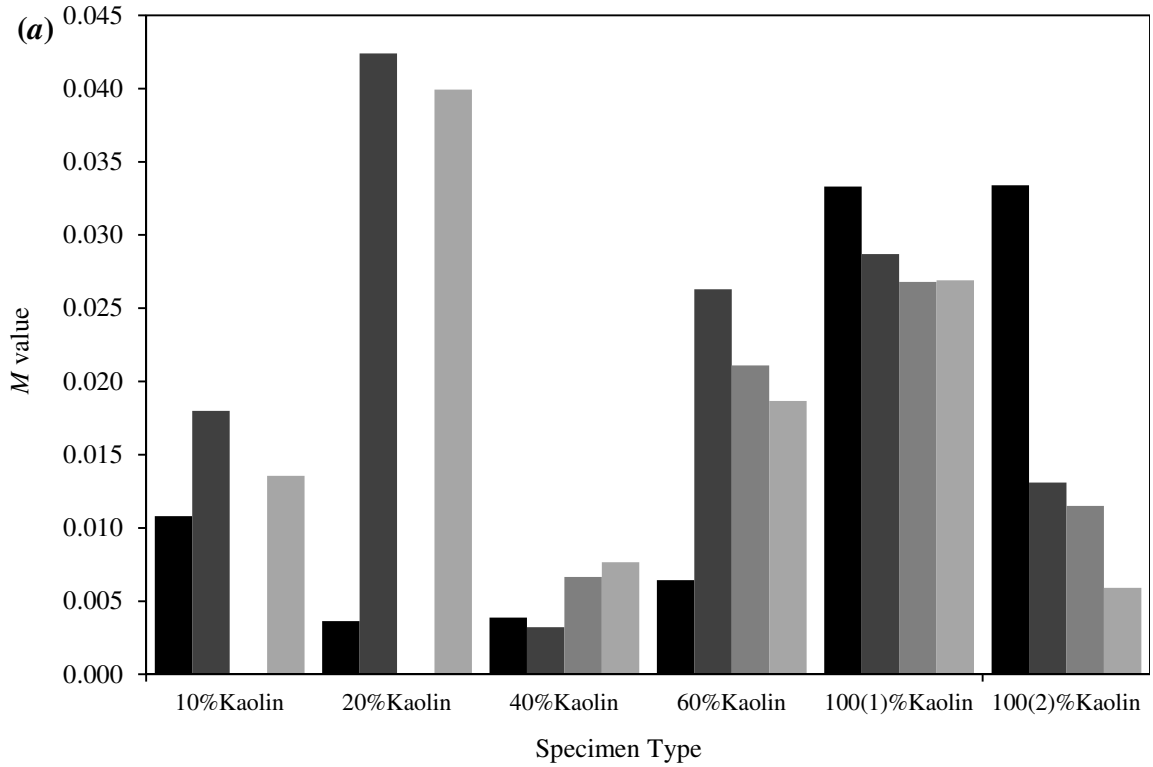
Figure 4.9 Mean of the erosion constants: (*a*) *M* value and (*b*) *n* value of each layer of soil specimens with different kaolin contents

One of the most important erosion parameters sought in this study is the critical shear stress ($\tau_c$), which was determined as the shear stress at which the best-fit curve of erosion rate versus bed shear stress intersects with the line of zero erosion rate. Values of $\tau_c$ and the average water content and bulk density of the corresponding sediment layers obtained from the experiments are listed in Table 4.7. In order to investigate the variance of $\tau_c$ between different layers for varying kaolin contents of the sediment mixtures, the average $\tau_c$ of each the three replicated runs was calculated and plotted in Figure 4.10. Values of critical shear stress of the soil mixture specimens used in this study range from 0.05 Pa to 1.8 Pa (Table 4.7), and the average $\tau_c$ increases with depth of the sediment layer in the mixtures with the same kaolin content (Figure 4.10).

Although the average value of $\tau_c$ shows the same increasing trend between layers for each soil mixture, the slope of this increasing trend is different between the silt-clay soil mixtures and 100% kaolin sediments. Specifically, the average $\tau_c$ increases as much as one order of magnitude from the top to the bottom layers in silt-clay soil mixtures, *i.e.* 10% to 60% kaolin content specimens. In contrast, the increment of average $\tau_c$ between sediment layers is much smaller for 100% kaolin content specimens. Based on the variations of sediment water content and bulk density of different sediment layers that have been described in section 4.4.1, $\tau_c$ of sediments is found to increase with bulk density (decrease with water content) of soil mixtures containing the same kaolin content. For sediments with similar bulk densities (water contents), $\tau_c$ increases with the increase of kaolin content in the soil mixtures (Table 4.7).

To estimate the overall relative experimental uncertainty in $\tau_c$ from the replicates, the coefficient of variation (CV) of values of $\tau_c$ was calculated for each sediment layer of the specimens with different kaolin contents:

$$CV_{\tau_c} = \frac{\sigma_{\tau_c}}{\mu_{\tau_c}} \tag{4.10}$$

where $\mu_{\tau_c}$ = mean of $\tau_c$ values and $\sigma_{\tau_c}$ = standard deviation of $\tau_c$ values from the replicates for each sediment layer. Although there are a few values of $\tau_c$ that appear to be outliers (Table 4.7), values of $CV_{\tau_c}$ for most of the sediment layers fall in the range between 10% to 20%. Overall, the average $CV_{\tau_c}$ of $\tau_c$ values for all the specimens is around 15%.

Table 4.7 Critical Shear Stress, water content, and bulk density of soil specimens

| Specimen type/ layer | Trial | Critical shear stress (Pa) | Water content (%w) | Bulk density (kg/m³) |
|---|---|---|---|---|
| 10% Kaolin Top | 1 | 0.0575 | 79.9 ± 4.1 | 1528 ± 18 |
| | 2 | 0.4903 | 76.5 ± 3.0 | 1544 ± 14 |
| | 3 | 0.3762 | 74.3 ± 11 | 1554 ± 50 |
| 10% Kaolin Middle | 1 | 0.8656 | 44.9 ± 3.5 | 1752 ± 30 |
| | 2 | 0.6008 | 45.8 ± 5.6 | 1743 ± 47 |
| | 3 | 0.6415 | 48.7 ± 2.0 | 1718 ± 16 |
| 10% Kaolin Bottom | 1 | 0.7016 | 35.5 ± 1.0 | 1849 ± 12 |
| | 2 | 0.8125 | 37.6 ± 1.0 | 1824 ± 11 |
| | 3 | 0.9205 | 37.3 ± 1.0 | 1828 ± 11 |
| 20% Kaolin Top | 1 | 0.0891 | 65.9 ± 2.7 | 1598 ± 15 |
| | 2 | 0.0956 | 66.2 ± 3.8 | 1596 ± 21 |
| | 3 | 0.2163 | 66.4 ± 2.9 | 1595 ± 16 |
| 20% Kaolin Middle | 1 | 1.1947 | 60.7 ± 2.5 | 1629 ± 16 |
| | 2 | 0.5982 | 60.8 ± 1.5 | 1629 ± 10 |
| | 3 | 1.6992 | 59.5 ± 3.9 | 1637 ± 25 |
| 20% Kaolin Bottom | 1 | 1.1571 | 54.0 ± 2.9 | 1675 ± 20 |
| | 2 | 1.4720 | 54.5 ± 2.4 | 1672 ± 17 |
| | 3 | 1.7527 | 54.1 ± 2.1 | 1674 ± 15 |
| 40% Kaolin Top | 1 | 0.3370 | 103.4 ± 4.1 | 1437 ± 12 |
| | 2 | 0.1111 | 104.3 ± 2.7 | 1434 ± 8 |
| | 3 | 0.1282 | 103.5 ± 3.5 | 1437 ± 10 |
| | 4[b] | 0.3503 | 103.0 ± 1.4 | 1438 ± 4 |
| 40% Kaolin Middle1 | 1 | 0.5342 | 93.8 ± 5.3 | 1469 ± 18 |
| | 2 | 0.7034 | 92.8 ± 2.9 | 1472 ± 10 |
| | 3 | 0.7344 | 94.3 ± 4.4 | 1467 ± 15 |
| | 4[b] | 0.6357 | 93.9 ± 1.2 | 1469 ± 4 |
| 40% Kaolin Middle2 | 1 | 0.6001 | 84.6 ± 3.5 | 1504 ± 14 |
| | 2 | 0.8411 | 83.3 ± 3.0 | 1509 ± 12 |
| | 3 | 1.3004 | 81.9 ± 5.2 | 1515 ± 22 |
| | 4[b] | 0.8954 | 87.0 ± 1.3 | 1494 ± 5 |

*(Table 4.7 continued)*

| | | | | |
|---|---|---|---|---|
| 40% Kaolin Bottom | 1 | 1.2828 | $79.0 \pm 2.8$ | $1528 \pm 12$ |
| | 2 | 1.0011 | $75.1 \pm 3.6$ | $1546 \pm 17$ |
| | 3 | 1.5828 | $76.7 \pm 4.9$ | $1538 \pm 22$ |
| | $4^b$ | 1.2067 | $73.7 \pm 1.8$ | $1553 \pm 9$ |
| 60% Kaolin Top | 1 | 0.0897 | $164.0 \pm 8.8$ | $1305 \pm 13$ |
| | 2 | 0.1083 | $164.8 \pm 9.0$ | $1304 \pm 13$ |
| | 3 | 0.0783 | $163.1 \pm 8.7$ | $1306 \pm 13$ |
| 60% Kaolin Middle1 | 1 | 1.1650 | $141.5 \pm 9.2$ | $1343 \pm 17$ |
| | 2 | 0.8162 | $142.6 \pm 9.9$ | $1341 \pm 18$ |
| | 3 | 0.8579 | $142.1 \pm 15$ | $1342 \pm 26$ |
| 60% Kaolin Middle2 | 1 | 0.7348 | $130.5 \pm 6.5$ | $1365 \pm 14$ |
| | 2 | 1.3347 | $125.9 \pm 7.5$ | $1375 \pm 16$ |
| | 3 | 0.9077 | $126.7 \pm 12$ | $1374 \pm 26$ |
| 60% Kaolin Bottom | 1 | 1.4487 | $97.4 \pm 6.2$ | $1454 \pm 20$ |
| | 2 | 1.6021 | $97.2 \pm 6.6$ | $1455 \pm 21$ |
| | 3 | 1.3473 | $94.0 \pm 6.2$ | $1276 \pm 7$ |
| 100% Kaolin(1)$^a$ | Top | 0.9445 | $182.8 \pm 5.6$ | $1277 \pm 9$ |
| | Middle1 | 0.9951 | $182.2 \pm 7.3$ | $1298 \pm 12$ |
| | Middle2 | 1.0030 | $166.7 \pm 8.5$ | $1314 \pm 7$ |
| | Bottom | 1.0125 | $156.3 \pm 4.3$ | $1388 \pm 6$ |
| 100% Kaolin(2)$^a$ | Top | 0.9738 | $119.1 \pm 2.4$ | $1403 \pm 3$ |
| | Middle1 | 1.1479 | $113.3 \pm 1.3$ | $1406 \pm 11$ |
| | Middle2 | 1.2031 | $112.1 \pm 4.4$ | $1413 \pm 8$ |
| | Bottom | 1.3125 | $109.5 \pm 2.8$ | $1276 \pm 7$ |

[a] Two different initial water contents were used to prepare 100% kaolin specimens, $w$=160% for 100%Kaolin(1) and $w$ =100% for 100%Kaolin(2). Only one experimental run was conducted for each layer of 100% Kaolin(1)or (2) under one bed shear stress condition.

[b] This run was conducted in winter (December 2011) while all others were conducted during spring or summer (May to August 2011). Result of the fourth run of flume experiment shows that temperature effect on the critical shear stress is insignificant.
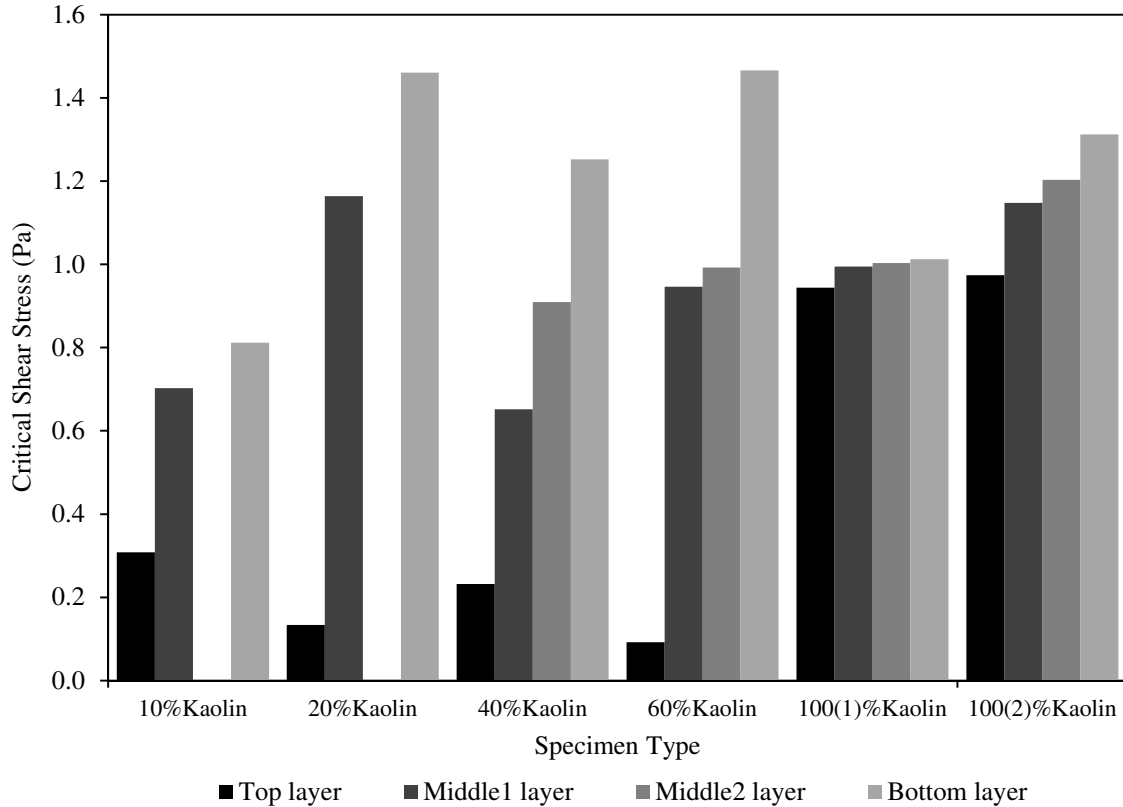
Figure 4.10 Mean of the critical shear stress of each layer of soil specimens with different kaolin contents

## 4.3 Sediment Rheological Characteristics

### 4.3.1 Flow Curves

Soil specimens were prepared, sectioned by extrusion in the flume apparatus, and then preserved in plastic soil specimen containers for subsequent rheological analysis. The plastic containers were securely sealed to prevent potential loss of water content from the soil specimens. Before a rheometer test started, the soil specimens were re-mixed by the blender, and then settled naturally in the rheometer cup for 24 hours. During the rheometer tests, shear stress, shear strain, and strain rate were measured and recorded by the rheometer with the stress-control testing procedure as described in

section 3.4. By plotting the shear stress versus the strain rate, the flow curve of a specimen is obtained. Figure 4.11 shows the measured flow curves of some selected specimens with different bulk densities and kaolin contents.
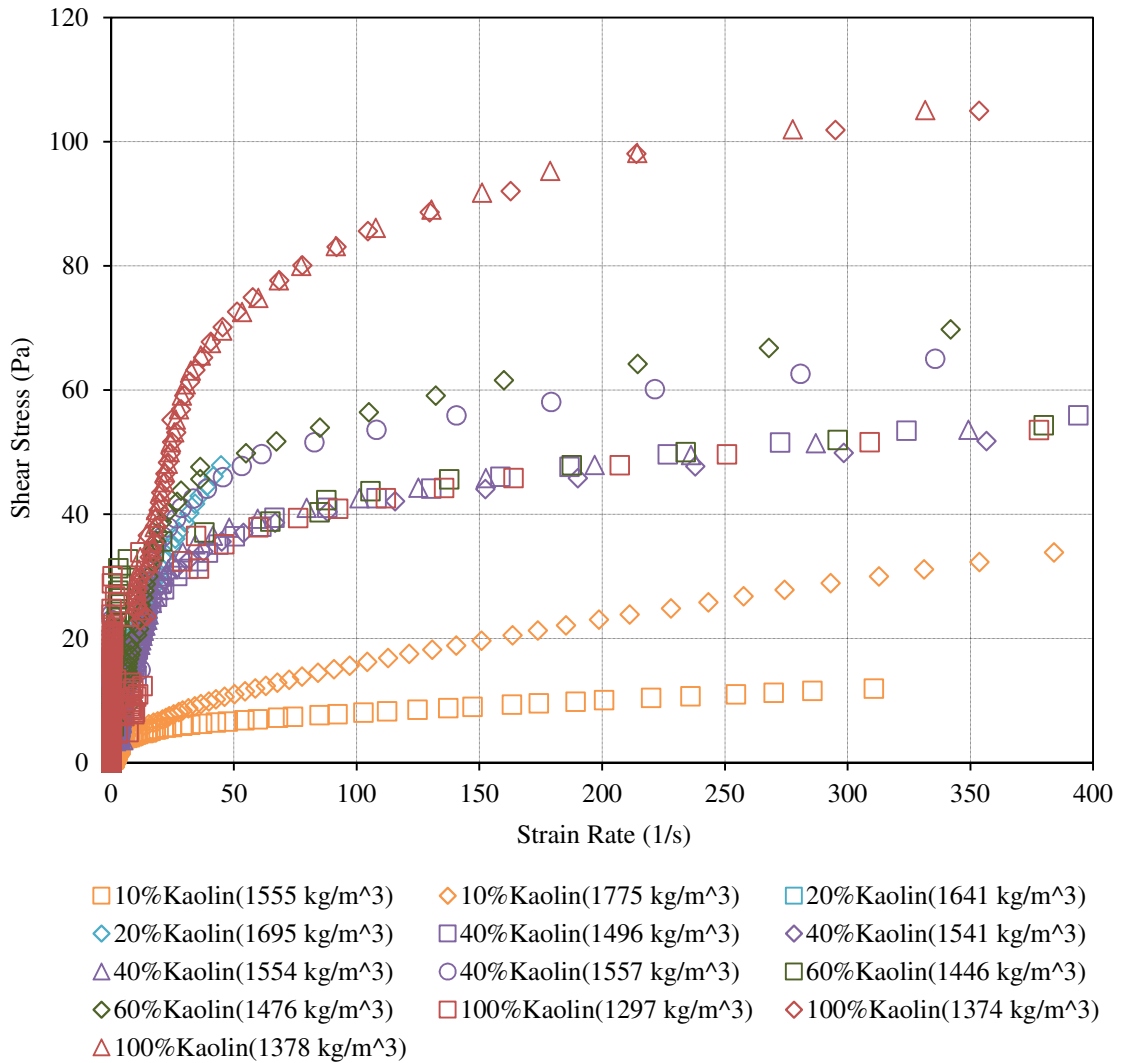


Figure 4.11 Measured flow curves of soil mixtures containing different kaolin proportions from rheometer tests

From Figure 4.11, the flow curves show convex trends suggesting the shear-thinning behavior of the soil mixtures in this study. This shear-thinning behavior can be approximated by a stepwise linear relationship consisting of two linear stress-strain rate lines with different slopes corresponding to the low and high strain rate regions, respectively. Generally, the flow curves start with a linear relationship between shear stress and strain rate in the low shear stress range and transition to another linear relationship with a smaller slope in the high shear stress range. When the shear stress is less than 20 Pa, many of the specimens have measured strain rates close to zero which indicates that a yield point can be determined for the specimens. In other words, the yield stress, a threshold of shear stress below which no strain rate can be detected by the experimental apparatus, may be determined in the range of shear stress smaller than 20 Pa for the soil mixtures in this study.

Comparison among specimens with different kaolin contents shows that to strain the specimens at the same rate, a larger shear stress is required when the specimen has a higher proportion of Georgia kaolin. For instance, a shear stress around 20 Pa is more than sufficient to strain 10% kaolin specimens at $100 \text{ s}^{-1}$; however, a shear stress close to 60 Pa is required to strain 40% or 60% kaolin specimens at the same rate. If the specimens contain the same kaolin content but have different bulk densities, and they are strained at the same rate, the applied shear stress is larger for the specimen with the higher bulk density. Therefore, it can be concluded that soil mixtures with higher kaolin content and/or higher bulk density require a larger shear stress to achieve the same strain rate, which implies a larger yield resistance or yield stress of the soil mixtures.

### 4.3.2 Yield Stress

In this study, three types of yield stress were determined from the shear strain-shear stress and shear stress-strain rate relationships by the methods demonstrated in Figure 3.14 to Figure 3.16. Specifically, the lower ($\tau_{y1}$) and upper ($\tau_{y2}$) yield stresses were determined by the graphical methods suggested by the rheometer manufacturer (Figure 3.14 and Figure 3.15). Determination of the yield stress ($\tau_y$) as illustrated in Figure 3.16 was based on the best-fit Herschel-Bulkley relationship of a measured flow curve using the Gauss-Newton algorithm. Although Bingham model has been widely used, it represents ideal plastic flow (Nguyen and Boger, 1992) and is recognized to be suitable only for describing the flow curve measurements at high strain rates (over 20 s$^{-1}$) (van Kessel, 1998). Thus the Herschel-Bulkley model is more appropriate than the Bingham model to describe the stress-strain rate relationship at low strain rates of fluid mud or hyperconcentrations (e.g. Julien and Lan, 1991; van Kessel, 1998).

Comparisons of the three yield stresses of each specimen are shown in the scatter plots in Figure 4.12. From Figure 4.12(*a*), values of $\tau_{y2}$ are significantly larger than those of $\tau_{y1}$, which is expected since $\tau_{y1}$ defines the transition from elastic behavior to plastic deformation and $\tau_{y2}$ corresponds to the transition between plastic deformation and viscous flows. However, the proportionality between $\tau_{y2}$ and $\tau_{y1}$ does not remain constant. Instead, $\tau_{y2}$ varies in the range of five to ten times the value of $\tau_{y1}$. Figure 4.12(*b*) shows the comparison of $\tau_{y1}$ and $\tau_{y2}$ to $\tau_y$, which is the value obtained from the best-fit Herschel-Bulkley equation. Although values of $\tau_{y1}$ have a similar order of magnitude to that of $\tau_y$, especially in the low stress range, they are not quite proportional

155

to $\tau_y$ over the full range. The value of $\tau_{y2}$ is approximately ten times the corresponding value of $\tau_y$ for each specimen.
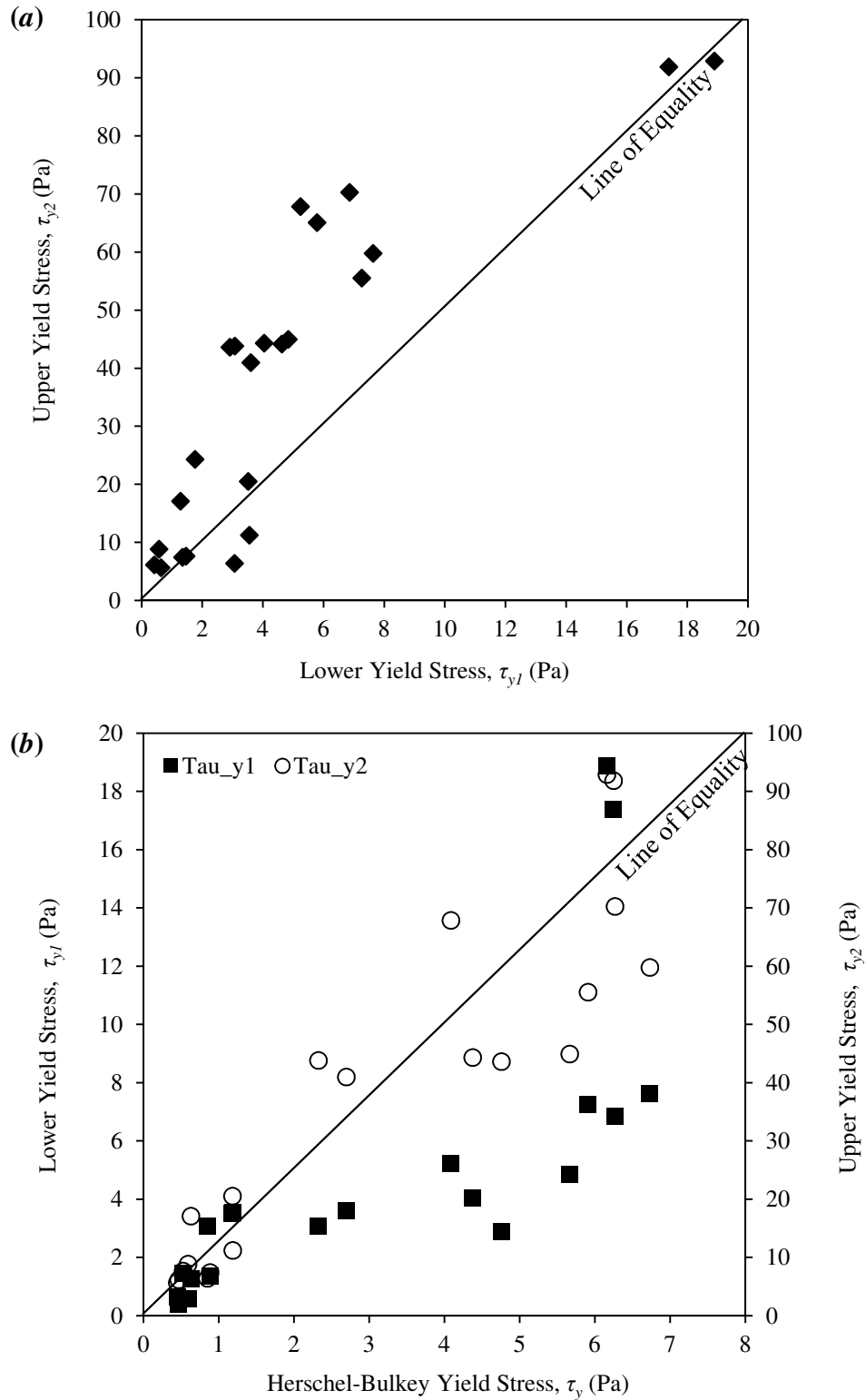
Figure 4.12 Comparison between different yield stresses: (*a*) upper yield stress ($\tau_{y2}$) versus lower yield stress ($\tau_{y1}$); (*b*) lower or upper yield stress versus Herschel-Bulkley yield stress

157

According to the graphical methods suggested by the rheometer manufacturer, determination of the lower or upper yield stress is obtained from the least-squares linear regression of the linear segments of the data series, which is readily implemented using commercial software such as Microsoft Excel. Unfortunately, the physical meaning of the graphical methods is unclear, and the methods have not been used in most previous studies on yield stress. Conversely, the Herschel-Bulkley equation is often applied to obtain the best-fit relationships of flow curves, especially in the studies of fine sediments or soft soils (Nguyen and Boger, 1992; van Kessel, 1998; Oveisy et al., 2009; Jain and Mehta, 2009). Therefore, the yield stress determined from the best-fit Herschel-Bulkley relationships of measured flow curves was chosen for further analysis in this study.

Table 4.8 shows the experiment constants ($k$ and $m$) and the yield stress ($\tau_y$) in the best-fit Herschel-Bulkley relationship (equation 2.40) of each flow curve of the soil specimens and the corresponding bulk and dry densities, and the volumetric concentration of solids.

The volumetric concentration of solids ($C_v$) is defined as the proportion of the volume of solids to the total volume, and it is usually shown as a percentage:

$$C_v = \frac{V_s}{V_t} \tag{4.11}$$

The solid volumetric concentration is directly related to the dry density, which can be obtained by $C_v \times \rho_s$. From Table 4.8, values of $C_v$ range from 18% to 50%, which is similar to the ranges of $C_v$ in many previous studies focusing on the rheological properties of mudflow or hyperconcentrations (e.g. O'Brien and Julien, 1988; Julien and

Lan, 1991). In fact, Kranenburg (1994) suggested that as sediment particle interactions increase with $C_v$, an aggregate network may form which results in a yield strength for fluid mud when $C_v > 8\%$ depending on the fractal dimension of the aggregates. While the critical value of $C_v$ at which a water-soil mixture behaves as a non-Newtonian fluid with a finite yield stress depends on the content of fine sediments in the mixture (Fei, 1981), the silt-clay mixtures in this study behaved as non-Newtonian fluids due to the high proportions of fine particles.

In Table 4.8, values of $k$, the proportionality constant between $(\tau - \tau_y)$ and the strain rate to the power $m$, $(\dot{\gamma})^m$, in equation 2.40, range from less than unity to more than 30, and increase as the kaolin content in the soil mixtures increase. The power on the strain rate ($m$) does not vary among soil specimens with different bulk densities and kaolin contents and most of them fall within the range between 0.3 and 0.6. Values of the yield stress range from 0.4 Pa to almost 7 Pa and they generally increase with the kaolin content and/or bulk density of the specimens as described in the previous section.

The overall relative experimental uncertainty in $\tau_y$ can be estimated from the replicated tests using specimens with the same kaolin content and similar bulk densities. In Table 4.8, results of specimens with similar bulk densities can be identified as replicated tests for soil mixtures with different kaolin contents, except for the 60% kaolin specimens. The coefficient of variation ($CV$) of values of $\tau_y$ was calculated as:

$$CV_{\tau_y} = \frac{\sigma_{\tau_y}}{\mu_{\tau_y}} \tag{4.11}$$

where $\mu_{\tau_y}$ = mean of $\tau_y$ values and $\sigma_{\tau_y}$ = standard deviation of $\tau_y$ values from the replicates. Overall, the average $CV_{\tau_y}$ of $\tau_y$ values for all the specimens is around 14%, which is similar to the overall experimental uncertainty in the critical shear stress $\tau_c$.

Table 4.8 Yield stress and experiment constants in the best-fit Herschel-Bulkley
equations of flow curves of soil mixtures with different kaolin contents

| Sample type | Volumetric concentration, $C_v$ | Dry density (kg/m³) | Bulk density (kg/m³) | $k$ value | $m$ value | Yield stress, $\tau_y$ (Pa) |
|---|---|---|---|---|---|---|
| 10% Kaolin | 33.8% | 893 | 1555 | 1.509 | 0.352 | 0.468 |
| | 34.1% | 900 | 1559 | 1.593 | 0.464 | 0.592 |
| | 41.7% | 1101 | 1684 | 1.109 | 0.406 | 0.446 |
| | 47.2% | 1247 | 1775 | 1.201 | 0.557 | 0.629 |
| | 49.2% | 1301 | 1809 | 1.446 | 0.645 | 0.885 |
| 20% Kaolin | 39.1% | 1033 | 1641 | 0.981 | 1.194 | 0.525 |
| | 42.1% | 1111 | 1689 | 5.125 | 0.586 | 1.182 |
| | 42.4% | 1121 | 1695 | 1.802 | 0.902 | 0.848 |
| | 42.9% | 1130 | 1701 | 4.141 | 0.627 | 1.184 |
| 40% Kaolin | 30.4% | 802 | 1496 | 10.178 | 0.280 | 2.322 |
| | 33.4% | 875 | 1541 | 6.095 | 0.350 | 2.694 |
| | 34.1% | 895 | 1554 | 4.588 | 0.396 | 4.758 |
| | 34.2% | 900 | 1557 | 8.821 | 0.363 | 4.086 |
| | 34.3% | 901 | 1557 | 9.649 | 0.309 | 5.910 |
| | 35.1% | 926 | 1573 | 30.748 | 0.236 | 6.268 |
| 60% Kaolin | 27.7% | 723 | 1446 | 14.544 | 0.204 | 5.663 |
| | 29.6% | 772 | 1476 | 7.988 | 0.346 | 6.730 |
| 100% Kaolin | 18.8% | 484 | 1297 | 7.497 | 0.314 | 4.375 |
| | 23.7% | 611 | 1374 | 14.258 | 0.321 | 6.247 |
| | 23.9% | 618 | 1378 | 15.874 | 0.305 | 6.160 |

## 4.4 Scanning Electron Microscope Images

Using the SEM technique, electron microscope images were taken for the materials, silica flour and Georgia kaolin, used in the specimen preparation, and then for the soil mixtures containing 10% to 100% kaolin content. Figure 4.13(*a*) and (*b*) show the SEM images of the air-dried silica flour and Georgia kaolin, respectively; these air-dried sediments represent the initial state of the materials before the specimen preparation procedure. Comparing the two images, both of them show various sizes of particles or aggregates. On the one hand, the image of silica flour shows larger angular silt particles with sharp edges and irregular shapes, along with small detritus scattering on the surface of larger particles and between the gaps. On the other hand, the image of air-dried Georgia kaolin consists of different sizes of kaolinite aggregates which are much less angular and close to spheres with a few exceptions. The kaolinite particles clustered together as aggregates due to humidity in the ambient conditions. From the experiment, the water content was around 6% to 8% in the air-dried Georgia kaolin.

Due to the ability to apply a variable pressure on the SEM used in this study (*Hitachi S-3700 VP*), electron microscope images are possible for a moisturized specimen with a limited resolution and magnification. Figure 4.13(*c*) and (*d*) show the images of a soil mixture of 100% kaolin (Georgia kaolin) before and after it had been oven dried, respectively. Although it became obviously more interesting and closer to the in situ condition with the existence of water as shown in Figure 4.13(*c*) compared to the oven-dried state shown in Figure 4.13(*d*), the interparticle arrangement of the particles was less illustrative due to the existing pore water. For example, the booklet structure formed by the F-F association of clay particles (Table 2.1) can be identified more apparently in

Figure 4.13(*d*). Considering the limitation of the SEM and the difficulty in analyzing the images, SEM images were taken for the oven-dried soil mixture specimens with different kaolin contents as described in section 3.5.
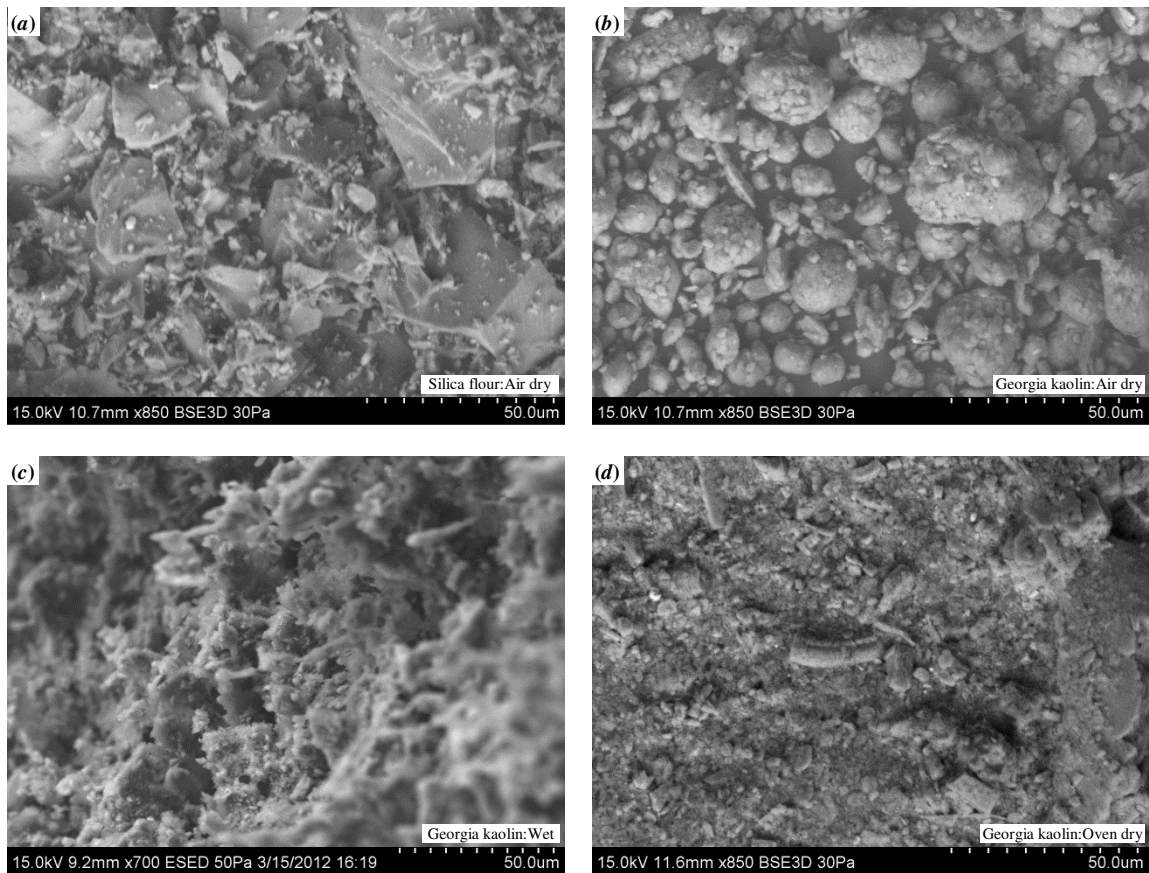


Figure 4.13 SEM images of: (*a*) air-dried silica flour, (*b*) air-dried Georgia kaolin, (*c*) mixed and wet Georgia kaolin (100% kaolin specimen), and (*d*) mixed and oven-dried Georgia kaolin (100% kaolin specimen)

Figure 4.14(*a*) to (*d*) shows the SEM images of the oven-dried silt-clay mixtures containing 10%, 20%, 40%, and 60% of Georgia kaolin, respectively. In Figure 4.14(*a*), the large, angular particles of silica flour exist with the clustered aggregates of Georgia kaolin, some of which fill part of the gaps between silt particles and the others cover the surface of the silt particles along with silt detritus. In the 10% kaolin content specimens, since the proportion of kaolin only accounted for 10% of the total weight, gaps between the silt particles cannot be filled by the kaolinite aggregates and resulted in the large, irregular voids in Figure 4.14(*a*). As the proportion of kaolinite sediments increased in the soil mixtures, more kaolinite aggregates filled the gaps in between and covered the surface of the silt particles. Therefore, the existence of the irregular voids and large, angular silt particles becomes less observable in Figure 4.14(*b*) to (*d*). Based on visual observation, one predominant interparticle structure may not be identified but different patterns of particle associations may be found in all of the four images such as F-F aggregations with either one of the E-F or E-E flocculated structures (Table 2.1; van Olphen, 1977). Although different patterns of particle associations can be observed visually and identified based on operator judgment, differences between the SEM images of soil mixtures with 20%, 40%, and 60% kaolin contents are difficult to be distinguished by naked eye observation. In addition, quantification of the proportions of different interparticle associations in a soil mixture specimen remains challenging.
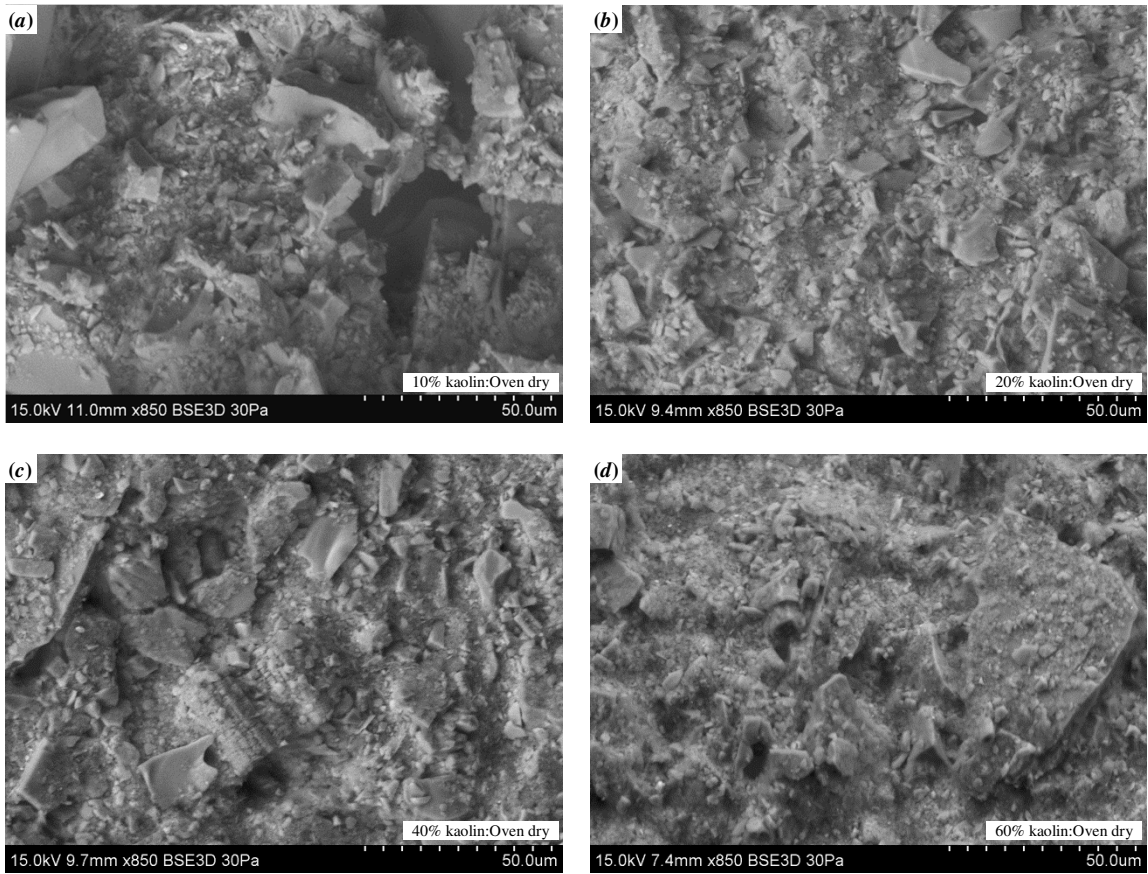
Figure 4.14 SEM images of oven-dried soil mixture specimens containing (*a*) 10% kaolin, (*b*) 20% kaolin, (*c*) 40% kaolin, and (*d*) 60% kaolin

# CHAPTER V

# ANALYSIS AND DISCUSSION

This chapter covers the analysis and discussion of the experimental results as described in Chapter IV. Firstly, physical properties of the soil mixture specimens in this study are compared with those of previous studies, including field-sampled and laboratory-mixed sediments. The previous studies include experimental results obtained by Navarro (2004) and Hobson (2008), who investigated geotechnical properties and erosion characteristics of field sediments from the river bed sediments near bridge foundations at sites that had been subject to large amounts of local scour around the state of Georgia. Secondly, relationships between the critical shear stress, yield stress, and physical properties of fine-grained sediments are constructed from regression analysis using the experimental data first, and then with the addition of the field data from studies of Navarro (2004) and Hobson (2008). Along with the analysis, uncertainties in the proposed relationships (equations) are examined, and the sensitivity of critical shear stress and yield stress to the physical properties affecting them are discussed. After that, a relationship between the critical shear stress and yield stress is obtained. Lastly, physical insights concerning the relationships between the erosion resistance and soil properties (clay content and bulk density) of fine-grained sediments are explored from the point of view of soil fabric and interparticle structure arrangement.

## 5.1 Sediment Properties Comparing with Field Data

### 5.1.1 Soil Classification

Based on the soil classification suggested in ASTM D2487-06, data for liquid limit and plasticity index of soil specimens used in this study, and river bed sediments sampled from the field in Georgia (Navarro, 2004; Hobson, 2008) and Texas (Briaud et al., 2001) are plotted on the plasticity chart as shown in Figure 5.1. The field data reported in the previous studies were collected from the river bed or riverine areas near bridge foundations at several rivers/creeks that had been subject to significant bridge scour in the states of Georgia and Texas. These data collection efforts were supported by the Georgia Department of Transportation (GDOT) and the National Cooperative Highway Research Program (NCHRP), respectively.

From the study by Briaud et al. (2001), the sediments collected from riverine areas in Texas are either lean clay (CL) or fat clay (CH) depending on the liquid limit. Among those sediments, seven out of the eleven specimens belong to CL due to a liquid limit smaller than 50%. From Navarro (2004) and Hobson (2008), river bed sediments around bridge foundations collected in Georgia contain both coarse- and fine-grained sediments. Most of the coarse-grained soil specimens belong to the classes of poorly graded sand with silt (SC-SM); silty sand (SM); silty, clayey sand (SC-SM); and clayey sand (SC). The fine-grained soil specimens were plotted in Figure 5.1, and the majority of them belong to lean clay (CL), silty clay (CL-ML), or silt (ML); a few of the specimens are fat clay (CH) or elastic silt (MH). Although organic matter exists in the field sediments from Georgia, the percentage of total organic matter was found to be between 0% and 7% in most of the specimens, and only two specimens belong to the

167

class of organic silt (OH) as reported in Hobson (2008). Therefore, the proportions of organic matter in the collected field sediments are generally not sufficient to dominate soil properties and place the sediments in the class of organic silt or clay.

The silt-clay soil mixtures prepared for this study are classified as silty clay (CL-ML) for kaolin contents less than 20% or lean clay (CL) for specimens with kaolin contents greater than 20%. While the 100% kaolin specimen belongs to lean clay, it plots near the limit between CL or OL and CH or OH regions. Because many of the fine-grained sediments from the field studies belong to the classes of silty clay, lean clay, or silt, the silt-clay mixtures used in this study may be considered to be representative of the majority even though not the full range of the field sediments.
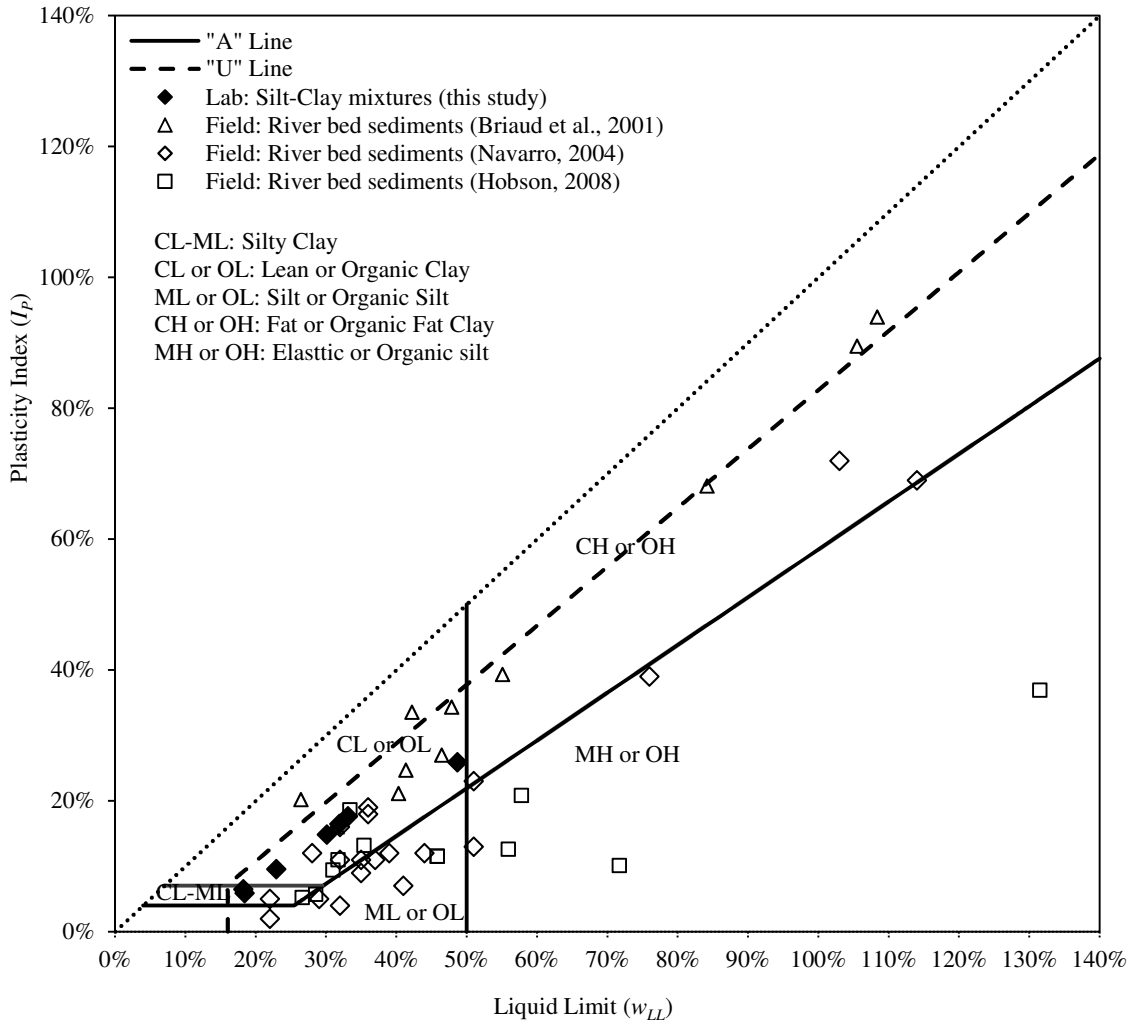
Figure 5.1 Plasticity chart: data of soil specimens used in this study and river bed
sediments in previous studies

### 5.1.2 Effects of Clay Content

The effect of clay content, i.e. proportion of particles smaller than 2 μm in diameter by weight, on the Atterberg limits of fine-grained sediments was investigated using laboratory-mixed specimens in this study and field-collected sediments studied by Navarro (2004) and Hobson (2008).Figure 5.2 shows the scatter plots with the best-fit relationships of liquid limit, plastic limit, and plasticity index versus clay content, respectively. Data points for the laboratory-mixed sediments are located in the region of lower clay content ($\leq 30\%$) along with those of the field sediments, which suggests that a single best-fit relationship can describe the effect on liquid limit, plastic limit, or plasticity index individually of both the laboratory and field sediments. The slopes of the best-fit linear equations are 1.01, 0.56, and 0.45 of relationships for liquid limit, plastic limit, and plasticity index versus clay content, respectively. As the slope of the best-fit equation describing the effect of clay content on liquid limit is the largest among the three, sensitivity of clay content to liquid limit is the most significant; that is, around twice its sensitivity to plastic limit or plasticity index. On the other hand, the best-fit slope of plastic limit versus clay content relationship is slightly larger than that of relationship of plasticity index versus clay content, indicating a higher sensitivity of clay content to plastic limit comparing to the case of plasticity index. Overall, Figure 5.2 suggests that the Atterberg limits of the fine-grained sediments increase with the increase of sediment clay content. Therefore, the elasticity and plasticity of fine sediments increase as the proportion of clay-size particles in the sediments increases.
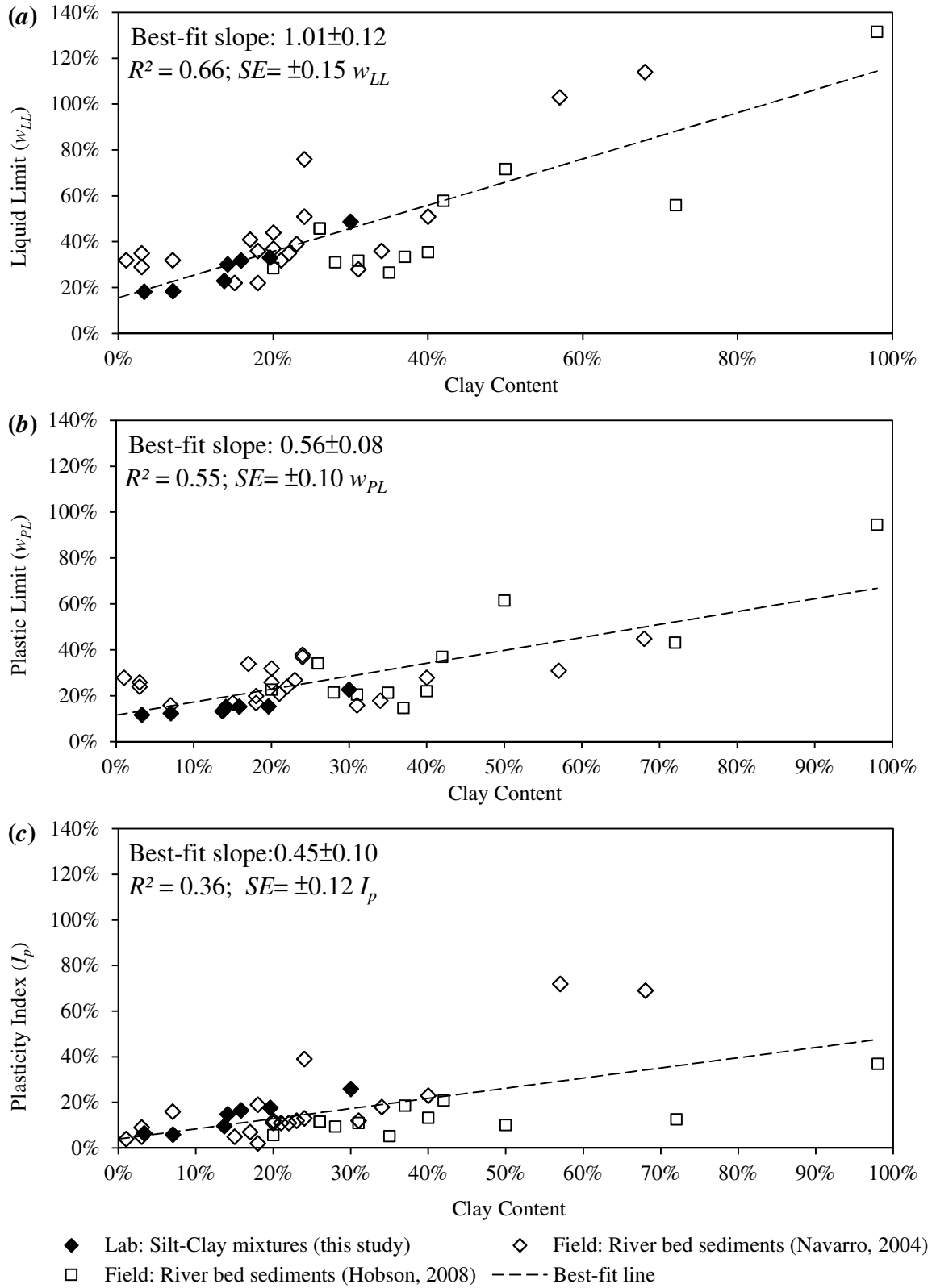
Figure 5.2 Effect of clay content on Atterberg limits: (*a*) Liquid limit, (*b*) Plastic limit; (*c*) Plasticity index

In order to show the intercorrelation between the physical properties of sediments, scatter plots of either of the two properties investigated in this research, including clay content, median particle size, bulk density, and water content, are shown in Figure 5.3 to Figure 5.8 in the following. In those figures, measurements of the physical properties from different sources of bed/benthic sediments proposed in some previous studies on the erosion behavior of fine-grained sediments were plotted along with the measurements in this study. Information regarding the sediments whose physical properties are plotted in Figure 5.3 to Figure 5.8 is shown in Table 5.1.

Table 5.1 Information of sediments used in Figures 5.3 to 5.8

| Literature | Sediment Source | Composition | Used in |
|---|---|---|---|
| Current Study | Laboratory prepared | Georgia Kaolin Ground Silt | Figure 5.3 to Figure 5.8 |
| Amos et al. (2004) | Field sampled: Tidal flats in Venice Lagoon | Benthic sediments | Figure 5.3 to Figure 5.8 |
| Bale et al. (2006) | Field sampled: Tamar Estuary | Surface bed sediments | Figure 5.8 |
| Briaud et al. (2001) | Field sampled: River bed around bridge sites in Texas | River bed sediments | Figure 5.6 to Figure 5.8 |
| Debnath and Chaudhuri (2010b) | Laboratory prepared | Kaolin/river bed mud with Sand mixture Consolidated bed | Figure 5.3, Figure 5.4, Figure 5.8 |
| Debnath et al. (2007) | Field sampled: Christchurch, New Zealand | Surface bed sediments in fresh- and salt-water | Figure 5.3 to Figure 5.8 |
| Gerbersdorf et al. (2007) | Field sampled: River Neckar, Germany | Bed sediments in riverine sites and reservoirs | Figure 5.3 |
| Geremew and Yanful (2011) | Laboratory prepared | Mine Tailings Casco Silt London Sand | Figure 5.5 |
| Hobson (2008) | Field sampled: River beds around the state of Georgia | River bed sediments with different depth | Figure 5.3 to Figure 5.8 |
| Houwing (1999) | Field sampled: Dutch Wadden Sea Coast | Cohesive sediments on Intertidal Mudflats | Figure 5.8 |
| Kothyari and Jain (2008) | Laboratory prepared | Gravel, sand, clay mixture Consolidated bed | Figure 5.3 and Figure 5.5 |
| Navarro (2004) | Field sampled: River beds around the state of Georgia | River bed sediments with different depth | Figure 5.3 to Figure 5.8 |
| Roberts et al. (1998) | Laboratory prepared | Pure Silt (Quartz particles) | Figure 5.3 to Figure 5.8 |
| Watts et al. (2003) | Field sampled: Tollesbury, Essex, UK | Intertidal sediments | Figure 5.3, Figure 5.4, Figure 5.8 |

As the effect of clay content on Atterberg limits, clay content influences sediment water contents in a similar fashion, especially for sediments which mostly consist of fine particles. Figure 5.3 shows the variation in water content as the proportion of clay particles in sediments increases. Although an increasing trend of water content with clay content is found in most of the data sets, the increasing rate of water content is different between sediments collected from different origins and with different compositions. Water contents of sediments that are mostly composed of fine particles, including the soil mixtures in this study and the field sediments collected in riverine sites near reservoirs (Gerbersdorf et al., 2007) and intertidal/tidal areas (Watts et al., 2003; Amos et al., 2004), increase significantly with the increase of clay content in the sediments. Nevertheless, sediments that contain coarse particles, including the river bed sediments near bridge foundations (Navarro, 2004; Hobson, 2008) and consolidated mixture beds (Kothyari and Jain, 2008; Debnath and Chaudhuri, 2010b), show a more gradual increasing trend in water content with clay content.

Some of the river bed sediments investigated by Navarro (2004) and Hobson (2008) contain high proportions of clay particles. However, due to a lower degree of saturation, water contents of these river bed sediments are generally lower than those of intertidal/tidal sediments. For the cases of mud-sand (Kothyari and Jain, 2008) and gravel-sand-clay mixture beds (Debnath and Chaudhuri, 2010b) prepared in the laboratory, water contents in sediments are generally low because of the consolidation process during the preparation of the beds. After being consolidated, soil particles were packed and the pore water space was limited. Thus water content was dependent on the degree of consolidation rather than clay content in those sediments.
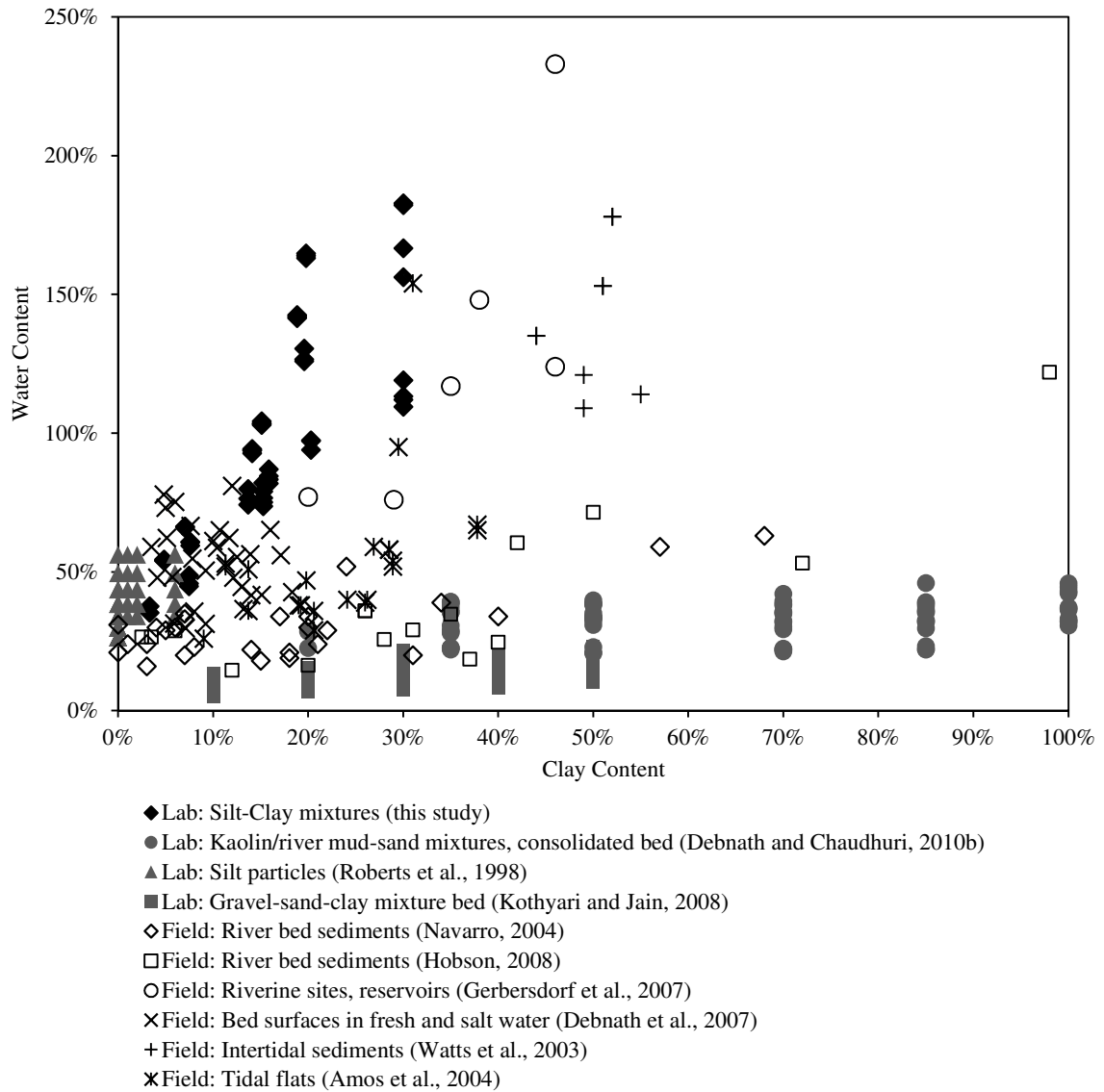
Figure 5.3 Water content versus clay content

In Figure 5.4, sediment bulk density was plotted versus the clay content. Unlike the case of water content which increases with clay content in most of the sediments, the bulk density does not seem to show discernible trends with clay content, especially in field sediments which contain coarse particles, e.g. Navarro (2004), Debnath et al. (2007), and Hobson (2008). Despite water content, coarse particles, including gravels and sands, account for a large proportion of the bulk density of soils since they tend to have a higher specific gravity compared to fine sediments. Particularly, the effect of coarse particles on bulk density is apparent in soils which consist of various particle sizes and are gap-graded. In contrast, values of bulk density are influenced by the proportions of clay in soils which are composed of find-grained sediments predominantly or with high clay content, like the sediments in this study and for those in the research of Amos et al. (2004) and Debnath and Chaudhuri (2010b). In those cases, bulk density decreases with the increase of clay content. Roberts et al. (1998) used quartz particles with controlled values of bulk density by adding specific amounts of water when preparing the specimens. The intertidal sediments studied by Watts et al. (2003) contain similar proportions of clay. Therefore, the relationship between bulk density and clay content is not illustrated in those two cases.
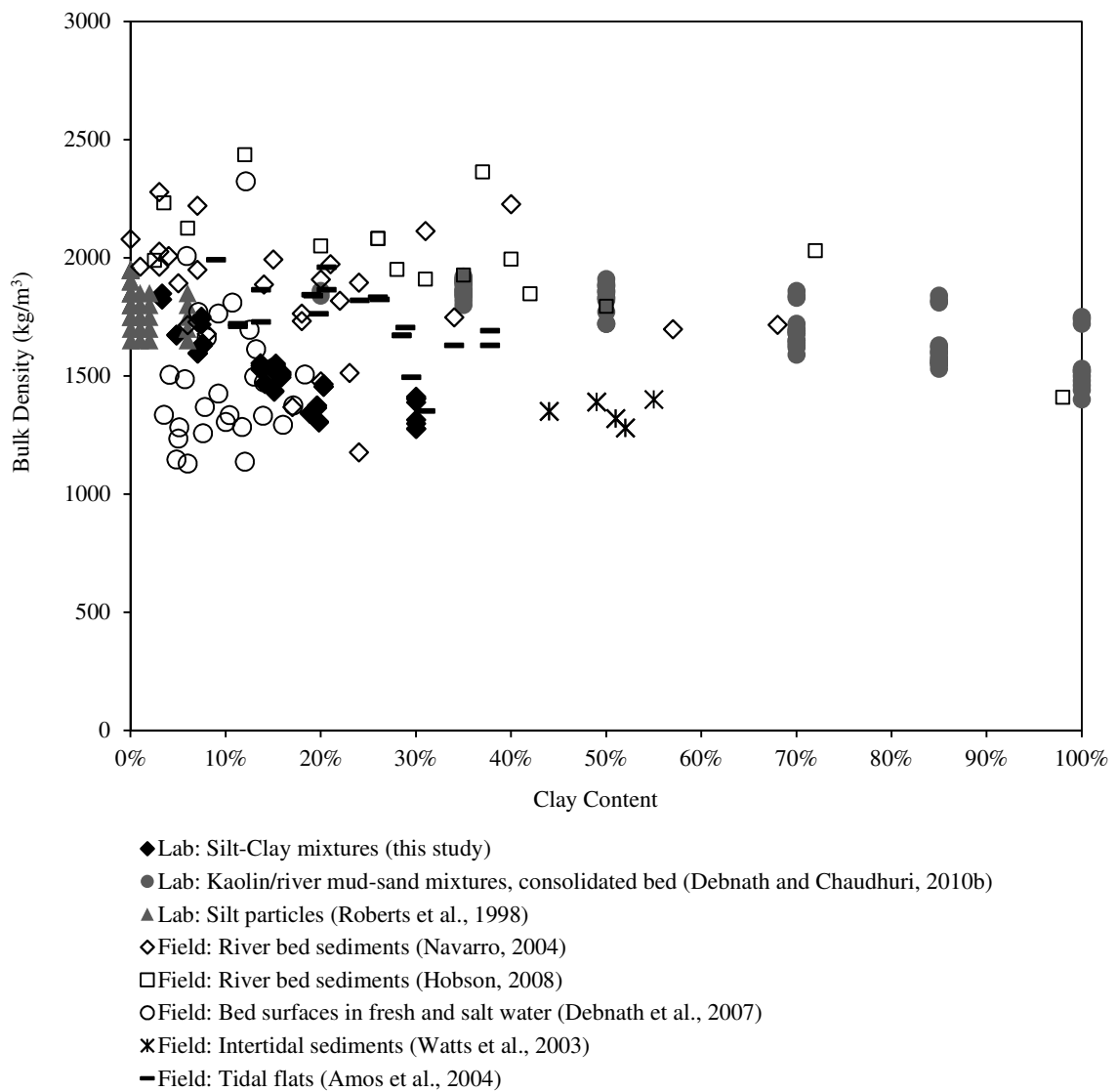
Figure 5.4 Bulk density versus clay content

The legend reads:

◆ Lab: Silt-Clay mixtures (this study)
● Lab: Kaolin/river mud-sand mixtures, consolidated bed (Debnath and Chaudhuri, 2010b)
▲ Lab: Silt particles (Roberts et al., 1998)
◇ Field: River bed sediments (Navarro, 2004)
□ Field: River bed sediments (Hobson, 2008)
○ Field: Bed surfaces in fresh and salt water (Debnath et al., 2007)
✳ Field: Intertidal sediments (Watts et al., 2003)
━ Field: Tidal flats (Amos et al., 2004)

Since clay content refers to the proportion of particles which are smaller than 2 μm in sediments, the median particle size ($d_{50}$) is expected to decrease as clay content increases if the sediments are not gap-graded. As shown in Figure 5.5, $d_{50}$ decreases by a similar rate as clay content increases in sediments from different origins, except for the data obtained in the studies of Roberts et al. (1998) and Kothyari and Jain (2008). In the experiments of Roberts et al. (1998), soil specimens were prepared with quartz particles in the silt size range with different size distributions controlled by the manufacturer. Therefore, the independence of $d_{50}$ relative to clay content in the data of Roberts et al. (1998) is attributed to the absence of clay in the sediments. Nevertheless, a small quantity of quartz particles which are smaller than 2 μm contribute to the clay content up to about 5% in one mixture used by Roberts et al. data.

The effect of clay content on $d_{50}$ is also insignificant in the data of Kothyari and Jain (2008). Due to the existence of gravel-size particles, which are larger and heavier compared to clay-size particles, values of $d_{50}$ are skewed by the coarse sediments even though the clay content is as high as 50%. In fact, soil properties and behavior of the gravel-sand-clay mixture beds studied by Kothyari and Jain (2008) resemble those of coarse sediments, which are not included in the scope of soil properties and behavior focusing on fine-grained sediments in this study. Despite these two exceptions, the proportion of clay particles influences $d_{50}$ similarly in sediments which consist of clay, silt, and/or fine to medium sand, no matter if they were prepared in the laboratory or collected in the field.
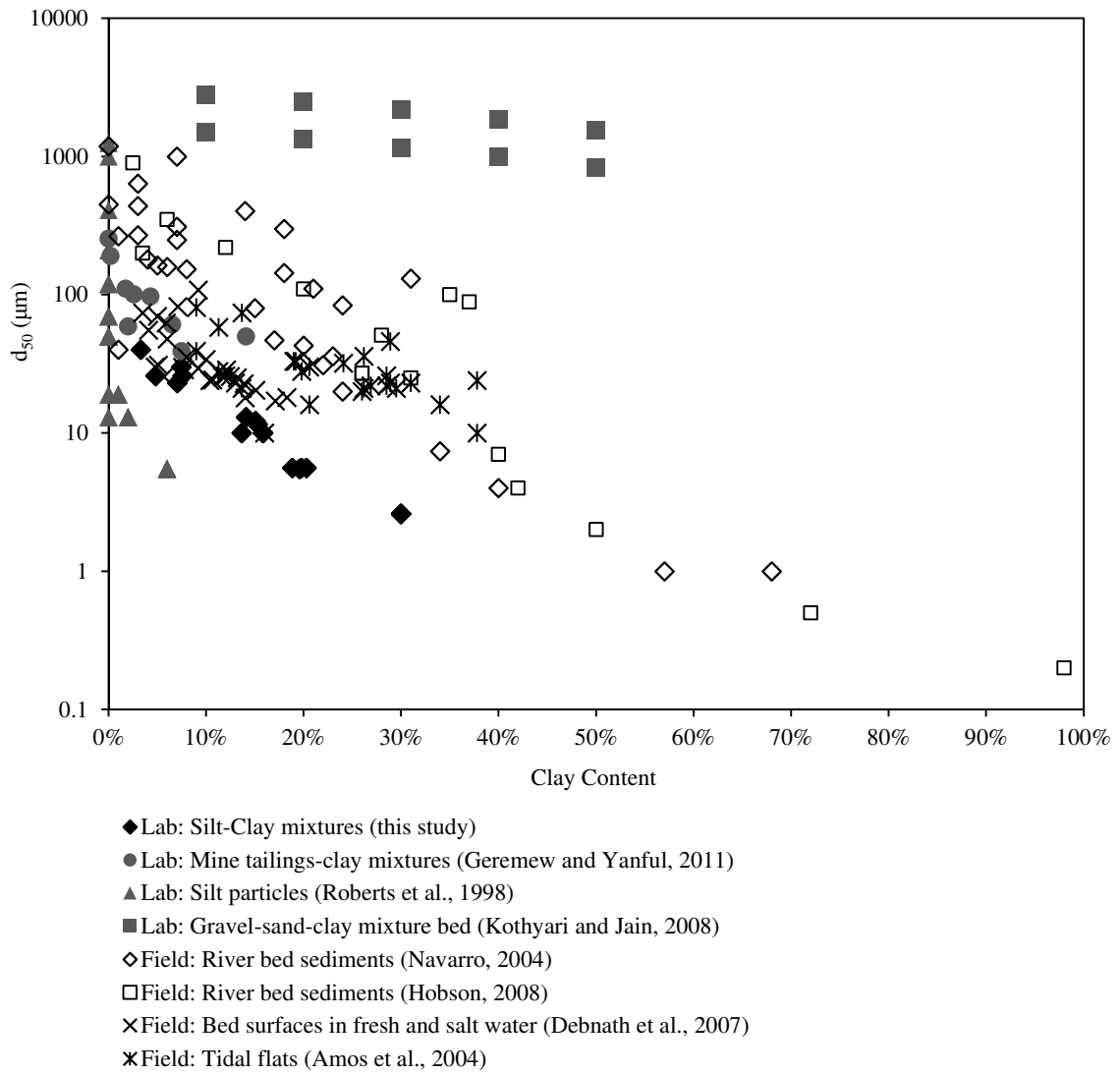
Figure 5.5 Median particle size versus clay content

The chart legend:

◆ Lab: Silt-Clay mixtures (this study)
● Lab: Mine tailings-clay mixtures (Geremew and Yanful, 2011)
▲ Lab: Silt particles (Roberts et al., 1998)
■ Lab: Gravel-sand-clay mixture bed (Kothyari and Jain, 2008)
◇ Field: River bed sediments (Navarro, 2004)
□ Field: River bed sediments (Hobson, 2008)
✕ Field: Bed surfaces in fresh and salt water (Debnath et al., 2007)
✖ Field: Tidal flats (Amos et al., 2004)

### 5.1.3 Effects of Median Particle Size

The effects of median particle size on water content and bulk density of sediments are shown in Figure 5.6 and Figure 5.7, respectively. As discussed previously, median particle size ($d_{50}$) and clay content are generally inversely correlated, i.e. $d_{50}$ decreases at a constant rate with the increase of clay content among sediments with different origins. Accordingly, water content is related inversely to $d_{50}$ as is clay content. In other words, water content decreases as $d_{50}$ increases, especially in sediments that are composed of predominately fine particles with $d_{50} < 63 \mu m$ (Figure 5.6). Specifically, water contents of the silt-clay mixtures in this study and field sediments collected in tidal and/or intertidal flats (Amos et al., 2004; Debnath et al., 2007) decrease rapidly as $d_{50}$ increases compared to the decreasing rates of water content of silt particles (Roberts et al., 1998) and river bed sediments (Briaud et al., 2001; Navarro, 2004; Hobson, 2008).

In Figure 5.7, bulk density increases gradually with $d_{50}$ in the studies by Roberts et al. (1998), Briaud et al. (2001), Navarro (2004), Hobson (2008), and the author. However, bulk density does not seem to depend on $d_{50}$ for the tidal/intertidal sediments as reported in Amos et al. (2004) and Debnath et al. (2007).

In the experiments of Roberts et al. (2008), a series of sediment samples was prepared with predetermined water contents in order to create different bulk densities of specimens with the same $d_{50}$. As a result, stacks of data points representing different water contents and bulk densities at a specific $d_{50}$ are shown in Figure 5.6 and Figure 5.7, respectively. Although both soil specimens used by Roberts et al. (1998) and the author are fine-grained sediments, the silt specimens prepared by Roberts et al. (1998) from

ground quartz  contain lower water contents at the same value of $d_{50}$ due to the absence of clay minerals.

In sediments collected from the field, water content and bulk density are affected by factors such as void ratio, degree of saturation, the existence of coarse particles and/or organic matter, and degree of consolidation according to the depth and age of the sediments. In the cases of river bed sediments (Briaud et al., 2001; Navarro, 2004; Hobson, 2008), water content is generally lower compared to laboratory prepared or tidal/intertidal sediments since they were not fully saturated. In addition, the existence of sand and/or gravel leads to a higher bulk density of river bed sediments than that of the silt-clay mixtures. In tidal/intertidal areas (Watts et al., Amos et al., 2004; Debnath et al., 2007), sediments are generally fines and are homogeneous in particle size with respect to the depth in the surface layer. Consequently, variation in bulk density in a narrow range of particle sizes could be attributed to different degrees of consolidation according to the depth and age of sediments but not the difference in $d_{50}$.

◆ Lab: Silt-Clay mixtures (this study)

▲ Lab: Silt particles (Roberts et al., 1998)

◇ Field: River bed sediments (Navarro, 2004)

□ Field: River bed sediments (Hobson, 2008)

△ Field: River bed sediments (Briaud et al., 2001)

✕ Field: Bed surfaces in fresh and salt water (Debnath et al., 2007)

✳ Field: Tidal flats (Amos et al., 2004)
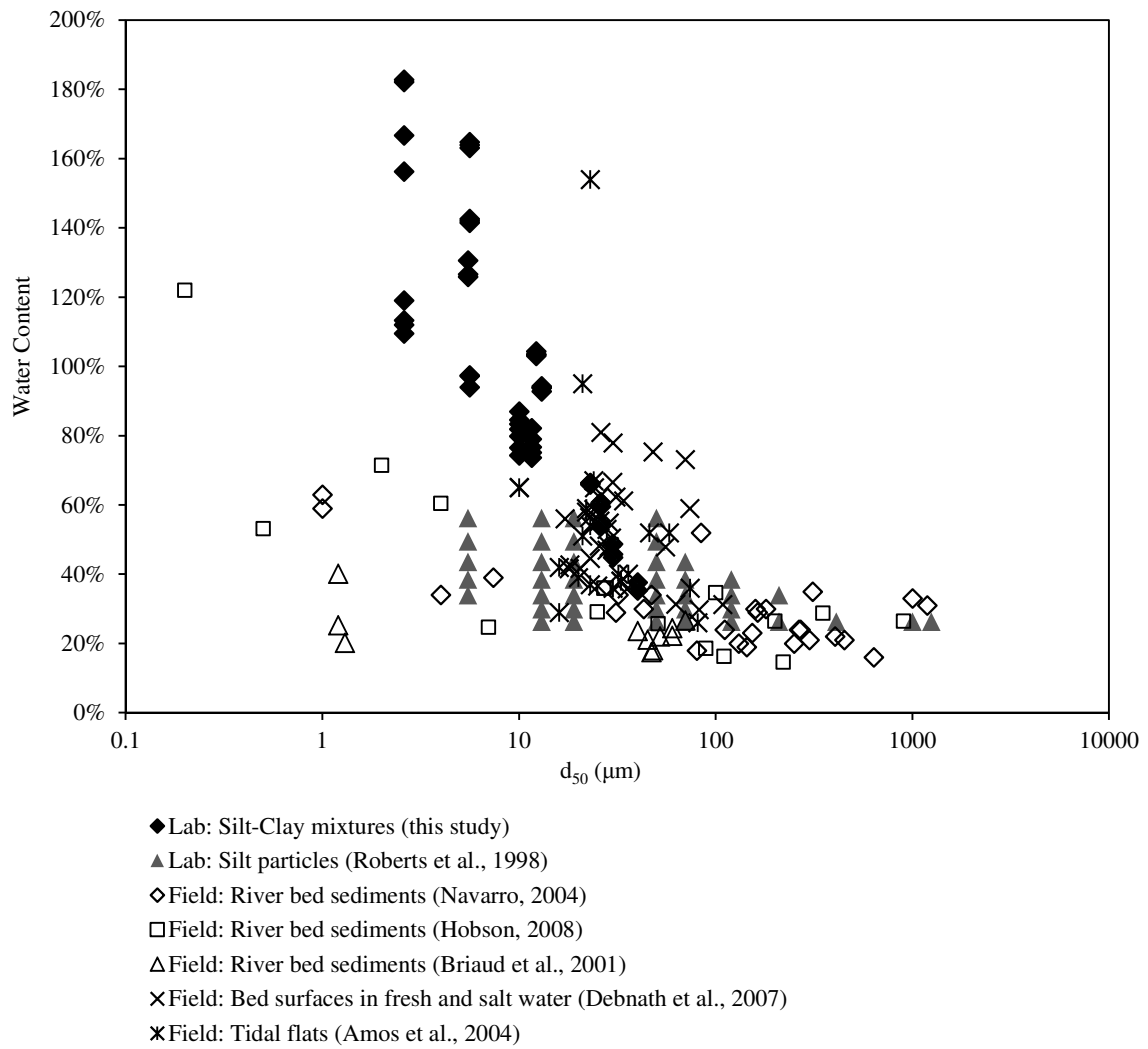
Figure 5.6 Water content versus median particle size
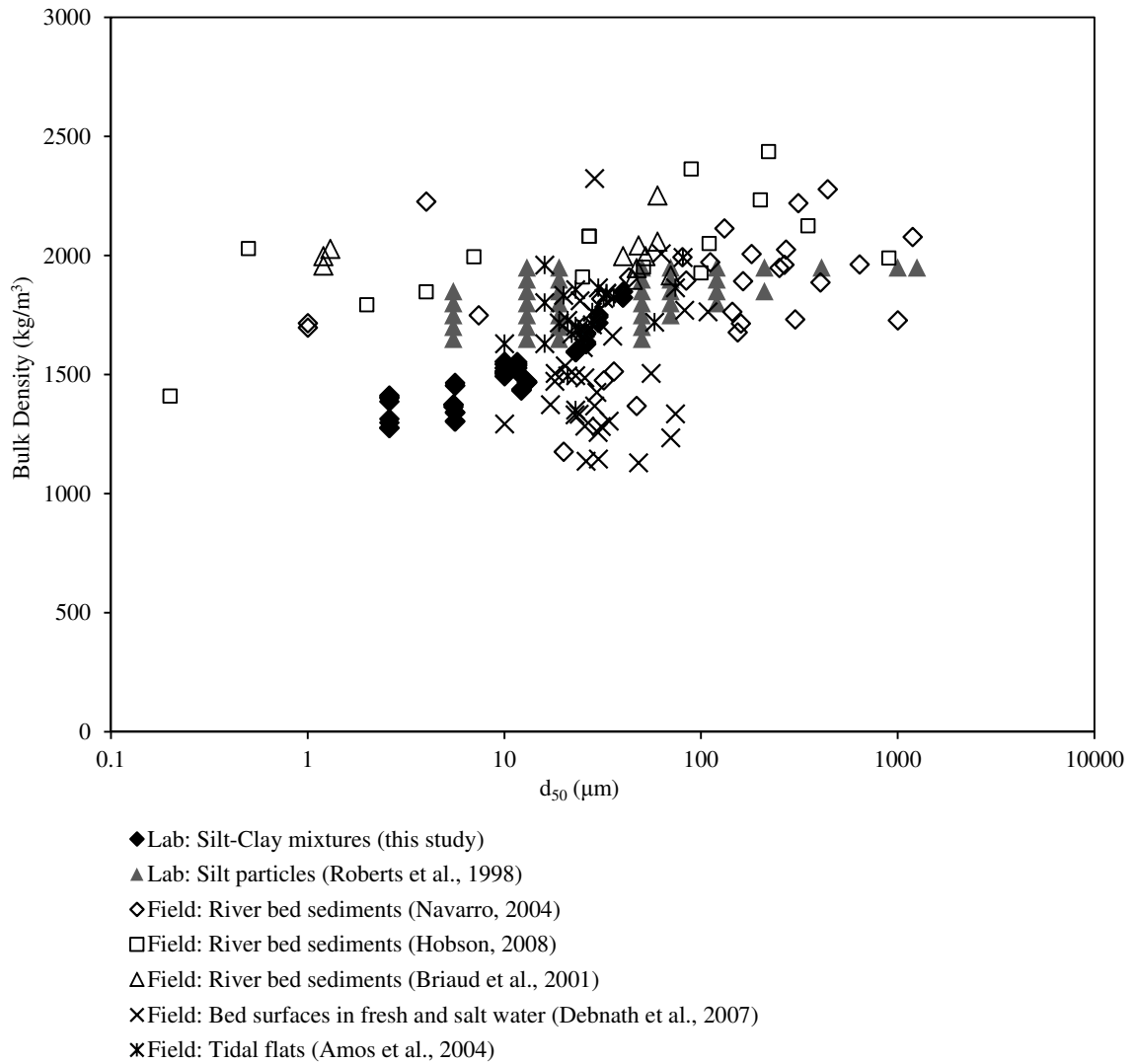
Figure 5.7 Bulk density versus median particle size

**5.1.4 Bulk Density versus Water Content**

As reported in the literature review, bulk density and water content of sediments are approximately inversely correlated since they both indicate the degree of consolidation or packing of sediments (Grabowski et al., 2011; Santamarina et al., 2001). In some studies (McNeil et al., 1996; Jepsen et al., 1997; Roberts et al., 1998), especially those that focus on benthic sediments, soil specimens were assumed to be saturated and thus bulk density and water content have been used interchangeably. The relationship between bulk density and water content is illustrated in Figure 5.8, in which data of laboratory prepared (Roberts et al., 1998; Debnath and Chaudhuri, 2010b) and field collected (Houwing, 1999; Briaud et al., 2001; Watts et al., 2003; Amos et al., 2004; Navarro, 2004; Bale et al., 2006; Debnath et al., 2007; Hobson, 2008) sediments reported in current and previous studies are included. Among those, the assumption of saturated soils was applied by Roberts et al. (1998) and the author to calculate bulk densities from measured water contents using equations 3.3 to 3.5. In all other studies, bulk densities were measured /estimated by the methodology specified in each of the studies.

As expected, bulk density generally decreases as water content of sediments increases (Figure 5.8). Most of the data collected from river beds (Briaud et al., 2001; Navarro, 2004; Hobson, 2008) and estuaries (Bale et al., 2006; Debnath et al., 2007) are located in the region of water content between 20% and 80%, and bulk density falls in the range of 1100 kg/m$^3$ to almost 2500 kg/m$^3$. The data points of intertidal/tidal mud flats cover a larger range of water content (20% to 180%) and a smaller range of bulk density (1300 kg/m$^3$ to 2100 kg/m$^3$), which happen to coincide with the data points from Roberts et al. (1998) and this study. This coincidence suggests that the assumption of saturated

184

soils is applicable to estimating bulk density from water content when the soil specimens are composed mostly fine sediments or collected from mudflats. However, the process of consolidation and the existence of coarse particles affect the relationship between bulk density and water content. For instance, data from the consolidated bed of laboratory-prepared kaolin/river mud-sand mixtures in the research of Debnath and Chaudhuri (2010b) plot in the same region with most river bed sediments for which bulk density varies more significantly within a small range of water content. In this case, the proportion of coarse sediments and the degree of consolidation are considered to be more significant than water content in influencing bulk density.
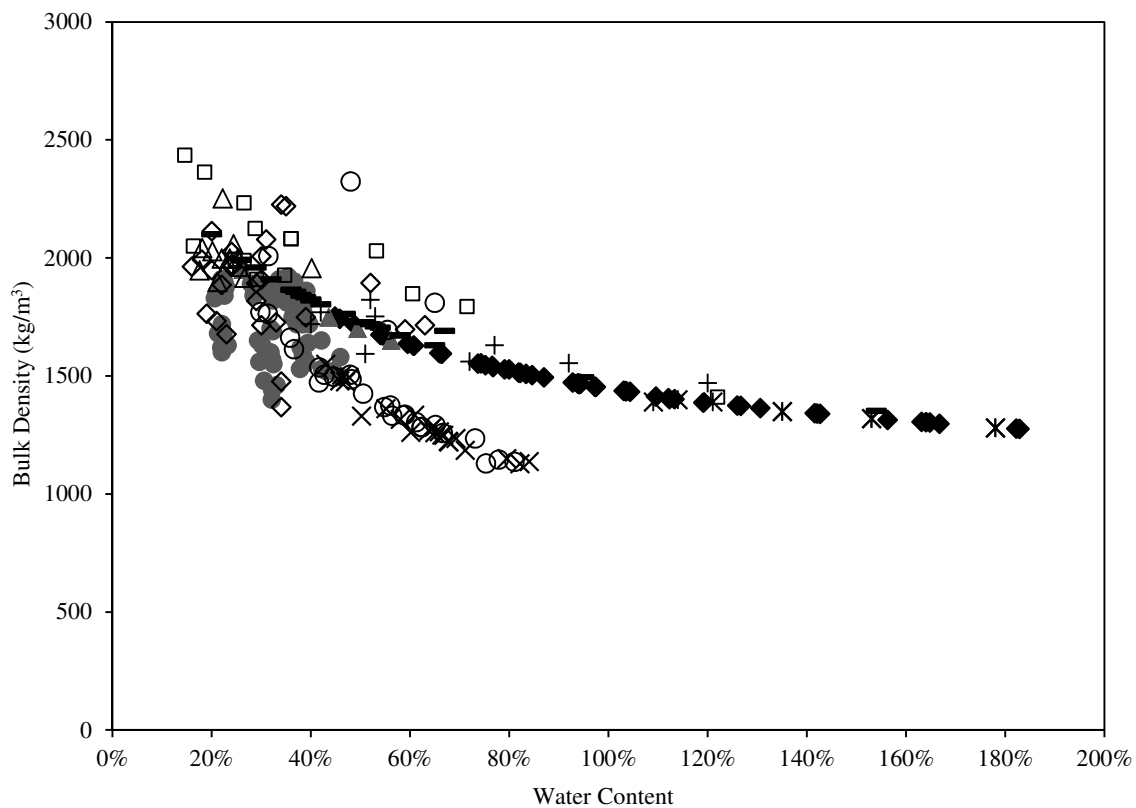
◆ Lab: Silt-Clay mixtures (this study)
● Lab: Kaolin/river mud-sand mixtures, consolidated bed (Debnath and Chaudhuri, 2010b)
▲ Lab: Silt particles (Roberts et al., 1998)
◇ Field: River bed sediments (Navarro, 2004)
□ Field: River bed sediments (Hobson, 2008)
△ Field: River bed sediments (Briaud et al., 2001)
○ Field: Bed surfaces in fresh and salt water (Debnath et al., 2007)
✕ Field: Estuary sediments (Bale et al., 2006)
+ Field: Intertidal mudflats (Houwing, 1999)
✖ Field: Intertidal sediments (Watts et al., 2003)
━ Field: Tidal flats (Amos et al., 2004)

Figure 5.8 Bulk density versus water content

**5.1.5 Summary**

In this section, comparisons are made between the silt-clay mixtures in this study and other laboratory-prepared or field-collected sediments studied by some previous researchers who focused on erosion behaviors of sediments containing fine particles. The intercorrelations among the soil physical properties were shown using the scatter plots in Figure 5.3 to Figure 5.8. In section 5.1.2, it was observed that increase of clay content in sediments generally leads to increase of water content (Figure 5.3) but decrease of bulk density (Figure 5.4) and median particle size (Figure 5.5). Stated in another way, increases in median particle size correspond to decreases in water content (Figure 5.6) and increases in bulk density (Figure 5.7). The latter observation of the inverse correlation between bulk density and water content was confirmed in Figure 5.8. Based on the discussion on soil classification and the physical properties, which have been recognized as important factors influencing sediment erosion and transportation behavior, the soil specimens studied in this research are justified to be representative of field sediments consisting of predominately fine-grained sediments. Despite the simplifications in this study associated with artificially prepared soil mixtures, such as absence of coarse sediments and organic matter, and high degrees of saturation, erosion behavior and rheological characteristics of the specimens in this study are expected to be typical and applicable to field sediments that are classified as silty clay and/or clayey soils without large organic matter content.

**5.2 Multiple Regression Analysis**

From previous studies (e.g. Hobson, 2008; Grabowski et al., 2011), some of the geotechnical characteristics of soils as detailed in Chapter 3 are considered as possible

predictors in a multiple regression analysis to determine the response variable of interest in this study; that is, the critical shear stress or yield stress of fine-grained sediments. These geotechnical characteristics include:

- water content (decimal fraction): $w$

- clay content (decimal fraction of particles smaller than 2 μm by mass): $Clay$

- bulk density (kg/m$^3$): $\rho_b$

- median particle size (μm) $d_{50}$

The remaining characteristics, such as specific gravity and Atterberg limits, were excluded for the following reasons. Specific gravity ($G_s$) was excluded due to the small range of variation. Specifically, $G_s$ varies from 2.58 to 2.65 among the silt-clay mixtures in this study. In the case of field sediments as reported by Hobson (2008), $G_s$ varies from 2.4 to 2.8, which is still considered to be relatively small. Atterberg limits were excluded since they can be determined only for soils showing plastic behavior, which requires a significant amount of clay content.

### 5.2.1 Subset Selection

In linear regression analysis, a set of $(p-1)$ predictors can generate $2^{(p-1)}$ alternative models. For instance, in this study, four predictors are included to estimate the response variable, which results in $2^4 = 16$ different possible subset models. As more predictors are included, the number of alternative subset models soon becomes unmanageable as less significant predictors are added. Therefore, subset selection procedures are commonly applied to indentify the most influential predictors. The goal is to generate a small group of regression models that result in "good" predictions according

to a specified criterion. This study follows the best subsets selection procedure as applied in the research by Navarro (2004) and Hobson (2008). Then a small group of best subsets are selected, depending on the calculated values of the criterion, to progress to the final linear regression relationship. Among many criteria for comparing regression models that have been developed, three of the criteria that penalize models with larger numbers of predictors are selected to apply in this study (Kutner et al., 2004): the adjusted coefficient of multiple determination ($R^2_{a,p}$), Mallows' $C_p$, and Akaike's information criterion ($AIC_p$).

For the sake of the following discussion, a response variable, its mean, and the predicted values from a regression model that depends on predicting variables $x_{ki}$ ($k$=the index of prediction variables and $i$=the index of data points), are symbolized as $y$, $\bar{y}$, and $\hat{y}$, respectively. The coefficient of multiple determination, $R^2$, measures the proportion of the total variance that the regression model explains and is given by:

$$R^2 = \frac{SS_R}{SS_T} = 1 - \frac{SS_E}{SS_T} \tag{5.1}$$

where $SS_R$ represents the variance in $y$ explained by the regression model; $SS_E$ represents the unexplained variance (random variance) in $y$; and $SS_T$ represents the total variance in $y$. The mathematical relationships to determine these values are:

$$SS_T = \sum_{i=1}^{n}(y_i - \bar{y})^2 \tag{5.2}$$

$$SS_R = \sum_{i=1}^{n}(\hat{y}_i - \bar{y})^2 \tag{5.3}$$

$$SS_E = \sum_{i=1}^{n}(y_i - \hat{y})^2 \tag{5.4}$$

where $i = 1, 2, ..., n$ and $n =$ the total number of observations. The criterion of $R_p^2$ calls for

the use of $R^2$ for a regression model which consists of a specified number of parameters,

$p$, i.e. $(p-1)$ predictors plus a constant term. Therefore, a high value of $R_p^2$ of a subset

model refers to a high goodness-of-fit, and thus the $x$ variables in the regression model

are identified as a "good" subset. Nevertheless, $R_p^2$ does not take into account the number

of parameters in a regression model, and its value can never decrease as the number of $x$

variables increases. For this reason, the adjusted coefficient of multiple determination,

$R_{a,p}^2$, is used as an alternative criterion to estimate the goodness-of-fit of a regression

model with $(p-1)$ predicting variables:

$$R_{a,p}^2 = 1 - \left(\frac{n-1}{n-p}\right)\left(\frac{SS_E}{SS_T}\right) \tag{5.5}$$

Thus $R_{a,p}^2$ increases as more predicting variables are added to the regression model until

the increase in $R_{a,p}^2$ becomes too small to offset the loss of an additional degree of

freedom, or until $R_{a,p}^2$ decreases with the addition of a predicting variable.

Based on the concept of total mean squared error ($MS_{E,all}$), the subset selection

criterion Mallows' $C_p$ measures the goodness-of-fit of the model of selected predicting

variables and can be calculated as:

$$C_p = \frac{SS_{E,p}}{MS_{E,all}} - (n-2p) = \frac{SS_{E,p}}{SS_{E,all}/(n-(p_{all}-1)-1)} - (n-2p) \tag{5.6}$$

where $SS_{E,p}$ = the sum of the squares of error of the model being evaluated, $p-1=$ the number of predictors used in the evaluated model; $SS_{E,all}$ = the sum of the squares of error of the model which consists of all available predictors; and $p_{all}-1=$ the total number of available predictors. In using the $C_p$ criterion, subsets of predictors are sought for which the $C_p$ is small and close to $p$, the number of parameters in the model.

Besides $R_{a,p}^2$ and $C_p$, Akaike's information criterion ($AIC_p$) is another popular alternative that provides a penalty for adding predictors. The mathematical form of $AIC_p$ is given as:

$$AIC_p = n\ln(SS_{E,p}) - n\ln(n) + 2p \qquad (5.7)$$

When using the $AIC_p$ criterion, a good fit is indicated by a small value of $AIC_p$. This criterion generally works well for models with small $SS_{E,p}$. In the linear regression analysis, subsets of the possible predictors, mentioned previously in this section (water content, clay content, bulk density, and median particle size), were initially selected by a stepwise subset selecting procedure based on $AIC_p$ criterion. Secondly, the value of $C_p$ for the model with the selected predictors was compared to that for the full model, which consists of all the predictors, for validation. After that, the dependency among the selected predictors was investigated to determine if the inclusion of an interaction term is appropriate before the final regression model is determined based on the regression statistics including $R_{a,p}^2$ and the standard error of the estimates. The discussion of dependency between predictors is detailed in the next section.

### 5.2.2 Dependency among Predictors

After the subset of predictors was selected based on the criteria, the issue of intercorrelation, i.e. the dependency among predicting variables, was investigated. When predicting variables of a regression model are not independent of one another, adding or deleting a predicting variable changes the regression coefficients. In addition, the individually estimated regression coefficient may not show its statistical significance even though a definite statistical relationship exists between the response variable and the predictor. In some cases, an interaction term, the product of any pair of correlated predicting variables, may be added to the regression model as another predicting variable to describe the relationship between the response and predicting variables to the full extent possible. The intercorrelation among predictors can be diagnosed simply by the scatter plot of each pair of predictors. For instance, Figure 5.3 to Figure 5.8, which were presented previously, show the scatter plots of the possible predictors in this study, and the dependency among the predictors is suggested by the systematic patterns of the data points.

One of the formal methods to detect the intercorrelation among predictors that is commonly accepted is the use of variance inflation factors (*VIF*). The mathematical expression of the variance inflation factor of a predicting variable $x_k$, denoted by $(VIF)_k$, is:

$$(VIF)_k = \left(1 - R_k^2\right)^{-1} \qquad k = 1, 2, ..., p-1 \qquad (5.8)$$

where $R_k^2 =$ the coefficient of multiple determination when $x_k$ is regressed on the other $p-2$ predicting variables in the model. Then the mean of *VIF* values, denoted by $\left(\overline{VIF}\right)$, can be calculated as:

$$\left(\overline{VIF}\right) = \frac{\sum\limits_{k=1}^{p-1}(VIF)_k}{p-1} \tag{5.9}$$

When $\left(\overline{VIF}\right)$ is considerably larger than unity, it is indicative of a serious issue of intercorrelation among the predictors (Kutner et al., 2004).

In regression analysis, the appropriateness of a regression model can be evaluated by the scatter plots of residuals ($e_i$) versus the response and predicting variables. Residuals are the difference between the measured value and the estimated value of the response variable by the regression model of each sample:

$$e_i = y_i - \hat{y}_i \tag{5.10}$$

If two predictors, $x_1$ and $x_2$, are selected to construct a regression model, the residuals obtained by fitting the response variable, $y$, without the interaction term ($x_1x_2$) is plotted against $x_1x_2$ to determine if $x_1x_2$ should be included in the regression model. If the data points show a trend in this plot, an interaction effect is suggested to be present. Thus $x_1x_2$ should be included in the regression model (Kutner et al., 2004).

### 5.2.3 Regression Model Assessment

Once subsets of predictors were selected and the intercorrelation had been diagnosed, linear regression models were constructed. Then the goodness-of-fit of the proposed regression models was assessed to evaluate the performance of the models. Several goodness-of-fit criteria have been used in the subset selection procedure as defined by equations 5.5 to 5.7. Values of these criteria change as predictors are added or omitted. Thus those criteria are mainly applicable to a comparison of different regression results evaluated from the same set of possible predictors. In this study, the final statistic

used for model selection was the standard error, *SE*, which is an average value of errors of a regression model:

$$SE = \sqrt{\frac{SS_E}{n-p}}$$

(5. 11)

From the equation above, *SE* has the same unit as the response variable does, and it is commonly used as an expression of the average uncertainty in the estimates of the response variable.

From the studies of Navarro (2004) and Hobson (2008), which used the same erosion flume and experimental procedure, different forms of the regression models applied to similar subsets of predicting variables were proposed, such as log-log, semi-log, or power relationships. In those cases, different nonlinear regression models with the same predictors selected for the linear model have been applied. Then the goodness of fit of each of the models was assessed by computing its standard error to determine the final form of the regression model.

### 5.3 Predicting Critical Shear Stress from Sediment Properties

### 5.3.1 Critical Shear Stress Relationship

To determine the regression model of critical shear stress using the geotechnical characteristics (i.e. $w$ , *Clay* , $\rho_b$ , and $d_{50}$ ) as predictors, the procedures of subset selection, intercorrelation investigation, and regression model assessment have been applied. In the subset selection procedure, the $AIC_p$ value of the initial model which included all possible predictors was calculated first. Then by eliminating one predictor, four potential subset models were obtained; and the $AIC_p$ value of each subset was

194

compared with that of the initial model. If one of the subsets resulted in a smaller $AIC_p$ value than the initial model, the selection continued to eliminate two predictors and searched for a subset model with smaller $AIC_p$. Steps of eliminating predictors from the initial model terminated when the minimum $AIC_p$ was found. In this research, the minimum values of $AIC_p$ were obtained from subsets composed of at least three predictors for predicting critical shear stress, yield stress, and their dimensionless forms. Therefore, only the regression statistics of the initial model and subsets composed of three predictors are shown in the following discussion (Table 5.2 to Table 5.9).

From the subset selection procedure, three predictors were selected to produce the potential regression models (Potential model(1) in Table 5.2). Then the $VIF_k$ of each selected predictor was calculated to indicate the intercorrelation of the predictors. Meanwhile, the addition of interaction terms of the selected predictors was considered. Sequentially, the potential regression models were constructed from combinations of the selected predictors as shown in Table 5.3. Subsequently, the optimal regression model was selected through model assessment based on adequacy of the addition of the interaction term and the minimum value of $SE$. Finally, the optimal regression model was selected through model assessment based on adequacy of the addition of the interaction term and the minimum value of $SE$.

Table 5.2 Subset predictor selection of critical shear stress regression model

| Models | Predictor Used | | | | $AIC_p$ | $C_p$ | SE |
|---|---|---|---|---|---|---|---|
| | $w$ | $\rho_b$ | Clay [a] | $d_{50}$ | | | |
| Initial | √ | √ | √ | √ | -70.52 | 5.00 | 0.37 |
| **Potential(1)** | **√** | **√** | **√** | | **-72.42** | **3.09** | **0.37** |
| Potential(2) | √ | √ | | √ | -69.02 | 6.19 | 0.38 |
| Potential(3) | √ | | √ | √ | -57.08 | 19.55 | 0.45 |
| Potential(4) | | √ | √ | √ | -66.48 | 8.68 | 0.40 |

[a] Refers to the fraction of particles smaller than 2 µm by mass

Table 5.3 Summary of potential critical shear stress regression models

| Potential models | Predictor used | | | | $R^2$ | $R_a^2$ | SE |
|---|---|---|---|---|---|---|---|
| | $w$ | $\rho_b$ | Clay [a] | Interaction term | | | |
| 1 | √ | √ | √ | | 0.54 | 0.50 | 0.37 |
| 2 | √ | | √ | | 0.31 | 0.27 | 0.45 |
| 3 | | √ | √ | | 0.46 | 0.43 | 0.39 |
| 4 | √ | | √ | √ | 0.59 | 0.56 | 0.35 |
| **5** | | **√** | **√** | **√** | **0.62** | **0.59** | **0.33** |

[a] Refers to the fraction of particles smaller than 2 µm by mass

From Table 5.3, the chosen regression model for predicting critical shear stress of the silt-clay soil mixtures in this study was:

$$\hat{\tau}_c = -25.99 + 0.016\rho_b + 91.97Clay - 0.049(\rho_b \times Clay) \tag{5.12}$$

The statistics relating to the goodness-of-fit of this model are: $R^2 = 0.62$, $R_a^2 = 0.59$, and

$SE_{\tau_c} = \pm 0.33\ Pa$. The predicted critical shear stress values ($\hat{\tau}_c$) were plotted against the

measured critical shear stress values ($\tau_c$) in Figure 5.9.

From equation 5.12, positive effects of bulk density and clay content on critical shear stress are indicated by the coefficients of these two terms. This finding is consistent with many previous studies, such as Mitchener and Torfs (1996), Houwing (1999), Panagiotopoulos et al. (1997), Amos et al. (2004), Bale et al. (2006, 2007), Barry et al. (2006), and Geremew and Yanful (2011) as reviewed in sections 2.4.2 and 2.4.3, showing that the erosion resistance of sediments increases as bulk density and/or clay content increase. This is because that the increase of bulk density makes the soils more solid and the increase of clay content provides more interparticle attraction which pulls sediments together (Watts et al., 2003; Amos et al., 2004; Debnath et al., 2007; Grabowski et al, 2011). Nevertheless, a negative correlation between bulk density and clay content especially in soils composed of fine-grained sediments predominantly has been diagnosed (Figure 5.4). Thus the interaction term in equation 5.12, that is the product of bulk density and clay content, offsets a part of the additive effects on the critical shear stress accounting for the negative correlation between the two predictors. Equation 5.12 is only valid in estimating values of critical shear stress of soils consisting of predominantly fine-grained sediments since clay content is one of the main predictors.
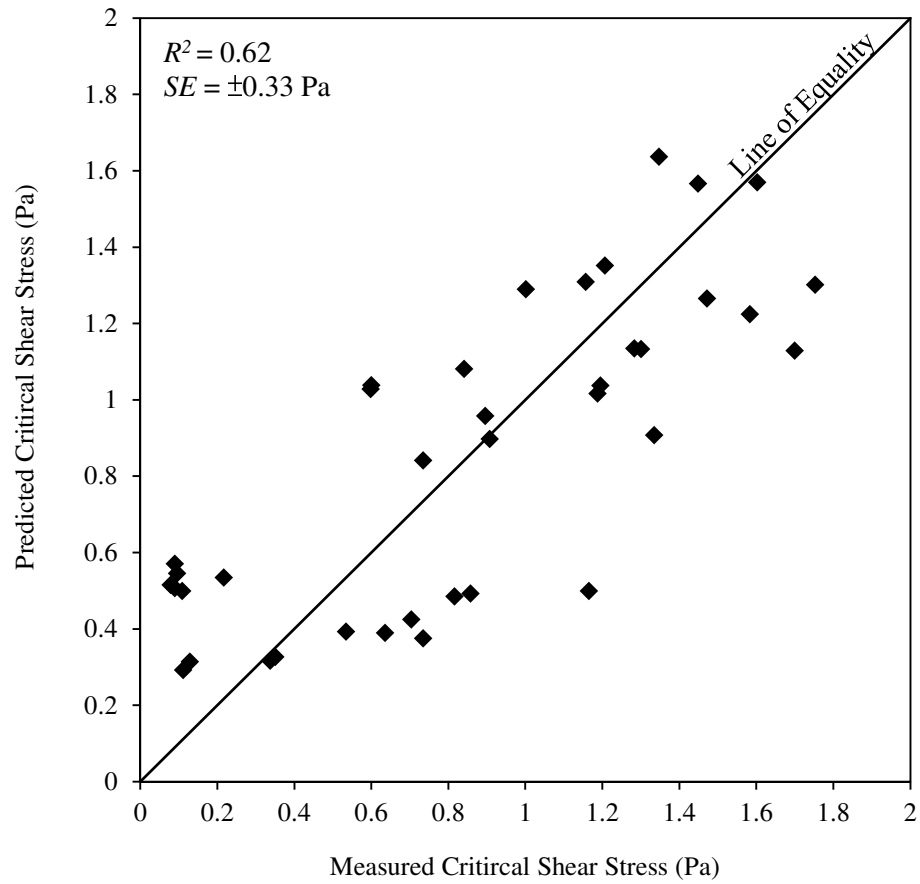
Figure 5.9 Predicted critical shear stress versus measured values

Best-fit curves calculated from equation 5.12 by setting *Clay* equal to different values show the relationships between the critical shear stress and bulk density of sediments with specified clay contents. Theses curves are shown in Figure 5.10 with the measured critical shear stresses obtained in this study and those in Roberts et al. (1998). In the figure, the best-fit curves showing the variation of critical shear stress with bulk density in sediments are closer to one another in the range of 3% to 15% clay contents. The relatively narrow spacing of these curves within a small range of clay content indicates a more rapid change of the critical shear stress-bulk density relationship, and it can be inferred that soil properties and erosion behavior transition from coarse-sediment to fine-sediment primarily within the range of clay content of 3% to 15% as reported in the literature (Alvarez-Hernandez, 1990, Dade and Nowell, 1991; Mitchener and Torfs, 1996; Panagiotopoulos et al., 1997).

While the critical shear stress is influenced positively by both bulk density and clay content in the low bulk density range, the effect of clay content on the critical shear stress diminishes as bulk density increases. The best-fit curves for different clay contents converge as bulk density increases to 1900 kg/m$^3$ in Figure 5.10, and above this value, bulk density becomes the major determining factor for the critical shear stress. The converge point of bulk density (1900 kg/m$^3$) may be considered as an upper limit of bulk density when applying equation 5.12 to predict critical shear stress. In reality, sediments with high bulk densities (over 2000 kg/m$^3$) are mostly composed of coarse particles (Navarro, 2004; Hobson, 2008) and thus equation 5.12 is not applicable since it was developed for the case of fine-grained sediments. From another point of view, in soils composed of coarse sediments predominantly, the erosion resistance mainly comes from

the weight of coarse particles due to gravity (Sturm, 2001; Santamarina, 2001; Sheppard et al., 2004).

Measurements of the critical shear stress of silt specimens from Roberts et al. (1998) coincide with the proposed regression model (equation 5.12) by plotting to the right of the 3% clay content best-fit curve, along with a few data points of the soil mixtures with clay content less than 3% in this study. Although the silt specimens in the experiments of Roberts et al. (1998) did not contain clay minerals, a small quantity of quartz particles which are smaller than 2 μm contribute to the clay content up to about 5% in one of the mixtures. Measurements of this mixture from Roberts et al. (1998) are indicated by the upper curve of the open diamonds in Figure 5.10, which coincides with the data points of 0%~3% Clay mixtures in this study (closed circles).

In the experiments of Roberts et al. (1998), the stacks of data points (open diamonds in Figure 5.10) representing different critical shear stress at a specific bulk density result from the quartz particles with different $d_{50}$ but are prepared with the same predetermined water content. In Figure 5.10, at the same bulk density, silt specimens with a smaller $d_{50}$ of Roberts et al. (1998) resulted in a higher critical shear stress. Among the stacks of open diamonds, two series of data points from Roberts et al. (1998) show high bulk densities (close to 2000 kg/m$^3$). Nevertheless, the $d_{50}$ of those silt specimens from Roberts et al. (1998) is not as small as clay-size; thus lower values of critical shear stress were found compared to those of the soil mixtures with 0%~3% Clay in this study. Comparison between data from Roberts et al. (1998) and the data of this study (closed circles) shows that the existence of clay (Georgia kaolin in this study) provides cohesion

between particles and increases the critical shear stress even though the proportion of clay was as low as 3% or less.
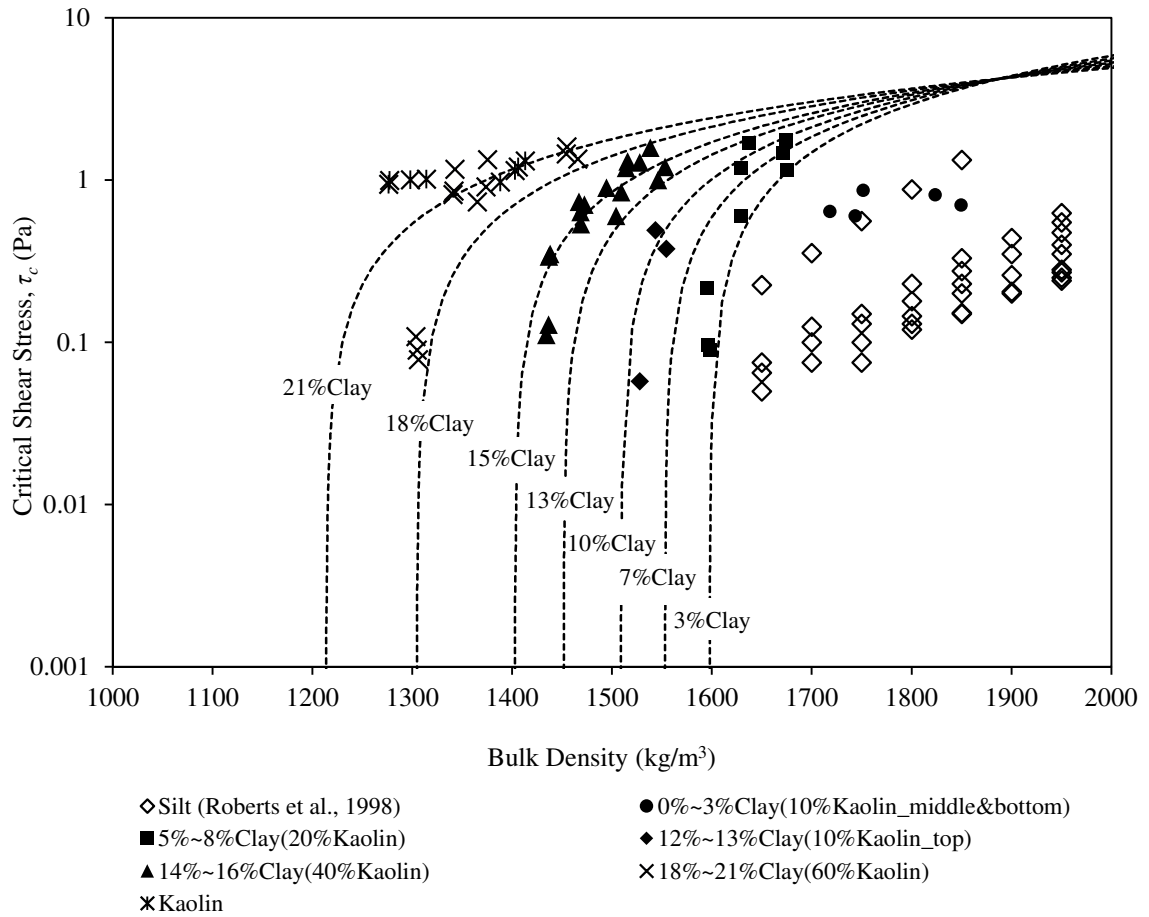


Figure 5.10 Plot of critical shear stress versus bulk density with clay content as a parameter of fine-grained sediments

From the river bed sediments collected in the field around the state of Georgia (Navarro, 2004; Hobson, 2008), Hobson (2008) proposed a multiple linear regression model to predict $\tau_c$ as:

$$\hat{\tau}_c = -0.303 + 26.6 Fines - 55.7 OM + 3.23 d_{50} \tag{5.13}$$

where $Fines$ = the content of silt- and clay-size particles by mass (decimal fraction) and $OM$ = organic matter content (decimal fraction). The comparison between equations 5.12 and 5.13 suggests that (1) a similar effect of clay and fine contents to the critical shear stress is found in equations 5.12 and 5.13, respectively; (2) $OM$ is not considered in equation 5.12 due to the absence of organic matter in the specimens of this study; (3) $d_{50}$ is included in equation 5.13 instead of $\rho_b$ because of the coarse sediments in the field-collected specimens studied by Navarro (2004) and Hobson (2008).

### 5.3.2 Dimensionless Form of Critical Shear Stress Relationship

For coarse (noncohesive) sediments of relatively uniform size, the critical shear stress is given as a function of the submerged specific weight of the sediment ($\gamma_s - \gamma_w$), grain diameter, $d$, water density, $\rho_w$, and water viscosity, $\mu$ (Sturm, 2001):

$$\tau_c = f_1(\gamma_s - \gamma_w, d, \rho_w, \mu) \tag{5.14}$$

From dimensional analysis, equation 5.14 results in:

$$\tau_c^* = \frac{\tau_c}{(\gamma_s - \gamma_w)d} = f_2\left(\frac{d\sqrt{\tau_c/\rho_w}}{\mu/\rho_w}\right) = f_2\left(\frac{d \cdot u_c^*}{\nu}\right) = f_2(Re_c^*) \tag{5.15}$$

where $u_c^* = $ critical shear velocity, and $\tau_c^*$ and $\mathrm{Re}_c^*$ are dimensionless variables, introduced as *Shields parameter* and *critical boundary Reynolds number*, respectively. These two parameters were developed by Shields (1936) to describe incipient sediment motion in the Shields diagram, which has been widely used by hydraulic engineers. The Shields parameter can be interpreted as the ratio of the applied bed shear stress to gravitation force per unit volume at critical conditions, and it represents a dimensionless form of critical shear stress which takes the submerged specific weight of sediments into account. In accordance with the work of Navarro (2004) and Hobson (2008), values of Shields parameter of the silt-clay soil mixtures were calculated from the measured $\tau_c$ and $d_{50}$ in this study. Then a regression analysis was applied to the Shields parameter as the response variable. In this analysis, the possible predicting variables which would go through the subset selection procedure remained as the four predictors mentioned in section 5.2.1. Through the procedures of the regression model determination as described in the previous section (5.2.1), Table 5.4 and Table 5.5 show the result of subset selection and the statistics of potential regression models of Shields parameter, respectively.

Table 5.4 Subset predictor selection of Shields parameter regression model

| Models | Predictor Used | | | | $AIC_p$ | $C_p$ | SE |
|---|---|---|---|---|---|---|---|
| | $w$ | $\rho_b$ | Clay [a] | $d_{50}$ | | | |
| Initial | √ | √ | √ | √ | 139.63 | 5.00 | 3.49 |
| Potential(1) | √ | √ | √ | | 144.33 | 9.48 | 3.67 |
| Potential(2) | √ | √ | | √ | 211.02 | 144.74 | 6.81 |
| **Potential(3)** | **√** | | **√** | **√** | **137.63** | **3.00** | **3.45** |
| Potential(4) | | √ | √ | √ | 141.55 | 6.70 | 3.58 |

[a] Refers to the fraction of particles smaller than 2 μm by mass

Table 5.5 Summary of potential Shields parameter regression models

| Potential models | Predictor used | | | | $R^2$ | $R_a^2$ | SE |
|---|---|---|---|---|---|---|---|
| | $w$ | Clay [a] | $d_{50}$ | Interaction term | | | |
| 1 | √ | √ | √ | | 0.86 | 0.85 | 3.45 |
| 2 | √ | √ | | | 0.81 | 0.80 | 4.02 |
| 3 | √ | | √ | | 0.38 | 0.36 | 7.24 |
| **4** | **√** | **√** | | **√** | **0.88** | **0.88** | **3.17** |
| 5 | | √ | √ | √ | 0.74 | 0.73 | 4.72 |

[a] Refers to the fraction of particles smaller than 2 μm by mass

From Table 5.5, the model determined to predict Shields parameters of the silt-clay mixtures in this study is given as:

$$\hat{\tau}_c^* = 8.46 - 27.76w + 73.69Clay + 83.22(w \times Clay) \tag{5.16}$$

The statistics relating to the goodness-of-fit of this model are: $R^2 = 0.88$, $R_a^{\,2} = 0.88$, and

$SE_{\tau_c^*} = \pm 3.17$. The predicted Shields parameter values ($\hat{\tau}_c^*$) were plotted against the

measured values ($\tau_c^*$) in Figure 5.11.

From equation 5.16, a negative and a positive effect on Shields parameter of water content and clay content, respectively, are indicated by the coefficients with opposite signs of these two terms. This finding is confirmed by the studies of Watts et al. (2003), Amos et al. (2004), and Bale et al. (2006), who concluded that the erosion resistance of fine-grained sediments increases as water content decreases but as clay content increases. In soils of predominantly fine sediments, a decrease of water content often leads to an increase in bulk density (Debnath et al., 2007; Grabowski et al., 2011). Thus, effects of the predictors on the erosion resistance of fine sediments shown in equations 5.12 and 5.16 can be explained in the same manner. In addition, the interaction term between water and clay contents in equation 5.16 is positive, which is illustrated by the positive correlation between them as shown in Figure 5.3. Comparing to equation 5.12, the regression model predicting Shields parameter of fine-grained sediments (equation 5.16) takes the submerged weight and particle size into account and results in a better prediction (with higher values of $R^2$ and $R_a^{\,2}$) of the erosion resistance using two dimensionless predictors, i.e. water and clay contents (in decimal fractions).
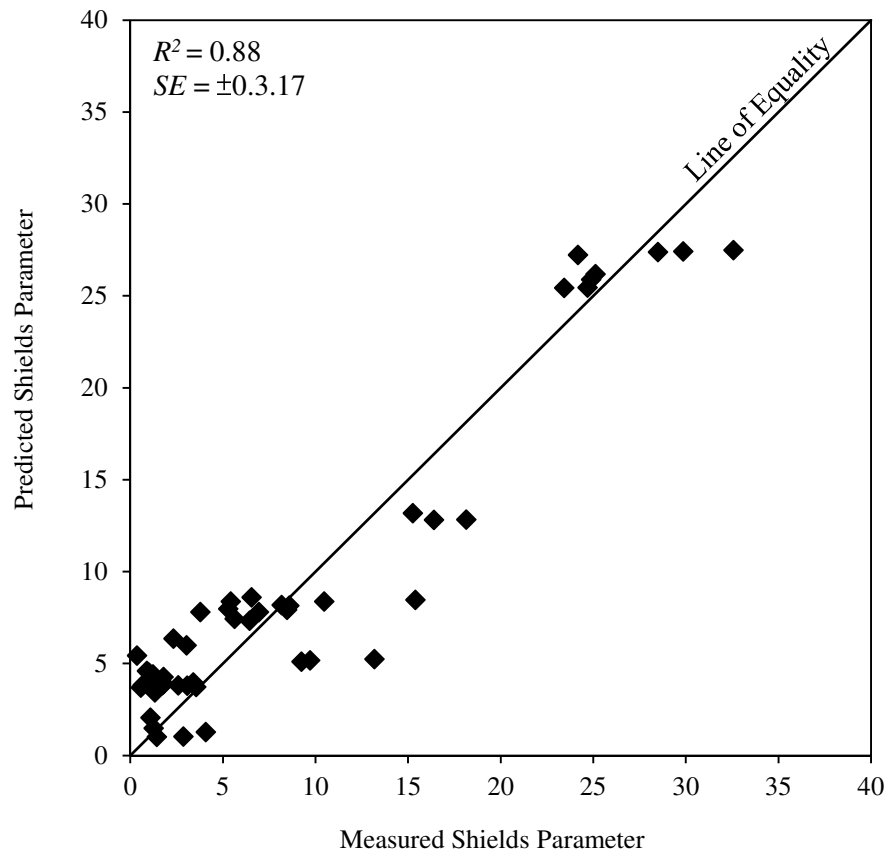
Figure 5.11 Predicted Shields parameter versus measured values

In Figure 5.12, the measured Shields parameters were plotted against the water contents of the silt-clay mixtures in this study; the best-fit curves of equation 5.16 with specified clay contents are shown as well. The pattern of the best-fit curves shows a reverse trend in Figure 5.12 in comparison with those in Figure 5.10 due to the inverse relationship between water content and bulk density. Because the maximum pore water content is subject to the clay content, the data points which plot in the high water content area in Figure 5.12 belong to the soils with higher clay or kaolin content. Meanwhile, they have larger Shields parameters due to the smaller $d_{50}$ of the soils. For instance, a clay content that is at least 15% or close to 20% is expected in a soil specimen of 200% water content according to the figure.

The 30%-clay content best-fit curve coincides with the data points from pure kaolin specimens of which the fraction of particles smaller 2 μm by mass, i.e. the definition of clay content used in this study, was around 0.3 based on the grain size distribution. In this case, the effect of clay content diminished as the soils became homogeneous and the Shield parameters were still influenced, but insignificantly, by the water content. Although it is unreasonable to expect zero water content of fine-grained sediments collected in erosion-prone areas, the lower bound of water content ( $w = 0\%$ ) may be considered as the contribution of the cohesion caused by clay particles to the erosion resistance. For soils with water contents as low as 10%, the Shields parameter increases from 10 to more than 30 as clay content increases from 3% to 30%. The Shields parameters calculated from the Roberts et al. (1998) data were plotted in Figure 5.12 as well. Depending on the grain size distributions, the proportions of clay-size particles ranged from 0% to 6% despite the fact that the sediments were composed of quartz

particles. Roberts et al. (1998) data generally agreed with equation 5.16 because most of

their data points plot in the area of clay content smaller than 7%.
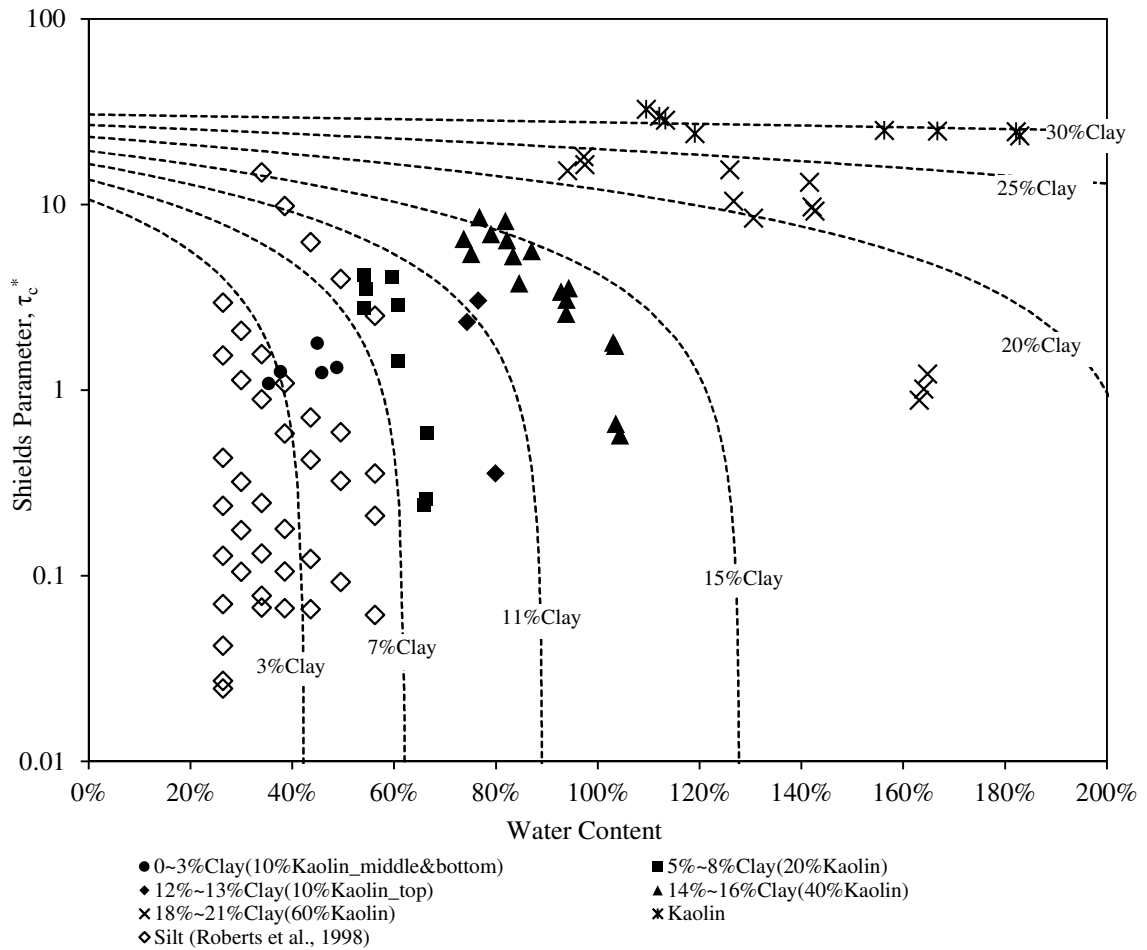


Figure 5.12 Shields parameter versus water content with best-fit curves of equation 5.15

While equation 5.16 was constructed based on the silt-clay mixtures in this study and thus was meant to predict the Shields parameter of soils consisting of fine sediments predominantly, it was also applied to  the prediction of the Shields parameters of river bed sediments collected in the field and investigated by Navarro (2004) and Hobson (2008). Data points of the current and previous studies were plotted in Figure 5.13 (*a*) and (*b*), along with the best-fit curves obtained from equation 5.16 in part (*a*) and the following equation fitted to all the data in part (*b*):

$$\hat{\tau}_c^* = 6.88 - 22.66w + 74.24Clay + 68.06(w \times Clay) \tag{5.17}$$

Equation 5.17 was constructed using the same predictors, $w$, *Clay* , and their interaction term, as in equation 5.16, but the coefficients were estimated based on all the data including the river bed sediments from Navarro (2004) and Hobson (2008), and the quartz particles from Roberts et al. (1998), in addition to the soil specimens of this study.

In comparing the two regression models (equations 5.16 and 5.17), the clay content contributes to the Shields parameter equivalently in both models, indicated by the similar values of the coefficient. However, the negative effect of water content was less significant in equation 5.17 since the bulk density was not chiefly dependent on water content of soils with coarse sediment content. For the same reason, the positive correlation between the water content and clay content in such soils was less obvious; thus, it led to a smaller coefficient of $w \times Clay$ in equation 5.17. Performance of the two models was evaluated by calculating the goodness-of-fit criteria, mainly $R^2$ and $SE_{\tau_c^*}$, of the predicted Shields parameters by using equation 5.16 and 5.17, respectively. These quantities are: $R^2 = 0.56$, $SE_{\tau_c^*} = \pm 5.97$ and $R^2 = 0.57$, $SE_{\tau_c^*} = \pm 5.65$ of equation 5.16 and 5.17, respectively. Based on these criteria, equations 5.16 and 5.17 show almost

equally good performance although the latter were constructed using all the available data sets. In other words, the regression model constructed using only the data of the silt-clay mixtures in this study can explain almost the same proportion of the total variance in the field sediment data as that can be explained by the model which was constructed using the data from both the laboratory and field specimens.

In Figure 5.13, the percentage of clay content is shown in the label next to each data point of the field sediments. With a few exceptions, the field data points plotting below the 7% clay content best-fit curve generally contain clay proportions from 2% to 8% in both plots of the figure. In addition, an increasing trend of clay content was observed among the field data with Shields parameters larger than 10, which agrees with the best-fit curves. However, due to the heterogeneity of the size distributions and the existence of coarse particles in the field sediments, the unexplained variance by the regression model with respect to the field data is expected. Furthermore, the majority of the field data has a $d_{50}$ classified as sand or gravel while only a few samples were representative of the silt-size range based on a $d_{50}$.
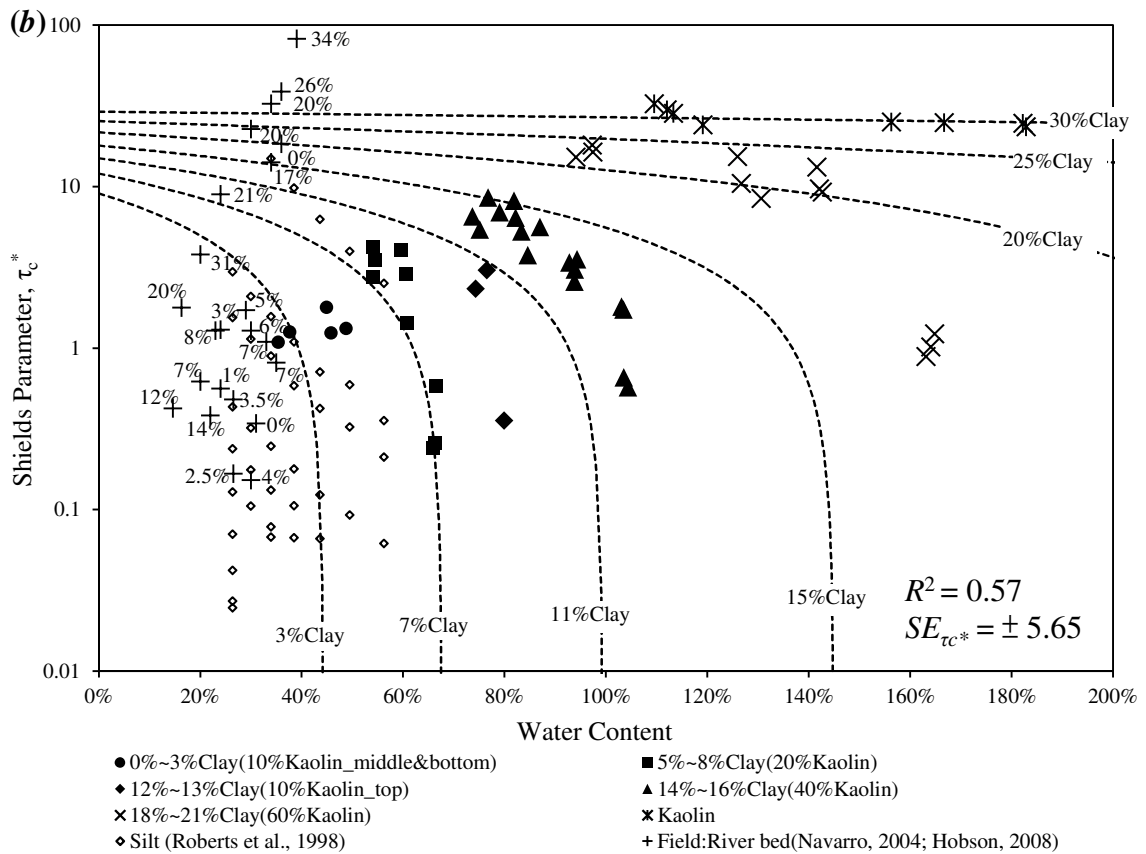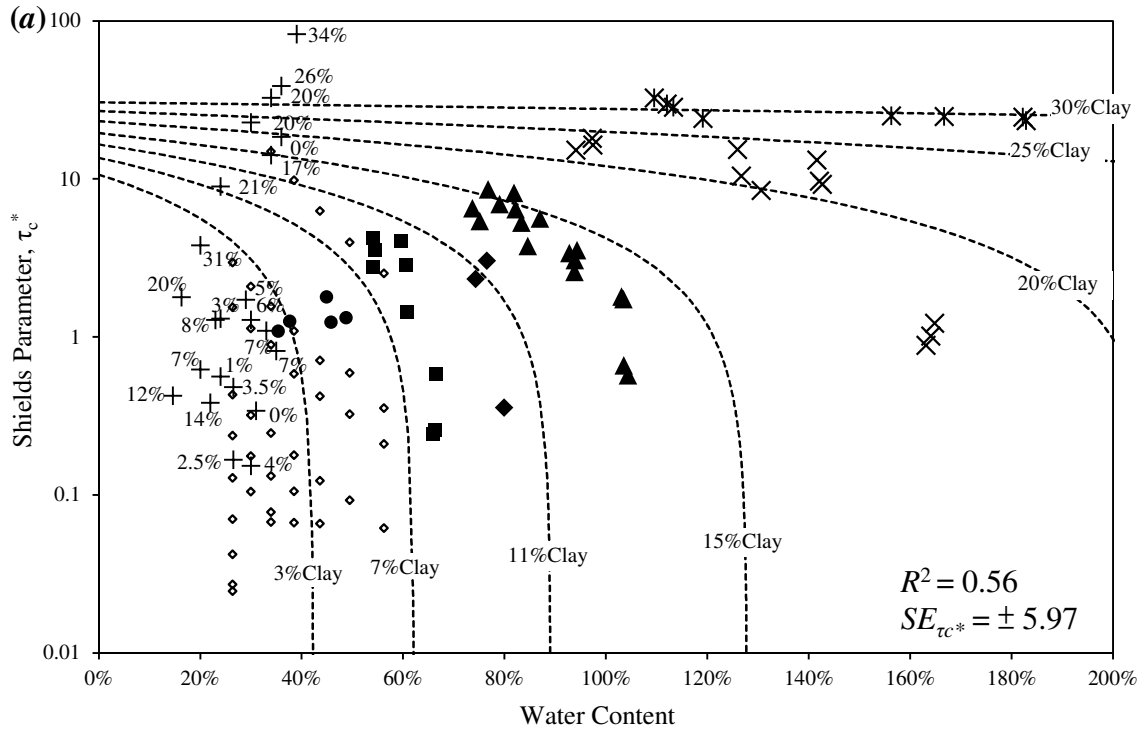
Figure 5.13 Shields parameter versus water content (field data included); best-fit curves obtained by fitting the data: (*a*) in this study only and (*b*) with field data

In the research of Hobson (2008), the Shields parameter of the river bed sediments composed of coarse and fine particles (Navarro, 2004; Hobson, 2008) can be predicted by the fine content as:

$$\hat{\tau}_c^* = 0.211 \times 10^{3.35 Fines} \tag{5.18}$$

Equation 5.18 illustrates the effect of fine, cohesive particles on the erosion resistance of soil mixtures with a $d_{50}$ larger than silt-size but consisting of both coarse and fine particles. Overall, Shields parameter was originally developed for non-cohesive coarse sediments. Thus for coarse and non-cohesive sediments, the widely used Shields diagram is still one of the most applicable methods to estimate the erosion resistance of the soils. When the content of fines (silt and clay) is taking into account to predict the Shields parameters of field sediments with $d_{50}$ larger than silt-size, the nonlinear regression models proposed by Hobson (2008) (equations 5.13 and 5.18) provide other alternatives. The regression models (equations 5.12 and 5.16) constructed in this study provides yet another possible solution to estimate the erosion resistance of fine, cohesive sediments through predicting the Shields parameter, which has been commonly used for coarser sediments.

## 5.4 Predicting Yield Stress from Sediment Properties

### 5.4.1 Yield Stress Relationship

In the literature, the yield stress of soil-water mixtures composed of fine, cohesive sediments has been reported to depend on the volumetric concentration of solids. Particularly, many of the previous studies, e.g. Fei (1981), O'Brien and Julien (1988),

and Cousset (1994), suggested a power relationship between the yield stress and the solid volumetric concentration as shown in the following:

$$\tau_y = \alpha_y e^{\beta_y C_v} \tag{5.19}$$

where $\alpha_y$ and $\beta_y$ are experimental constants. From those studies, $\alpha_y$ and $\beta_y$ ranged from $7.07 \times 10^{-4}$ to 2.60 and 7.82 to 32.7, respectively. The experimental constants varied not only among different studies but deviated depending on the source/type of sediments within a study. It is concluded that values of $\alpha_y$ and $\beta_y$ are case dependent and only one set of values of $\alpha_y$ and $\beta_y$ is applicable to describe one particular type of soil mixture. Power relationships between $\tau_y$ and $C_v$ were also found in the silt-clay mixtures of this study. While the resulting $\alpha_y$ and $\beta_y$ coincide with the ranges reported in the literature, different values of $\alpha_y$ and $\beta_y$ were obtained depending on the kaolin content of the mixtures. Obviously, a more general model is expected to estimate the yield stress by considering sediment source or composition of a mixture in addition to the solid concentration or density.

As discussed previously in section 2.9, the yield stress may be considered as a shear stress threshold above which the flow motion of cohesive sediments initiates due to the breakage of interparticle bonds. Based on this concept, the same subsets of predictors in the regression models relating to the critical shear stress should be applicable in the regression analysis of the yield stress. As shown in Table 5.6, the result of subset selection for the yield stress regression model confirms with this assumption. Furthermore, the statistics of the potential regression models of yield stress shown in

Table 5.7 indicates that the optimal regression model of the yield stress has the same form as that of the critical shear stress (equation 5.12).

Table 5.6 Subset predictor selection of yield stress regression model

| Models | Predictor Used | | | | $AIC_p$ | $C_p$ | SE |
|--------|---|---|---|---|---------|-------|-----|
| | $w$ | $\rho_b$ | $Clay$ $^a$ | $d_{50}$ | | | |
| Initial | √ | √ | √ | √ | 19.78 | 5.00 | 1.47 |
| **Potential(1)** | **√** | **√** | **√** | | **17.84** | **3.05** | **1.43** |
| Potential(2) | √ | √ | | √ | 26.37 | 11.05 | 1.77 |
| Potential(3) | √ | | √ | √ | 17.89 | 3.07 | 1.43 |
| Potential(4) | | √ | √ | √ | 20.52 | 5.21 | 1.53 |

$^a$ Refers to the fraction of particles smaller than 2 μm by mass

Table 5.7 Summary of potential yield stress regression models

| Potential models | Predictor used | | | | $R^2$ | $R_a^{\,2}$ | SE |
|------------------|---|---|---|---|-------|-----|-----|
| | $w$ | $\rho_b$ | $Clay$ $^a$ | Interaction term | | | |
| 1 | √ | √ | √ | | 0.71 | 0.66 | 1.43 |
| 2 | √ | | √ | | 0.71 | 0.68 | 1.39 |
| 3 | | √ | √ | | 0.62 | 0.58 | 1.59 |
| 4 | √ | | √ | √ | 0.72 | 0.66 | 1.42 |
| **5** | | **√** | **√** | **√** | **0.73** | **0.68** | **1.38** |

$^a$ Refers to the fraction of particles smaller than 2 μm by mass

The regression model predicting the yield stress of the silt-clay soil mixtures in this study is given as:

$$\tau_y = -24.67 + 0.012\rho_b - 59.17Clay + 0.079(\rho_b \times Clay) \tag{5.20}$$

The statistics relating to the goodness-of-fit of this model are: $R^2 = 0.73$, $R_a^2 = 0.68$, and

$SE_{\tau_y} = \pm 1.39 Pa$. The predicted yield stress ($\hat{\tau}_y$) is shown plotted against the measured

yield stress ($\tau_y$) in Figure 5.14. From these statistics (higher $R^2$ and $R_a^2$), the regression

model gives a better fit of the yield stress compared to equation 5.12, which predicts the

critical shear stress using the same predictors. Besides $R^2$ and $R_a^2$, the relative standard

error ($\dfrac{SE}{\mu}$, $\mu =$ mean of the measurements) can be used to compare the goodness-of-fit

between equations 5.12 and 5.20. Specifically, $\left(\dfrac{SE}{\mu}\right)_{\tau_c} = \pm 0.40$ and $\left(\dfrac{SE}{\mu}\right)_{\tau_y} = \pm 0.45$,

which indicates that equation 5.12 and 5.18 result in similar performances of predicting

the critical shear stress and yield stress, respectively. From equation 5.20, a positive

effect of bulk density but a negative effect of clay content on the yield stress is suggested.

Despite the fact that the existence of clay provides interparticle attraction, bulk density

decreases substantially in soft soils (e.g. Amos et al., 2004; Gerbersdorf et al., 2007) due

to the increasing water content as clay content increases. Thus the decrease in yield stress

caused by the clay content increase can be explained by observing that the cohesion from

clay is not sufficient to overcome the decrease in sediment bulk density due to a higher

clay proportion. Because bulk density and clay content influences the prediction of yield

stress oppositely, the coefficient of the product term, $\rho_b \times Clay$, is positive while $\rho_b$ and

*Clay* are negatively correlated (Figure 5.4). Alternatively, the positive effect of

$\rho_b \times Clay$ on the yield stress accounts for the cohesion of clay, which competes with the

negative effect of *Clay* on the yield stress due to bulk density decrement.
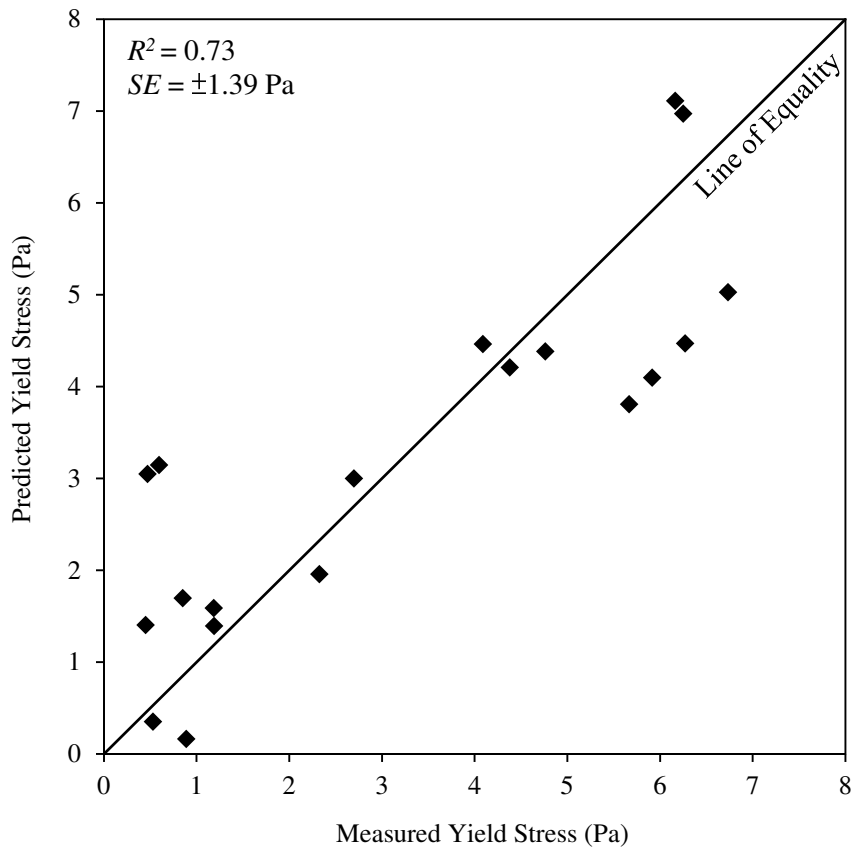
Figure 5.14 Predicted yield stress versus measured values

216

Figure 5.15 shows the best-fit curves calculated from equation 5.20 by setting

*Clay* equal to different values, illustrating the relationships between the yield stress and

bulk density of sediments with specified clay contents. A similar trend was found in the

best-fit curves predicting the yield stress as those for critical shear stress (Figure 5.10).

That is, bulk density and clay content both affect the yield stress in the low bulk density

range; then the influence of clay content decreases as bulk density increases. However,

clay content still affects the yield stress prediction even though the bulk density of soils is

high. Due to the limitation of most commercial rheometers, only the yield stress values of

soils composed mostly of fine sediments can be obtained from the rheometer tests, and

thus the yield stress has been discussed commonly in the scope of fine-grained sediments

(Nguyen and Boger, 1992; van Kessel, 1998; Barnes and Nguyen, 2001; Hobson, 2008).

As equation 5.20 was developed for fine-grained sediments, the high bulk density region

of this relationship is applicable to fine sediments with high bulk densities because of low

water contents but not to sediments with a high proportion of coarse particles.

Notwithstanding some studies as reviewed in section 2.9 that have investigated the yield

stress measurements of soils containing coarse particles, such as heterogeneous mudflow

and debris flow by devices other than rheometers, they are not included in the scope of

this research.
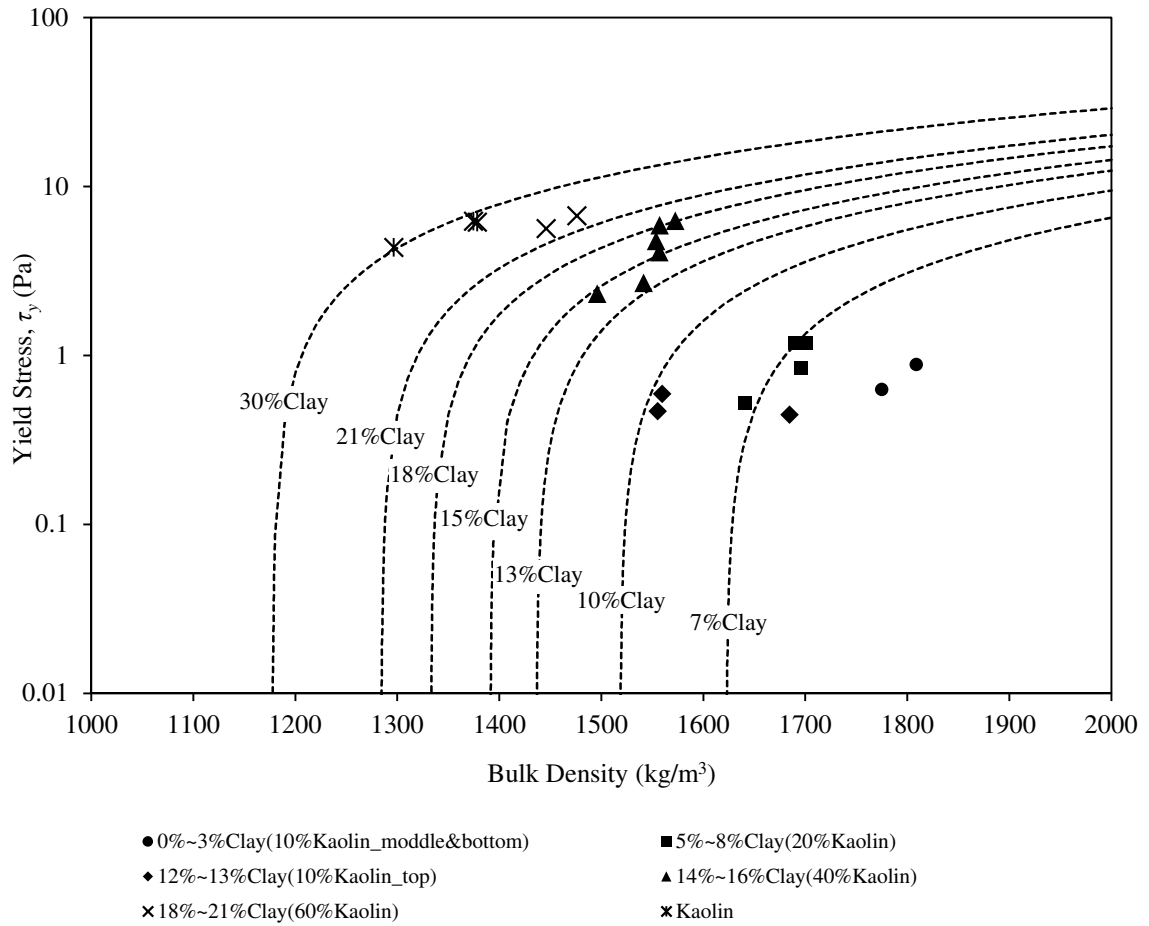
Figure 5.15 Plot of yield stress versus bulk density with clay content as a parameter of fine-grained sediments

### 5.4.2 Dimensionless Form of Yield Shear Stress Relationship

As shown in equation 5.16, the Shields parameter represents a dimensionless form of the critical shear stress. For the sake of comparison, a dimensionless yield stress ($\tau_y^*$) was developed by substituting the yield stress for the critical shear stress in the Shields parameter, which is shown as:

$$\tau_y^* = \frac{\tau_y}{(\gamma_s - \gamma_w)d} \tag{5.21}$$

where $d = d_{50}$ in accordance with the analysis of $\tau_c^*$. Dade et al. (1992) investigated the erosion resistance of muds by analyzing the balance of forces acting on cohesive grains at the threshold of motion. They considered the equilibrium between the lift and drag forces imposed by the flow and the gravitational, frictional, and cohesive forces of the sediments. From their study, the ratio of interparticle adhesion or cohesion force ($F_A$) to the submerged weight of a soil particle ($W_s$), $F_A/W_s$, was defined as the relevant predictor of motion of particles at the sediment-water interface. The parameter $F_A/W_s$ was assumed to be proportional to the dimensionless yield stress in the form of equation 5.21 with constants representing the effect of particle shape and particle packing angle. In their study, Dade et al. (1992) considered $\tau_y^*$ to be a useful measure of particle cohesion in the erosion resistance analysis of cohesive sediments. Since $F_A$ is recognized to result from the presence of van der Waals attraction and electrostatic forces in clay suspensions (Dade et al., 1992; Mahmood et al., 2001), it is rational to assume that $\tau_y^*$ is affected by the predictors of the Shields parameter for cohesive sediments including water and clay contents.

The procedures including subset selection and intercorrelation investigation were also applied to propose the potential regression models for the dimensionless yield stress. From Table 5.8, neither $AIC_p$ nor $C_p$ was improved by excluding any one of the predicting variables. Nevertheless, the second lowest values of $AIC_p$ and $C_p$ are found in the subset of $w$, $Clay$, and $d_{50}$ (Potential model(3) in Table 5.8). In addition, since bulk densities were calculated from measurements of water content, which resulted in a direct dependency between $\rho_b$ and $w$ of the silt-clay specimens in this study, $\rho_b$ was excluded from the selected subset predictors. Therefore, the selected subset predictors remained as $w$, $Clay$, and $d_{50}$ in accordance with the regression analysis of the Shields parameter.

Table 5.8 Subset predictor selection of dimensionless yield stress regression model

| Models | Predictor Used | | | | $AIC_p$ | $C_p$ | SE |
|---|---|---|---|---|---|---|---|
| | $w$ | $\rho_b$ | $Clay$ $^a$ | $d_{50}$ | | | |
| Initial | √ | √ | √ | √ | 115.29 | 5.00 | 11.15 |
| Potential(1) | √ | √ | √ | | 122.64 | 12.04 | 13.30 |
| Potential(2) | √ | √ | | √ | 164.39 | 151.0 | 32.96 |
| **Potential(3)** | **√** | | **√** | **√** | **116.36** | **5.57** | **11.60** |
| Potential(4) | | √ | √ | √ | 116.68 | 5.97 | 11.83 |

$^a$ Refers to the fraction of particles smaller than 2 μm by mass

Table 5.9 Summary of potential dimensionless yield stress regression models

| Potential models | Predictor used | | | | $R^2$ | $R_a^{\,2}$ | SE |
|---|---|---|---|---|---|---|---|
| | w | Clay [a] | $d_{50}$ | Interaction term | | | |
| 1 | √ | √ | √ | | 0.95 | 0.94 | 12.60 |
| 2 | √ | √ | | | 0.90 | 0.89 | 19.94 |
| 3 | √ | | √ | | 0.73 | 0.70 | 32.23 |
| **4** | **√** | **√** | | **√** | **0.95** | **0.94** | **12.05** |
| 5 | | √ | √ | √ | 0.84 | 0.82 | 25.11 |

[a] Refers to the fraction of particles smaller than 2 μm by mass

The potential regression model of the dimensionless yield stress and their statistics are tabulated in Table 5.9. From the table, the optimal regression model of the dimensionless yield stress using three predictors is composed of $w$, $Clay$, and the interaction term, Explicitly, the regression model to predict $\tau_y^*$ was obtained as:

$$\hat{\tau}_y^* = 83.27 - 280.43w + 531.88Clay + 684.22(w \times Clay) \tag{5.22}$$

The statistics relating to the goodness-of-fit of this model are: $R^2 = 0.95$, $R_a^{\,2} = 0.94$, and $SE_{\tau_y^*} = \pm 12.05$; and the predicted values ($\hat{\tau}_y^*$) were plotted against the measurements of the dimensionless yield stress ($\tau_y^*$) in Figure 5.16. According to the statistics, the dimensionless yield stress is predicted with more accuracy than the yield stress, which agrees with the case of the Shields parameter and the critical shear stress. In addition to the comparison of $R^2$ and $R_a^2$, the relative standard errors are $\left(\dfrac{SE}{\mu}\right)_{\tau_y^*} = \pm 0.23$ and

$\left(\dfrac{SE}{\mu}\right)_{\tau_c^*} = \pm 0.39$ of equations 5.22 and 5.16, respectively, which suggests a better performance of equation 5.22 in predicting $\tau_y^*$ than equation 5.16 in predicting $\tau_c^*$.

Comparing equations 5.16 and 5.22, all of the predicting variables, i.e. $w$, $Clay$, and $w \times Clay$, affect $\hat{\tau}_y^*$ in the same directions as their effects on $\hat{\tau}_c^*$. Therefore, the explanations regarding the influences of water and clay contents on erosion resistance of fine-grained sediments apply here to the yield stress, which is one of the most important rheological characteristics of soft soils (van Kessel, 1998; Barnes, 1999; Czibulya et al., 2010). ). Although there is agreement in signs of the coefficient of each term in equation 5.22, the magnitude is generally one order larger than the coefficient of the corresponding term in equation 5.16. This deviation in magnitude of the coefficients is expected because values of $\tau_y^*$ (Figure 5.16) are five to ten times higher than the corresponding values of $\tau_c^*$ (Figure 5.11). The relationship between the yield stress ($\tau_y$ and $\tau_y^*$) and the critical shear stress ($\tau_c$ and $\tau_c^*$) will be discussed in detail in the next section.
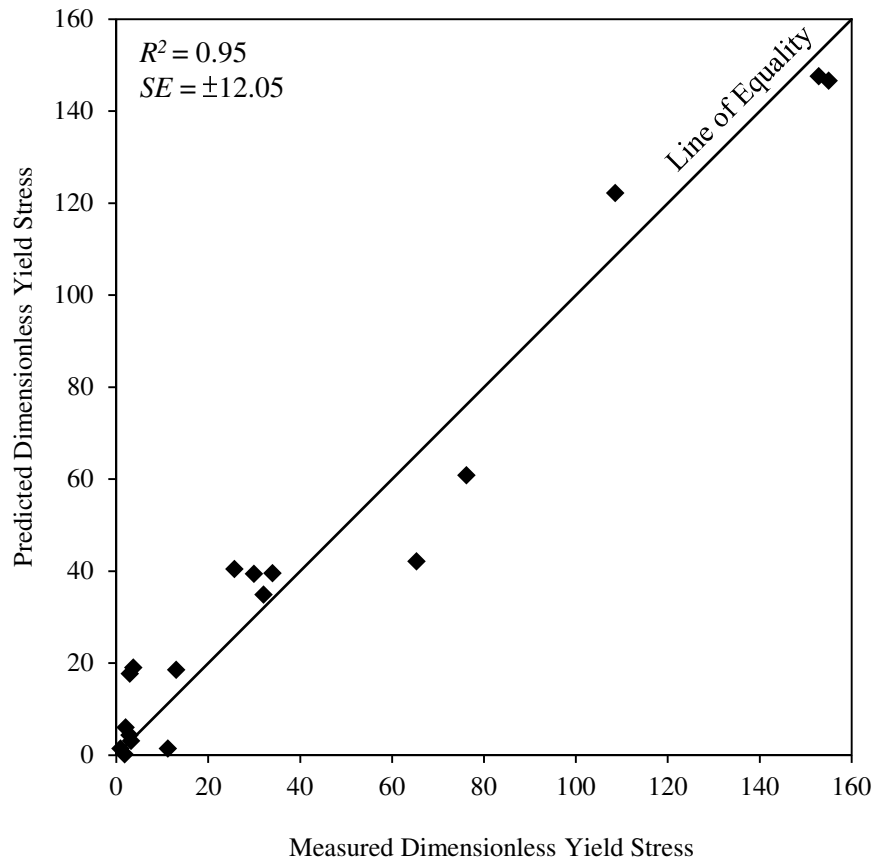
Figure 5.16 Predicted dimensionless yield stress versus measured values

In Figure 5.17, values of the measured dimensionless yield stress were plotted against the water contents of the silt-clay mixtures in this study; the best-fit curves of equation 5.22 with specified clay contents are shown as well. For the same reason as is discussed in section 5.3.2 for Figure 5.12, sediments with a smaller $d_{50}$ led to a larger value of $\tau_y^*$ since the increment of $\tau_y$ was not sufficient to cover the smaller decrease in $(\gamma_s - \gamma_w)d_{50}$ due the decrease in $d_{50}$, which was caused by a higher clay content. Meanwhile, a higher clay content increases the maximum pore water capacity and thus led to a soil specimen with a higher water content. As shown also in Figure 5.12, data points for 100% kaolin specimens agree with the 30%-clay content best-fit curve in Figure 5.17. In soils composed of one material and are thus homogeneous, water content becomes the major predictor of $\tau_y^*$. In the low water content region where $w$ is around 5% to 10%, the best-fit curves for different clay contents show the contribution of the interparticle attraction to $\tau_y^*$. Mainly, $\tau_y^*$ increases with the increase of clay content which leads to a strengthened interparticle network. It can be concluded that the geotechnical properties of soils, including bulk density, water content, and clay content, influence the rheological characteristics (yield stress) in a similar fashion as they affect the erosion threshold (critical shear stress) of fine-grained sediments.
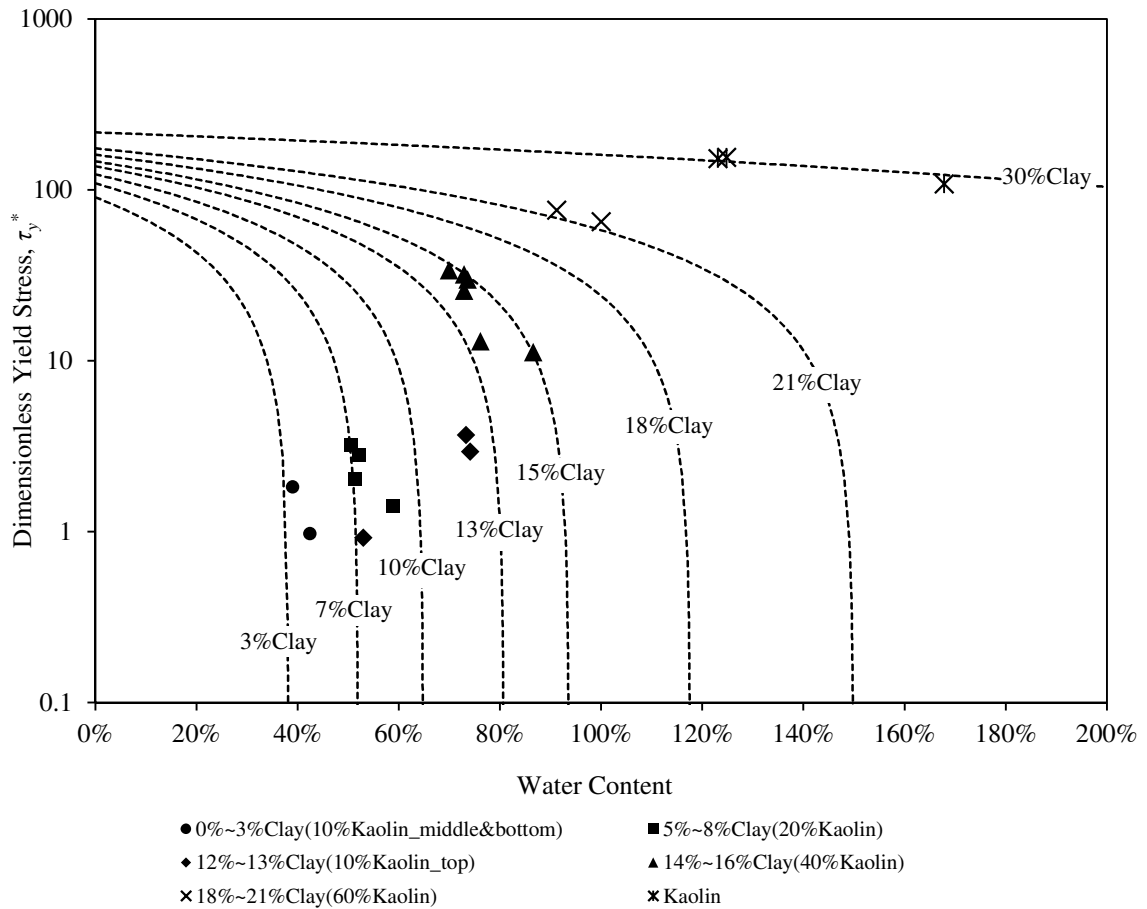
Figure 5.17 Dimensionless yield stress versus water content with clay content as a parameter of fine-grained sediments

## 5.5 Relationship between Yield Stress and Critical Shear Stress

The erosional strength of fine, cohesive sediments is usually represented by the critical shear stress. On the other hand, the yield strength of fine sediments is represented by the yield stress (e.g. Dade et al., 1992; Williams and Williams, 1989), which can be obtained by extrapolating to the zero strain rate of a flow curve in rheological tests.

In a research of mud erosion resistance, Williams and Williams (1989) related the yield stress and critical shear stress through a systematic analysis of fine sediment properties. They proposed a potential scaling for the critical shear stress, which is given by (Dade et al., 1992):

$$\tau_L \leq \tau_c \leq \tau_y \tag{5.23}$$

where $\tau_L$ = the upper limit of shear stress under which fine sediments show linear viscoelastic behavior. Therefore, a shear stress with a magnitude between $\tau_L$ and $\tau_y$ results in a nonlinear viscoelastic deformation because of an incipient breakdown of some weak interparticle bonds. Due to the partial breakdown of interparticle bonds, this stress value can be considered as the threshold of bed shear stress at which particles/aggregates movement initiates, i.e. $\tau_c$ . When the stress exceeds $\tau_y$ , the breakage of most interparticle bonds leads to an irreversible flow deformation. Thus, the yield stress is considered as an upper bound of the critical shear stress.

Empirical correlations of the yield stress and critical shear stress have been suggested by previous researchers such as Migniot (1968) and Ostubo and Muraoka (1988). In particular, Migniot (1968) proposed two relationships corresponding to high and low yield strength muds, respectively. The high yield strength muds referred to the

cohesive sediments with $\tau_y$ larger than 1.6 Pa and the low yield strength muds were those with values of $\tau_y$ smaller than 1.6 Pa. In the research of Migniot (1968), values of $\tau_c$ were approximately one quarter of the corresponding $\tau_y$ values for high yield strength muds. On the other hand, $\tau_c$ was proportional to the square root of $\tau_y$ for low yield strength or weakly cohesive muds. Based on this concept, positive correlations are expected between the yield stress and critical shear stress of the silt-clay mixtures in this study. Measurements of the critical shear stress plotted versus the corresponding yield stress of the silt-clay mixtures are shown in Figure 5.18, along with the relationships of $\tau_c$ and $\tau_y$ proposed by Migniot (1968).
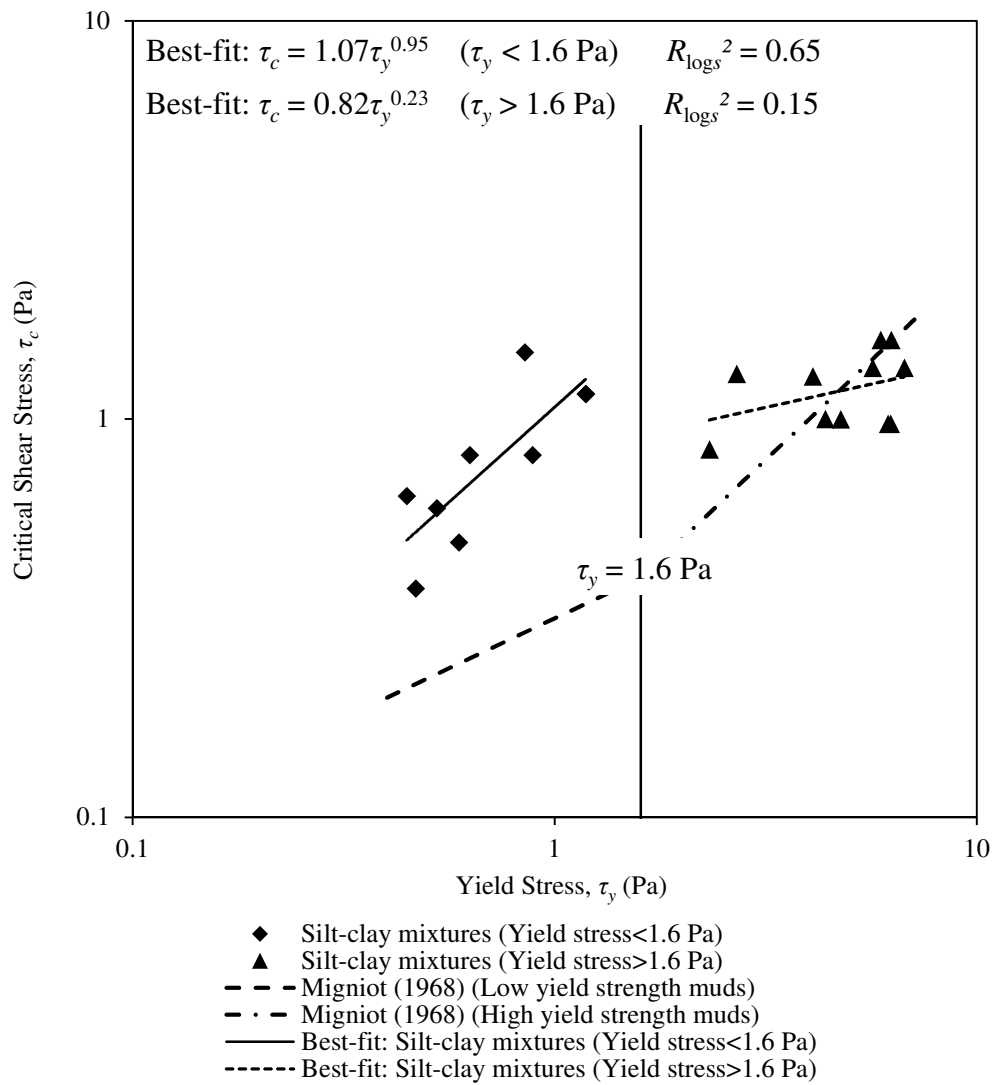
Figure 5.18 Measurements of critical shear stress versus yield stress of the silt-clay mixtures in this study

As shown in Figure 5.18, the measurements in this study do not follow Migniot (1968)'s relationships exactly. However, the criterion of Migniot (1968) distinguishing high or low yield strength sediments is still applicable to the data in this research. Data points for the silt-clay mixtures in this study cluster into two groups depending on whether $\tau_y$ is smaller or larger than 1.6 Pa. From Table 4.8, the soil mixtures with 10% and 20% kaolin contents belong to the low yield strength muds and the others (40% to 100% kaolin content specimens) belong to the high yield strength muds. The correlation between $\tau_c$ and the corresponding $\tau_y$ of the silt-clay mixtures in this study can be described quantitatively by best-fit power relationships as follows:

$$\hat{\tau}_c = 1.07\left(\tau_y\right)^{0.95} \qquad \text{if } \tau_y < 1.6 Pa \tag{5.24}$$

$$\hat{\tau}_c = 0.82\left(\tau_y\right)^{0.23} \qquad \text{if } \tau_y > 1.6 Pa \tag{5.25}$$

Based on Migniot (1968)'s classification, equations 5.24 and 5.25 describe the correlation between $\tau_c$ and $\tau_y$ for low and high yield strength muds, respectively. From equation 5.24, values of $\tau_c$ and $\tau_y$ are similar for the low yield strength muds ($\tau_y < 1.6$ Pa); nevertheless, magnitudes of $\tau_c$ is slightly smaller than 0.23 power of the corresponding $\tau_y$ for the high yield strength muds ($\tau_y > 1.6$ Pa) as shown in equation 5.25.

Although equations 5.24 and 5.25 provide an estimation of the critical shear stress using yield stress for low and high yield strength muds, respectively, one single equation which can describe the relationship between $\tau_c$ and $\tau_y$ of both low and high yield strength fine sediments is desired. Therefore, the dimensionless form of the critical shear stress (i.e. Shields parameter, $\tau_c^*$) and yield stress (i.e. dimensionless yield stress, $\tau_y^*$)

were used and plotted in Figure 5.19. Consequently, $\tau_c^*$ can be directly related to $\tau_y^*$ by

a best-fit power equation:

$$\hat{\tau}_c^* = 1.42\left(\tau_y^*\right)^{0.55}$$ (5.26)

For comparison, Table 5.10 shows the statistics of equations 5.24 to 5.26.

Table 5.10 Statistics of the relationships between the yield stress and critical shear stress

| Equation | $R^2_{\log s}$ | $R^2_{a \log s}$ | $SE_{\log s}$ | $SE_{\log s}/\mu_{\log s}$ [a] |
|----------|----------------|------------------|---------------|-------------------------------|
| 5.24 | 0.65 | 0.60 | ±0.12 | ±1.05 |
| 5.25 | 0.15 | 0.06 | ±0.09 | ±1.28 |
| 5.26 | 0.96 | 0.96 | ±0.09 | ±0.12 |

[a] $\mu_{\log s}$ is the mean value of the logs of the critical shear stress or Shields parameter measurements
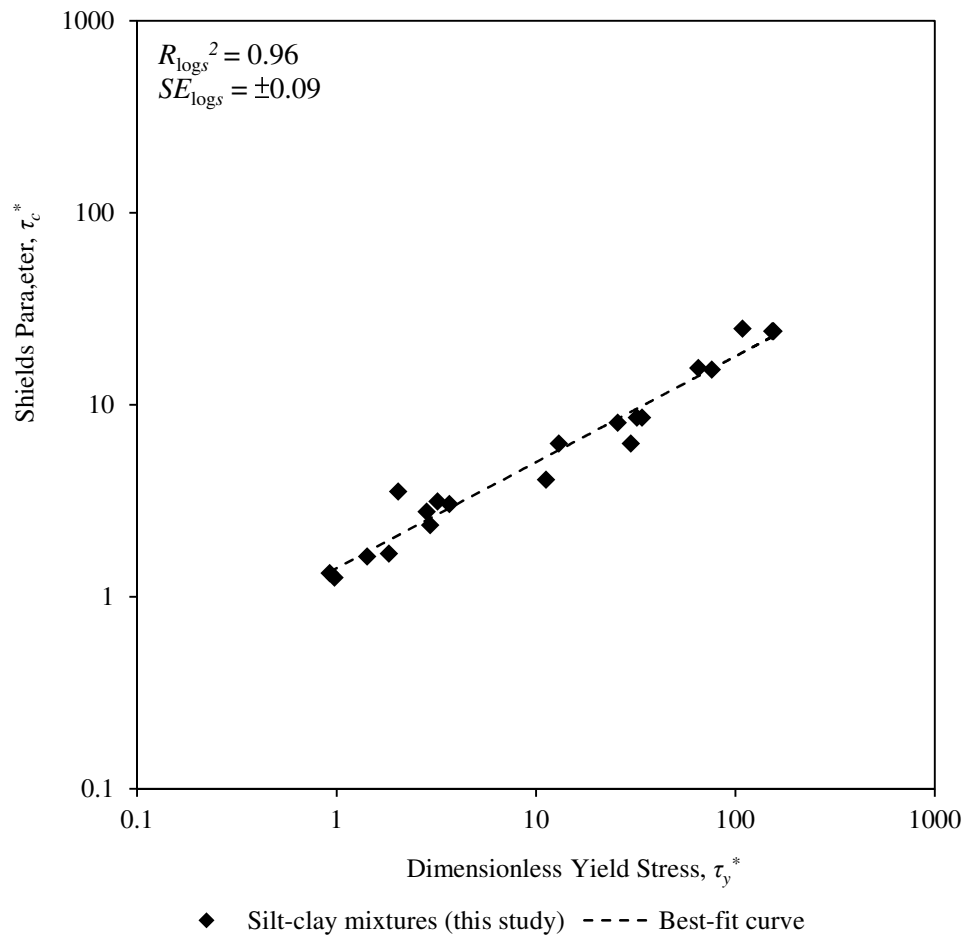
Figure 5.19 Measurements of dimensionless critical shear stress (Shields parameter) versus dimensionless yield stress of the silt-clay mixtures in this study

From Table 5.10, equation 5.26 predicts the response variable well with a small relative standard error ($SE_{\log s}/\mu_{\log s} = \pm 0.12$). In contrast, equations 5.24 and 5.25 predict the response variable with larger uncertainty with $SE_{\log s}/\mu_{\log s}$ of $\pm 1.05$ and $\pm 1.28$, respectively, due to the scattering of the data points as shown in Figure 5.18. The high goodness-of-fit of equation 5.26 not only indicates good predictions of the Shields parameter using the dimensionless yield stress, but implies the integration of relationships between $\tau_c$ and $\tau_y$ for low and high yield strength muds (i.e. equations 5.24 and 5.25) into a single relationship. The comparison between Figure 5.18 and Figure 5.19 illustrates that two groups of data points in Figure 5.18 collapse to a single trend line (Figure 5.19) covering the range from low to yield stress as $\tau_c$ and $\tau_y$ were non-dimensionalized by being divided by $(\gamma_s - \gamma_w)d_{50}$ and became $\tau_c^*$ and $\tau_y^*$, respectively.

Based on the concept of the balance of forces, the interpretation of the Shields parameter, $\tau_c^*$, is the ratio of bed shear stress ($\tau_c$) to the submerged weight per unit surface area of a grain ($(\gamma_s - \gamma_w)d$) at the critical stage of sediment incipient movement. Similarly, the dimensionless yield stress, $\tau_y^*$, can be interpreted as the ratio of interparticle cohesion force ($\tau_y$) to the submerged weight of particles ($(\gamma_s - \gamma_w)d$) at the yield point. Therefore, $\tau_c^*$ and $\tau_y^*$ represent the dimensionless form of $\tau_c$ and $\tau_y$, respectively, and consider the effect of gravitation force by including the submerged weight.

Accordingly, the collapse of the two groups of data points in Figure 5.18 can be considered to result from the inclusion of the gravitation force (or submerged weight) as a

reference force, into the erosion resistance of fine-grained sediments. Furthermore, the submerged weight is directly related to the size of particles or $d_{50}$. In other words, for fine-grained sediments, the relationships between $\tau_c$ and $\tau_y$ for low and high yield strength muds are integrated into one equation when the particle size is taken into account. This conclusion may seem to contradict the concept of neglecting the effect of particle size (or submerged weight) as Santamarina (2001) discussed with respect to the importance of forces in erosion resistance for coarse vs. fine-grained sediments. Actually, the relative influence of the submerged weight of fine sediments is still small in comparison with that of coarse sediments when estimating the erosion resistance of soils consisting of particles with a wide range of sizes. In this case, the proportion of fine particles in the soils became important due to the interparticle cohesion of fine sediments. From the studies of Navarro (2004) and Hobson (2008), the Shields parameter was found to be a function of the fine content ( *Fines* ) and the dimensionless particle size ( $d_*$ ) as:

$$\hat{\tau}_c^* = 0.644 \times 10^{2.68\,Fines}\, d_*^{\,-0.409} \tag{5.27}$$

where *Fines* is in decimal fraction by mass and $d_* = \sqrt[3]{\dfrac{(\gamma_s - \gamma_w)d_{50}^3}{v^2}}$ .

Hobson (2008) further considered that $d_*$ might be a redundant predictor for the Shields parameter of the sediments studied in Navarro (2004) and Hobson (2008), and he proposed another relationship as shown in equation 5.18. The regression statistics for equations 5.27 and 5.18 are $R^2_{\log s} = 0.90$ ; $SE_{\log s} = \pm 0.28$ and $R^2_{\log s} = 0.88$ ; $SE_{\log s} = \pm 0.30$ , respectively. Notwithstanding equation 5.18 gives similar regression statistics as equation 5.27 does using *Fines* alone, the exclusion of $d_*$ in equation 5.18

neglects the influence of flow's viscous effect on the erosion process carried by $d_*$ (Hobson, 2008). Thus Hobson (2008) considered equation 5.27 as a more adequate relationship to predict the Shields parameter of the sediments studied in Navarro (2004) and Hobson (2008).

From multiple regression analysis, Hobson (2008) related the dimensionless lower yield stress ($\tau_{y_1}^*$) with $d_*$ as:

$$\tau_{y_1}^* = 1.45 \times 10^6 d_*^{-3.04} \tag{5.28}$$

where $\tau_{y_1}^*$ was calculated by $\dfrac{\tau_{y_1}}{(\gamma_s - \gamma_w)d_{50}}$ and $\tau_{y_1}$ is the lower yield stress obtained by the graphical method as illustrated in Figure 3.14. By rearranging equations 5.27 and 5.28, the relationship of $\tau_c^*$ and $\tau_{y_1}^*$ was proposed as (Hobson, 2008):

$$\hat{\tau}_c^* = 0.644 \times 10^{2.48 Fines} \left( \frac{\tau_{y_1}^*}{1.45 \times 10^6} \right)^{0.134} \tag{5.29}$$

where $\tau_{y_1}^*$ has the same mathematical form as $\tau_y^*$ in equation 5.26 for this study, which was calculated by $\dfrac{\tau_y}{(\gamma_s - \gamma_w)d_{50}}$ and $\tau_y$ is the yield stress obtained by fitting a flow curve with the Herschel-Bulkley Model as illustrated in Figure 3.16. In this research, values of $\tau_y$ were determined as the shear stress at which the fitting curves of Herschel-Bulkley Model intercept with the axis of shear stress for zero strain rate (Figure 3.16) instead of the graphical methods shown in Figure 3.14 and Figure 3.15 for the following reasons. First, the critical point at which strain rates start to be non-zero may be illustrated and described physically by the Herschel-Bulkley Model. Second, rather than the mechanical

strength which describes the failure of an entire sediment plan, the $\tau_y$ obtained using Figure 3.16 defines the occurrence of incipient flow movement which can be observed at the same scale of incipient particle/aggregate movement at the critical shear stress $\tau_c$.

The comparison between equations 5.26 and 5.29 suggests that the Shields parameter is related to the dimensionless form of yield stresses as power relationships. In addition to the power relationship between $\tau_c^*$ and $\tau_{y_1}^*$, *Fines* is included in equation 5.29 to account for the interparticle cohesion of fine sediments.

In this study, only fine-grained sediments were considered and the soil specimens were mixed from Georgia kaolin and ground silt in this study. The content of fines, *Fines*, is excluded in equation 5.26 since *Fines* equals to 100% for all the specimens in this study. From another aspect, if *Fines* in equation 5.29 is designated as 100%, the equation can be reduced to the form of equation 5.26. In other words, a power equation can relate the Shields parameter with the dimensionless yield stress if the soils are composed of fine sediments only (silt + clay) in Hobson's (2008) result.

From the discussion above, interparticle cohesion of fines plays a more significant role in providing the erosion resistance of sediments when sediment particle size decreases. While content of fines or muds (e.g. *Fines*) has been applied in many of the previous studies, the clay content (*Clay*) can be considered as a more specific parameter carrying the information of interparticle force since clay particles within mud actually provide the interparticle cohesion (van Ledden et al., 2004). In equation 5.26, the information of interparticle cohesion is not carried directly by the inclusion of *Clay* but by $d_{50}$ in the denominator indirectly. In section 5.1, Figure 5.5 shows the negative

correlation of $d_{50}$ with *Clay* of sediments from different sources, especially in soils composed primarily of fine sediments. In other words, a higher *Clay* results in a smaller $d_{50}$, which leads to a higher erosion resistance ($\tau_c$) of soils composed primarily of fine sediments as shown in Figure 2.3 and Figure 2.4. Furthermore, the yield stress ($\tau_y$) of fine-grained sediments is affected by *Clay* (as shown in equation 5.20) and thus by $d_{50}$. Therefore, the nondimensionalization of $\tau_c$ and $\tau_y$ may be interpreted as the inclusion of the effect of *Clay* expressed indirectly through $d_{50}$. Since the content of clay controls the interparticle cohesion in fine sediments and thus the yield stress, the inclusion of clay content effect accounts for the difference between low and high yield strength muds. Finally, the relationship between erosional strength ($\tau_c$) and yield strength ($\tau_y$) of fine-grained sediments can be illustrated by the power equation of $\tau_c^{*}$ and $\tau_y^{*}$ (equation 5.26).

## 5.6 Effects of pH Value and Ionic Strength on Particle Structure and Erosion Resistance

In this section, physical insights related to the proposed regression models, which predict fine sediment erosion resistance as a function of soil physical properties including clay content and bulk density, are explored from the perspective of particle structure under different pore water chemistry conditions.

As erosion resistance, i.e. critical shear stress, of cohesive (fine-grained) sediments has been recognized to depend on the microstructure due to interparticle forces (Zreik et al., 1998), researchers have made efforts in this area using kaolinite sediments, such as investigating the mechanisms of particle attachment and detachment by

calculating the total interaction force between particles (Mahmoon et al., 2001) and the effects of pore water chemistry (e.g. pH, organic matter, and ionic strength) on erosion resistance due to different interparticle structures (Keith et al., 1998; Ravisangar et al., 2001; Ravisangar et al., 2005). In this study, effects of pore water chemistry, including pH value and ionic strength, on the settling characteristics, bulk density, and critical shear stress of the silt-clay mixtures are discussed based on the conclusions from the previous studies.

In Table 4.5, the average pH value and specific conductivity of the pore water in each type of the soil mixture specimens with different kaolin contents are shown. While the tap water used to prepare the soil specimens was neutral (pH~7), the addition of kaolinite sediments in the mixtures decreased the pH and conductivity of the soil slurry. From conductivity, ionic strength can be estimated using the empirical equations for groundwater. Two of the equations which have been commonly applied were presented by Lind et al. (1959) and Russell (1976), respectively, and are given as:

$$IS = 1.4769 \times 10^{-5} \kappa_s + 0.00015 \tag{5.28}$$

$$IS = 1.6 \times 10^{-5} \kappa_s \tag{5.29}$$

where $IS$ = the ionic strength ($M$) and $\kappa_s$ = the specific conductivity ( $\mu S/cm$ ). Both equations 5.28 and 5.29 were used to estimate the ionic strength of pore water in the soil mixture specimens from the measurements of specific conductivity as reported in Table 4.5. As a result, values of $IS$ of all the soil mixtures range from $2 \times 10^{-3}$ to $3 \times 10^{-3}$ M using either one of the equations. According to Ravisangar et al. (2005), the pore water ionic strength of the soil mixtures in this study is classified as a low ionic strength condition (<0.004 M).

Under low ionic strength conditions, the particle associations and settling characteristics of kaolinite particles are more sensitive to pH than under high ionic strength conditions. Characteristics of the settling behavior of the soil mixtures with different kaolin contents were observed during specimen preparation and can be shown in Figure 3.1. During the settling period of 24 hours, a dispersed suspension was observed in the soil specimen composed of silica flour only, i.e. 0% kaolin content, while flocculated suspensions existed in all the other specimens with kaolin contents from 10% to 100%. Depending on the proportions of kaolin in the soil mixtures, flocculation of particles occurred and a clear, distinct interface between settling flocs and overlying water formed faster as the kaolin content increased. Meanwhile, pH of pore water decreased from 5.90 to 4.55 when kaolin content increased from 10% to 100% (Table 4.5).

The settling behavior can be explained by the discussion of particle associations and pH conditions as reviewed in Chapter II (Hillier, 1995; Mahmood et al., 2001; Ravisangar et al., 2001; Ravisangar et al., 2005). Accordingly, the edge-to-face (E-F) association is found predominantly under low pH (<5.5) conditions and flocculation occurs because of stronger van der Waals and short-range attractive forces caused by the compressed electrical double layer of charges on the face and edge of kaolinite particles. In contrast, edges of kaolinite particles become more negative as pH value increases which leads to electrostatic repulsion between particles and thus sediments tend to disperse in the suspension. In addition, the face-to-face (F-F) interaction becomes the dominant type under high pH (>7) conditions because the edge-to-edge (E-E) and edge-to-face (E-F) arrangements decrease correspondingly under such conditions.

Conditions of mixed particle associations instead of one predominant type found in soils were discussed in Mahmood (1996) and Ravisangar et al. (2005). From their discussion, aggregates of F-F association often link up with E-F and E-F arrangements to produce a continuous network. In this case, the dominant interparticle forces are the van der Waals and short-range attractions, and the settling behavior may consist of closely packed F-F aggregates which flocculate in E-F and/or E-E associations. In this study, one predominant particle association was unable to be identified in the SEM images (Figure 4.14) of the silt-clay mixtures by naked eye, which suggests mixed particle associations in all of the soil specimens with different kaolin contents.

Ravisangar et al. (2005) found relationships between critical shear stress and bulk density of kaolinite sediment beds with different particle structures achieved by varying the pore water chemistry. For comparison, the experimental results in this study were plotted with the best-fit lines of Ravisangar et al. (2005)'s results as shown in Figure 5.20. Since the variation of critical shear stress with bulk density has been illustrated in Figure 5.10 and discussed in section 5.3.1, the discussion here focuses on the best-fit trend line of each data series in this study with those corresponding to particle associations suggested by Ravisangar et al. (2005). The slopes of the best-fit lines generated from measurements of 20%-, 40%- and 60%-kaolin content specimens indicate a similar trend in comparison to the relationship suggesting an E-F structure (Ravisangar et al., 2005). Even though a predominant particle association is not shown in the SEM images of those specimens, similar sedimentation heights were observed in Figure 3.1, which suggests that the particle structures of 20% to 60% kaolin specimens may be very similar. While the predominant E-F and predominant F-F associations are two limiting cases, sediments

239

with combinations of both associations may fall between these limits, such as the soil specimens in this study. Furthermore, due to the existence of silt particles, which are usually not charged at the surface and thus provide relatively small interparticle forces, the critical shear stress of the silt-clay mixtures is generally lower than that of kaolinite sediments found by Ravisangar et al. (2005).

In Figure 5.20, data points of the 100%-kaolin content specimens show two distinctive groups at bulk densities around 1300 and 1400 kg/m$^3$, respectively. This is because different amounts of tap water were added during specimen preparation, and thus two types of 100%-kaolin content specimens were prepared. Each group of the data represents the individual type of 100%-kaolin content specimens. Therefore, a best-fit trend line was not generated for the 100%-kaolin content specimens since the data points came from two types of specimens prepared separately.

The stratification of bulk density with depth of sediments can be affected by the settling behavior of suspensions with different predominant particle associations. From the research of Ravisangar et al. (2005), relatively weak bulk density stratification with depth was found in settling of flocculated suspensions with primarily E-F associations. On the other hand, a strong stratification of bulk density with depth was formed by dispersed suspensions with F-F associations predominantly (Ravisangar, 2001; Ravisangar et al., 2005). Based on the relationships of bulk density with sediment depth shown in Figure 4.1, stratification of bulk density with depth was found to be significant in 10% kaolin specimens, but the stratification became less obvious with the increase of specimen kaolin content. Using the findings in Ravisangar et al. (2005), the decreasing bulk density stratification with specimen kaolin content found in Figure 4.1 may be

240

explained as transitions of particle structures from a case with a larger proportion of F-F association to a case with more E-F associations.

Although mixed particle associations were suggested from the SEM image of 10%-kaolin content specimens, the best-fit slope of the data points in Figure 5.20 results in a value between E-F and F-F structures, but closer to the latter. Since the 10%-kaolin specimens had an average pH value of 5.90, this intermediate value of the slope may be interpreted as a transition between E-F and F-F structures occurring under conditions of pH values from 5.5 to 7 (Ravisangar et al., 2001; 2005). In addition, strong density stratification has been shown in Figure 4.1($a$), which suggests settling from dispersed suspensions and a favorable F-F structure. From the analysis of grain size distribution as shown in Figure 4.2, segregation in settling was found in 10%-kaolin content specimens due to a significant proportion of large, heavy silt particles which settled down individually and rapidly along with a few large kaolinite aggregates during the initial settling period; then smaller or lighter silt particles and kaolinite aggregates settled progressively. Accordingly, the strong stratification of bulk density in 10%-kaolin content specimens shown in Figure 4.1($a$) and Figure 5.20 was mainly attributed to segregation during the settling process.
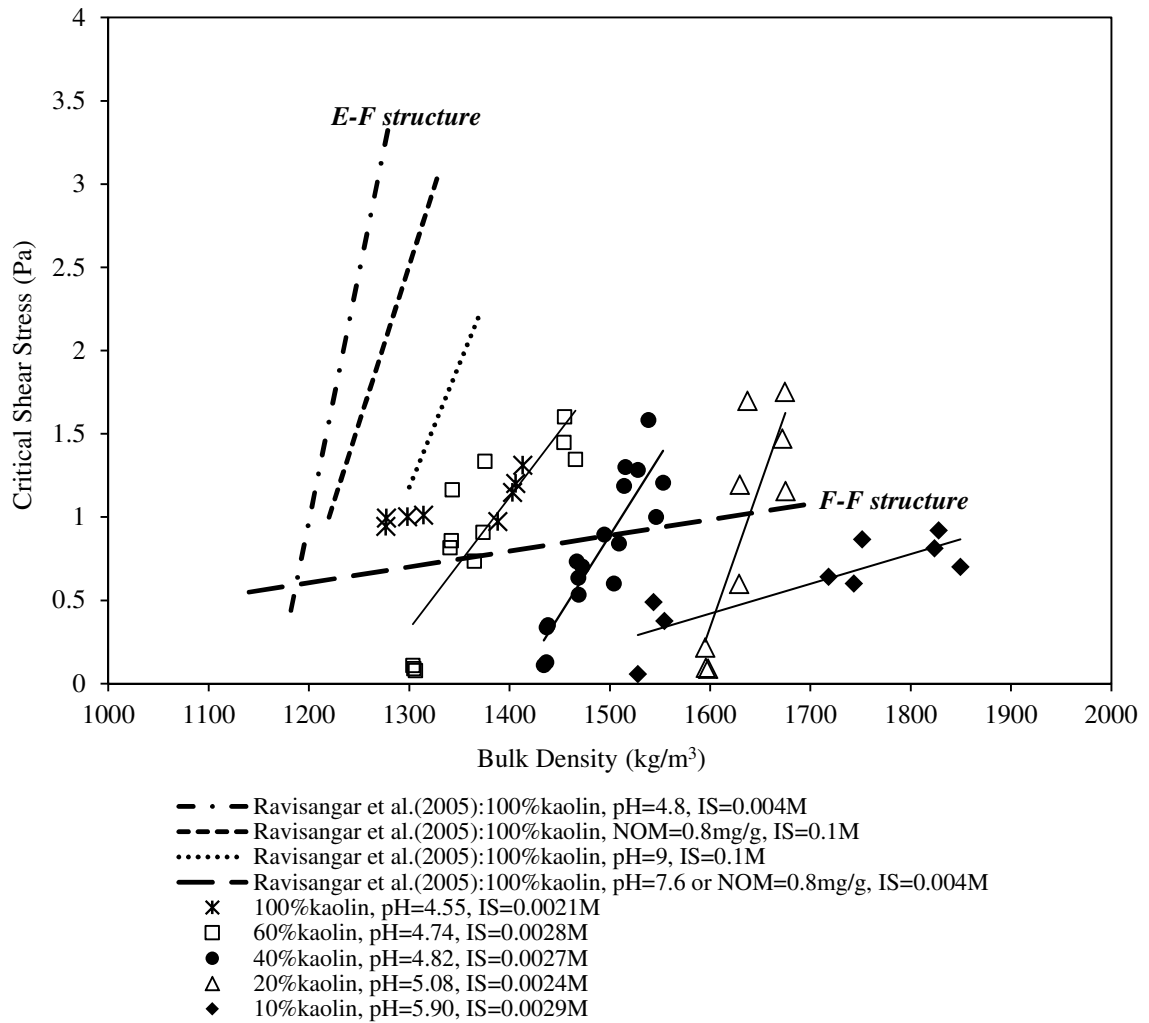
Figure 5.20 Relationships between critical shear stress and bulk density referring to particle associations

In summary, this study provides a methodology to estimate the values of critical shear stress for soils composed of predominantly fine sediments without using the erosion flume devices/experiments. Specifically, the Shields parameter can be predicted as a function of clay content and water content (equation 5.16), which can be carried out by conventional geotechnical tests. If rheometer tests are available to obtain values of the yield stress, the power equation proposed in this study (equation 5.26) provides a prediction of the Shields parameter with less uncertainty than equation 5.16 does. In this study, the equations are composed from the results of the soil mixtures with median particle size ($d_{50}$) from 2 μm to 40 μm, water content ($w$) from 135% to 185%, bulk density from 1200 kg/m$^3$ to 1900 kg/m$^3$, and clay content (*Clay*) from 3% to 30%. The pore water in the specimens had low ionic strength (0.002 M to 0.003 M) and pH values from 4.5 to around 6.

Since the proposed relationships (equations 5.16 and 5.26) are based on the experimental results using specimens with the described properties, these relationships are valid and applicable to soils that are composed of predominantly fine sediments having (1) bulk density less than 2000 kg/m$^3$, (2) $d_{50}$ in the range of silt-size particles, and (3) pore water of low ionic strength and pH values from 4 to close to neutral. For application, a $d_{50}$ of 100 μm can be a division for choosing between the relationships proposed by Hobson (2008), equations 5.27 and 5.29, and those from this research (equations 5.16 and 5.26). Specifically, the Shields parameter of sediments with $d_{50} > 100$ μm can be predicted using the equations of Hobson (2008); for sediments with $d_{50} < 100$ μm, equations 5.16 and 5.26 from this research should be applied to obtain values of the Shields parameter.

# CHAPTER VI

# CONCLUSIONS AND RECOMMENDATIONS

## 6.1 Summary

In this study, the erosion resistance of fine-grained sediment and the factors affecting it were investigated and discussed through several experiments and analyses using soil specimens of laboratory prepared silt-clay mixtures. The soil specimens were prepared with different silt and clay proportions by varying the ratio between the dry weights of ground silica and Georgia kaolin in the mixtures. Results for soil physical properties (e.g. grain size distribution, water content, bulk density), erosion rates, flow curves, and SEM images were obtained from several laboratory procedures, which included geotechnical tests, hydraulic flume experiments, rheometer tests, and the SEM technique, respectively. Then through regression analysis, values of the critical shear stress and yield stress for each specimen were obtained from the erosion rates and flow curve, respectively. After that, multiple regression analysis was applied to construct the relationships among soil physical properties, the critical shear stress, and the yield stress. Based on the research of Ravisangar et al. (2001; 2005) and the SEM images, effects of pore water chemistry, including pH and ionic strength, on bulk density and the critical shear stress of the silt-clay mixtures were discussed from the aspect of interparticle associations of sediments.

## 6.2 Conclusions

Based on the values of liquid limit and plasticity index, the soil specimens used in this study were classified as low plastic silty clay (CL-ML) when the kaolin content was lower than 20% by dry weight, and as medium to high plastic lean clay (CL) for the cases of higher kaolin contents. These classifications were found to be representative of field sediment samples collected in Georgia at bridge foundation sites throughout the state.

In comparison to the results of the literature review on fine-grained sediment erosion resistance, inter-correlations among the soil physical properties including water content, clay content, median particle size, and bulk density of the specimens in this study were illustrated and validated. For fine sediments, bulk density and water content are generally inversely correlated, and the increase of clay content leads to the decrease of median particle size and bulk density, but the increase of water content.

The bulk density of sediments within a specimen increased with depth as observed in the field. From Figure 4.1, the bulk density stratification with depth was found most obvious in the 10% kaolin specimens and the stratification diminished as kaolin contents increased. While the evidence of particle segregation was found only in 10% kaolin specimens from grain size distributions (Figure 4.2), the bulk density stratifications with depth in all the other specimens resulted primarily from the decrease in water content caused by the self-weight consolidation of sediments.

Due to the increase in bulk density with depth, the erosion rate was high at the surface of sediments (top layer) and then it decreased with depth of each specimen. The concave-up curves describing the relationships between erosion rate and bed shear stress were indicated by the exponents of the excess shear stress ($n$ in equation 2.17) larger than

unity in the cases of 10% to 60% kaolin specimens. For the 100% kaolin specimens, a linear erosion rate-bed shear stress relationship was indicated by a value of $n$ (in equation 2.17) close to unity of each specimen. In all of the soil specimens, the critical shear stress at zero erosion rate was found to be approximately 0.1 Pa in the top sediment layer, which was recognized as the "fluff layer" reported in the literature. Then the critical shear stress increased due to the increase in bulk density with depth in each specimen.

The comparison among specimens with similar bulk densities showed that the specimen with a higher kaolin/clay content resulted in a larger critical shear stress due to the interparticle forces provided by clay particles.

The flow curves obtained from the rheometer tests showed a yield stress with shear-thinning behavior for all the silt-clay soil mixtures in this study. These flow curves were fitted successfully by the Herschel-Bulkley model with the exponent of $(\tau - \tau_y)$ smaller than unity for the shear-thinning behavior. Similar to the variation of the critical shear stress with bulk density and clay content, the yield stress increased with bulk density within soil specimens of the same kaolin content. Among specimens with similar bulk densities, a higher yield stress was obtained in the specimen with a higher kaolin/clay content. The dependence of yield stress and critical shear stress on the same factors establishes the existence of a relationship between critical shear stress from the flume tests and yield stress from the rheometer tests.

Relationships between the soil physical properties and the critical shear stress or yield stress were expressed quantitatively through multiple regression analysis. For soils which consist predominantly of fine, cohesive sediments, both critical shear stress and

yield stress can be predicted as a function of bulk density and clay content (equations 5.12 and 5.20).

In dimensionless form, the Shields parameter and dimensionless yield stress can be predicted as a function of water content and clay content (equations 5.16 and 5.22). In comparison to the equation proposed by Hobson (2008), which predicts the Shields parameter of the river bed sediments as a function of fines (silt + clay) content ($Fines$) alone, equation 5.16 is proposed to predict the Shields parameter for soils composed of predominantly fine-grained sediments as a function of clay content ($Clay$) and water content ($w$). It is suggested that the equation proposed by Hobson (2008) can be used to predict the critical Shields parameter for Georgia soils with $d_{50} > 100$ μm while equation 5.16 developed in this thesis is limited to prediction of Shields parameter for $d_{50} < 100$ μm.

Positive correlations between the critical shear stress and yield stress of low and high yield strength muds have been discussed in the literature (e.g. Migniot, 1968). Based on the yield strength criterion proposed by Migniot (1968), the silt-clay mixtures in this study can be classified as either low or high yield strength muds depending on whether the yield stress is smaller or larger than 1.6 Pa. In this study, a relationship was found to estimate the critical shear stress as a function of the yield stress for the mixtures classified as either low or high yield strength muds, respectively. In dimensionless form, a single power equation was proposed to describe the relationship between the Shields parameter and dimensionless yield stress (equation 5.26) for all the soil specimens in this study. In equation 5.26, the effect of interparticle cohesion represented by clay content, which is different in low and high yield strength sediments, was taken into account through the

inclusion of $d_{50}$, and thus a single relationship was proposed for both low and high yield

strength sediments. The high value of the coefficient of determination ($R^2_{a\log s} = 0.96$) of

equation 5.26 suggests that the Shields parameter of the silt-clay mixtures can be

predicted by the corresponding dimensionless yield stress. In other words, the erosion

resistance of soils which consist of predominantly fine sediments can be predicted

without applying hydraulic flume devices/experiments, but as a function of the yield

stress obtained from rheometer tests.

Based on the values of pH and ionic strength, as well as the behavior of bulk

density stratification with depth, the silt-clay mixtures with 20% to 100% kaolin contents

are suggested to have a predominantly E-F association and are consistent with the study

of Ravisangar et al. (2005) on pure kaolin. This tentative hypothesis is based on

observations of the aggregated settling behavior, and the similar slopes of the best-fit

trend lines between critical shear stress and bulk density for E-F associations (Figure

5.20). On the other hand, the settling behavior of 10% to 60% kaolin mixtures could also

be caused by a physical mechanism, such as settling of large kaolinite particles along

with some small silt/kaolinite particles attached at the edge, rather than an electrical

mechanism (flocculation) between silt and kaolinite particles. While the best-fit line of E-

F structure proposed by Ravisangar et al. (2005) represents a limiting case, mixtures of

particle associations with E-F, E-E, and F-F structures are often observed in reality, and

this was confirmed with the SEM images of the soil mixtures in this study. Due to the

particle segregation in the settling of 10%-kaolin specimens, a strong density

stratification with depth was observed. Consequently, the data points of 10%-kaolin

specimens in Figure 5.20 show a trend similar to the best-fit line of the F-F structure from Ravisangar et al. (2005).

Overall, this study investigates the erosion resistance, rheological characteristic, and effects of soil physical properties for fine-grained sediments. The regression models developed in this study, either multilinear or power relationships, quantify the influences of the soil properties on the critical shear stress and yield stress, as well as the correlation between the two stresses. In application, for sediments with $d_{50} < 100$ μm and composed of silty/clayey soils without large organic matter content, values of critical shear stress can be estimated initially and efficiently using the soil physical properties that can be measured by conventional geotechnical tests. Furthermore, the yield stress can be obtained from rheometer tests and thus can be used to predict the critical shear stress of fine-grained sediments. Therefore, this research provides a methodology for predicting the critical shear stress of fine sediment beds in engineering applications related to risk assessment associated with failure of the foundations of hydraulic structures such as bridges.

## 6.3 Research Contributions

Through the laboratory work and data analysis of fine-grained sediments completed in this research, it has been shown that specific soil physical properties or alternatively the rheological characteristics of soils can be used to predict the erosion resistance of fine-grained sediments. The effects of the soil physical properties and pore water chemistry on the erosion resistance of fine sediments are illustrated by supportive data, and the physics is explained with the concept of interparticle structure. The multilinear regression model developed to predict the critical shear stress or Shields

249

parameter of fine sediments using bulk density/water content and clay content is an extension of the proposed relationships in the literature, most of which included either bulk density or clay/fine content only as the predicting variable. Additionally, using the same variables as for the erosion resistance prediction, the (dimensionless) yield stress of fine sediments can be predicted by the regression models. This finding is an advance in the methodology of predicting erosion resistance since an equation predicting the yield stress from soil physical properties of fine sediments has not been proposed previously in the literature. Most important of all, the equation which predicts the Shields parameter representing the dimensionless form of the critical shear stress for erosion as a function of the dimensionless yield stress of fine-grained sediments is proposed in this study for the first time.

Although more experiments using both field and laboratory prepared specimens are expected to expand the applicability of the proposed equations, this research contributes to a better understanding of the erosional and yield strengths of fine-grained sediments with different soil physical properties, and provides a methodology to predict the erosion resistance of cohesive sediment beds in hydraulic engineering applications.

## 6.4 Recommendations for Future Research

Based on current and previous studies, potential future work in the subject of fine-grain sediment erosion and transport behavior should continue the investigation of relationships between soil physical properties, pore water chemistry, rheological characteristics, and erosion resistance of the sediments. In the future, the applicability of the results from this research may be expanded in the following proposed studies:

- To investigate difference in interparticle cohesion dependent on clay minerals, use different types of clay, such as illites or bentonites, as specimens, and compare the erosional and yield strengths of soils with different clay minerals.

- To validate the relationships of critical shear stress versus bulk density for different predominant particle associations dependent on pore water chemistry, control the pH value, ionic strength, or even add organic matter to the silt-clay soil mixtures.

- To build the connections between erosion data obtained from laboratory prepared specimens and field collected sediments, include and integrate results from other field studies in addition to the previous research presented by Ravisangar et al. (2001; 2005), Navarro (2004), and Hobson (2008).

- To strengthen physical understanding of the relationships among erosion resistance, soil properties, and interparticle structure of fine sediments, apply techniques of SEM image analysis such as pattern recognition for a more quantitative description of particle associations and soil fabric.

# REFERENCES

Aberle, J., Nikora, V., McLean, S., Doscher, C., McEwan, I., Green, M., Goring, D., and Walsh, J. (2003). "Straight benthic flow-through flume for in situ measurement of cohesive sediment dynamics." *J. Hydraul. Eng.*, 129(1), 63-67.

Aberle, J., Nikora, V., and Walters, R. (2004). "Effects of bed material properties on cohesive sediment erosion." *Mar. Geol.*, 207(1-4), 83-93.

Aberle, J., Nikora, V., and Walters, R. (2006). "Data interpretation for in situ measurements of cohesive sediment erosion." *J. Hydraul. Eng.*, 132(6), 581-588.

Ackerman, C. T., Fleming, M. J., and Brunner, G. W. (2008). "Hydrologic and hydraulic models for performing dam break studies." W. B. Roger and W. Jr. Raymond, eds., American Society of Civil Engineers, 285.

Alvarez-Hemandez, E. (1990). "The influence of cohesion on sediment movement in channels of circular cross section," Ph.D. thesis, University of Newcastle upon Tyne.

Amos, C. L., Bergamasco, A., Umgiesser, G., Cappucci, S., Cloutier, D., DeNat, L., Flindt, M., Bonardi, M., and Cristante, S. (2004). "The stability of tidal flats in venice lagoon--the results of in-situ measurements using two benthic, annular flumes." *J. Marine Syst.*, 51(1-4), 211-241.

Amos, C. L., Daborn, G. R., Christian, H. A., Atkinson, A., and Robertson, A. (1992). "In situ erosion measurements on fine-grained sediments from the bay of fundy." *Mar. Geol.*, 108(2), 175-196.

Amos, C. L., Grant, J., Daborn, G. R., and Black, K. (1992). "Sea carousel--a benthic, annular flume." *Estuar. Coast. Shelf S.*, 34(6), 557-577.

Amos, C. L., Umgiesser, G., Ferrarin, C., Thompson, C. E. L., Whitehouse, R. J. S., Sutherland, T. F., and Bergamasco, A. (2010). "The erosion rates of cohesive sediments in venice lagoon, Italy." *Cont. Shelf Res.*, 30(8), 859-870.

Ancey, C. (2007). "Plasticity and geophysical flows: A review." *J. Non-Newton. Fluid*, 142(1-3), 4-35.

Ansari, S. A., Kothyari, U. C., and Kittur, G. a. R. (2003). "Influence of cohesion on scour under submerged circular vertical jets." *J. Hydraul. Eng.*, 129(12), 1014-1019.

Ariathurai, C. R. (1874). "A finite element model for sediment transport in estuaries," PhD thesis, University of California, Davis, CA.

Ariathurai, R., and Arulanandan, K. (Year). "Erosion of cohesive soils." *Proc. Am. Soc. Civil Eng., J. Hydraul. Div.*, 279-283.

Ariathurai, R., and Krone, R. B. (Year). "Finite element model for cohesive sediment transport." *Proc. Am. Soc. Civil Eng., J. Hydraul. Div.*, 323-338.

Arup Kumar, S., and Mimi Das, S. (2006). "Dam break hydraulics in natural rivers." G. Randall, ed., American Society of Civil Engineers, 69.

ASTM C136 (2001). "Standard test method for sieve analysis of fine and coarse aggregate." West Conshohochen, P., American Society for Testing and Materials.

ASTM D422-63 (2002). "Standard test method for particle-size analysis of solids." West Conshohochen, P., American Society for Testing and Materials.

ASTM D3418 (2005). "Standard test method for liquid limit, p. l., and plasticity index of soils." West Conshohochen, PA, American Society for Testing and Materials.

ASTM D 854 (2006). "Standard test methods for specific gravity of soil solids by water pycnometer" West Conshohochen, P., American Society for Testing and Materials.

ASTM D 1140 (2000). "Standard test methods for amount of material in soils finer than the No. 200 (75-μm) sieve." West Conshohochen, P., American Society for Testing and Materials.

ASTM D 2216 (2005). "Moisture content of soil." West Conshohochen, P., American Society for Testing and Materials.

ASTM D 2487 (2006). "Standard Practice for Classification of Soils for Engineering Purposes (Unified Soil Classification System)." West Conshohochen, P., American Society for Testing and Materials.

Avena, M. J., Valenti, L. E., Pfaffen, V., and De Pauli, C. P. (2001). "Methylene blue dimerization does not interfere in surface-area measurements of kaolinite and soils." *Clays and Clay Minerals*, 49(2), 168-173.

Avnimelech, Y., Ritvo, G., Meijer, L. E., and Kochba, M. (2001). "Water content, organic carbon and dry bulk density in flooded sediments." *Aquacultural Engineering*, 25(1), 25-33.

Awal, R., Nakagawa, H., Kawaike, K., Baba, Y., and Zhang, H. (Year). "Study on glacial lake outburst flood." *International Symposium on Water and Sediment Disasters in East Asia*, 213-222.

Bale, A. J., Stephens, J. A., and Harris, C. B. (2007). "Critical erosion profiles in macro-tidal estuary sediments: Implications for the stability of intertidal mud and the slope of mud banks." *Cont. Shelf Res.*, 27(18), 2303-2312.

Bale, A. J., Widdows, J., Harris, C. B., and Stephens, J. A. (2006). "Measurements of the critical erosion threshold of surface sediments along the tamar estuary using a mini-annular flume." *Cont. Shelf Res.*, 26(10), 1206-1216.

Bardou, E., Ancey, C., Bonnard, C., and Vulliet, L. (2003). "Classification of debris flow deposits for hazard assessment in alpine areas." In: *Debris flow mechanics and mitigation conference*, C. L. Chen and D. Rickenmann, eds., Mills Press, Davos, 799–808.

Barnes, H. A. (1999). "The yield stress---a review or 'παντα ρει'--- everything flows?" *J. Non-Newton. Fluid*, 81(1-2), 133-178.

Barnes, H. A., and Nguyen, Q. D. (2001). "Rotating vane rheometry --a review." *J. Non-Newton. Fluid*, 98(1), 1-14.

Barry, K. M., Thieke, R. J., and Mehta, A. J. (2006). "Quasi-hydrodynamic lubrication effect of clay particles on sand grain erosion." *Estuar. Coast. Shelf S.*, 67(1-2), 161-169.

Basudhar, P. K., and Dey, A. (2010). "Applicability of burger model in predicting the response of viscoelastic soil beds." *GeoFlorida*, 2611-2620.

Bingham, E. C. (1922). *Fluidity and plasticity*, McGraw-Hill, New York.

Black, K., and Cramp, A. (1995). "A device to examine the in situ response of intertidal cohesive sediment deposits to fluid shear." *Cont. Shelf Res.*, 15(15), 1945-1954.

Black, K. S., and Paterson, D. M. (1997). "Measurement of the erosion potential of cohesive marine sediments: A review of current in situ technology." *J. Mar. Environ. Eng.*, 4(1), 43–83.

Black, K. S., Tolhurst, T. J., Paterson, D. M., and Hagerthey, S. E. (2002). "Working with natural cohesive sediments." *J. Hydraul. Eng.*, 128(1), 2-8.

Briaud, J. L., Chen, H. C., Li, Y., and Nurtjahyo, P. (2004). "Sricos-efa method for complex piers in fine-grained soils." *J. Geotech. Geoenviron.*, 130(11), 1180-1191.

Briaud, J. L., and Ting, F. C. K. (2001). "Erosion function apparatus for scour rate predictions." *J. Geotech. Geoenviron.*, 127(2), 105-113.

Briaud, J.-L., and Ting, F. C. K. (1999). "Sricos: Prediction of scour rate in cohesive soils at bridge piers." *J. Geotech. Geoenviron.*, 125(4), 237-246.

Brunauer, S., Emmett, P. H., and Teller, E. (1938). "Adsorption of gases in multimolecular layers." *J. Am. Chem. Soc.*, 60(2), 309-319.

Carravetta, A., Fecarotta, O., Martino, R., and Sabatino, C. (2010). "Assessment of rheological characteristics of a natural Bingham-plastic mixture in turbulent pipe flow." *J. Hydraul. Eng.*, 136(10), 820-825.

Carreau, P. J. (1968). "Rheological equations from molecular network theories," Ph.D. Thesis, University of Wisconsin, Madison.

Carrivick, J. L. (2010). "Dam break - outburst flood propagation and transient hydraulics: A geosciences perspective." *Journal of Hydrology*, 380(3-4), 338-355.

Casson, N. (1959). *Rheology of disperse system*, Pergamon, London, U.K.

Castro-Orgaz, O., and Hager, W. H. (2011). "Turbulent near-critical open channel flow: Serre's similarity theory." *J. Hydraul. Eng.*, 137(5), 497-503.

Cetina, M., Rajar, R., Hojnik, T., Zakrajšek, M., and Mario Krzyk. (2006). "Case study: Numerical simulations of debris flow below Stoze, Slovenia." *J. Hydraul. Eng.*, 132(2), 121-130.

Chanson, H., Jarny, S., and Coussot, P. (2006). "Dam break wave of thixotropic fluid." *J. Hydraul. Eng.*, 132(3), 280-293.

Collyer, A. A., ed. (1993). *Techniques in rheological measurement*, 1st Ed., Chapman & Hall, London, U.K.

Collyer, A. A., and Clegg, D. W., eds. (1988). *Rheological measurement*, Elsevier Applied Science Publishers Ltd, Essex IG11 8JU, England.

Cornelisse, J. M., Mulder, H. P. J., Houwing, E. J., Williamson, H. J., and Witte, G. (1997). "On the development of instruments for in situ erosion measurements." N. Burt, R. Parker, and J. Watts, eds., Wiley, New York, 175–186.

Costa, J. E., and Schuster, R. L. (1988). "The formation and failure of natural dams." *Geol. Soc. Am. Bull.*, 100, 1054-1068.

Coussot, P., and J.M. Piau. (1995). "A large-scale field coaxial cylinder rheometer for the study of the rheology of natural coarse suspensions." *J. Rheol.*, 39, 105–124.

Coussot, P., Laigle, D., Arratano, M., Deganutti, A., and Marchi, L. (1998). "Direct determination of rheological characteristics of debris flow." *J. Hydraul. Eng.*, 124, 865–868.

Coussot, P., Raynaud, J. S., and Ancey, C. ( 2003). "Combined MRI-rheometry determination of the behavior of mud suspensions." In: *Debris flow mechanics and mitigation conference*, C. L. Chen and D. Rickenmann, eds., Mills Press, Davos, 291-301.

Cross, M. (1965). "Rheology of non-Newtonian fluids: A new flow equation for pseudo-plastic systems." *J. Coll. Sci.*, 20, 417–437.

Cui, P., Zhu, Y.-y., Han, Y.-s., Chen, X.-q., and Zhuang, J.-q. (2009). "The 12 may Wenchuan earthquake-induced landslide lakes: Distribution and preliminary risk evaluation." *Landslides*, 6(3), 209-223.

Czibulya, Z., Tomba'cz, E., Szegi, T. s., Miche'li, E., and Zsolnay, A. d. m. (2010). "Standard state of soil dispersions for rheological measurements." *Appl. Clay Sci.*, 48(4), 594-601.

Dade, W. B., and Nowell, A. R. M. (1991). "Moving muds in the marine environment." In: *Speciality Conference/WR Div.*, American Society of Civil Engineers, Seattle, WA, 54-71.

Dade, W. B., Nowell, A. R. M., and Jumars, P. A. (1992). "Predicting erosion resistance of muds." *Mar. Geol.*, 105(1-4), 285-297.

Dai, F. C., Lee, C. F., Deng, J. H., and Tham, L. G. (2005). "The 1786 earthquake-triggered landslide dam and subsequent dam-break flood on the Dadu river, southwestern china. ." *Geomorphology*, 65, 205–221.

Dang, C., Cui, P., and Cheng, Z.-l. (2009). "The formation and failure of debris flow-dams, background, key factors and model tests: Case studies from china." *Environmental Geology*, 57(8), 1901-1910.

De Blasio, F. V., Breien, H., and Elverhøi, A. (2011). "Modelling a cohesive-frictional debris flow: An experimental, theoretical, and field-based study." *Earth Surf. Processes*, 36(6), 753-766.

Debnath, K., and Chaudhuri, S. (2010a). "Bridge pier scour in clay-sand mixed sediments at near-threshold velocity for sand." *J. Hydraul. Eng.*, 136(9), 597-609.

Debnath, K., and Chaudhuri, S. (2010b). "Laboratory experiments on local scour around cylinder for clay and clay-sand mixed beds." *Eng. Geol.*, 111(1-4), 51-61.

Debnath, K., Nikora, V., Aberle, J., Westrich, B., and Muste, M. (2007). "Erosion of cohesive sediments: Resuspension, bed load, and erosion patterns from field experiments." *J. Hydraul. Eng.*, 133(5), 508-520.

Debnath, K., Nikora, V., and Grace, C. (2004). "Erosion of cohesive sediments in Canterbury streams." *The Water Balance, Book of Abstracts of the New Zealand Hydrological Society Symp., Queenstown, New Zealand*, 67–68.

Dennett, K. E., Sturm, T. W., Amirtharajah, A., and Mahmood, T. (1998). "Effects of adsorbed natural organic matter on the erosion of kaolinite sediments." *Water Environ. Res.*, 70(3), 268-275.

DiBiase, R. A., Whipple, K. X., Heimsath, A. M., and Ouimet, W. B. (2010). "Landscape form and millennial erosion rates in the san Gabriel mountains, ca." *Earth Planet. Sc. Lett.*, 289(1-2), 134-144.

Dickhudt, P. J., Friedrichs, C. T., and Sanford, L. P. (2011). "Mud matrix solids fraction and bed erodibility in the York river estuary, USA, and other muddy environments." *Cont. Shelf Res.*, 31(10, Supplement 1), S3-S13.

Droppo, I. G., Ross, N., Skafel, M., and Liss, S. N. (2007). "Biostabilization of cohesive sediment beds in a freshwater wave-dominated environment." *Limnol. Oceanogr.*, 52(2), 577-589.

Droppo, I. G., and Stone, M. (1994). "In-channel surficial fine-grained sediment laminae. Part I: Physical characteristics and formational processes." *Hydrol. Process.*, 8(2), 101-111.

Dunn, I. S. (1959). "Tractive resistance of cohesive channels." *J. Soil Mech. Found.*, 85, 1-24.

El Ganaoui, O., Schaaff, E., Boyer, P., Amielh, M., Anselmet, F., and Grenz, C. (2007). "Erosion of the upper layer of cohesive sediments: Characterization of some properties." *J. Hydraul. Eng.*, 133(9), 1087-1091.

Elfalan, D. (2008). "Hawaii dam break analysis follow-on actions." American Society of Civil Engineers, 438.

Erich, B. (2010). "Modeling rheological properties of coarse grained materials." *GeoFlorida*, 430-439.

Ettema, R., Kirkil, G., and Muste, M. (2006). "Similitude of large-scale turbulence in experiments on local scour at cylinders." *J. Hydraul. Eng.*, 132(1), 33-40.

Ettema, R., Melville, B. W., and Barkdoll, B. (1998). "Scale effect in pier-scour experiments." *J. Hydraul. Eng.*, 124(6), 639-642.

Feagin, R. A., Lozada-Bernard, S. M., Ravens, T. M., Moller, I., Yeager, K. M., and Baird, A. H. (2009). "Does vegetation prevent wave erosion of salt marsh edges." *Proceedings of the National Academy of Sciences*, 106(25), 10109-10113.

Fei, X. J. (1981). "Bingham yield stress of sediment water mixtures with hyperconcentration." *J. Sediment. Res.*, 3(Beijing, China), 19-28 (in Chinese).

Fread, D. L. (1988 (revised 1991)). "Breach: An erosion model for earthen dam failures." O. o. H. National Weather Service, Silver Spring, Md., ed.

Fread, D. L. (1984). "Dambrk: The NWS dam-break flood forecasting model." O. o. H. National Weather Service, Silver Spring, Md., ed.

Fread, D. L. (Year). "Nws fldwav model: The replacement of dambrk for dam-break flood prediction." *Dam Safety ' 93, Proc., 10th Annual ASDSO Conf., Association of State Dam Safety Officials, Lexington, KY.*, 177–184.

Gary, W. B. (2003). "Dam and levee breaching with HEC-RAS." B. Paul and D. Paul, eds., American Society of Civil Engineers, 49.

Gee, D. M., and Gary, W. B. (2005). "Dam break flood routing using HEC-RAS and NWS-fldwav." W. Raymond, ed., American Society of Civil Engineers, 401.

Gee, R. E., and Lyon, J. B. (1957). "Nonisothermal flow of viscous non-Newtonian fluids." *Ind. Eng. Chem.*, 49, 956-960.

Gerbersdorf, S., Jancke, T., and Westrich, B. (2007). "Sediment properties for assessing the erosion risk of contaminated riverine sites. An approach to evaluate sediment properties and their covariance patterns over depth in relation to erosion resistance. First investigations in natural sediments(11 pp)." *J. Soil. Sediment.*, 7(1), 25-35.

Gerbersdorf, S. U., Jancke, T., and Westrich, B. (2005). "Physico-chemical and biological sediment properties determining erosion resistance of contaminated riverine sediments — temporal and vertical pattern at the Lauffen reservoir/river Neckar, Germany. ." *Limnologica*, 35(3), 132-144.

Geremew, A. M., and Yanful, E. K. (2011). "Behavior of mine tailings under cyclic hydraulic loading." *Can. J. Civil Eng.*, 38(2), 131-140.

Goodell, C. R. (2005). "Dam break modeling for tandem reservoirs---a case study using HEC-RAS and HEC-HMS." W. Raymond, ed., American Society of Civil Engineers, 402.

Grabowski, R. C., Droppo, I. G., and Wharton, G. (2010). "Estimation of critical shear stress from cohesive strength meter-derived erosion thresholds." *Limnol. Oceanogr.-Meth.*, 8, 678-685.

Grabowski, R. C., Droppo, I. G., and Wharton, G. (2011). "Erodibility of cohesive sediment: The importance of sediment properties." *Earth-Sci. Rev.*, 105(3-4), 101-120.

Guidoux, C., Faure, Y.-H., Beguin, R., and Ho, C.-C. (2010). "Contact erosion at the interface between granular coarse soil and various base soils under tangential flow condition." *J. Geotech. Geoenviron.*, 136(5), 741-750.

Gularte, R. C., Kelly, W. E., and Nacci, V. A. (1980). "Erosion of cohesive sediments as a rate process." *Ocean Eng.*, 7, 539-551.

Gust, G., and Morris, M. J. (1989). "Erosion thresholds and entrainment rates of undisturbed in situ sediments." *J. Coastal Res.*, 5, 87-99.

Hackley, V. A., and Ferraris, C. F. (2001). "Guide to rheological nomenclature: Measurements in ceramic particulate systems." NIST, National Institute of Standards and Technology.

Hammarström, D. (2004). "A model for simulation of fiber suspension flows," Royal Institute of Technology, Stockholm, Sweden.

Hanlong, L., Cui, Y., Gao, H., Xiao, Y., and Sun, Y. (2011). "Modeling of rheological behavior of geomaterials based on fractional viscoelastic equation with variable parameters." *Instrumentation, Testing, and Modeling of Soil and Rock Behavior*, 107-114.

Hanson, G. J. (1990). "Surface erodibility of earthen channels at high stresses: Part I. Open channel testing. ." *T. Am. Soc. Agr. Eng.*, 33(1), 127-131.

Hanson, G. J. (1991). "Development of a jet index to characterize erosion resistance of soils in earthen spillways." *T. Am. Soc. Agr. Eng.*, 34, 2015-2020.

Hanson, G. J., and Simon, A. (2001). "Erodibility of cohesive streambeds in the loess area of the Midwestern USA." *Hydrol. Process.*, 15(1), 23-38.

Henry, H. H., and Raymond, W. (2008). "Advanced guidance on use of steady HEC-RAS." W. B. Roger and W. Jr. Raymond, eds., American Society of Civil Engineers, 201.

Herschel, W. H., and Bulkley, R. (1926). "Measurement of consistency as applied to rubber benzene solutions." *Proceedings of American Society for Testing Materials*(26), 621-633.

Hillier, S. (1995). *Erosion, sedimentation and sedimentary origin of clays*, Springer, New York.

Hjulström, F. (1939). "Transportation of detritus by moving water." In: *Recent marine sediments*, P. D. Trask, ed., Am. Assoc. Pet. Geol., Tulsa, , 5-31.

Hobson, P. M. (2008). "Rheologic and flume erosion characteristics of Georgia sediments from bridge foundations," Master Thesis, Georgia Institute of Technology, Atlanta, GA.

Hoepner, M. A. (2001). "Stability of cohesive sediments from flume and rheometer measurements," Master Thesis, Georgia Institute of Technology, Atlanta, GA.

Holtz, R. D., and Kovacs, W. D. (1981). *An introduction of geotechnical engineering*, Prentice Hall, New York.

Houwing, E. J. (1999). "Determination of the critical erosion threshold of cohesive sediments on intertidal mudflats along the Dutch Wadden sea coast." *Estuar. Coast. Shelf S.*, 49(4), 545-555.

Houwing, E.-J., and van Rijn, L. C. (1998). "In situ erosion flume (ISEF): Determination of bed-shear stress and erosion of a kaolinite bed." *J. Sea Res.*, 39(3-4), 243-253.

Houwink, R. (1958). *Elasticity, plasticity and structure of matter*, 42 Ed., Dover, New York.

Hu, H. (2005b). "Analysis on the percentage of clay influencing characteristics and mechanism of rheological parameters of Sullage soft-soil." *Geotech. Eng. World*, 11, 34-36.

Hu, H. (2005a). "The influencing characteristics and mechanism of water content on rheological parameters of soft-soil." *Geotech. Eng. Tech.*, 19(3), 134-136.

Hu, H., and Zhou, X. Z. (2011). "Research on factors influencing characteristics experimentation and mechanism of rheological parameters of soft-soil." *Adv. Mat. Res.*, 243-249, 3123-3127.

Huynh, N., Isobe, M., Kobayashi, T., and Watanabe, A. (1990). "An experimental study on rheological properties of mud in the coastal waters." *Proceedings of Coastal Engineering JSCE*, 37, 225–229 (in Japanese).

Israelachvili, J. (1992). *Intermolecular and surface forces*, 2 Ed., Academic Press, New York.

Jacobs, W. (2009). "Erosion of sand-mud mixtures," Ph.D. thesis, Delft University of Technology Delft, Netherlands.

Jain, M., and Mehta, A. J. (2009). "Role of basic rheological models in determination of wave attenuation over muddy seabeds." *Cont. Shelf Res.*, 29(3), 642-651.

Jepsen, R., Roberts, J., and Lick, W. (1997). "Effects of bulk density on sediment erosion rates." *Water Air Soil Poll.*, 99(1), 21-31.

Jesse, R., Rich, J., Doug, G., and Wilbert, L. (1998). "Effects of particle size and bulk density on erosion of quartz particles." *J. Hydraul. Eng.*, 124(12), 1261-1267.

Jiang, J., Ganju, N. K., and Mehta, A. J. (2004). "Estimation of contraction scour in a riverbed using serf." *J. Water. Port C.*, 130(3), 215-218.

Jiang, Q., and Watanabe, A. (1995). "Rheological properties of soft mud and a numerical model for its motion under waves." *Coast. Eng. Japan*, 38(2), 195–214.

Jing, L., and Ridd, P. V. (1996). "Wave-current bottom shear stresses and sediment resuspension in Cleveland bay, Australia." *Coast. Eng.*, 29(1-2), 169-186.

Julien, P. Y., and Lan, Y. (1991). "Rheology of hyperconcentrations." *J. Hydraul. Eng.*, 117(3), 346-353.

Jumars, P. A., and Nowell, A. R. M. (1984 ). "Effects of benthos on sediment transport — difficulties with functional grouping." *Cont. Shelf Res.*, 3(2), 115-130.

Karmaker, T., and Dutta, S. (2011). "Erodibility of fine soil from the composite river bank of Brahmaputra in India." *Hydrol. Process.*, 25(1), 104-111.

Karunarathna, H., and Tanimoto, K. (1996). "Long-period water surface fluctuations on a horizontal coastal shelf with a steep seaward face." *Coast. Eng.*, 29(1-2), 123-147.

Klubertanz, G., Laloui, L., and Vulliet, L. (2009). "Identification of mechanisms for landslide type initiation of debris flows." *Eng. Geol.*, 109(1-2), 114-123.

Koichi, U., Toshihiko, K., Gordana, K.-B., Felix Kofi, A., Shigeya, M., and Junichiro, T. (2009). "Case study: Hydraulic modeling of runoff processes in Ghanaian inland valleys." *J. Hydraul. Eng.*, 135(7), 539-553.

Kothyari, U. C., and Jain, R. K. (2008). "Influence of cohesion on the incipient motion condition of sediment mixtures." *Water Resour. Res.*, 44(4), W04410.

Kranenberg, C. (1994). "The fractal structure of cohesive sediment aggregates." *Estuar. Coast. Shelf S.*, 39, 451-460.

Krone, R. B. (1999). "Effects of bed structure on erosion of cohesive sediments." *J. Hydraul. Eng.*, 125(12), 1297-1301.

Kuijper, C., Comelisse, I. M., and Winterwerp, I. C. (1989). "Research on erosive properties of cohesive sediments." *J. Geophys. Res.*, 94(CIO), 14341-14350.

Kutner, M., Nachtsheim, C., Neter, J., and Li, W. (2004). *Applied linear statistical models*, 5th Ed., McGraw-Hill/Irwin, New York.

Lee, K. T., and Lin, Y.-T. (2006). "Flow analysis of landslide dammed lake watersheds: A case study." *Journal of the American Water Resources Association*, 42(6), 1615-1628.

Leont'yev, I. O. (1996). "Numerical modelling of beach erosion during storm event." *Coast. Eng.*, 29(1-2), 187-200.

Li, M.-H., Hsu, M.-H., Hsieh, L.-S., and Teng, W.-H. (2002). "Inundation potentials analysis for Tsao-Ling landslide lake formed by chi-chi earthquake in Taiwan." *Natural Hazards*, 25(3), 289-303.

Lick, W. (1982). "The transport of contaminants in the great lakes." *Annu. Rev. Earth Pl. Sc.*, 10, 327-253.

Lick, W., Lijun, J., and Gailani, J. (2004). "Initiation of movement of quartz particles." *J. Hydraul. Eng.*, 130(8), 755-761.

Lick, W., and McNeil, J. (2001). "Effects of sediment bulk properties on erosion rates." *The Science of The Total Environment*, 266(1-3), 41-48.

Liddel, P. V., and Boger, D. V. (1996). "Yield stress measurements with the vane." *J. Non-Newton. Fluid*, 63(2-3), 235-261.

Lind, J. E., Zwolenlink, J. J., and Fuoss, R. M. (1959). "Calibration of conductance cells at 25 degrees with aqueous solutions of potassium chloride." *J. Am. Chem. Soc.*, 81, 1557.

Liu, F., Fu, X., and Wang, G. (Year). "Physically based simulation of dam breach development for Tangjiashan quake dam, china." *International Symposium on Water and Sediment Disasters in East Asia*, 197-212.

Lyklema, J. (1991). *Fundamentals of interface and colloid science - volume I: Fundamentals*, Academic Press, New York.

Maa, J. P. Y., Wright, L. D., Lee, C. H., and Shannon, T. W. (1993). "Vims sea carousel: A field instrument for studying sediment transport." *Mar. Geol.*, 115(3-4), 271-287.

MacArthur, R., Wong, K., and Bennett, T. (2008). "Hydrologic modeling for dam break analyses in Hawai'i." W. B. Roger and W. Jr. Raymond, eds., American Society of Civil Engineers, 286.

Macchione, F., and Sirangelo, B. (1988). "Study of earth dam erosion due to overtopping." *Proc. Technical Conf. on Hydrology of Disasters, WMO, Geneva*, 212-219.

Mackin, J. H. (1948). "Concept of the graded river." *Geol. Soc. Am. Bull.*, 59, 463-512.

Mahmood, T. (1996). "The mechanics of asymmetric particle release during filter backwashing and migration of colloids," PhD thesis, Georgia Institute of Technology, Atlanta.

Mahmood, T., Amirtharajah, A., Sturm, T. W., and Dennett, K. E. (2000). "A micromechanics approach for attachment and detachment of asymmetric colloidal particles." *Colloid. Surface. A*, 177(2-3), 99-110.

Mahmood, T., Amirtharajah, A., Sturm, T. W., and Dennett, K. E. (2001). "A micromechanics approach for attachment and detachment of asymmetric colloidal particles." *Colloid. Surface. A*, 177(2), 99-110.

Major, J. J., and Pierson, T. C. (1992). "Debris flow rheology: Experimental analysis of fine-grained slurries." *Water Resour. Res.*, 28(3), 841-857.

Malkin, A. Y. (1994). *Rheology fundamentals*, ChemTec Publishing.

Malkin, A. Y., and Isayev, A. I. (2006). *Rheology - concepts, methods, & applications*, ChemTec Publishing.

Martino, R. (2003). "Experimental analysis on the rheological properties of a debris-flow deposit." In: *Debris flow mechanics and mitigation conference*, C. L. Chen and D. Rickenmann, eds., Mills Press, Davos, 363–373.

Mazurek, K. A., Rajaratnam, N., and Sego, D. C. (2001). "Scour of cohesive soil by submerged circular turbulent impinging jets." *J. Hydraul. Eng.*, 127(7), 598-606.

McNeil, J., Taylor, C., and Lick, W. (1996). "Measurements of erosion of undisturbed bottom sediments with depth." *J. Hydraul. Eng.*, 122(6), 316-324.

Mehta, A. J. (1991). "Review notes on cohesive sediment erosion. In kraus, n. C., Gingerich, k. J., and Kriebel, d. L., editors." *Coastal Sediments*, 1, 40-53.

Mehta, A. J., Hayter, E. J., Parker, W. R., Krone, R. B., and Teeter, A. M. (1988). "Cohesive sediment transport. I: Process description " *J. Hydraul. Eng.*, 115(8), 1076-1093.

Mehta, A. J., and Lee, S. C. (1994). "Problems in linking the threshold condition for the transport of cohesionless and cohesive diment grain." *J. Coastal Res.*, 10(1), 170-177.

Mehta, A. J., and Partheniades, E. (1982). "Resuspension of deposited cohesive sediment beds." *18th International Conference on Coastal Engineering, Coastal Engineering Research Council*, Cape Town, South Africa.

Melville, B. W. (1997). "Pier and abutment scour: Integrated approach." *J. Hydraul. Eng.*, 123(2), 125–136.

Meter, D. M., and Bird, R. B. (1964). "Tube flow of non-Newtonian polymer solutions: Part I. Laminar flow and rheological models." *AICHE J.*, 10(878-881).

Michael J Bovis, M. J. (2000). "The July 29, 1998, debris flow and landslide dam at Capricorn creek, mount meager volcanic complex, southern coast mountains, British Columbia. ." *Canadian Journal of Earth Sciences*, 37(10), 1321-1334.

Migniot, C. (1968). "Etude des propriétés physiques de différents sédiments très fins et de leur comportement sous des actions hydrodynamiques." *La Houille Blanche*, 7, 591-620.

Miller, M. C., McCave, I. N., and Komer, P. D. (1977). "Threshold of sediment motion under unidirectional currents." *Sedimentology*, 24, 507-527.

Mishra, P. K., Prasad, S. S., Babu, B. M., and Varalakshmi, L. R. (2001). "Bentonite as an ameliorant in an Alfisol---a laboratory study." *J. Irrig. Drain. E.*, 127(2), 118-122.

Mitchener, H., and Torfs, H. (1996). "Erosion of mud/sand mixtures." *Coast. Eng.*, 29(1-2), 1-25.

Murray, H. H. (2007). *Applied clay mineralogy-occurrences, processing and application of kaolins, bentonites, palygorskite-sepiolite, and common clays*, Elsevier, Oxford, UK.

Navarro, H. R. (2004). "Flume measurements of erosion characteristics of soils at bridge foundations in Georgia," Master Thesis, Georgia Institute of Technology, Atlanta, GA.

Nguyen, Q. D., and Boger, D. V. (1992). "Measuring the flow properties of yield stress fluids." *Annu. Rev. Fluid Mech.*, 24(1), 47-88.

Nowell, A. R. M., McCave, I. N., and Hollister, C. D. (1985). "Contributions of Hebble to understanding marine sedimentation." *Mar. Geol.*, 66(1-4), 397-409.

O'Brien, J. S., and Julien, P. Y. (1985). "Physical properties and mechanics of hyperconcentrated sediment flows." *Proc. of the Specialty Conference on Delineation of Landslides, Flash Flood and Debris Flow Hazards in Utah*, Utah Water Research Laboratory, 260-279.

O'Brien, J. S., and Julien, P. Y. (1988). "Laboratory analysis of mudflow properties." *J. Hydraul. Eng.*, 114(8), 877-887.

Osman, A. M., and Thorne, C. R. (1988). "Riverbank stability analysis: I. Theory." *J. Hydraul. Eng.*, 114(2), 134-150.

Ostwald, W. (1925). "Ueber die geschwindigkeitsfunktion der viskositat disperser systeme." *I. Kolloid-Z.*, 36, 99-117.

Otsubo, K., and Muraoka, K. (1988). "Critical shear stress of cohesive bottom sediments." *J. Hydraul. Eng.*, 114(10), 1241-1256.

Oveisy, A., Hall, K., Soltanpour, M., and Shibayama, T. (2009). "A two-dimensional horizontal wave propagation and mud mass transport model." *Cont. Shelf Res.*, 29(3), 652-665.

Owen, M. W. (1975). "Erosion of Avonmouth mud." *Hydraulics Research Station, Report INT 150*, 17.

Panagiotopoulos, I., Voulgaris, G., and Collins, M. B. (1997). "The influence of clay on the threshold of movement of fine sandy beds." *Coast. Eng.*, 32(1), 19-43.

Parchure, T. M., and Mehta, A. J. (1985). "Erosion of soft cohesive sediment deposits " *J. Hydraul. Eng.*, 111(10), 1308-1326.

Paris, R., Fournier, J., Poizot, E., Etienne, S., Morin, J., Lavigne, F., and Wassmer, P. (2010). "Boulder and fine sediment transport and deposition by the 2004 tsunami in Lhok Nga (western Banda ache, Sumatra, Indonesia): A coupled offshore-onshore model." *Mar. Geol.*, 268(1-4), 43-54.

Partheniades, E. (1965). "Erosion and deposition of cohesive soil." *J. Hydraul. Eng.*, 91(1), 105-139.

Partheniades, E., Cross, R. H., and Ayora, A. (1968). "Further results on the deposition of cohesive sediments." In: *Proc., J th Coast. Engrg. Cont*, American Society of Civil Engineers, New York, 723-742.

Partheniades, E., Kennedy, J. F., Etter, R. J., and Hoyer, R. P. (1966). "Investigations of the depositional behavior of fine cohesive sediments in an annular rotating channel." Ralph M. Parsons Hydrodynamic Lab., MIT, Cambridge, Mass.

Paterson, D. M. (1989). "Short-term changes in the erodibility of intertidal cohesive sediments related to the migratory behavior of epipelic diatoms." *Limnol. Oceanogr.*, 34(1), 223-234.

Picornell, M., and Nazarian, S. (1992). "Behavior of unsaturated clayey soils at high strain rates." Content for Geotechnical and Highway Materials Research, The University of Texas at El Paso, El Paso, Texas.

Postma, H., ed. (1967). *Sediment transport and sedimentation in the estuarine environment*, Publ., Washington, D.C.

Ranjan, G., and Rao, A. R. S. (2000). *Basic and applied soil mechanics*, 2nd ed. Ed., New edge international publishers, New Delhi, India.

Raudkivi, A. J., and Ettema, R. (1983). "Clear-water scour at cylindrical piers." *J. Hydraul. Eng.*, 109(3), 338–350.

Raveendran, P., and Amirtharajah, A. (1995). "Role of short range forces in particle detachment during filter backwashing." *J. Environ. Eng.*, 121, 860-868.

Ravens, T. M., and Gschwend, P. M. (1999). "Flume measurements of sediment erodibility in Boston harbor." *J. Hydraul. Eng.*, 125(10), 998-1005.

Ravisangar, V. (2001). "The role of sediment chemistry in stability and resuspension characteristics of cohesive sediments," Ph.D. Thesis, Georgia Institute of Technology, Atlanta.

Ravisangar, V., Dennett, K. E., Sturm, T. W., and Amirtharajah, A. (2001). "Effect of sediment ph on resuspension of kaolinite sediments." *J. Environ. Eng.*, 127(6), 531-538.

Ravisangar, V., Sturm, T. W., and Amirtharajah, A. (2005). "Influence of sediment structure on erosional strength and density of kaolinite sediment beds." *J. Hydraul. Eng.*, 131(5), 356-365.

Reddi, L., Lee, I.-M., and Bonala, M. (2000). "Comparison of internal and surface erosion using flow pump tests on a sand-kaolinite mixture." *Geotech. Test. J.*, 23(1), 116-122.

Reddi, L. N., and Bonala, M. V. S. (1997). "Critical shear stress and its relationship with cohesion for sad-kaolinite mixtures." *Can. Geotech. J.*, 34(1), 26-33.

Rehmi, R. K., Nakagawa, H., Kawaike, K., Baba, Y., and Zhang, H. (Year). "Analysis of landslide dam failure due to transient seepage." *International Symposium on Water and Sediment Disasters in East Asia*, 64-71.

Remaˆıtre, A., Malet, J.-P., Maquaire, O., Ancey, C., and Locat, J. (2005). "Flow behaviour and runout modelling of a complex debris flowing a clay-shale basin." *Earth Surf. Proc. Land.*, 30, 479–488.

Righetti, M., and Lucarelli, C. (2007). "May the shields theory be extended to cohesive and adhesive benthic sediments?" *J. Geophys. Res.*, 112(C5), C05039.

Roberts, J., and Jepsen, R. (1998). "Effects of particle size and bulk density on erosion of quartz particles." *J. Hydraul. Eng.*, 124(12), 1261-1267.

Roberts, J. D., Jepsen, R. A., and James, S. C. (2003). "Measurements of sediment erosion and transport with the adjustable shear stress erosion and transport flume." *J. Hydraul. Eng.*, 129(11), 862-871.

Russell, L. L. (1976). "Chemical aspects of groundwater recharge with wastewaters," PhD thesis, University of California at Berkley, Berkley.

Sanford, L. P. (2008). "Modeling a dynamically varying mixed sediment bed with erosion, deposition, bioturbation, consolidation, and armoring." *Comput. Geosci.*, 34(10), 1263-1283.

Sanford, L. P., and Maa, J. P. Y. (2001). "A unified erosion formulation for fine sediments." *Mar. Geol.*, 179(1-2), 9-23.

Santamarina, J. C. (2001). "Soil behavior at the microscale: Particle forces. Proc. Symp. Soil behavior and soft ground construction, in honor of Charles c. Ladd." pages 1–32.

Santamarina, J. C., Klein, K. A., and Fam, M. A. (2001). *Soils and waves: Particulate materials behavior, characterization and process monitoring*, John Wiley & Sons Ltd., New York.

Santamarina, J. C., Klein, K. A., Wang, Y. H., and Prencke, E. (2002). "Specific surface: Determination and relevance." *Can. Geotech. J.*, 39(1), 233-241.

Schatzmann, M., Fischer, P. F., and Bezzola, G. R. (2003). "Rheological behavior of fine and large particle suspensions." *J. Hydraul. Eng.*, 129, 796–803.

Schramm, G. (1994). *A practical approach to rheology and rheometry*, HAAKE, Karlsruhe, Germany.

Shang, Y., Yang, Z., Li, L., Liu, D., Liao, Q., and Yangchun, W. (2003). "A super-large landslide in Tibet in 2000: Background, occurrence, disaster, and origin." *Geomorphology*, 54, 225–243

Sharif, A., and Atkinson, J. (2012). "Model for surface erosion of cohesive soils." *J. Hydraul. Eng.*, 138(7), 581-590.

Sheng, Y. P., and Lick, W. (1979). "The transport and resuspension of sediments in a shallow lake. ." *J. Geophys. Res.*, 84, 1809-1826.

Sheng, Y. P., and Villaret, C. (1989). "Modeling the effect of suspended sediment stratification on bottom exchange processes." *J. Geophys. Res.*, 94(CIO), 14429-14444.

Sheppard, D. M., Odeh, M., and Glasser, T. (2004). "Large scale clearwater local pier scour experiments." *J. Hydraul. Eng.*, 130(10), 957-963.

Shibayama, T., and An, N. (1993). "A visco-elastic-plastic model for wave mud interaction." *Coast. Eng. Japan*, 36(1), 67–89.

Shibayama, T., Aoki, T., and Sato, S. (1989). "Mud mass transport rate due to waves: A viscoelastic model." IAHR:B567-B574.

Shieh, C. L., Chen, Y. S., Tsai, Y. J., and Wu, J. H. (2009). "Variability in rainfall threshold for debris flow after the chi-chi earthquake in central Taiwan, china." *International Journal of Sediment Research*, 24(2), 177-188.

Shieh, C.-L., Ting, C.-H., and Pan, H.-W. (2008). "Impulsive force of debris flow on a curved dam." *International Journal of Sediment Research*, 23(2), 149-158.

Shields, A. (1936). "Applications of similarity principles and turbulence research to bedload movement. Laboratory," California Institute of Technology, Hydrodynamics Laboratory Publication 167, USDA, Soil Conservation Service Cooperative, Pasadena, CA.

Shugar, D., Kostaschuk, R., Ashmore, P., Desloges, J., and Burge, L. (2007). "In situ jet-testing of the erosional resistance of cohesive streambeds." *Can. J. Civil Eng.*, 34(9), 1192-1195.

Sisko, A. W. (1958). "The flow of lubricating greases." *Ind. Eng. Chem.*, 50(1789-1792 ).

Sky, M., and Chaudhry, M. H. (1989). "Dam-break flows in curved channel." *J. Hydraul. Eng.*, 115(11), 1465-1478.

Smerdon, E. T., and Beasley, R. T. (1961). "Critical tractive forces in cohesive soils." *Agr. Eng.*, 42(1), 26-29.

Soares, C. G., Ferreira, A. M., and Cunha, C. (1996). "Linear models of the time series of significant wave height on the southwest coast of Portugal." *Coast. Eng.*, 29(1-2), 149-167.

Soltanpour, M., and Samsami, F. (2011). "A comparative study on the rheology and wave dissipation of kaolinite and natural Hendijan coast mud, the Persian gulf." *Ocean Dynam.*, 61(2), 295-309.

Steven, R. A., and Terry, L. J. (1991). "Riprap design for overtopping flow." *J. Hydraul. Eng.*, 117(8), 959-972.

Stone, M., Emelko, M. B., Droppo, I. G., and Silins, U. (2011). "Biostabilization and erodibility of cohesive sediment deposits in wildfire-affected streams." *Water Res.*, 45(2), 521-534.

Sturm, T. W. (2001). *Open channel hydraulics. Textbook series in water resources and environmental engineering*, 2 Ed., McGRaw Hill, New York.

Ternat, F., Boyer, P., Anselmet, F., and Amielh, M. (2008). "Erosion threshold of saturated natural cohesive sediments: Modeling and experiments." *Water Resour. Res.*, 44(11), W11434.

Thomsen, L., and Gust, G. (2000). "Sediment erosion thresholds and characteristics of resuspended aggregates on the western European continental margin." *Deep Sea Research Part I: Oceanographic Research Papers*, 47(10), 1881-1897.

Ting, F. C. K., Briaud, J.-L., Chen, H. C., Gudavalli, R., Perugu, S., and Wei, G. (2001). "Flume tests for scour in clay at circular piers." *J. Hydraul. Eng.*, 127(11), 969-978.

Tolhurst, T. J., Black, K. S., Paterson, D. M., Mitchener, H. J., Termaat, G. R., and Shayler, S. A. (2000). "A comparison and measurement standardization of four in situ devices for determining the erosion shear stress of intertidal sediments." *Cont. Shelf Res.*, 20(10-11), 1397-1418.

Tolhurst, T. J., Black, K. S., Shayler, S. A., Mather, S., Black, I., Baker, K., and Paterson, D. M. (1999). "Measuring the in situ erosion shear stress of intertidal sediments with the cohesive strength meter (csm)." *Estuar. Coast. Shelf S.*, 49(2), 281-294.

Torfs, H., Mitchener, H., Huysentruyt, H., and Toorman, E. (1996). "Settling and consolidation of mud/sand mixtures." *Coast. Eng.*, 29(1-2), 27-45.

van Kessel, T. (1998). "Rheology of cohesive sediments: Comparison between a natural and an artificial mud." *J. Hydraul. Res.*, 36(4), 591-612.

van Ledden, M., van Kesteren, W. G. M., and Winterwerp, J. C. (2004). "A conceptual framework for the erosion behaviour of sand-mud mixtures." *Cont. Shelf Res.*, 24(1), 1-11.

van Olphen, H. (1977). *An introduction to clay colloid chemistry*, 2nd Ed., John Wiley & Sons, New York.

Van Prooijen, B. C., and Winterwerp, J. C. (2010). "A stochastic formulation for erosion of cohesive sediments." *J. Geophys. Res.*, 115(C1), C01005.

Velde, B. (1995). *Origin and mineralogy of clays*, Springer, New York.

Villaret, C., and Paulic, M. (1986). "Experiments on the erosion of deposited and placed cohesive sediments in an annular flume and a rocking flume." Florida, Gainesville.

Wahl, T. L. (1998). "Prediction of embankment dam breach parameters—a literature review and needs assessment." *Dam Safety Rep. No. DSO-98-004,U.S. Dept. of the Interior, Bureau of Reclamation, Denver.*

Wahl, T. L. (2004). "Uncertainty of predictions of embankment dam breach parameters." *J. Hydraul. Eng.*, 130(5), 389-397.

Wang, G., Fu, X., Liu, F., and Zhang, J. (Year). "Emergency analysis and treatment of quake lakes in Wenchuan earthquake-hit regions, china." *International Symposium on Water and Sediment Disasters in East Asia*, Kyoto, Japan, 24-35.

Watts, C. W., Tolhurst, T. J., Black, K. S., and Whitmore, A. P. (2003). "In situ measurements of erosion shear stress and geotechnical shear strength of the intertidal sediments of the experimental managed realignment scheme at Tollesbury, Essex, UK." *Estuar. Coast. Shelf S.*, 58(3), 611-620.

Widdows, J., Brinsley, M. D., Bowley, N., and Barrett, C. (1998). "A benthic annular flume for in situ measurement of suspension feeding/biodeposition rates and erosion potential of intertidal cohesive sediments." *Estuar. Coast. Shelf S.*, 46(1), 27-38.

Williams, P. R., and Williams, D. J. A. (1989). "Rheometry for concentrated cohesive suspensions." *J. Coastal Res.*, Spec. Iss.5, 151-164.

Williamson, H., and Ockenden, M. (1996). "Isis: An instrument for measuring erosion shear stress in situ." *Estuar. Coast. Shelf S.*, 42(1), 1-18.

Winterwerp, J. C., and van Kesteren, W. G. M. (2004). *Introduction to the physics of cohesive sediment in the marine environment*, Elsevier, Amsterdam.

Wittler, R. J., Greimann, B. P., and Wahl, T. L. (2004). "Emergency dam break analyses following the Cerro Grande fire near los Alamos, new Mexico." P. Don and S. Gerald, eds., American Society of Civil Engineers, 438.

Wongil, J., Song, C. R., Jinwon, K., Cheng, A. H. D., and Al-Ostaz, A. (2011). "Erosion study of new Orleans levee materials subjected to plunging water." *J. Geotech. Geoenviron.*, 137(4), 398-404.

Yasuda, K. (1979). "Investigation of the analogies between viscometric and linear viscoelastic properties of polystyrene fluids," Ph.D. Thesis, Massachusetts Institute of Technology Cambridge, MA.

Yin, J., and Tong, F. (2011). "Influence of sand content on the stress-strain behavior of silicon sand mixed bentonite in crs condition." *Geo-Frontiers*, 2689-2698.

Young, I. R., and Verhagen, L. A. (1996). "The growth of fetch limited waves in water of finite depth. Part 1. Total energy and peak frequency." *Coast. Eng.*, 29(1-2), 47-78.

Young, I. R., and Verhagen, L. A. (1996). "The growth of fetch limited waves in water of finite depth. Part 2. Spectral evolution." *Coast. Eng.*, 29(1-2), 79-99.

Young, I. R., Verhagen, L. A., and Khatri, S. K. (1996). "The growth of fetch limited waves in water of finite depth. Part 3. Directional spectra." *Coast. Eng.*, 29(1-2), 101-121.

Young, R. A. (1977). "Seaflume: A device for in-situ studies of threshold erosion velocity and erosional behavior of undisturbed marine muds." *Mar. Geol.*, 23(1-2), M11-M18.

Zhang, Q., Lei, T., and Zhao, J. (2008). "Estimation of the detachment rate in eroding rills in flume experiments using an re-tracing method." *Geoderma*, 147(1-2), 8-15.

Zreik, D. A., Krishanappan, B. G., Germaine, J. T., Madsen, O. S., and Ladd, C. C. (1998). "Erosional and mechanical strengths of deposited cohesive sediments." *J. Hydraul. Eng.*, 124(11), 1076-1085.